Effect of Surface Treatment on Joint Performance and Fracture Morphology in Adhesively Bonded Al-Si Coated Ultra-High Strength Steel

by

Chi-Hsiang Liao

A thesis
presented to the University of Waterloo
in fulfillment of the
thesis requirement for the degree of
Master of Applied Science
in
Mechanical and Mechatronics Engineering

Waterloo, Ontario, Canada, 2020

Author’s Declaration

I hereby declare that I am the sole author of this thesis. This is a true copy of the thesis, including any required final revisions, as accepted by my examiners.

I understand that my thesis may be made electronically available to the public.

Abstract

The Corporate average fuel economy (CAFE) standard set by the National Highway Traffic Safety Administration (NHTSA) has prompted automotive manufacturers to produce increasingly fuel efficient vehicles. Lightweighting of vehicle structures to reduce carbon dioxide emissions can be enabled by advanced materials such as hot stamped ultra-high strength steel (UHSS), but requires new joining solutions for integration in future multi-material structures. Structural adhesives enable multi-material joining, and have been used to enhance the joint performance for mono-material structures to achieve improved joint strength and stiffness. However, implementation of adhesive joining for hot stamped UHSS requires an appropriate surface treatment to maximize the joint strength and to address delamination of the brittle intermetallic coating formed on the steel during processing.

The present study investigated adhesive joining (3M™ Impact Resistant Structural Adhesive 7333, 3M™ Canada Company) of a hot stamped UHSS (Usibor® 1500-AS, ArcelorMittal Dofasco) using three surface preparation techniques: degrease using acetone (ACE), grit-blast (GB) treatment, and adhesion promotor (AP) treatment following grit-blasting. Three hot stamping thermal treatments were considered with three quenching die temperatures: room temperature (RT), 400°C, and 700°C, which varied the yield strength of the steel, and created some differences in the morphology of the intermetallic coating. The overall work examined the surface treatments for adhesive joining of hot stamped UHSS, intermetallic coating delamination mechanism and the adhesive failure morphology under different adhesive joint configurations.

Adhesively joined adherends were evaluated using the single-lap shear (SLS) test to investigate the nine material conditions (three surface treatments, three steel thermal processing treatments). The measured joint strength of the GB and AP conditions were 60% and 56%, respectively, higher than the baseline ACE treatment (p <.001). The higher strength achieved from the GB treatment was attributed to removal of the intermetallic coating.

The ACE treatment did not remove the intermetallic coating and resulted in the lowest joint strength with the largest variability of the conditions tested, attributed to intermetallic coating delamination. The intermetallic coating morphology included microcracks and Kirkendall voids, which facilitated coating delamination. The intermetallic coating delamination was associated with a measured SLS joint rotation of 2.5°-2.8° for all three thermal treatments, while the measured joint strength decreased as the thermal treatment temperature increased (22 MPa to 14 MPa). This decrease in joint strength was attributed to the lower yield strength of the adherend material enabling the critical joint rotation to be achieved at a lower applied load. Plastic deformation in the SLS adherends was observed in the GB and AP treatments for the 400°C and 700°C thermal treatments. No plastic deformation was identified for the RT thermal treatment.

The fracture surfaces from four types of adhesively bonded test specimens (Mode I opening, Mode II shear, Mixed-Mode at 45° (MM45), and SLS) comprising steel adherends without any surface coating were investigated using an optical digital microscope. Analysis of the fracture surfaces revealed qualitative differences in the morphology for different modes of loading. Shear hackles were observed for Mode II loading, while Mode I demonstrated facets on the fracture surface. The fracture surfaces were quantified using the arithmetic mean roughness (Ra). Mode I demonstrated the lowest roughness (50 µm) while Mode II had the highest Ra (103 µm), attributed in part to the shear hackles. The MM45 (80 µm) and SLS (73 µm) demonstrated intermediate roughness values, corresponding to mixed mode loading. Thus, it was found that qualitative and quantitative assessment of fracture surfaces could be associated with the mode of loading, and mode mixity.

Ultra-high strength boron steel provides an important design option for vehicle structural engineers, with high strength achieved through thermal processing but resulting in a brittle intermetallic coating that present challenges for adhesive joining. The present study investigated adhesive joint strength for boron steel, and the corresponding intermetallic coating failure pathways and their effect on joint strength measured using a single-lap shear test. The importance of surface treatment to remove the intermetallic coating was critical to achieve high joint strength with low variability.

Acknowledgements

I would like to express my gratitude towards my colleagues, friends, and family. I will start off by thanking my supervisors Duane Cronin and Michael Worswick for their astonishing mental strength and stamina from Day 1 of my master's program to the final stretch of thesis editing. They did it all in spite of their family responsibilities and other commitments. Thank you for making my palms sweat whenever I see your names on the email notifications during the last few weeks of thesis editing. It strengthened my mental toughness. A special shout-out to Duane for all the time he spent listening to my lengthy responses to simple yes/no questions. You have been teaching me to go straight to the point. I'll continue to work on it.

I also would like to thank the sponsors of my research project: Natural Sciences and Engineering Research Council (NSERC), Honda R&D Americas, ArcelorMittal Dofasco, and 3M™ Canada for their support of future engineers.

To my fellow adhesive group members, with whom I spent a lot of my lab times: Brock Watson, Brian Liu, and Luis Trimiño, we have faced and solved "sticky" challenges together and I will cherish these moments. I am particularly grateful to Brock who always work above and beyond for the best interest of the group despite always saying: "every man for himself". Shout-out to the adhesive group alumni - Yogi Nandwani who helped me get into the groove in the lab when I first started.

To the staff at Engineering Machine Shop (Jorge Cruz, Phill Laycock, Mark Kuntz, Charlie Boyle, Graeme Adair, Andrew Urschel, Brian Shuh, and Rick Forgett), your expert advice to the graduate students was instrumental to the research progress. I had the pleasure to work with Jeff Wemp, Andy Barber, Neal Griffett, Mark Griffett, and Tom Gawel who sharpened my problem solving skills.

Furthermore, I particularly enjoyed being part of the Flat Die Design Team and collaborating with Ryan George and Eckhard Budziarek. Our countless technical drawing sessions were of great fun. The amazing metallurgical micrographs are results of the polishing techniques shared by Kaab Omer. I would also like to thank Cameron O'Keeffe for providing the materials needed to complete the testing.

To the fellow IMMC members: Ahmed Ibrahim, Aleksander L. Rycman, Ania Polak, Bartlomiej Pilarczyk, David Bruneau, David Shen, Devon Hartlen, Dilaver Singh, Donata Gierczycka, Fiona Khor, Jeffrey Barker, Marwan Darweesh, Matheus A. Correia, Michael Bustamante, Miguel A. Corrales, Prasannaah Hadagali, Prusodman Sathananthan, Ramin C. Dehaghani, Mayank Kalra, Nancy Evans, Timothy Lasswell, Yu Zeng, I was going to dedicate each of you with individual funny anecdotes that we shared, but that would have taken too many pages. It has been a privilege to have met and known you all and I have learned a lot from you. I have enjoyed all our group outings together (food adventures, ski trips, basketball games, our Fridays at grad house, Secret Santa, etc.).

To my friends and lab buddies at EC4: Alireza Mohamadizadeh, Armin Abedini, Cale Peister, Farinaz Jeyranpourkhameneh, Farzad Sharifpour, Jacqueline Noder, José Imbert-Boyd, Kyubin Han, Massimo Di Ciano, Negar Baghbanaghaie, Pedram Samadian, Sante DiCecco, and Zohreh Asaee, I have enjoyed my time with you all and thank you for welcoming me with open arms and for laughing at my bad jokes, which unfortunately, further boosted my confidence.

To Wanis Nafos: we got a few good championship runs for the intramural basketball t-shirts, even though we did not reach the finals, we did well.

Finally, I want to thank my mom, my sister, and my dad for believing in me and for never giving up on me. It is hard to show gratitude through words alone, but I want to thank you for being with me every step of the journey.

Table of Contents

List of Figures

List of Tables

Chapter 1. Introduction

1.1 Motivation for Research

The National Highway Traffic Safety Administration (NHTSA) has set out a guideline and requirement for increasing vehicle fuel-efficiency through the Corporate Average Fuel Economy (CAFÉ) standards that began in 1975. To support this initiative, automotive manufacturers are conducting research and development on new efficient powertrain designs, incorporate advanced lightweight structural materials, and optimized Body-in-White (BIW) design to meet the target fuel efficiency (23.1 km/L (54.5 US miles per gallon) for light-duty vehicles by 2025 (Carley *et al.*, 2019). The body structure of a typical light-duty vehicle (LDV), classified as a vehicle with a gross weight of 3856 kg (8500 lbs) or less, represents 23 % to 28% of the total vehicle weight (U.S. Department of Energy, 2013; Birky *et al.*, 2017). With this significant contribution of the total weight from the body, lightweighting of the BIW is a key strategy to improve the fuel economy of vehicles (Cheah, 2010; Kim *et al.*, 2010; Martinsen *et al.*, 2015). The BIW is the structural component of a motor vehicle, also responsible for absorbing incoming impact during a vehicle collision and is built to protect the passengers by safely decelerating the vehicle and intentionally diverting the impact energy away from the passenger compartment (Du Bois *et al.*, 2004). The approach to lightweighting incorporates advanced materials such as aluminum, carbon fibre reinforced plastic (CFRP), magnesium, and advanced high strength steel (AHSS) to produce a multi-material lightweight vehicle (MMLV) by taking advantage of either the high strength or the low density of each material to reduce mass and meet the specific requirements of each component in the BIW.

Adhesive joining is a material assembly solution that can play a role in the fabrication of a MMLV. An important advantage of adhesive joining is the superior load distribution that results from the large joining surface area relative to a localized joining technique, such as resistance spot welding (RSW), self-piercing

rivets, and mechanical fasteners (Mallick, 2010). The increased stiffness and torsional resistance of the vehicle body due to use of adhesive joints further improve vehicle handling. The adhesive material can act as a barrier between dissimilar materials, such as CFRP and steel, thereby minimizing possible galvanic corrosion (Tavakkolizadeh and Saadatmanesh, 2001), which could affect the durability of the joint (Nguyen *et al.*, 2012). Adhesive joints also reduce noise, vibration, and harshness (NVH) in the vehicle structure (Ghaffari *et al.*, 2012).

Since the early 80s, the application of AHSS has steadily been replacing traditional mild steel starting with door and bumper beams being the first components made of AHSS (Figure 1.1) (Taylor and Clough, 2018). Structural BIW components, such as A- and B-pillars, side sills and roof rails, are designed to limit intrusion during side-impact collisions and are often made of ultra-high strength steel (UHSS), with tensile strengths as high as 1.5 GPa. In addition, UHSS offers automotive manufacturers the opportunity to use thinner sheet metals (*i.e.* downgauge), which contributes to reduction of the BIW weight, while maintaining or improving crash performance. The hot stamping manufacturing process, also known as hot forming die quenching (HFDQ), is capable of transforming a quenchable boron alloyed steel (*e.g.* 22MnB5 or Usibor® 1500-AS steel), with an initial tensile strength of 600 MPa, into a UHSS component with a tensile strength of 1.5 GPa (Vaissiere *et al.*, 2002). With advancement in manufacturing technology, the level of ductility and strength of Usibor® 1500-AS can be tailored during the in-die quenching stage of the hot stamping process, commonly known as tailored hot stamping (THS), in which in-die heaters are used to control local quench rate and introduce local soft regions with higher energy absorption (George *et al.*, 2012; Omer *et al.*, 2017).

Hot stamped steel has a layer of protective coating, described as an intermetallic layer, that prevents corrosion and decarburization during heat treatment (*i.e.* the austenitization process in the direct hot stamping process) to preserve the surface finish and mechanical properties of the sheet metal (Fan and De Cooman, 2012). A widely used boron steel has a hot dipped aluminum-silicon coating that transformed into an Al-Si-Fe intermetallic coating after the austenitization process. Unfortunately, an adhesive joint structure with such coating encounters premature failure due to coating delamination (Wolf *et al.*, 2011). To date,

there has not been a clear explanation of the failure mechanism for Al-Si coating delamination in adhesive joints, although the brittle nature of the coating has been associated with coating failure (Lundgren, 1989). Coating delamination failure has been reported for coating systems such as galvanized steel (Lundgren, 1989), galvanneal coated steel (Wolf *et al.*, 2011; Fujimoto *et al.*, 2018), and Al-Si coated steel (Kolnerova *et al.*, 2017).

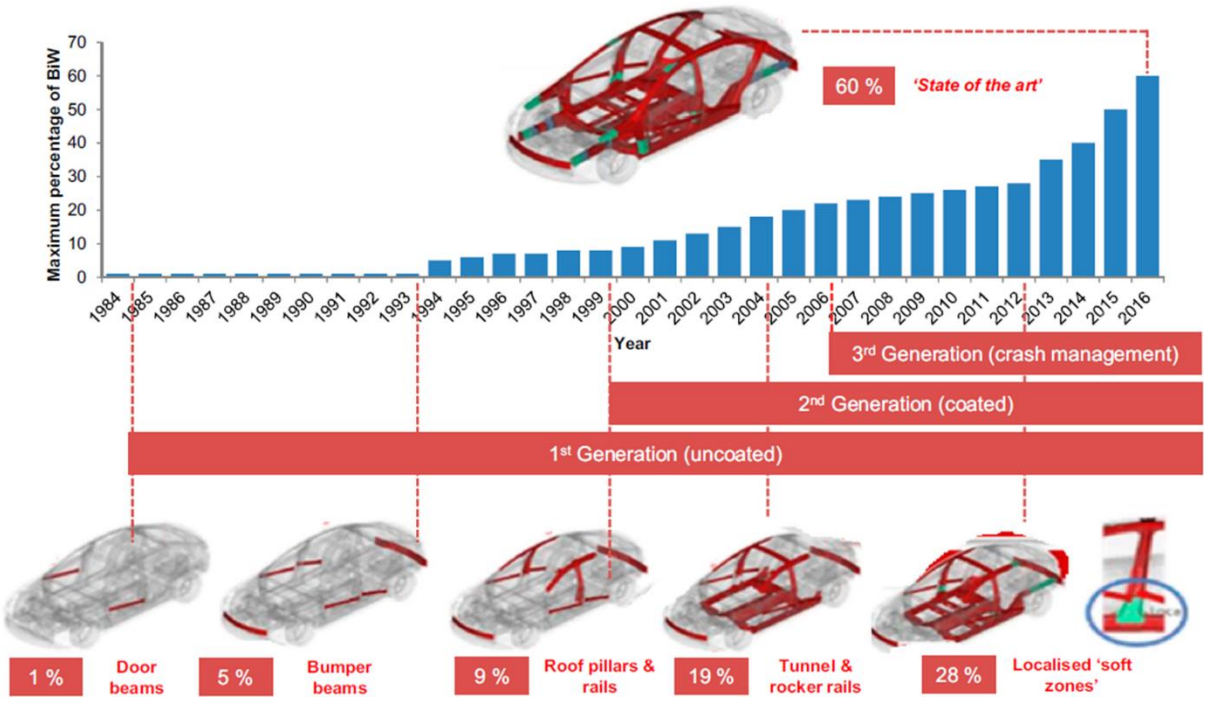

Figure 1.1: Growth of UHSS (hot stamped) steel parts in Body-in-White (BIW) (Taylor and Clough, 2018)

Structural adhesives are already being used in modern vehicles to join UHSS structural components of BIW (Figure 1.2b), in conjunction with conventional joining techniques such as RSW (Martinsen *et al.*, 2015). RSW has challenges when joining dissimilar coating systems in various AHSS alloys. Ighodaro *et al.* (2016) noted a significant decrease in joint strength of a resistance spot welded joint between an aluminum-silicon (Al-Si) coated and a galvannealed (*i.e.* zinc-based coating) AHSS and explained that different thermal and electrical properties between the two coating systems in the formed spot weld led to the drop in joint strength.

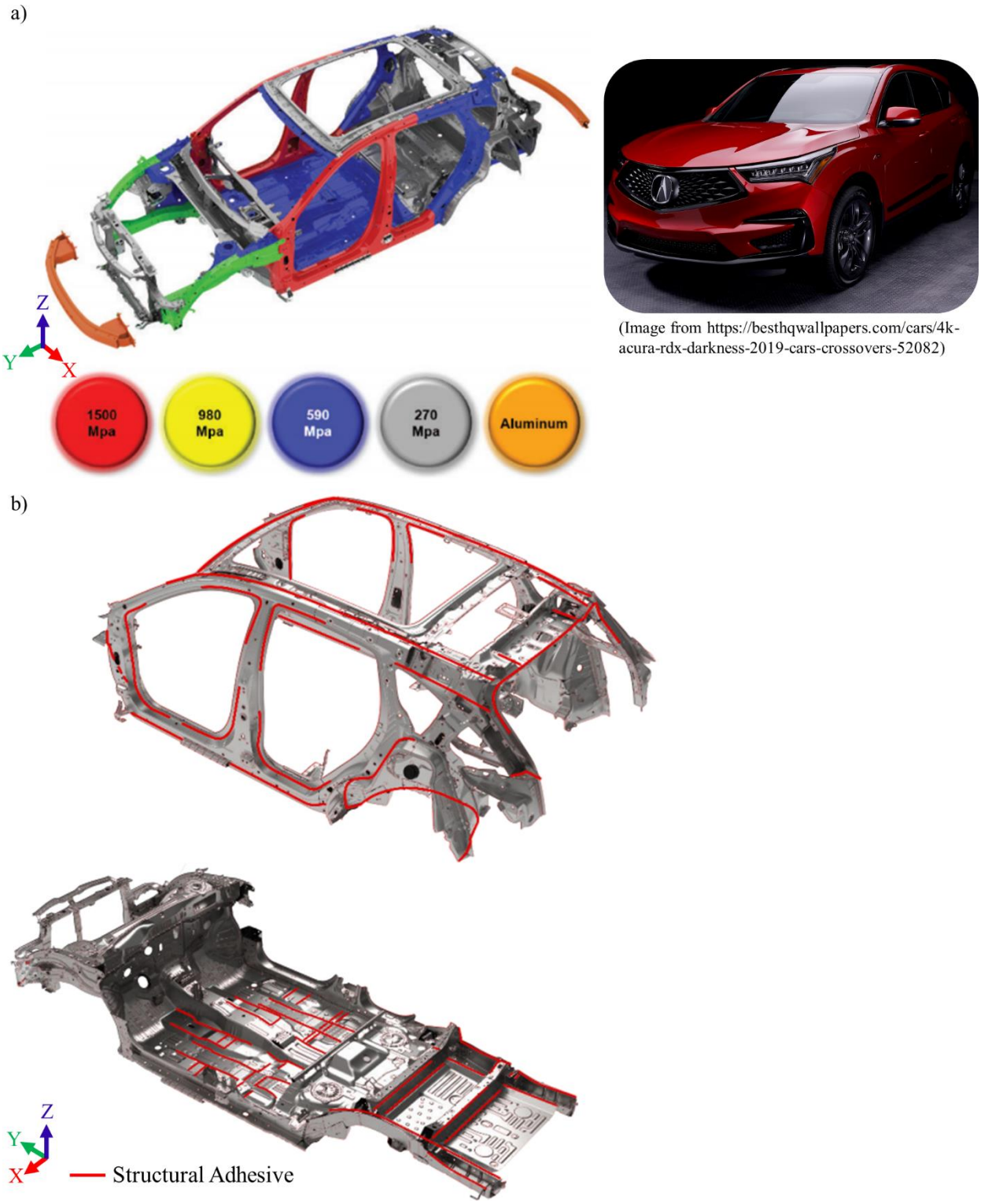

Figure 1.2: Body-in-White (BIW) of sport utility vehicle (SUV); a) structural components color-coded including: high-strength and advanced high-strength steel, and aluminum parts with associated tensile strength (in MPa), b) location where the structural adhesive was applied (red lines) (figures adapted from Honda Motor Co., 2019)

An essential process during the preparation of an adhesive joint is the surface treatment applied to the adherends that promotes a strong adhesion at the interface between the metal and the adhesive (Park *et al.*, 2010.; Baldan, 2012). A recent extensive surface preparation study was conducted on mild steel by Fernando *et al.* (2013) who found grit-blasting surface treatment resulted in higher adhesive strength over solvent degrease and hand grinding treatment; however, that study did not consider the effect of surface treatment on quenchable Al-Si coated boron alloyed steel 22MnB5 and the effect of thermal treatment on adhesive joint strength, which is relevant to the implementation of adhesively bonded tailored hot stamped structures.

A primary goal in adhesive joining is to achieve the maximum joint strength, which can depend on surface preparation, and may be related to the type of adhesive joint failure observed, such as failure within the adhesive layer (cohesive failure), at the interface (interfacial failure), at the adherend (adherend failure), or coating delamination (Ikegami *et al.*, 1996; da Silva *et al.*, 2008; Banea *et al.*, 2015). A fractography analysis can then identify the origin of fracture and the crack propagation in an adhesively bonded structure (Zhang *et al*., 2008; Teixeira de Freitas and Sinke, 2015) enabling a better understanding of the joint performance. Although quantification of adhesive fracture surfaces has been considered using surface roughness (Ameli *et al.*, 2011), to date there has been no detailed assessment of qualitative and quantitative analysis of the fracture surface on structural adhesive tested under various loading conditions.

1.2 Research Objectives and Approach

The overall goal of the current research was to better understand the effect of surface preparation on joint performance and fracture processes within adhesive joints of hot stamped Usibor® 1500-AS, and among adhesive joints loaded under different modes of loading. To this end, several research objectives were pursued.

The first objective was to examine the effect of surface treatment on adhesive joint strength by conducting a series of single-lap shear tests. The test specimens were made from ultra-high strength steel (ArcelorMittal Dofasco, Usibor® 1500-AS) with various levels of ductility to examine the thermal treatment effect on adhesive joint response and strength. The structural adhesive used in this study was a two-part Impact Resistant Structural Adhesive (IRSA) 7333 manufactured by 3M™. Overall, the test matrix for this study comprised nine test cases with a combination of three types of surface treatments and three thermal treatments.

The second objective was to investigate the failure mechanism of the Al-Si-Fe intermetallic coating delamination for UHSS-adhesive joint configurations. The intermetallic coating generated on the test specimens in this study was compared against the literature to identify the associated defects and coating thickness variations. Two types of mechanical tests (a modified butt joint and single-lap shear test) were performed to determine the intermetallic coating resistance to failure, under pure tensile loading and mixed-mode loading, to understand the root cause of the intermetallic coating delamination.

The third objective was to propose a fractographic analysis methodology that qualitatively and quantitatively assessed adhesive joint fractures and compares the adhesive fractures caused by different modes of loading. Four (4) different types of adhesive joints from different modes of loading were analyzed.

1.3 Thesis Outline

Chapter 2 of this thesis opens with a review of the mechanical properties of UHSS, the direct hot stamping process to produce the current UHSS, and the microstructures achieved from different thermal treatments applied in this study. In the same chapter, the relevant background is reviewed concerning toughened adhesive mechanical properties, adhesive joint mechanical testing, adhesive fracture morphology, and the existing quantitative techniques used to assess fracture surfaces. Chapter 3 describes the manufacturing

process used to prepare the test specimens (single-lap shear and modified butt joint specimen), surface treatment procedures, in-die quenching of UHSS, and the testing methodology used to investigate adhesive fracture. Next, Chapter 4 presents the experimental results from the surface treatment study, the Al-Si-Fe intermetallic coating delamination study, the adhesive fracture topography, and the fracture profiles of adhesive joints under different loading conditions. Chapter 5 discusses the effect of surface treatments and thermal treatments on adhesive joint strength and the failure mechanism of the Al-Si-Fe intermetallic coating for this UHSS. Differences observed in adhesive fracture morphology are presented in terms of qualitative identification of the differences in fracture features and quantitative characterization of the surface roughness parameters calculated from the fracture profiles. Chapter 6 ends by highlighting the main conclusions drawn from this investigation and providing some recommendations for future experimental work.

Chapter 2. Background

2.1 Ultra-High Strength Steel

Ultra-high strength steels (UHSSs) are classified as having a tensile strength above 780 MPa (Mega *et al.*, 2004). The body-in-white (BIW) structure of a vehicle requires high intrusion resistance for crashworthiness and for this reason, the A-pillar, B-pillar, and rocker panel are commonly made of UHSS (Karbasian and Tekkaya, 2010). This section covers the mechanical properties of a specific UHSS, 22MnB5 boron steel, and the hot forming die quenching process (HFDQ) (also known as hot stamping or press hardening), including the cooling rate effect, which determines the microstructure and controls the ductility of the boron steel. An important enabler of UHSS is the application of an aluminum-silicon (Al-Si) coating, providing corrosion resistance and limiting decarburization of the steel during HFDQ.

2.1.1 22MnB5 Boron Ultra-High Strength Steel

Boron steel grades (*e.g.* 22MnB5, 27MnCrB5, and 37MnB4) can be processed into UHSS using a HFDQ process (Naderi, 2007). Among the listed boron alloys, 22MnB5 is the most common steel grade researched and implemented in the automotive industry for use in crash management (intrusion resistant) components (Vaissiere *et al.*, 2002; Hein and Wilsius, 2008; Karbasian and Tekkaya, 2010). The 22MnB5 material used in the study is referred to as boron steel throughout this work.

Boron steel has a good hardenability and achieves the status of UHSS after HFDQ. The mechanical properties of boron steel make it a compelling option for the automotive industry to adopt and develop a lighter body-in-white by using thinner sheet metal while meeting crashworthiness requirements for passenger safety. As-received 22MnB5 has a ferritic-pearlitic microstructure with a tensile strength of 600

MPa (Merklein and Lechler, 2006); however, by following the HFDQ process, the boron steel can have an ultimate tensile strength as high as 1500 MPa (Figure 2.1). In the chemical composition of boron steel (Table 2.1), the carbon (C) content is critical to the strength of the steel, and boron (B) promotes the hardenability of the metal by delaying the solid-state phase transformation of softer microstructures such as bainite or ferrite while maximizing the fraction of martensite resulting from the quenching operation (Karbasian and Tekkaya, 2010). Manganese (Mn) and chromium (Cr) also facilitate the hardenability of the steel, but to a lesser extent compared to boron.

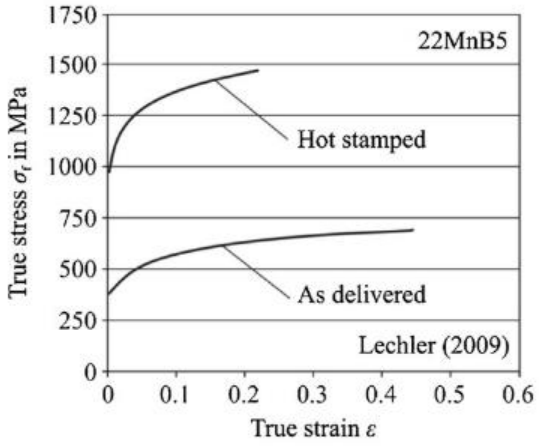

Figure 2.1: 22MnB5 boron steel true stress vs true strain curve before and after hot stamping (Karbasian and Tekkaya, 2010 used with permission from ELSEVIER)

Table 2.1: Boron steel (Usibor® 1500-P) chemical alloying composition (weight %) (George *et al.*, 2012)

Element	Symbol	Composition (Weight %)
Carbon	C	0.22
Manganese	Mn	1.23
Phosphorus	P	0.008
Sulfur	S	<0.001
Silicon	Si	0.25
Copper	Cu	0.03
Nickel	Ni	0.02
Molybdenum	Mo	<0.02
Chromium	Cr	0.20
Columbium	Cb	<0.008
Vanadium	V	<0.008
Aluminum	Al	0.03
Tin	Sn	0.01
Titanium	Ti	0.037
Nitrogen	N	0.044
Boron	B	0.004

2.1.2 Hot Forming Die Quenching

Hot forming die quenching (HFDQ) of boron steel in this work follows a direct hot stamping process under which forming and quenching of the part take place simultaneously (Figure 2.2). The direct hot stamping process begins with the austenitization of the steel at 900 °C to 950 °C, with a dwell time of 3 min to 10 min depending on the sheet thickness (Fan *et al.*, 2009; Karbasian and Tekkaya, 2010; Omer *et al.*, 2018). The austenitization temperature is set above the phase transformation temperature from ferrite to austenite. Ferrite and pearlite microstructures in the as-received boron steel transform into a homogeneous austenite microstructure by the end of the austenitization process. Next, the heated blank is quickly transferred to the die, keeping the temperature above 780°C during the forming and quenching operation to avoid the

formation of bainitic or ferritic grains (Vaissiere *et al*., 2002). The forming and quenching operation are executed in a single step and normally utilize a cooled die to ensure a high quench rate. The use of heated dies offers the capability to tailor the mechanical properties based on the cooling rate applied at the heated sheet. The final grain structure in the boron steel follows the continuous cooling transformation (CCT) diagram of the respective material (Figure 2.3).

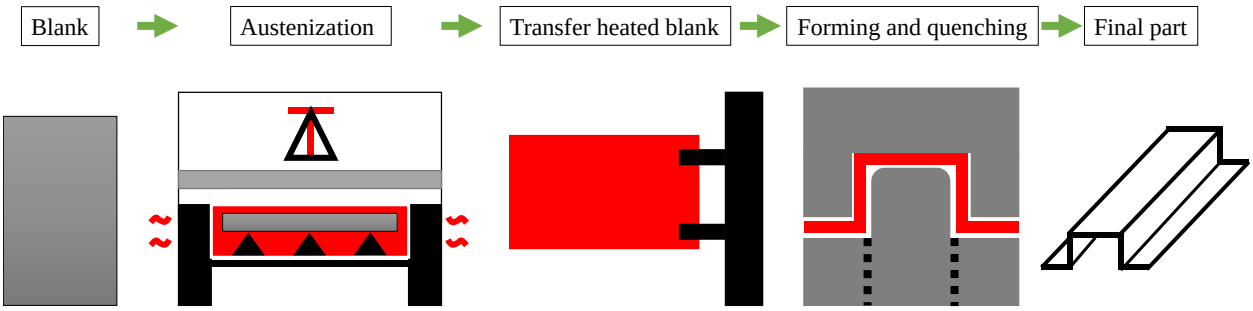

Figure 2.2: Hot forming die quenching process: direct hot stamping

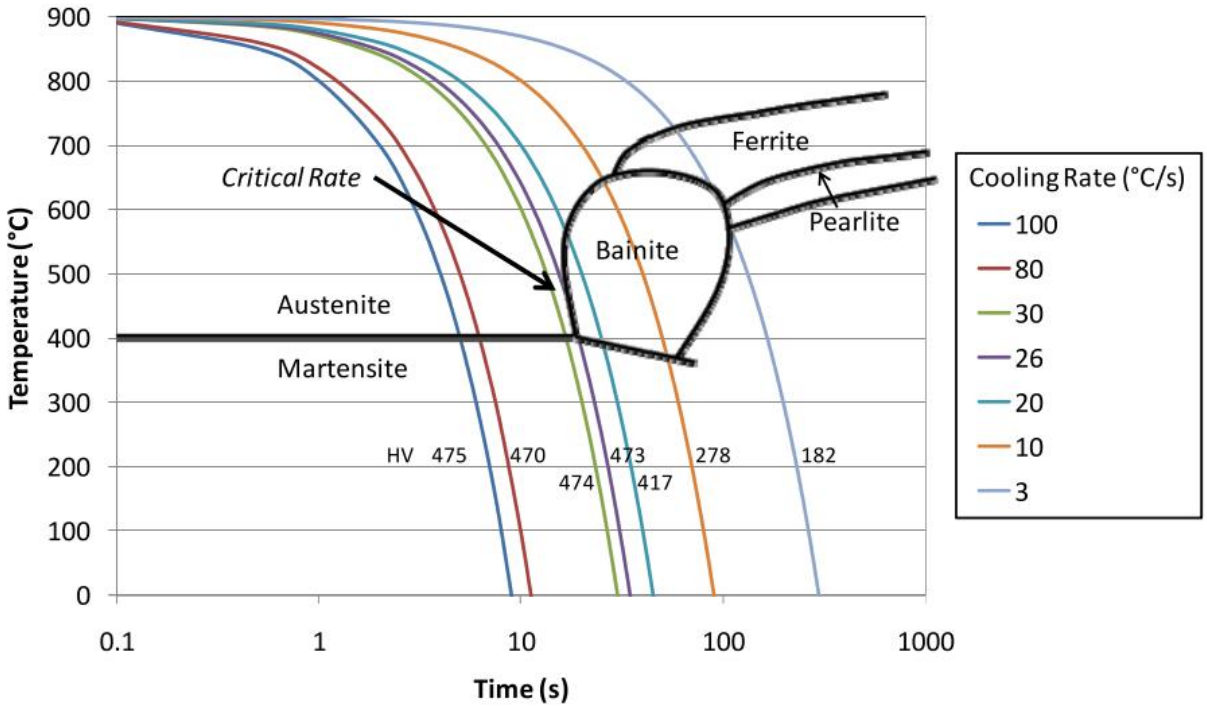

Figure 2.3: Continuous cooling transformation (CCT) diagram of 22MnB5 steel showing the microstructure formed at the applied cooling rate and the corresponding Vickers hardness (George, 2011)

Studies have shown that a fully martensitic microstructure is formed in the boron steel for a critical cooling rate of at least 27 to 30°C/sec (Karbasian and Tekkaya, 2010; George *et al.*, 2012). The steel die surface at room-temperature (RT) was able to meet the required critical cooling rate to produce fully martensitic boron steel (George *et al.*, 2012; Omer *et al.*, 2017). The fully martensitic steel was reported to have ultimate tensile strength ranging between 1447 MPa to 1589 MPa (Table 2.2). A martensitic microstructure features fine grains and randomly oriented crystalline structure (Figure 2.5) that contribute to an increase in resistance to dislocation motion (Bardelcik *et al.*, 2010).

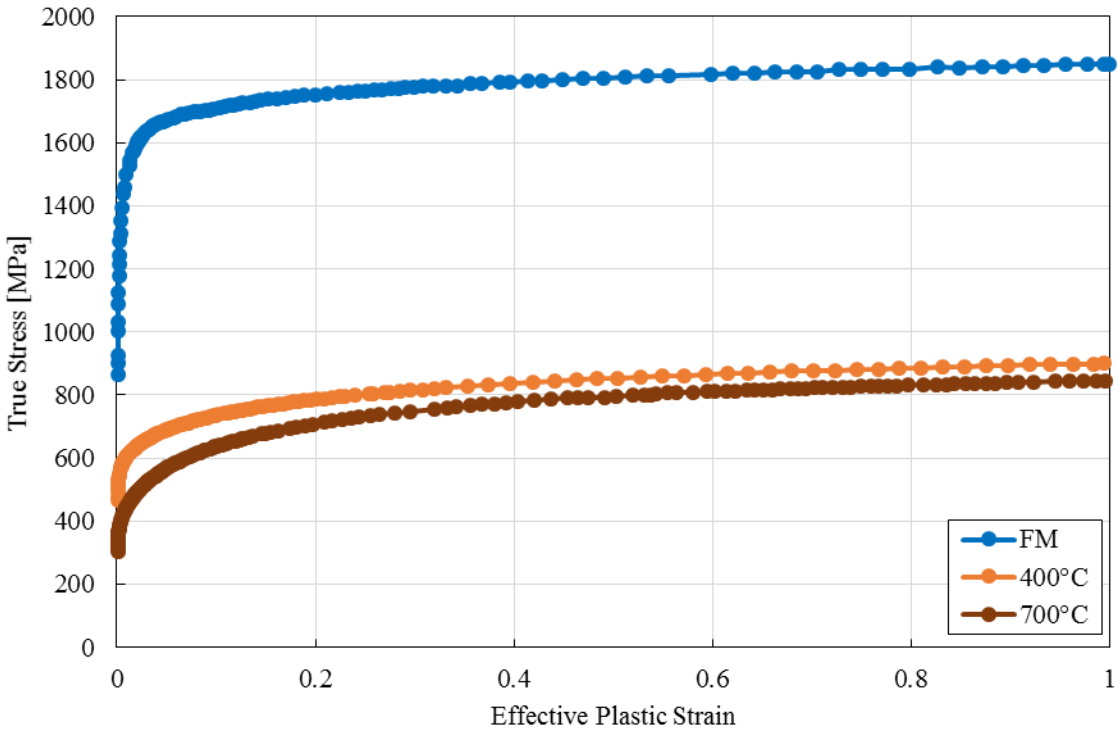

Figure 2.4: True stress vs. effective plastic strain flow stress curves of boron steel under three thermal treatments: oil quenched (fully martensitic (FM), in-die quenched at 400°C and at 700°C) (digitized experimental data from ten Kortenaar, 2016)

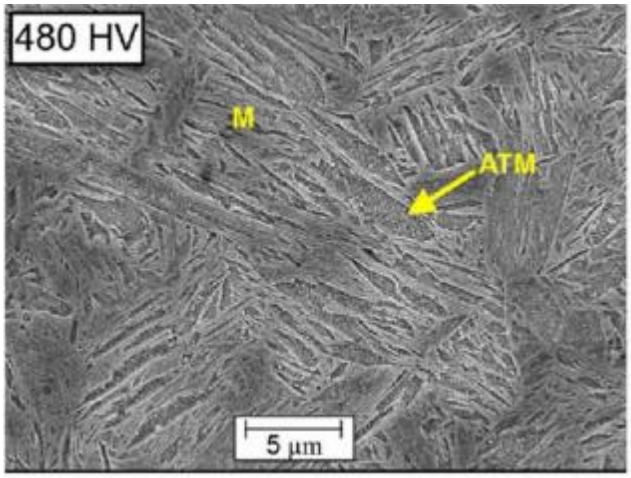

Figure 2.5: Microstructure of a quenched 22MnB5 boron steel (1.2 mm thick) obtained by applying a critical cool rate of at least 27 °C/sec through in-die cooling at room temperature (RT) - microstructure showed fine needle-like grains with random orientation (Omer *et al.*, 2018 used with permission from SPRINGER NATURE)

To increase the ductility of boron steel, a sub-critical cooling rate can be achieved by using heated dies that reduce the cooling rate within the boron sheet, thereby forming ductile phases according to the CCT diagram. As a result, the ductile boron steel has reduced hardness and material strength (Figure 2.4). Omer *et al.* (2018) obtained a Vickers hardness of 258 HV that corresponded to approximately a subcritical cooling rate of 10 °C/sec (Figure 2.3). The authors noted a mixture of soft phases such as bainite, ferrite, and pearlite developed in the boron steel (Figure 2.6). Such a cooling rate was reached by generating a die surface temperature of 400°C. As the die surface temperature increased to 700 °C, a Vickers hardness of 193 HV was measured (Omer *et al.*, 2018) and approximately matched the hardness for a cooling rate of 3 °C/sec according to the CCT diagram (Figure 2.3). Large pearlite and ferrite grains were observed in the microstructure (Omer *et al.*, 2018) (Figure 2.6) and increased the ductility of the metal. The Vickers hardness of the boron steel with the slower cooling rate was found to decrease in conjunction with the ultimate tensile strength (Table 2.2). Ultimately, the HFDQ offers an opportunity to tailor the boron steel and executes the forming and quenching simultaneously on a part that can have tailored mechanical properties based on the local cooling rate.

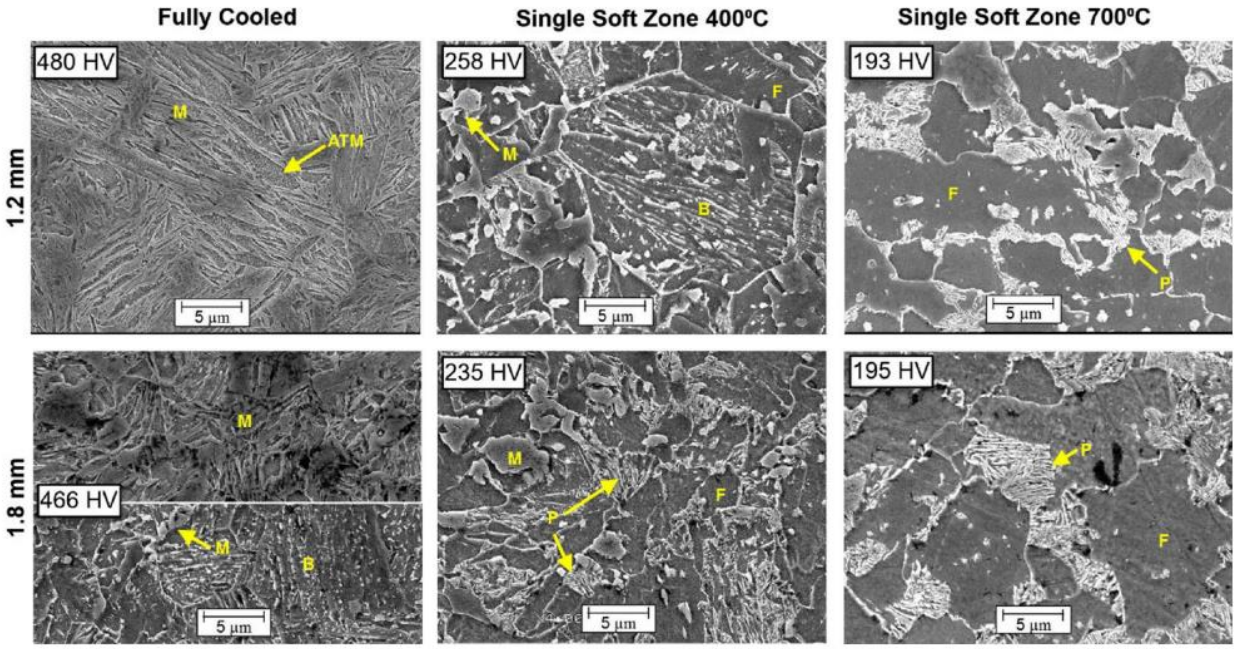

Figure 2.6: Grain structure of boron steel (1.2 mm thick and 1.8 mm thick) in-die quenched at three different thermal treatment: RT (room temperature), 400°C, and 700°C with corresponding Vickers value (Omer *et al.*, 2018 used with permission from SPRINGER NATURE)

Table 2.2: Ultimate tensile strength of boron steel and corresponding average Vickers hardness as a function of in-die quenching temperature (room temperature, 400°C, and 700°C)

Quenching Temperature	Room Temperature (RT)			400°C		700°C
Literature	Bardelcik *et al.* (2012)	O'Keeffe (2018)	George *et al.* (2012)	George *et al.* (2012)	O'Keeffe (2018)	O'Keeffe (2018)
Ultimate tensile strength [MPa]	1447	1548	1589	794	817	671
Average Vickers hardness	466	486	505	262	262	211

Uniaxial tensile test at a strain rate of : Bardelcik *et al.*(2012) 0.0028 / s

O'Keeffe (2018) 0.001 / s

George *et al.* (2012) 1.0 / s

2.1.3 22MnB5 Boron Steel Aluminum-Silicon Intermetallic Coating

A protective coating using aluminum-silicon (Al-Si) is applied via hot dipping to boron steel to prevent decarburization (*i.e.* loss of carbon content) during the austenitization process and oxidation (Ghiotti *et al.*, 2011; Fan and De Cooman, 2012). The aluminum component of the coating prevents the carbon from leaving the base metal as carbon migrates toward the surface during the austenitization process. An Al_2O_3 layer is formed at the outer surface of the Al-Si coating during the austenitization process, which is a barrier to prevent corrosion at the surface once the HFDQ is completed (Fan *et al.*, 2012). The presence of Si influences the development of intermetallic phases at the interface between the base metal and Al during the austenitization process. One study found that an increase in silicon content in the coating prevents the continuous growth of the intermetallic layer during the austenitization process (Windmann *et al.*, 2014). The as-received Al-Si coating thickness ranges between 15 to 25 µm (60 to 100 gm/m^2 per side) (Figure 2.7a) (Jenner *et al.*, 2010; Fan *et al.*, 2010). After the austenitization process, the Al-Si coating transforms into a multi-layer Al-Fe-Si intermetallic coating with a diffusion layer above the base metal that is made up of α-Fe (Figure 2.7b).

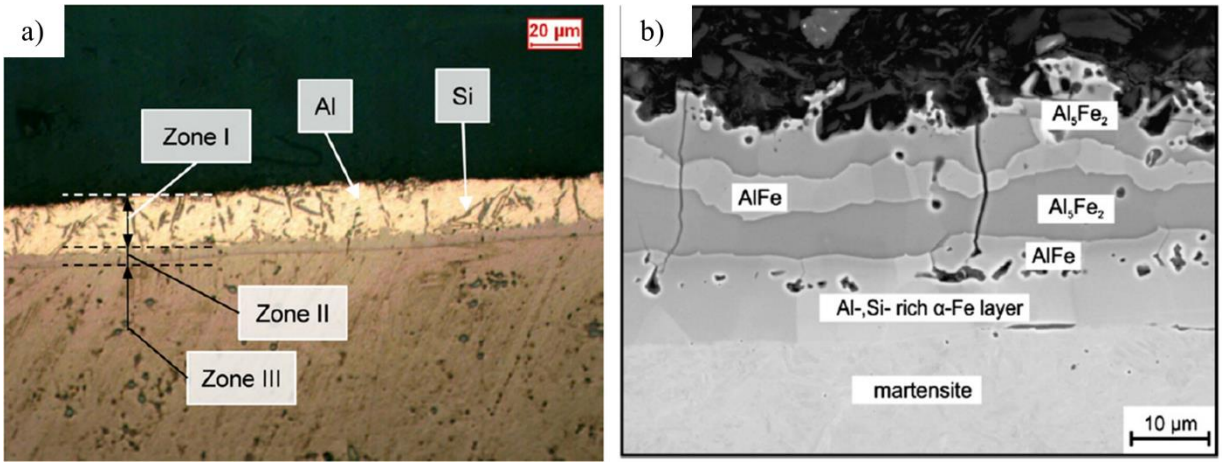

Figure 2.7: Al-Si coated boron steel; a) as-received Al-Si condition (Ghiotti *et al.*, 2011 used with permission from ELSEVIER) b) Al-Fe-Si intermetallic coating (after 6 min of soak time at 920 °C) (Windmann *et al.*, 2014 used with permission from ELSEVIER)

During the austenitization process, Al-Si coating, with a melting temperature of 577°C to 600 °C (Fan *et al.*, 2010; Karbasian and Tekkaya, 2010), transforms into a molten state on top of the base metal. Within the first two minutes of austenitization, the iron (Fe) from the base metal diffuses into the molten Al-Si coating and has a faster diffusivity into the Al-Si coating compared to aluminum (Windmann *et al.*, 2013).

a)

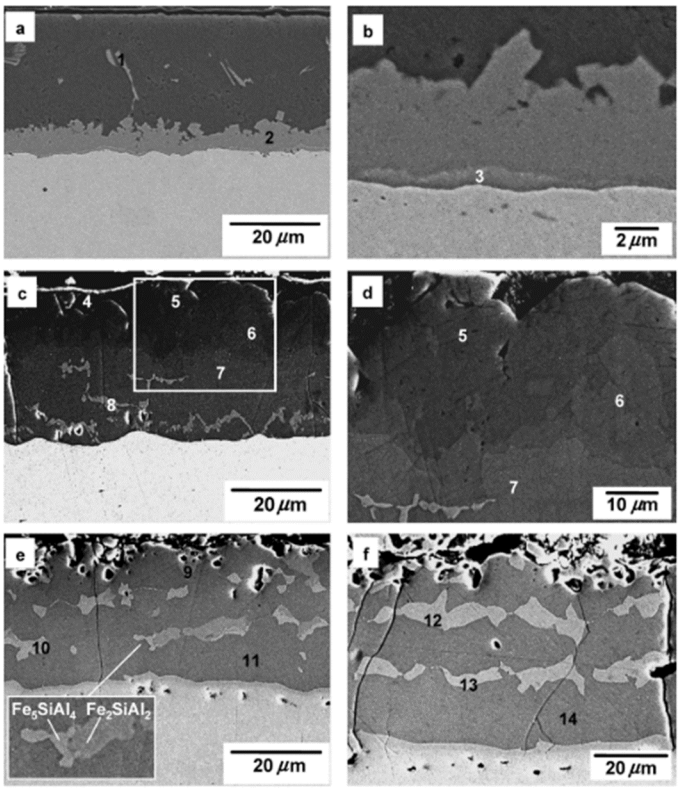

b)

Location on micrograph	Fe[at.%]	Si[at.%]	Al[at.%]	Phase
1	18	10	72	Fe_2SiAl_7
2	22	12	66	Fe_2SiAl_7
3	23	1	75	$FeAl_3$
4	2	2	91	Pure Al
5	24	11	66	Fe_2SiAl_7
6	26	5	69	Fe_2Al_5
7	31	5	64	$FeAl_2$
8	37	15	48	Fe_2SiAl_2
9	39	16	45	Fe_2SiAl_2
10	49	15	36	Fe_5SiAl_4
11	32	3	65	$FeAl_2$
12	52	13	35	Fe_5SiAl_4
13	49	13	38	Fe_5SiAl_4

Figure 2.8: Al-Si coating development at austenitization temperature of 930°C; a) the coating morphology transformation from as-received to soak time of 8 minutes, b) atomic % of Fe, Si, and Al at different layers of the intermetallic coating throughout the austenitization process (Fan *et al.*, 2010 used with permission from ELSEVIER)

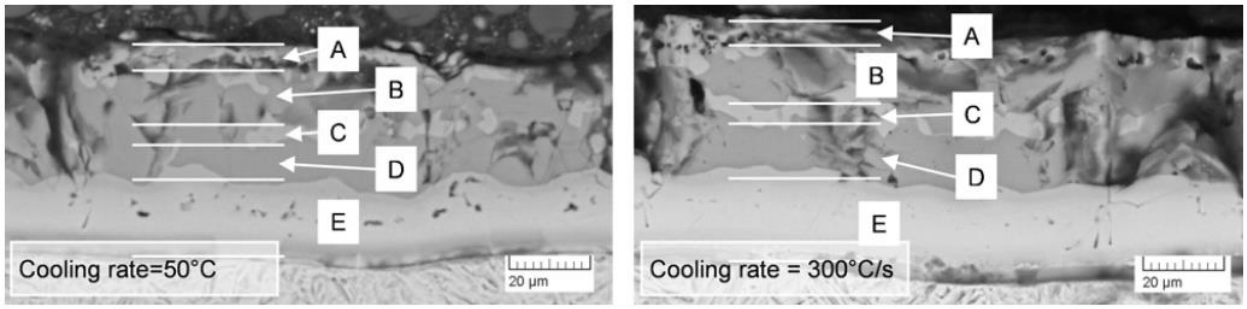

Figure 2.9: Al-Fe-Si intermetallic coating development comparison of two different cooling rates (50℃/s vs 300℃/s) (Ghiotti *et al.*, 2011 used with permission from ELSEVIER)

Al-Fe-Si intermetallic coating has a high hardness (900 to 1150 HV0.05) and a low fracture toughness of 1 MPa$\sqrt{m}$ (Kobayashi and Yakou, 2002; Köster *et al.*, 1993). The α-Fe layer at the diffusion layer is more ductile than the intermetallic layers, which are part of the overall Al-Fe-Si intermetallic coating (Figure 2.10). Within the overall Al-Fe-Si intermetallic coating, there is a ductile Fe_3Al phase with a microhardness of 320 HV0.025/15 and a hard phase Fe_3Al with a microhardness of 600 HV0.025/15 (Kobayashi and Yakou, 2002).

The developed Al-Fe-Si intermetallic coating, following the HFDQ process, presents defects such as microcracks, Kirkendall voids, and surface porosity in the intermetallic coating (Figure 2.10). Microcracks are formed due to different thermal expansion coefficients in the components of the intermetallic coating (Al, Si, Fe, *etc.*) (Jenner *et al.*, 2010; Gui *et al.*, 2014). The difference in ductility within the overall intermetallic coating layer is also reflected by the tips of the microcracks that arrest in the vicinity of the softer layer of the diffusion layer (α-Fe) (Figure 2.10). An increase in austenitization temperature and longer soak time mitigates the crack formation in the intermetallic coating (Windmann *et al.*, 2014). However, such an austenitization cycle is not considered in this study to ensure the boron sheets produced have intermetallic coating similar to the ones reported in the literature (Bardelcik *et al.*, 2012; O'Keeffe, 2018; George *et al.*, 2012) which reflects current industrial practice. The formation of Kirkendall voids is caused by the differential rate of mass transfer between Fe and Al during the austenitization process. Such

voids are present at a distinct layer near the top of the diffusion layer (Figure 2.10) (Fan *et al.*, 2010; Jenner *et al.*, 2010).

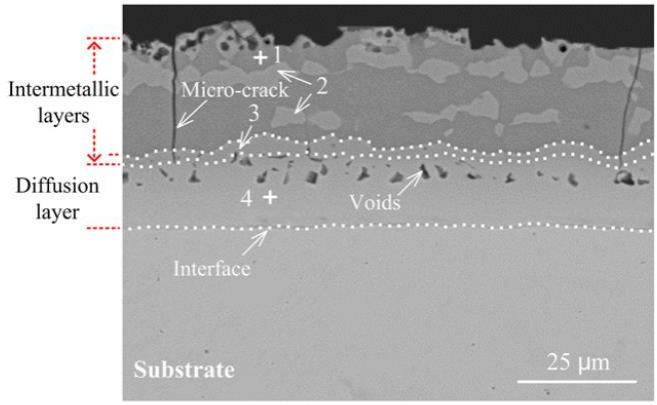

Figure 2.10: Defects observed in a developed Al-Fe-Si intermetallic coating (Wang *et al.*, 2017 used with permission from ELSEVIER)

After the HFDQ, the coated sheet metal has higher surface roughness compared to the as-received sheet (Suehiro *et al.*, 2003; Jenner *et al.*, 2010), potentially related to the diffusion of the intermetallic coating (Figure 2.11). The rough surface finish offers an anchoring effect that demonstrates good paintability (Suehiro *et al.*, 2003).

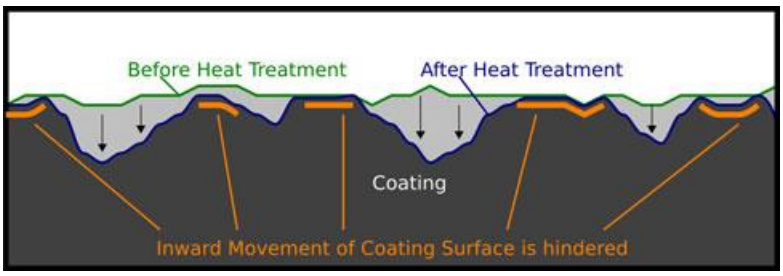

Figure 2.11: Diagram of a cross-section of Al-Si coating development before and after heat treatment (Jenner *et al.*, 2010 used with permission from SPRINGER NATURE)

When the heated blanks are stretched and bent during the HFDQ, microcracks in the coating can turn into large microcracks (Figure 2.12) (Wang *et al.*, 2017). The intermetallic coating of a quenched sheet does not deform plastically due to its high hardness (Jenner *et al.*, 2010).

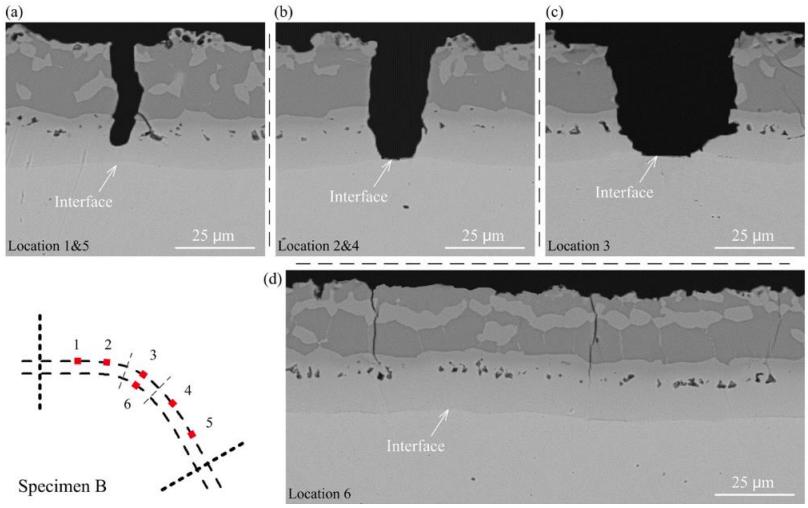

Figure 2.12: Cross-section of a coated steel demonstrating different degrees of growth in width in the microcracks at various location in a bent sheet (Wang *et al.*, 2017 used with permission from ELSEVIER)

Coating delamination strength measurement methods

One of the possible adhesive joint failures associated with coated metal adherends (material that is to be bonded to another using adhesive) was coating delamination (Figure 2.13), in which the coating detaches from the base metal, resulting in lower joint strength (Lundgren, 1989). Wolf *et al.* (2011) conducted single-lap shear (SLS) tests using galvanneal (GA) coated high strength steel with a crash-resistant structural adhesive and noted that the adhesive removed the GA coating (Figure 2.13). Lundgren (1989) also noted the coating delamination in the adhesive joint and attributed the coating delamination to the brittle nature of the zinc-iron and zinc-nickel coating on the steel. With the microcrack and void defects formed in the Al-Fe-Si intermetallic coating (Fan *et al.*, 2010), coupled with low ductility of the coating (Köster *et al.*, 1993), delamination is likely to occur in an adhesive joint test. This outcome prompted the development of a test methodology that quantifies the coating adhesion strength using adhesive joints under specific modes of loading. Schiel *et al*. (2015) used a modified butt joint configuration to determine the tensile properties of coated specimens with GA coating, body panel paint, and Al-Si coating (Figure 2.14). In addition, the single-lap shear joint configuration was used to demonstrate the coating delamination as well (Wolf *et al.*,

2011; Hertveldt *et al.*, 1999; Lundgren, 1989) (Table 2.3). Additional information on single-lap shear and butt joint tests are presented in the Section (2.2.2).

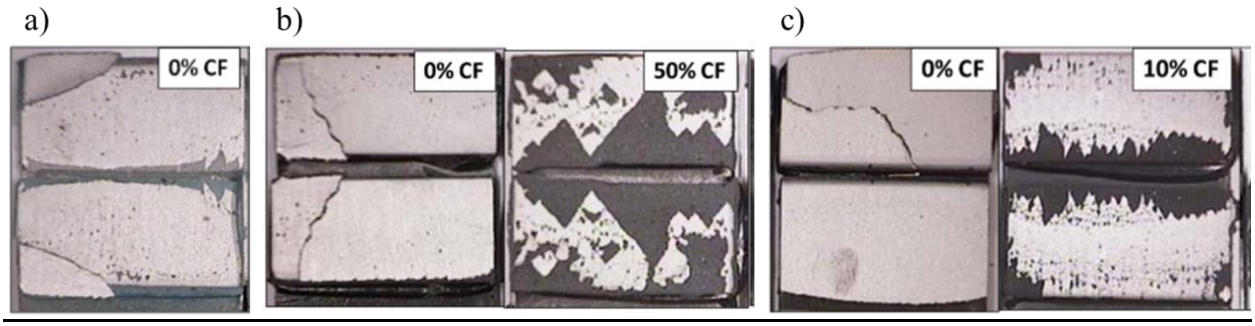

Figure 2.13: Galvanneal (GA) coated steel coating failure in single-lap shear configuration (% CF=area % of cohesive failure) a) 1-part crash-resistant epoxy b) 1-part toughened epoxy c) 1-part structural hem-flange epoxy (figures adapted from Wolf *et al.*, 2011)

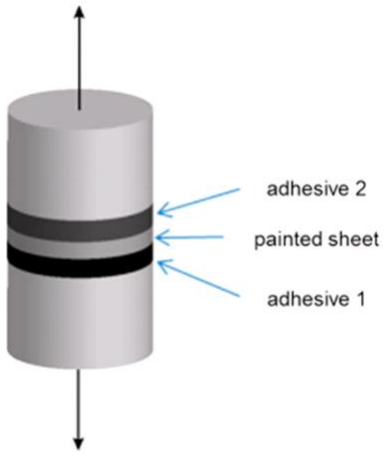

Figure 2.14: Modified butt joint test to determine the cohesive strength of the coating/paint (DIN 15870) (Schiel *et al.*, 2015 used with permission from ELSEVIER)

Table 2.3: Summary of mechanical testing reported coating delamination under single-lap shear joint

Authors	Coating System	Mechanical test	Adhesive / Adherend System	Reported results
Lundgren, 1989	**Zinc coated steel:** Hot Dip Galvanized, Electrogalvanized, Zinc Rich Paint	Simple overlap joint	**Adhesive:** 1-part epoxide (structural adhesive for hem-flange bonding) **Adherend:** Re-oiled surface with sheet thickness ranged from 0.67 mm to 0.82 mm thick	**9 MPa** to **14 MPa**
Hertveldt *et al.* [1999]	Galvannealed coating	Modified single-lap shear joint (with added backing strip)	**Adhesive:** Heat cured – 1-part epoxy **Adherend:** Deep drawing quality steel and high strength steel	**<10 MPa** to **18.0 MPa**
Wolf *et al.* [2011]	Galvannealed coating	Single-lap shear test	**Adhesives:** A: 1-part epoxy crash resistant structural adhesive B: 1-part epoxy toughened structural adhesive C:1-part epoxy structural hem-flange adhesive **Adherends (w/o backing plate):** (adherend #1) extra deep drawing steel interstitial-free EDDS (IF); 0.7 mm thick (adherend #2) 590 Dual Phase (DP); 1.6 mm thick	A: (adherend #1) **14.1±0.4 MPa** B: (adherend #1) **13.4±0.4 MPa** (adherend #2) **31.3±1.0 MPa** C: (adherend #1) **10.9±0.5 MPa** (adherend #2) **30.2±1.2 MPa**
Schiel *et al.* [2015]*	Al-Fe-Si intermetallic coating	Single-lap shear test	**Adhesive:** 1-part non-toughened epoxy **Adherend:** Boron-manganese alloyed steel (22MnB5)	Quasi-static @ 5 mm/min **17.1±2.2 MPa** Dynamic @ 2 m / sec **33.6±3.6 MPa**

* The test average and standard deviation are obtained through digitization of the test results in the literature

2.2 Toughened Structural Adhesive

Progress in adhesive research has broadened the possibility of joining similar and dissimilar materials in products found in the consumer electronics, aerospace, and automotive industries. Adhesive used in engineering applications is generally categorized as structural adhesive, with varying composition and properties, depending on the application (Table 2.4). Epoxies are commonly used as structural adhesives. In automotive vehicles, structural adhesives are used for body structure bonding (*e.g.*, body panels, pillars, and rocker panels) and the hemming operation (sheet metal joining through bending/folding) for doors and hood (Chiang and McKenna, 1995; Fujimoto *et al.*, 2018). Furthermore, toughened epoxy is a structural adhesive currently adopted in the automotive sector to join structural parts of the vehicle (Grant *et al.*, 2009; Schiel *et al.*, 2015; Banea *et al.*, 2018) due to its high strength, modulus and high fracture toughness as well as ease of application (Banea and da Silva, 2009).

A toughened epoxy typically contains rubber particle additions with diameters ranging from 0.5 μm to 10 μm, depending on the adhesive formulation (Yee and Pearson, 1986). The added rubber particles increase the fracture strain of the adhesive (Kinloch *et al.*, 1983) and improve its ductility. Yee and Pearson (1986) found that the added rubber particles promoted shear deformation and became sites of cavitation, which are the primary sources of the toughening mechanism in the adhesive.

Aluminum particles can be incorporated in the adhesive formulation to improve the thermal and electrical conductivity of the adhesive (Kim *et al.*, 2011). In the application of weldbonding, a hybrid joint made up of resistance spot welding and adhesive bonding, the metallic particles in the adhesive improve the electrical conductivity during a welding operation that results in smaller heat affected zone (HAZ) compared to an adhesive formulated with lower conductivity (Darwish and Ghanya, 2000). The Al particles sizes can be less than 50 μm in diameter (Kahraman and Al-Harthi, 2005), but can also go as high as 100 μm (Kilik and Davies, 1989) or 160 μm (Darwish *et al.*, 1991). There is also the economic motivation of substituting some of the resin content with fillers, thereby reducing the production cost of the adhesive.

Epoxy adhesive generally comes in the form of a film or viscous fluid that can be formulated as a single- or two-part adhesive. Upon adhesive application, the adhesive joint system undergoes a curing process at a temperature and duration specified by the manufacturer. At the end of the curing cycle, the adhesive transforms into a solid state. Epoxy adhesives are thermosets in which the individual polymer chains link to neighbouring chains (*i.e.* cross-link) in the form of covalent bonds and the crosslink density, after cure, increases significantly. Carbas *et al.* (2014) found improved strength and stiffness in adhesives when the cure temperature is increased, but below the glass transition temperature, T_g, that marks the transition between glassy and rubbery state. The authors also found a curing temperature above T_g would result in deterioration of the mechanical properties of epoxy adhesives by polymer chain degradation.

Adhesive curing can be initiated either at room temperature or in a heated environment depending on the adhesive used. A room temperature curing adhesive requires longer curing time, which is not ideal in a production setting (Petrie, 2006) compared to an elevated-temperature cure. However, elevated-temperature curing can induce residual stresses, particularly in the case of joining dissimilar materials, from the cure shrinkage in the adhesive (Petrie, 2006). Elevated-temperature curing for adhesives is commonly used in the automotive industry (Grant *et al.*, 2009; Schiel *et al.*, 2015; Fujimoto *et al.*, 2018), in which the adhesive is applied before paint application and the paint bake cycle is used to simultaneously bake or cure the paint as well as to cure the adhesive (Schiel *et al*., 2015).

Table 2.4: Advantages and limitations of typical thermosetting resins for adhesives and sealants (table adapted from Kim *et al.*, 2011)

	Advantages	Limitations
Epoxy	• High strength • Good solvent resistance • Good gap-filling capabilities • Good heat resistance • Wide range of formulations • Relatively low cost	• Exothermic reaction • Exact proportions needed for optimum properties • Short pot life
Polyurethanes	• Various cure times • Tough • Excellent flexibility even at low temperature • One- or two-component, room or elevated-temperature cure • Moderate cost	• Both uncured and cured are moisture sensitive • Poor heat resistance • May revert with heat and moisture • Short pot life • Special mixing and dispensing equipment required
Cyanoacrylates	• Rapid room-temperature cure • One-component system • High tensile strength • Long pot life • Good adhesion to metal • Dispense easily from package	• High cost • Poor durability on some surfaces • Limited solvent resistance • Limited elevated-temperature resistance • Bonds skin
Modified acrylics	• Good flexibility • Good peel and shear strengths • No mixing required • Will bond dirty(oily) surfaces • Room-temperature cure • Moderate cost	• Low hot-temperature strength • Slower cure than with cyanoacrylates • Toxic • Flammable • Odor • Limited open time • Dispensing equipment required
Phenolics	• Good heat resistance • Good dimensional stability • Inexpensive • Modification of toughness by adding elastomeric resins	• Brittle • Possibility of pollution due to formaldehyde as curing agent

2.2.1 Mechanical Properties of Bulk Adhesive and Adhesive Joint

Untoughened adhesive exhibits linear elastic tensile stress-strain response followed by brittle fracture at the peak stress, with small plastic deformation (Figure 2.15). A toughened adhesive, with rubber particle additions, demonstrates improved ductility and toughness (quantified by the area under the stress-strain curve) through damage mechanisms such as cavitation around the rubber particles and shear band formation that result in strain hardening response that ultimately leads to higher strain at failure, but typically with a reduced failure strength compared to untoughened adhesive.

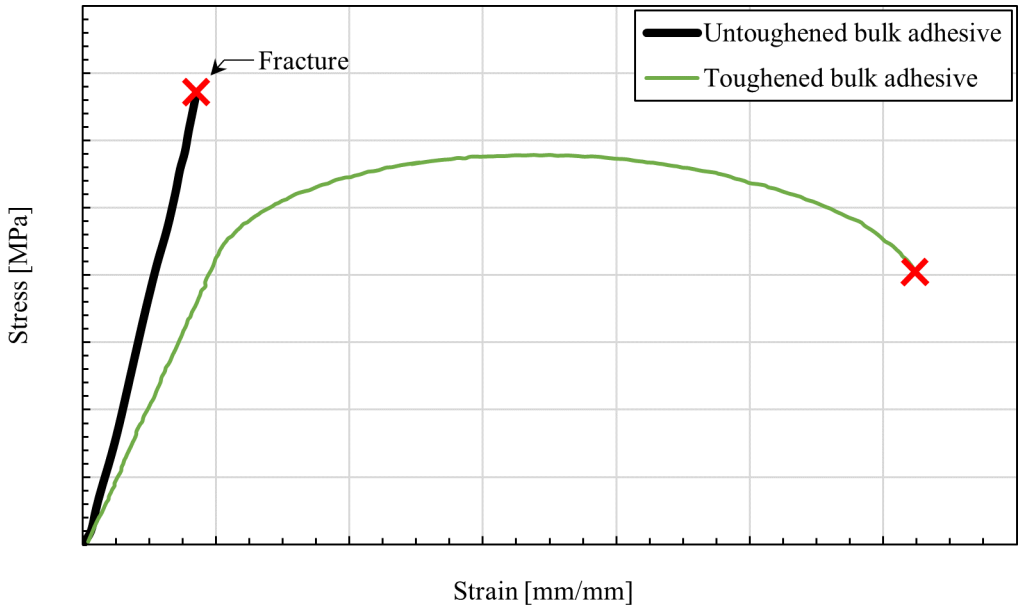

Figure 2.15: Typical stress-strain response of the brittle and ductile bulk adhesive

Adhesive generally exhibits viscoelastic behaviour with a dependence of the mechanical properties on the deformation rate (Gilat *et al.*, 2005; Siviour and Jordan, 2016). Under quasi-static or low rate of deformation, there is sufficient time for the intramolecular polymer chains in the adhesive to stretch until failure during the test. Under a high rate of deformation, the polymer chains resist high rate testing, while the intramolecular polymer chains are unable to resist the load at such high rate. As a result, the modulus and failure strength of a toughened structural adhesive typically increase with increasing strain rate, while the

strain at failure decreases (Trimiño and Cronin, 2016), resulting in reduced ductility with increasing strain rate (Gilat *et al.*, 2005).

Table 2.5: Mechanical properties of two-part toughened epoxy, impact resistant structural adhesive (properties adapted from 3M, 2016)

Mechanical Properties	**Value**
Elastic Modulus, E **(GPa)** *ASTM D638*	2.1
Elongation **(%)** *ASTM D638*	2 to 3
Ultimate Tensile Strength, UTS **(MPa)** *ASTM D638*	35
Fluid Property	**Value**
Mixed Viscosity (centipoise)	150000 to 200000

The mechanical properties of an adhesive joint, such as critical energy release rate (G_C) (*i.e.* energy required to propagate a crack over a unit area) are not only dependent on strain rate (Marzi *et al.*, 2009), but also on bond line thickness (Kinloch and Shaw, 1981; da Silva *et al.*, 2010). Although the bulk toughened epoxy properties are commonly measured (da Silva *et al.*, 2006; Watson *et al.* 2019), the epoxy material response at the joint behaves differently (Kinloch and Shaw, 1981). The large difference in modulus of elasticity (*i.e.* stiffness) between the metal adherends and the adhesive generates a confinement effect that restricts the growth of a plastic deformation zone, also referred to as fracture process zone (FPZ). A typical steel material has around 100 times higher modulus of elasticity than a toughened epoxy (*e.g.* 207 GPa *vs.* 2 GPa) (Table 2.5) (Askeland *et al.*, 2011; 3M, 2016). The high elastic modulus of the adherends creates a constraint that limits the energy dissipation to within a thin bond line configuration when a crack propagates under load, thereby resulting in a low G_C compared to the bulk material (Kinloch and Shaw, 1981). The authors experimented with a thin bond line thickness of 0.15 mm and found the measured critical energy release rate to be small compared to that of the bulk material. As the bond line thickness increased, a peak G_C was achieved and was higher than that of the bulk material. This increased bond thickness enabled the

development of the plastic deformation zone without restriction from the confinement effect (Kinloch and Shaw, 1981). As the bond thickness increased further, the critical energy release rate of bulk material is measured in an adhesive joint configuration, because the constraint from the adherends is no longer applied to the adhesive. With the larger bond line thickness, the volume of the plastic zone is also reduced, which caused the critical energy release rate to decrease (Figure 2.16) (Kinloch and Shaw, 1981).

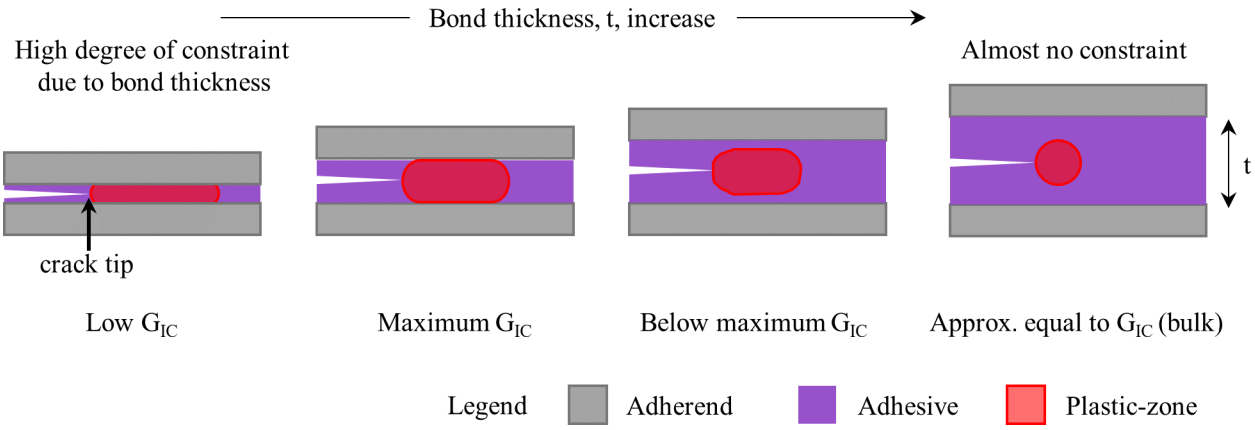

Figure 2.16: Illustration of constraint effect from adherends bond thickness effect in relation to critical energy release rate under the tensile opening, G_{IC}; as bond thickness becomes sufficiently large, there would be no constraint applied to the adhesive from the stiff adherends (figure adapted from Kinloch and Shaw, 1981)

2.2.2 General Loading Conditions on Adhesive Joints, Modes of Loading and Test Methods for Adhesive Joints

An adhesive joint structure can be loaded under tension, compression, shear, cleavage, or peel (Figure 2.17). A joint under tension or compression experiences a uniform load normal to the bond area. A butt joint is an example of a mechanical test to determine the tensile strength of the adhesive (ASTM D2094-00) (ASTM D2094-00, 2014). Shear loading deforms the adhesive by pulling adherends that causes an opposing-sliding motion between adherends and adhesives. The thick adherend lap-shear experiment is a standard test (ASTM D 5656-10) used to measure the shear properties of the adhesive (ASTM D5656-10, 2017). A cleavage load induces a peak force at one leading edge of the bond area and no load on the opposite side of the leading edge. An adhesive joint made of flexible adherends can result in a peel load in which the peak

load is applied to one leading edge of the joint. A standardized T-peel test is used to measure relative peel resistance of an adhesive joint that is made of flexible adherends (ASTM D 1876-08) (ASTM D 1876-08, 2015).

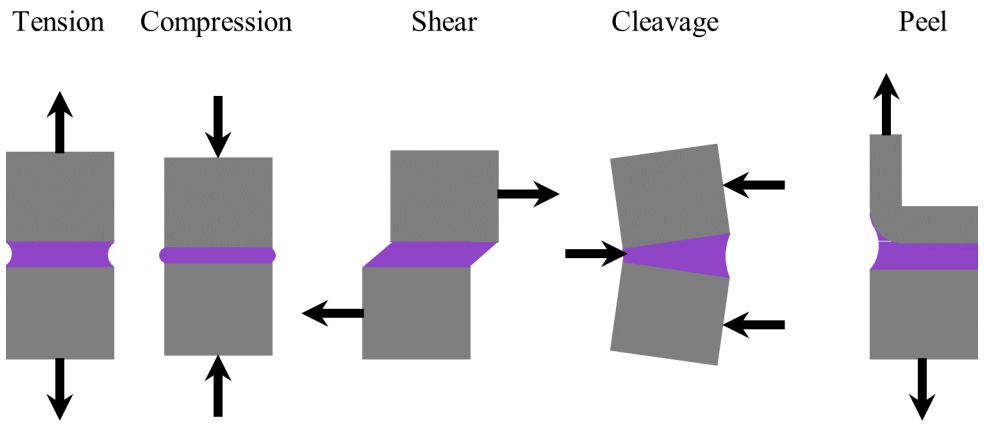

Figure 2.17: Basic loading conditions of an adhesively bonded joints

The single-lap shear (SLS) test is commonly used to assess adhesive joint strength of similar and dissimilar materials (Banea *et al.*, 2018), determine the effectiveness of the surface treatment (Critchlow *et al.*, 2000; da Silva *et al.*, 2009a; Aakkula and Saarela, 2014), effects of bond thickness (Banea *et al.*, 2015), bond length effect (Imanaka *et al.*, 2017), and validate numerical models (Nandwani, 2015; Campilho *et al.*, 2012; Watson *et al.*, 2019). The SLS test specimen is easy to assemble, low cost to manufacture and can be modified to examine geometrical effects such as the bond length (Karachalios *et al.*, 2013), adherend thickness (da Silva *et al.*, 2008), and bond thickness (Arenas *et al.*, 2010) without major changes to the test setup. There are different types of ASTM single-lap shear configurations, e.g. the adhesive mechanical test standards, ASTM D1002-10 and ASTM D3165-07, are used to determine the joint strength of a given adhesive system and compare engineering shear stress at failure from different adhesive/adherend combinations, but are not suited for basic characterization of the adhesive due to the presence of mixed-mode loading arising from the asymmetry of the test sample (Figure 2.18a and Figure 2.18b) (ASTM D1002-10, 2019; ASTM D3165-07, 2014). The difference between the two standards lies in the usage of

backing plates in the test specimen. ASTM D3165-07 test specimen has the added backing plates that align the loading at the overlap to reduce the bending load and increase the stiffness of the specimen. ASTM D5656-10 test provides shear stress-shear strain properties of the adhesive that can be used for the design and analysis of the adhesive joint (Figure 2.18c) (ASTM D5656-10, 2017).

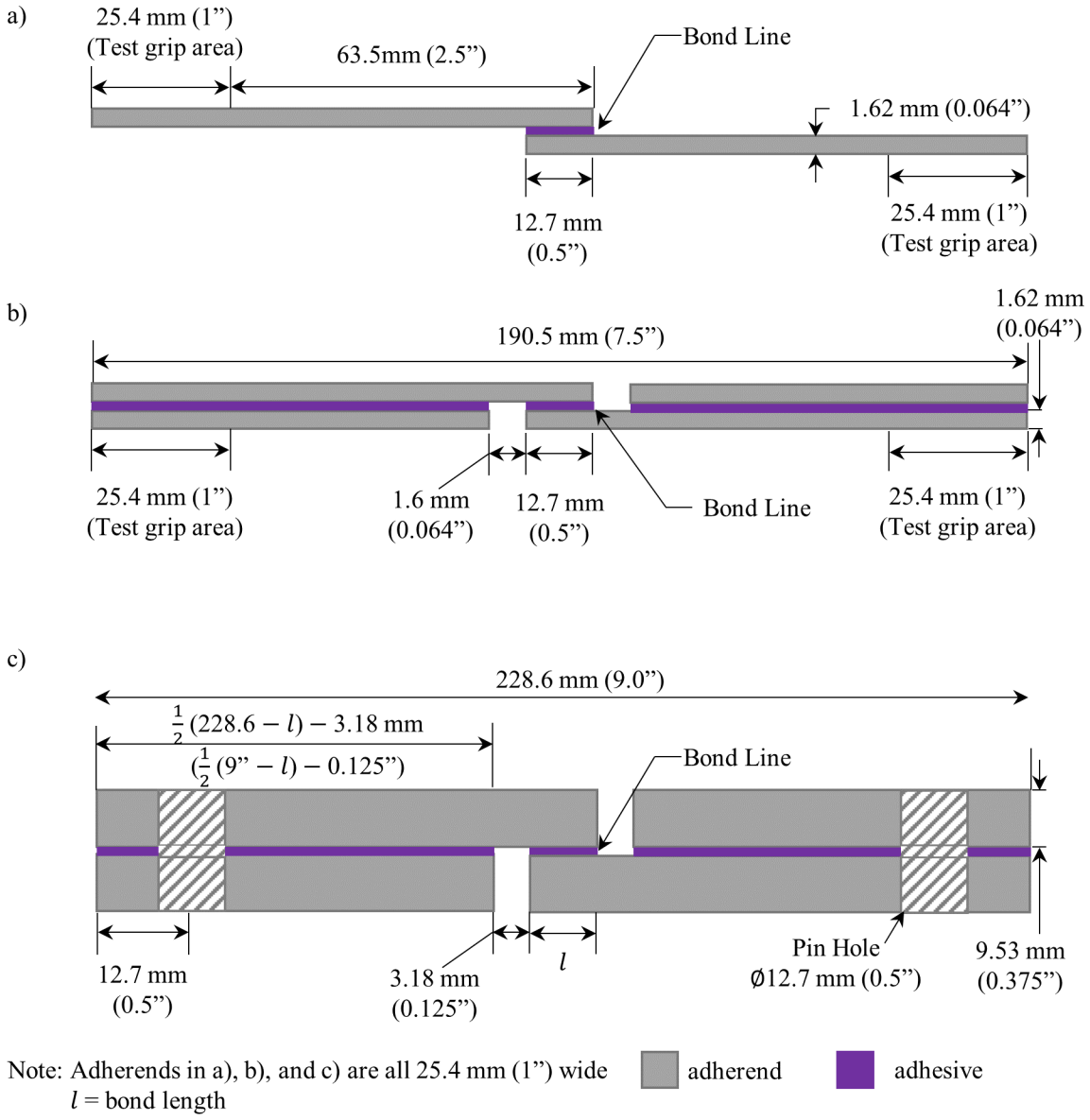

Figure 2.18: Standard test method of different adhesive joint configurations; a) ASTM D 1002 - 10 (ASTM D 1002 - 10, 2019), b) ASTM D 3165 - 07 (ASTM D 3165 - 07, 2014), c) ASTM D 5656 - 10 (ASTM D 5656 - 10, 2017) (illustrations are not to scale)

From ASTM D1002 or ASTM D3165 test, the shear strength is used in practice to assess the performance of surface treatments. With the assumption of rigid adherends (*i.e.* no plastic deformation), the shear strength (τ_{max}) represents the average nominal shear stress applied across the bond area. However, it is important to note that the adhesive in the single-lap shear test experiences mixed-mode loading due to the eccentric loading on the adhesive that leads to an out-of-plane bending moment at the leading edges of the bond (da Silva *et al.*, 2009b). Watson *et al.* (2019) quantified the SLS joint kinematics by measuring the joint rotation relative to the loading direction and noted the difference between SLS specimens made of similar and dissimilar materials (aluminum, magnesium, and UHSS). A closed-form analysis done by Goland and Reissner (1944) showed a cup-shaped (bathtub shaped) shear and peel stress distribution across the bond length, with stress concentrations at the leading edges of the bond (Figure 2.19). The peel stress arises due to the eccentric loading, and as the joint rotates, the adhesive experiences the peeling load. Nonetheless, the average nominal shear stress (*i.e.* shear strength (τ_{max})) is a common metric used to determine the adhesive joint strength (Reis *et al.*, 2011; Watson *et al.*, 2019).

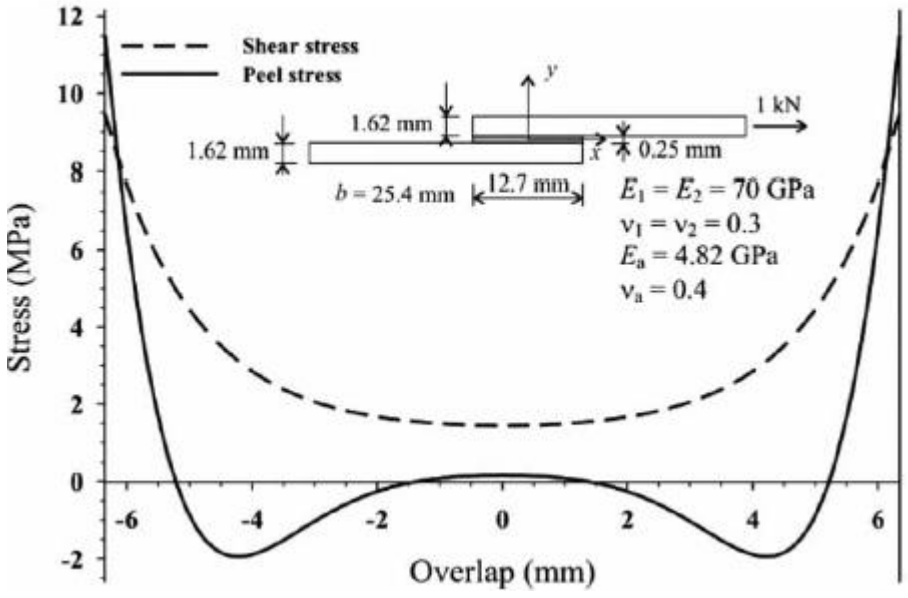

Figure 2.19: Shear stress and peel stress distribution across the bond length of the single-lap shear test following closed formed analysis by Goland and Reissner (da Silva *et al.*, 2009b)

A spew fillet is the result of an excess adhesive that overflows out of the bond area and cured around the bond edges (Figure 2.20). In the stress distribution across the bond length of a SLS test specimen, the presence of a spew fillet reduces the stress concentration at the ends of the overlap (Tsai and Morton, 1995; Lang and Mallick, 1998; Crocombe and Adams, 1981), resulting in a higher joint strength compared to the case without the spew fillet. Lang and Mallick noted a drop in peel and shear stress, which improved the joint strength in the finite element analysis of a single-lap joint that included a spew fillet (1998). Grant *et al*. (2009) noted little change in joint strength with and without a 45° spew fillet for thin bond lines (0.1 mm to 0.5 mm), but as the bond line thickness increased (1 mm to 3 mm), the effect of the spew fillet became apparent in terms of a higher joint strength. Karachalios *et al.* (2013) conducted single-lap shear experiments specifically with a thin bond thickness (0.1 mm) using adherends from mild, medium carbon steel, and high strength steel that resulted in similar findings, in which no difference in the joint performance was found between the cases with spew and without spew fillet. However, Critchlow (1997) did report a higher variability in the joint strength of test specimens with spew fillets (Table 2.6).

Figure 2.20: Side view of single-lap shear test specimen with spew fillet at the leading edges of the overlap

Table 2.6: Adhesive joint ultimate load using 1.2 mm thick mild steel from single-lap shear samples with full fillet (excess adhesive overflow without specified shape), half fillet (one side of fillet removed), and no fillet (results adapted from Critchlow, 1997)

Adhesive	Fillet Geometry	Joint Strength (N)	Percentage variation
Toughened Epoxide	Full	3491 ± 253	7.2
	Half	3311 ± 59	1.8
	None	3229 ± 64	2.0
Non-toughened Epoxide	Full	2705 ± 121	4.5
	Half	2425 ± 132	5.4
	None	2157 ± 57	2.6

In the framework of fracture mechanics, the field focuses on crack propagation in the material and study the resistance of a material to fracture. Under an adhesive joint configuration, the material of interest, in this case the adhesive, has a pre-crack that can be loaded under tensile opening (Mode I), in-plane shear (Mode II), and out-of-plane shear (Mode III) (Figure 2.21). Experiments are designed to induce loading that causes a pre-crack to propagate under the intended mode of loading and measure the respective fracture toughness properties of adhesive, such as the critical energy release rate, taken as the energy required to generate new fractured surface over a unit area.

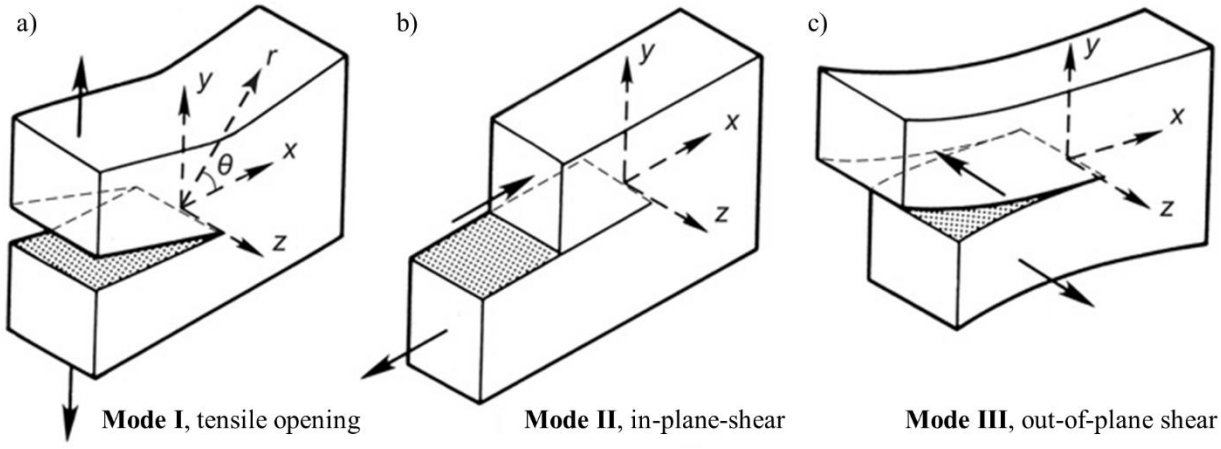

Figure 2.21: Loading Modes: a) Mode I (tensile opening), b) Mode II (in-plane shear), c) Mode III (out-of-plane shear) (Kanninen and Popelar, 1985)

Double cantilever beam (DCB) and tapered double cantilever beam (TDCB) are standardized tensile opening (Mode I) test geometries (ASTM D3433-99) used to measure critical energy release rate, G_{IC} (ASTM D3433-99, 2012; Lopes *et al.*, 2016) (Figure 2.22a). To cause crack growth in the adhesive joint, the elastic energy stored in the beams (adherends) accumulates to the point that reaches the threshold to advance the crack and create new fracture surface area. A recent development in Mode I testing, called the rigid double cantilever beam (RDCB), was proposed by Dastjerdi *et al.* (2013) (Figure 2.23a). Similar to the standardized tests, the RDCB measures the G_{IC} of the adhesive, but the analysis method is only valid if the adherends are largely rigid (*i.e.* nondeformable).

A typical commercial one-part toughened epoxy has a critical energy release rate of 3.6 kJ/m^2 (Marzi *et al.*, 2009). Watson *et al.* (2019) experimented with RDCB samples with a two-part toughened structural adhesive and measured a critical energy release rate of 3.06 kJ/m^2 under quasi-static, room temperature conditions. As mentioned at the end of Section 2.2.1, the fracture toughness depends on the bond thickness and strain rate. The relatively lightweight RDCB specimen has the advantage of measuring fracture toughness at a higher strain rate with minimal inertial effect compared to the standardized DCB or TDCB specimens.

End notch flexural (ENF) testing is used to measure the Mode II fracture toughness of an adhesive joint (da Silva *et al.*, 2010) (Figure 2.22b). A more compact geometry called the bonded shear sample (BDS) was developed to determine the adhesive joint response under pure shear and measures shear strength and critical energy release rate, G_{IIC} (Watson, 2019) (Figure 2.23b). Under a combined mode of loading with tension and shear, Mixed-Mode bending (MMB) and Arcan tests are common mechanical tests that produce mixed mode loading at the adhesive bond with the flexibility of inducing various degrees of load mixity (Figure 2.22c). With the large size and weight of the specimens and the specialized test apparatus to induce the intended mode of loading, the adhesive response under high strain rate conditions using such geometries would have a significant inertia effect. Thus, Watson (2019) designed a coupon level adherend geometry

such as BDS and a Mixed Mode loading adherend geometry that induces a 45° loading at the adhesive (Figure 2.23c).

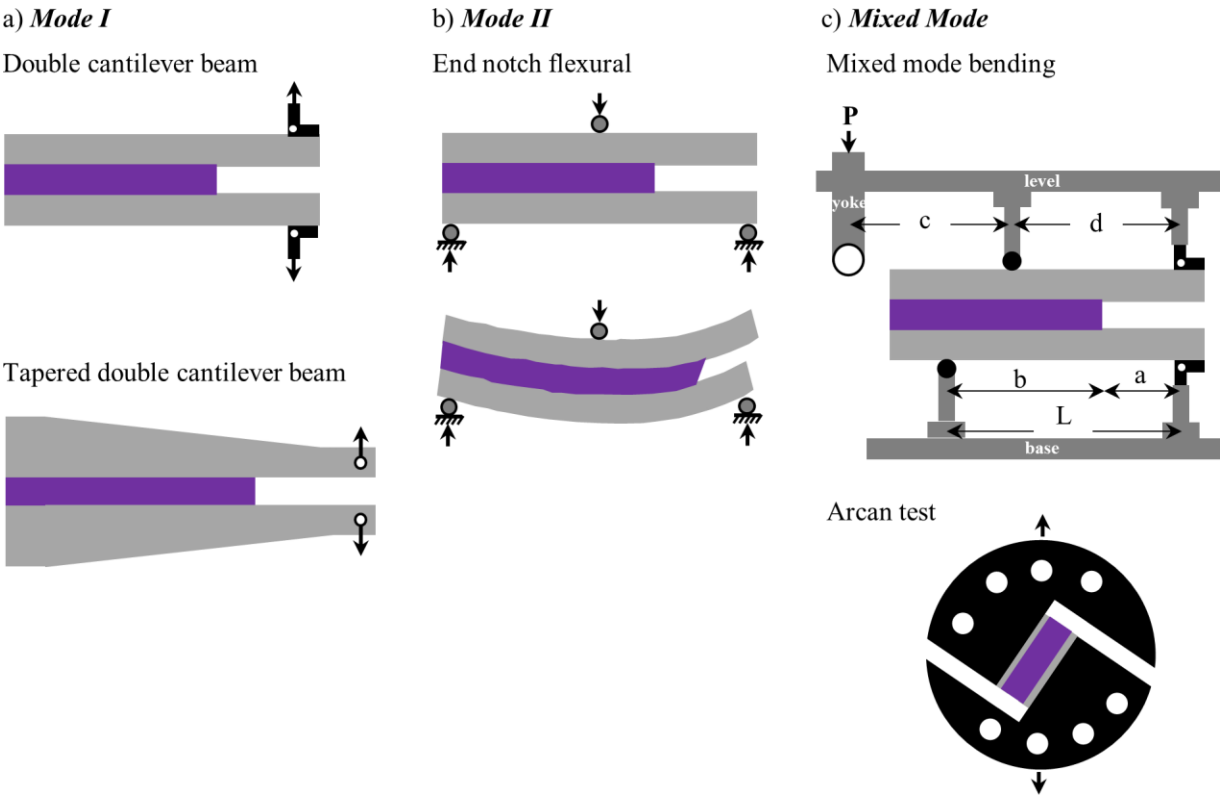

Figure 2.22: Adhesively bonded joints for fracture toughness measurements; a) Double cantilever beam (DCB) or tapered double cantilever beam (TDCB), b) end notch flexural test, and c) Mixed Mode bending and Arcan test

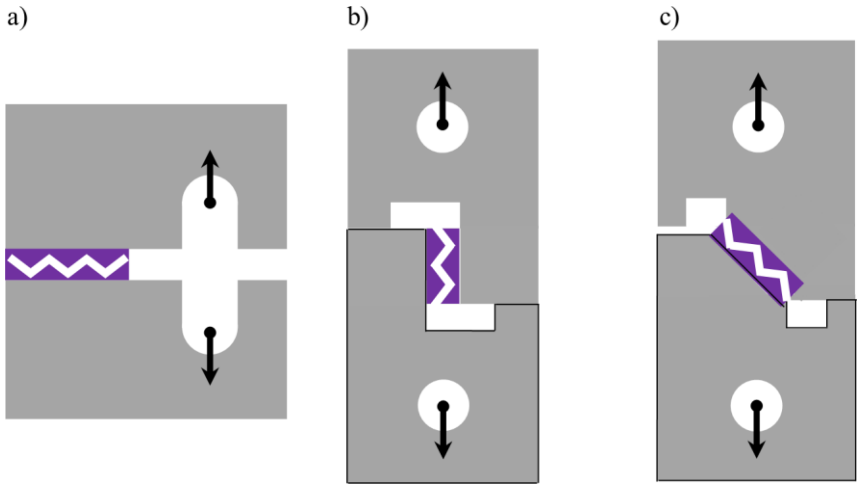

Figure 2.23: Adhesive joint test geometries; a) rigid double cantilever beam (RDCB) test under Mode I, b) bonded shear test (BDS) under Mode II, and c) Mixed-Mode loading at 45°

2.2.3 Adhesive Joint Failure

Four types of adhesive joint failure are commonly observed: cohesive failure, interfacial failure, coating failure, and adherend failure. Cohesive failure occurs within the adhesive material (Figure 2.24c) and is desirable since this indicates the maximum strength of the adhesive was achieved within the joint (Spaggiari and Dragoni, 2013; Ebnesajjad, 2014). Interfacial failure occurs at the interface between the adhesive and the adherend (Figure 2.24a), typically indicating a low interface strength associated with the method of adherend surface preparation. Such failure is also commonly referred to as adhesive failure. In the case where a coating is applied to the adherends, such as aluminum-silicon (Al-Si) coating or galvanneal (GA) coating (Fan and De Cooman, 2012), the interface between the coating and adherend may delaminate leading to a coating failure (Figure 2.24b) (Lundrgen, 1989; Davis and Fay, 1993; Hertveldt *et al.*, 1999; Wolf *et al.*, 2011). An adherend failure occurs when the ultimate load supported by the adhesive exceeds the ultimate load corresponding to the strength of the adherends (Figure 2.24d). An adhesive joint failure may also present a combination of the aforementioned joint failure types (*e.g.*, interfacial combined with coating delamination, interfacial combined with cohesive failure etc.), defined as mixed failure.

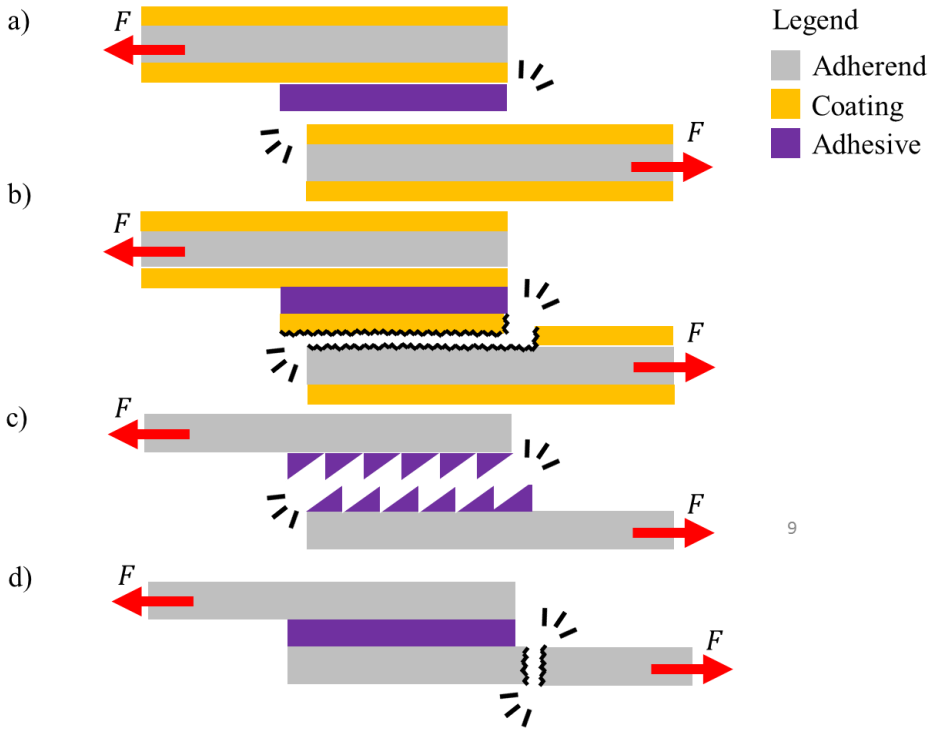

Figure 2.24: Adhesive failure types under single-lap shear configuration: a) interfacial failure (also known as adhesive failure), b) coating failure and c) cohesive failure, d) structure/adherend failure

2.3 Surface Treatments to Enhance Adhesive-Adherend Interfacial Strength

Surface treatment of the adherend surface that is to be bonded is a critical step to enhance the adhesive-adherend interface strength (Ebnesajjad, 2014), to achieve cohesive failure. The methods of surface preparation depend, to some extent, on the adherend material and specific adhesive. After an extensive search on possible surface treatments on steel, there are five categories of surface treatments for a wide range of steel alloys (Table 2.7). The current literature lacks a surface treatment comparative study on adhesive joint strength data for coated hot stamped boron steel using structural epoxies. In this section, six methods that are applicable to adhesively bonded ultra-high strength steels using structural epoxies are described below including surface cleaning and degreasing, grit-blast treatment, adhesion promotor treatment, acid-etch treatment, dry-ice blasting, and laser ablation treatment.

Table 2.7: Literature summary of surface treatment studies on different types of steel

	Surface Treatments						
Authors	Degreased	Mechanical Treatment	Chemical Treatment	Dry ice blasting	CO2 Laser Ablation	Additional Information	Adherend Material
Banea *et al.* [2018]	X	X				Grit-blasted and degreased (acetone)	High strength steel (DIN C65 heat treated) Aluminium alloy (AE 6082-T651)
Critchlow *et al.* [1998]	X	X			X	(1) degreased (ultrasonic cleaning in acetone) (2) combination of different chemical treatments; and (3) CO2 laser ablation	Hot dipped galvanized mild steel
Critchlow *et al.* [2000]	X	X	X			(1) degreased (1,1,1 trichloroethane), (2) grit-blasted and degreased, (3) grit-blasted, degreased and silane; and (4) combination of different chemical treatments	EN 42 J spring steel
da Silva *et al.* [2008]	X	X	X			(1) degreased, shot blasted with corundum, and cleaned with acetone; and (2) different chemical conversion coating applications	Low strength steel (DIN ST33) High strength steel (DIN C65 heat treated)
Fujimoto *et al.* [2018]	X					Degreased (ethanol)	Cold-rolled (CR) uncoated steel galvannealed (GA) plated steel
Ghosh *et al.* [2015]	X	X	X			Sandblasting plus ultrasonic cleaning (in acetone) and silane treatment	Stainless steel (SS) type 304 (plate) and stainless steel(SS) type 316 (rod)
Knox *et al.* [2000]	X	X	X			(1)Shot-blasted, (2) silane treatment, (3) corrosion inhibitor treatment (solvent degreased before implementing the treatment)	Mild steel

	Surface Treatments						
Authors	Degreased	Mechanical Treatment	Chemical Treatment	Dry ice blasting	CO2 Laser Ablation	Additional Information	Adherend Material
Sterrett [1981]			**X**			chemical etching surface treatment (sulphuric acid)	Stainless steel (SS) 301
Vazirani [1969]		**X**	**X**			(1) Sandblast treatment and (2) various concentration of chemical etching surface treatment (hydrochloric acid (HCL), phosphoric acid (H3PO4), etc.)	4340 High Strength Steel 1010 Cold Rolled Steel 1095 Cold Rolled Steel 302 CRES Steel 410 CRES Steel
Walker [1991]	**X**		**X**			Degreased (methyl ethyl ketone), grit-blasted and silane treatment (4 types)	Mild steel Stainless steel Aluminium
Wang *et al.* [2017]	**X**	**X**	**X**			(1) Grit-blasted, (2) Grit-blasted and degreased (ultrasonic cleaning in acetone), (3) Grit-blasted and resin pre-coated; and (4) Grit-blasted, degreased and resin pre-coated	Mild steel
Wolf *et al.* [2011]	**X**					Solvent wiped	Galvanneal(GA) coated steel (complex phase (CP), dual phase(DP), and transformation induced plasticity (TRIP))

2.3.1 Surface Cleaning and Degreasing

A sheet metal surface is typically covered with oil or lubricant intended to reduce tooling wear and promote the formability of the part during a stamping process. With respect to subsequent adhesive joining, the residual oil, lubricant and other contaminants prevent contact between the bare metal surface and the adhesive, which decreases the adhesive bond durability and strength (Ebnesajjad, 2014). Therefore, a degreasing step as a surface preparation method can be used to remove oil and contaminants present on the adherend surface. In some studies, the degreasing step has been incorporated as the last step of a series of pre-treatment such as mechanical surface treatment (Banea *et al.*, 2018) to remove residues (loose grit or dust) from the surfaces to be joined.

Common degreasing agents include: 1,1,1 trichloroethane (Critchlow *et al.*, 2000; ASTM D2651, 2016), acetone (Critchlow *et al.*, 1998; da Silva *et al*., 2008; ASTM D2651, 2016, and Banea *et al.*, 2018), methyl ethyl ketone (MEK) (Walker, 1991, Nandwani, 2015, and ASTM D2651, 2016), isopropanol (Bamberg *et al.*, 2018) and ethanol (Fujimoto *et al*., 2018).

It is worth noting that there are adhesives formulated to bond contaminated surfaces (Nandwani, 2015); however, these adhesives often require relatively uniform and controlled contamination of the surface to be bonded. Acrylic adhesive is another example of adhesive capable of establishing good joint strength made of materials with contaminated (oily or dirty) surfaces (Baldan, 2004; Kim *et al.*, 2011). Debski *et al.* (1986) suggested that such adhesives could function using two possible mechanisms: 1) displacement of the contaminants by the adhesive, allowing for direct contact between the metal surface and adhesive; 2) absorption of contaminants (oil) by the adhesive.

2.3.2 Grit-Blast Surface Treatment

Grit-blasting is a mechanical surface treatment that increases the surface roughness of the adherends by impacting the surface with an abrasive medium such as silicon carbide or alumina grit (Varacalle *et al.*,

2006) (Table 2.8) at a sufficient velocity to cause localized yielding of the surface. The increase in roughness is the result of abrasive medium impinging the surface and generating peaks and valleys across the treated surface (Figure 2.25b). The treatment also removes contaminants and weak oxide layers off the surface (Arnott *et al.*, 1993). Grit-blasting is a common surface treatment for adhesively joining steel substrates (Ebnesajjad, 2014). The treatment can be an effective way to control the final surface roughness of the adherend (Baldan, 2004), depending on the blast media (Harris and Beevers, 1999).

Table 2.8: List of grit-blast medium with hardness and relative cost (Ebnesajjad, 2014)

Blast Media	Hardness, [Moh]	Relative Cost Volume Basis
Walnut shells	1-4	19
Silicon carbide	9	50
Aluminum oxide	9	25
Glass bead	6	18
Plastic grit	3-4	30
Steel shot	6	27
Steel grit	6	n.a.
Sand, silica (silicon dioxide)	7	11
Sodium bicarbondate	2.5	n.a.

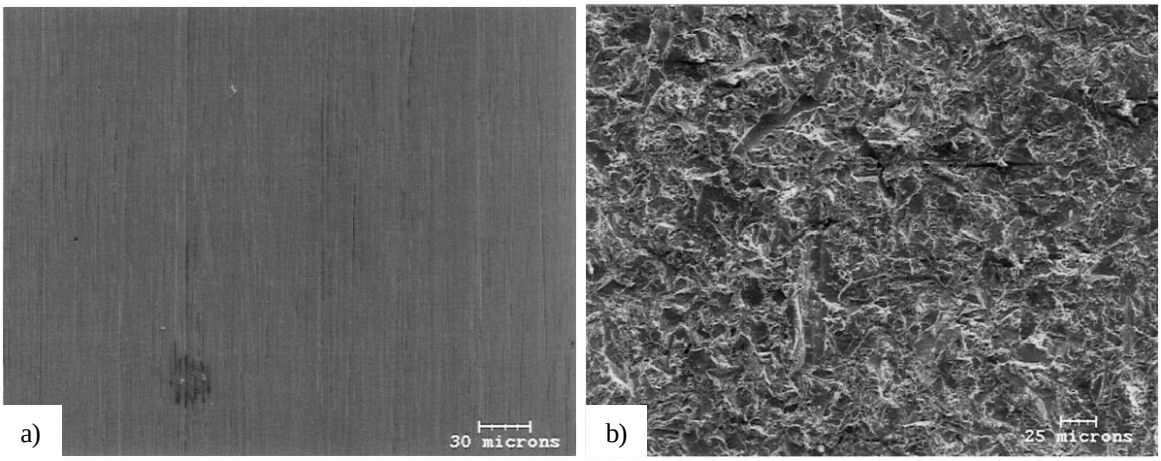

Figure 2.25: High-resolution SEM image of plain carbon steel surface a) degreased surface b) grit-blasted surface (Critchlow *et al.*, 2000 used with permission from ELSEVIER)

The roughening procedure is only effective if the blast medium is harder than the substrate (Ebnesajjad, 2014), since a softer medium would break upon impact without causing significant plastic deformation to

the substrate surface. Similarly, with softer metals such as aluminum and copper, relatively harder blast media such as alumina, sand and silicon carbide are not recommended since they can become embedded in the soft metal (Varacalle *et al.*, 2006). A reduction in air pressure during the grit-blasting procedure can mitigate such issues.

The improvement of adhesion from grit-blasting relative to surface cleaning and degreasing is best explained by the theory of mechanical interlocking (Özdemir *et al.*, 2016; Wang *et al*., 2017). As the media roughens the surface, the surface area for adhesive bonding is increased thus producing a mechanical interlock between the organic (adhesive) and inorganic (metal adherend) materials (Figure 2.26).

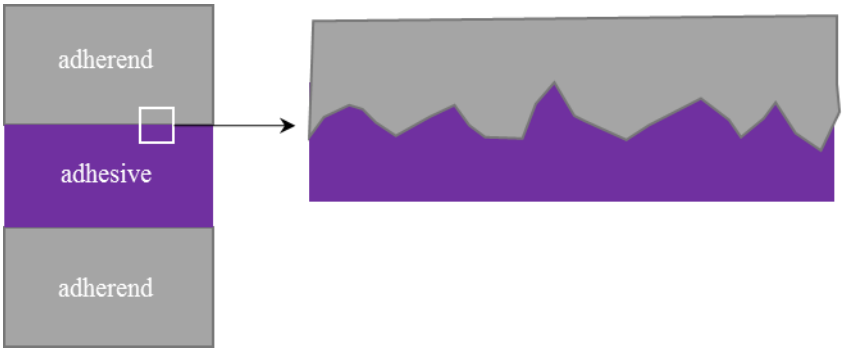

Figure 2.26: Illustration of the mechanical interlocking model

Conflicting conclusions were found when establishing the relationship between the surface roughness, such as the arithmetic mean roughness (Ra) of the adherend, and the adhesive joint strength. Harris and Beevers (1999) reported no difference in the joint strength of specimens that were grit-blasted using coarse grit (60 grit, Ra=3.2 µm) or fine grit (180/220 grit, Ra=1.3 µm). Cho *et al.* (2009) noted a critical value of surface roughness (Ra=3.55 µm) resulted in optimal joint strength and reported that the joint strength decreased if the surface roughness exceeded the critical roughness value of 6.82 µm. In contrast, Şekercíoğlu *et al.* (2003) reported an optimal Ra ranging between 1.5 to 2.5 µm for optimal joint shear strength and reported low shear strength for roughness below 1.0 µm or above 2.5 µm (Figure 2.27). A recent study by Boutar *et al.*

(2016) showed a better joint strength was obtained from a smooth surface with low roughness (Ra=0.6 μm) than a rough surface (Ra=3 μm). These conflicting findings may be due to difference in the adhesives and adherends used by the authors (Table 2.9). However, the underlying effect of grit-blasting or mechanical treatment using abrasive sandpaper may go beyond a simple physical change in the surface geometry, but also a change in the chemical properties of the surface (Harris and Beevers, 1999). A direct relationship between surface roughness and shear strength may be oversimplifying the adhesion phenomenon at the adhesive/adherend interface, however, the relationship can be used as a guide in designing an adhesive joint structure.

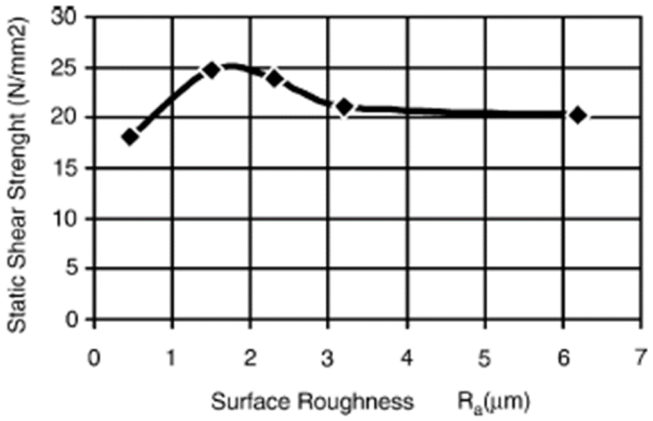

Figure 2.27: Relationship between surface roughness and the static shear strength (Şekercíoğlu *et al.*, 2003 used with permission from ELSEVIER)

Table 2.9: Summary of the surface roughness vs. joint strength relationship

Literature	Adherend Material	Surface treatment	Adhesive Type	Mechanical Test	Recommendation
Harris and Beevers (1999)	mild steel CR1 (1.6 mm thick)	grit-blast using alumina oxide at 0.4 MPa	two-part epoxy	single-lap joint	No difference in joint strength between fine (Ra= 1.3 µm) or coarse grits (Ra= 3.2 µm)
Cho *et al.,* (2009)	aluminum 2024-T3 (10 mm thick)	grit-blast using aluminum oxide at 0.5 MPa	two-part heat-resistant adhesive RTV88 (hyper-elastic adhesive)	single-lap joint	Shear strength decreases beyond the critical value Ra of 3.55 µm
Şekercíoğlu *et al.,* (2003)	general structural steel	abrasive sandpaper	anaerobic adhesive (commonly used for threadlockers)	pin and collar	Ra = 1.5 to 2.5 µm
Boutar *et al.*, (2016)	aluminum copper alloy (3 mm thick)	abrasive sandpaper	one-part polyurethane adhesive	single-lap joint	Ra = 0.6 µm

2.3.3 Adhesion Promotor

Adhesion promotors (also known as coupling agents) are chemical solutions applied on the surface of a metal adherend to improve the adhesion between the adhesive and the surface of the metal. The coupling agent acts as a bridge between an organic and an inorganic surface that results in better adhesion between the adhesive and the adherend (Critchlow *et al.* 2000; Ebnesajjad, 2014). It can be considered as a secondary adhesive that binds the surface of the metal to the surface of the primary structural adhesive (Figure 2.28). Evidence suggests that a covalent bond is established between epoxy and metal with the help of organosilane coupling agents (Packham, 2017). The adhesion promotor is reported to attach to the metal surface via covalent oxane bonds, which makes the metal more receptive to the epoxy (polymer). On the other side of the adhesive promotor, between the adhesive promotor and the adhesive, the adhesion mechanism is via chemical reactivity between the adhesive polymer and the silane coupling agent (Figure

2.28). The adhesion promotor diffuses into the initially liquid state of the polymer and participates in the curing process as the polymer is cured (Ebnesajjad, 2014).

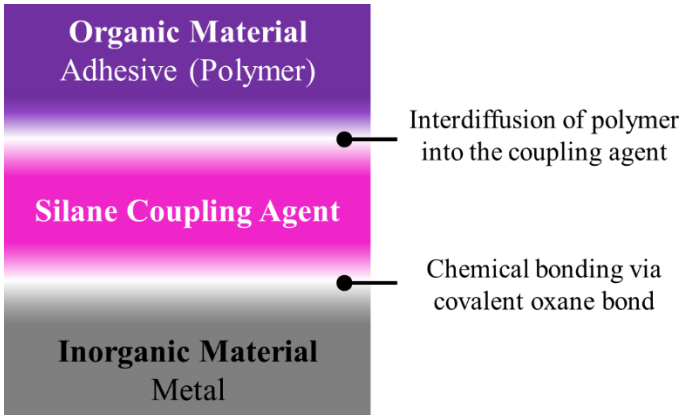

Figure 2.28: Illustration of adhesion promotor (*e.g.*, silane coupling agent) bond mechanism with adhesion promotor (*e.g.*, epoxysilane/aminosilane) participating in the adhesive curing (figure adapted from Ebnesajjad, 2014)

The additional benefit of the adhesion promotor is preservation of the joint strength over time by preventing formation of moisture at the adherend/adhesive interface (Gledhill *et al.*, 1990; Walker, 1991; Critchlow *et al.*, 2000; Plueddemann, 1988). Critchlow *et al.* (1997) have demonstrated the improved durability of the adhesive joint that received silane treatment (Table 2.10).

Table 2.10: Joint strengths of single-lap shear specimens (0.25 mm bond thickness with a 10 mm overlap and 20 mm wide) after bonding (initial) and after exposure to deionized (DI) water at 60°C, with different surface preparations (data adapted from Critchlow *et al.*, 1997)

Adherend	CR1 mild steel (1.2 mm thick)	
Adhesive	Araldite® 2007 AV 119 (Single-part epoxide)	
Overlap length	10 mm	
Surface Treatment	**Initial Joint Strength (N)**	**Joint strength (N) after exposure for 12 weeks**
Degrease only [a]	3550	3070
CO_2-Laser treatment, SET 30 sec [b]	5200	3920
CO_2-Laser treatment, SET 2760 min [b]	4940	3980
Grit-blast [c]	5240	5410
Grit-blast plus silane [d]	5160	5610

[a] Ultrasonic immersion degrease (using 'Super Purity' acetone) for a duration of 2 x 10 min period
[b] SET = surface exposure time before adhesive application;
[c] Degrease the first before using 80/120 grade alumina grit and degrease again after mechanical treatment
[d] Silane solution from Union Carbide A187 (1 % aqueous solution)

2.3.4 Acid-Etch Treatment for Steel

Acid-etch surface treatment can be applied to steel, resulting in a pit-like surface (Figure 2.29) that effectively increases the surface roughness. Following the aggressive acid-etch treatment on the steel surface, a deposit of graphite (*i.e.* smut) was removed by using solutions such as chromic acid, sulphuric acid, or chromium trioxide. After the desmutting stage, the acid etched steel has a uniform and thicker oxide layer on the surface, which improves the corrosion resistance (Allen and Alsalim, 1976). A wide range of etching solutions has been investigated to improve adhesive joints on steel adherends (Vazirani, 1969; Sterrett, 1981; Allen and Alsalim, 1976). The following chemical etching solutions were tested on different grades of steel adherends (as well as stainless steel) to determine the joint strength: potassium bromide (KBr), hydrochloric acid (HCl), hydrofluoric acid (HF), phosphoric acid (H_3PO_4), potassium iodide (KI), and sulphuric acid (H_2SO_4) (Vazirani, 1969; Sterrett, 1981) (Figure 2.29). The concentration of the acid and duration of the etch time also affect the shear strength (Sterrett, 1981), so they are also the factors to consider when implementing the acid-etch treatment. There are currently no published experimental data related to acid-etch treatment for Al-Si-Fe coated boron steel for adhesive joint bonding, but a HCl and HF mixture can be used as a coating striping solution to determine the coating weight and composition applied to the steel (ArcelorMittal, 2010).

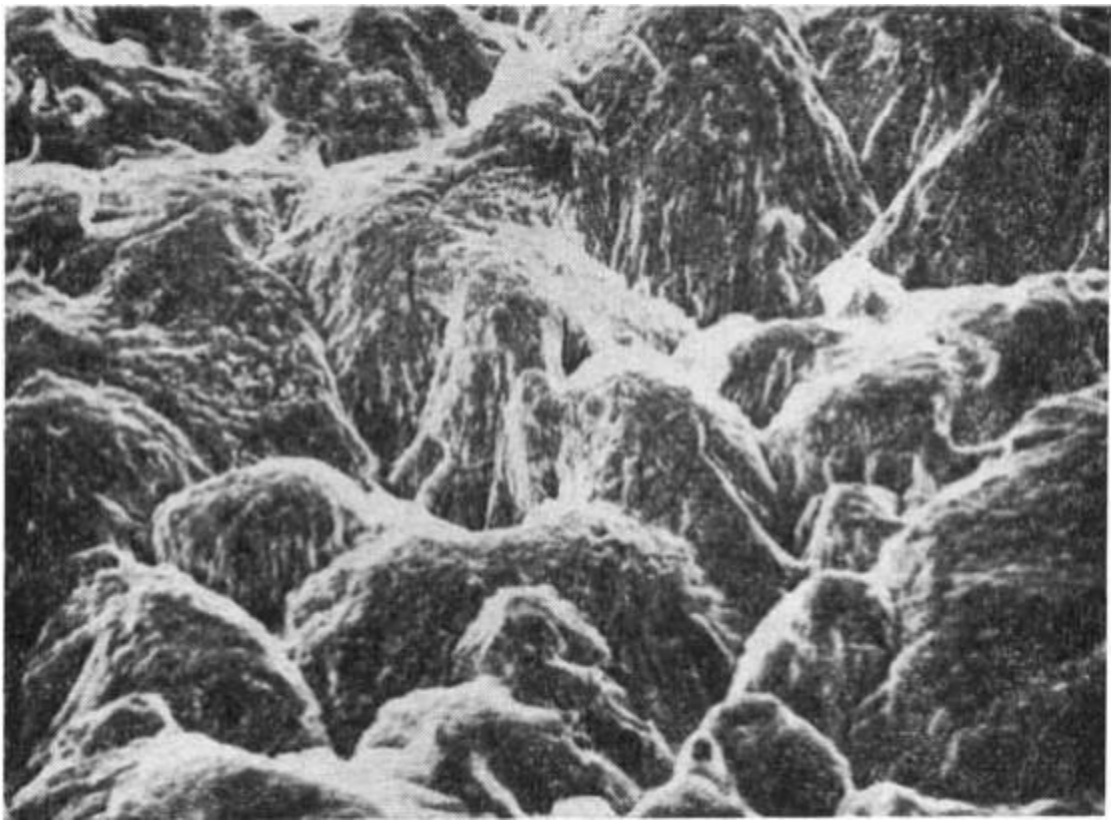

Figure 2.29: Sulphuric acid (H_2SO_4)/oxalic acid etched martensitic FV-520B stainless steel (x 1000) (Allen and Alsalim, 1976)

Allen and Alsalim (1976) and Sterrett (1981) recommended a desmutting step (e.g. with alkaline water) after etching and before the adhesive application to remove the deposited carbon (smut) and debris left on the surface, which showed an increase in strength and durability of the joint. Allen and Alsalim (1976) reported a strength improvement of 138% (from 49.1 MPa to 116.5 MPa using the napkin ring test made of stainless steel) between specimens with and without smut. The durability of an acid-etched stainless steel surface with the optimal acid concentration showed a 45% improvement in shear strength retention (977 hours *vs.* 537 hours under a static load of 14 MPa at 60°C and 100% relative humidity) (Sterrett, 1981). The resulting joint strength after acid-etching treatment depends on the duration of the etching and the etching agent used. The duration of the acid-etch can last from a few minutes to an hour with a significant difference in joint strength (Allen and Alsalim, 1976), which may not be an efficient or economic process

in high volume production. In addition, the acid-etch treatment may involve hazardous chemicals such as nitric acid.

2.3.5 Dry-Ice Blasting

Dry-ice blasting (also known as cryoblasting) uses solid carbon dioxide (CO_2) particles in the form of pellets travelling at high speed to break down contaminants and clean the surface of an adherend (Brewis *et al.* 1999). The dry-ice pellets (*e.g.* cylindrical shaped) can be projected at a blast pressure ranging from 0.9 MPa to 1.1 MPa (131 psi to 160 psi) for aluminum sheets (Brewis *et al*., 1999; Uhlmann and Mernissi, 2008) to strike the surface and remove dirt and contaminants. The impact against the metal surface causes the CO_2 particles to sublimate (Figure 2.31). Dry-ice blasting is also capable of roughening the surface similar to grit-blasting, which may improve the adhesion (Figure 2.31b). This surface treatment demonstrated an improvement of the adhesive strength on aluminum substrates compared to conventional procedures that used only a degreasing agent (Brewis *et al.*, 1999; Elbing *et al.*, 2003). Liu *et al.* (2011) showed that the collision between CO_2 particles and the contaminants on the surface resulted in better cleaning compared to an air jet cleaning. This type of surface treatment can be an alternative to replace the surface cleaning and degreasing step that uses solvents and reactive chemicals that may be harmful to the environment (Uhlmann and Mernissi, 2008).

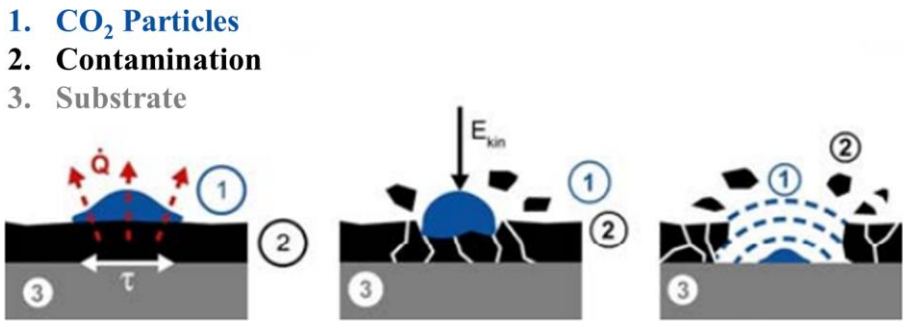

Figure 2.30 Dry-ice blasting treatment illustration (Uhlmann and Mernissi, 2008 used with permission from SPRINGER NATURE)

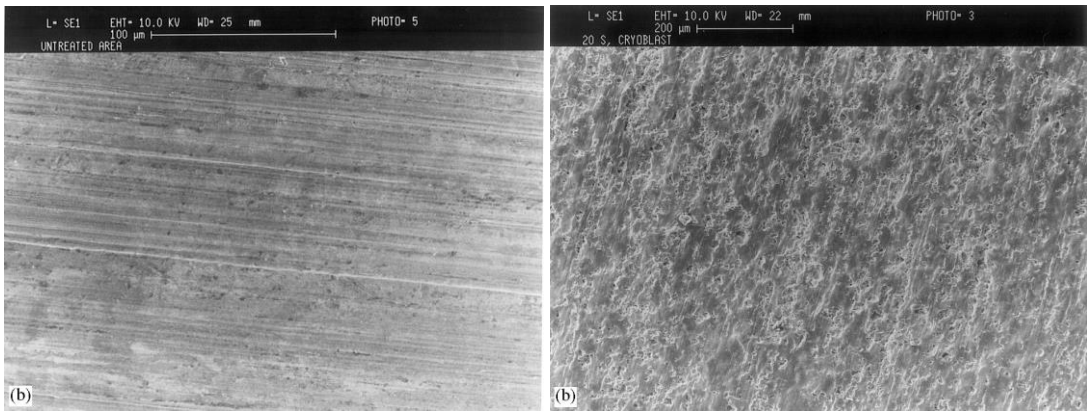

Figure 2.31: Aluminum 5251 post surface treatment SEM micrograph of a) degrease only, and b) dry-ice blasting for 20 seconds at 1 MPa (Brewis *et al.*, 1999 used with permission from ELSEVIER)

The results showed that the dry-ice blasting treatment applied to aluminum could achieve adhesive joint strength levels similar to chemical treatments (Brewis *et al.*, 1999; Elbing *et al.*, 2003; Uhlmann and Mernissi, 2008). Dry-ice blasting treatment on ultra-high strength steel has not been done for adhesive joints. Before conducting a surface treatment study related to dry-ice blasting, several experimental parameters should be considered and documented: velocity of the particle impact, dry-ice particle diameter, duration of the blast, and temperature of the dry-ice at the impact.

2.3.6 Laser-Based Ablation Treatment

Laser ablation can be an alternative to surface cleaning and degreasing treatment (Critchlow *et al.*, 1998; Critchlow *et al.*, 1997; Mandolfino *et al.*, 2015). This treatment is capable of removing organic contaminants on the adherend surfaces. Transversely excited atmospheric (TEA) carbon dioxide (CO_2) laser causes a physicochemical change to the bond area with the modification of surface topography and chemistry (Critchlow *et al.*, 1997) by emitting high energy through electrical discharge of CO_2 gas (Beaulieu, 1970). Critchlow *et al.* (1998) reported similar mean time-to-failure between the adhesive joint from TEA CO_2-laser treated mild steel compared to degreasing treatment with acetone, which demonstrated the similar durability of the treatments (Figure 2.32). The improvement was attributed to the improvement

in the surface wettability, which was quantified by the contact angle. The contact angle of a laser ablated surface was lower compared to that of a degreased-only surface (Critchlow *et al.*, 1997). Critchlow *et al.* (1998) conducted a parametric study of a hot dipped galvanized mild steel material treated by TEA CO_2 laser treatment under different number of pulses (10, 20 or 30 pulses). In particular, under the case of 20 pulses, the adhesive joint had similar initial joint strength and durability as that of degreased-only surface (Figure 2.32). The surface became organic contaminant-free and the thicker oxide layer increased from 60 to 140 nm after TEA CO_2 laser ablation. Since the laser-based ablation treatment does not require the additional step of disposal of used degrease solution, it is an attractive surface treatment solution for highly automated automotive industry.

Furthermore, Mandolfino *et al.* (2015) experimented with Ytterbium fibre laser treatment on aluminum alloy 6061-T6 adherends and reported an approximately 100% increase in joint strength compared to a degreased aluminum using acetone (19.4 MPa vs. 8.4 MPa). Wan *et al.* (2018) found that the surface topography becomes rougher and the surface roughness increases as the laser power level increases when treating an aluminum alloy. The authors also found that the rough surface created by the laser treatment played a key role in corrosion resistance and prevented salt solution penetrating the bond interface.

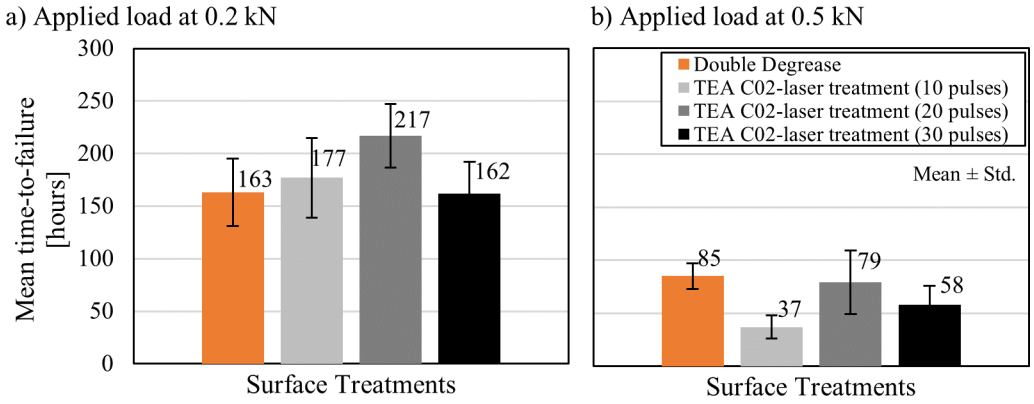

Figure 2.32: Mean time-to-failure of single-lap shear test to determine the durability of adhesive joints that were treated by acetone degrease solution and TEA CO_2 laser treatment; specimens were immersed in deionized water at 60°C with two applied loads a) 0.2 kN and b) 0.5 kN (data adapted from Critchlow *et al.*, 1998)

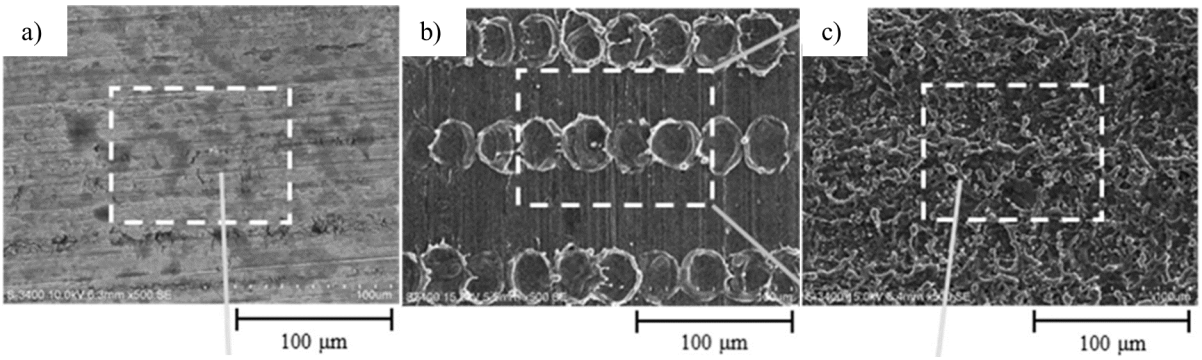

Figure 2.33: SEM images of the surface of Aluminum alloy 5052; a) untreated surface, b) laser ablated surface at low power level of 4 Watt without argon (Ar) shielding gas, and c) laser ablated surface at high power of 19.6 Watt without Ar shielding gas (Wan *et al.*, 2018 used with permission from ELSEVIER)

Adhesive joint strength from CO_2 laser ablation showed a higher variability (with standard deviation of 0.22 kN) than a double degrease treatment (with standard deviation of 0.08 kN) (Critchlow *et al.*, 1998), which could be a limiting factor to meet the demand of joint reliability for the automotive industry. Critchlow *et al.* (2008) also pointed out the high cost associated with the custom-built laser design associated with CO_2 laser and the requirement to use robots to manipulate the treatment.

2.4 Adhesive Fracture

Following mechanical test of adhesive joints, a post-failure analysis of the fracture surface enables: (i) identification of adhesive failure mode (cohesive, interfacial, or adherend failure), (ii) study of the toughening mechanism of the adhesive (Kinloch *et al.*, 1983; Pearson and Yee, 1986), (iii) investigation of the crack propagation process (Purslow, 1981; Zhang *et al.*, 2008), and (iv) interpretation of the adhesive failure mechanism using fracture features unique to the modes of loading (Teiseira de Freitas and Sinke, 2015).

2.4.1 Fracture surface morphology for epoxy adhesives

The fractographic analysis of epoxy highlights the difference in brittle fracture of non-toughened epoxy and the ductile fracture of toughened epoxy (Kinloch *et al.*, 1983). The non-toughened epoxy has an unstable crack propagation with "river" markings and smooth fracture surfaces (Figure 2.34a), while a toughened epoxy showed stable crack propagation with multiple fracture facets (Figure 2.35a). The qualitative assessment explained the difference in the measured force-displacement response (Figure 2.34b and Figure 2.35b).

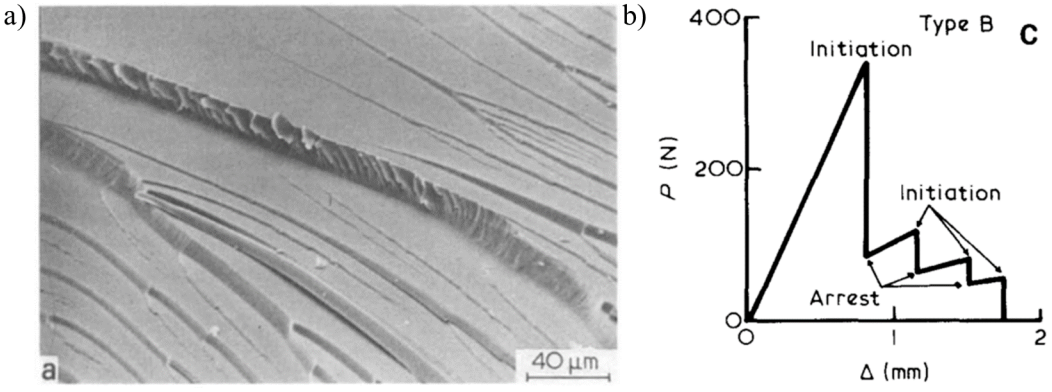

Figure 2.34: a) Non-toughened fracture of bulk epoxy with compact-tension (CT) specimen geometry that demonstrated unstable crack propagation and river-line fracture surface, b) load-displacement (P-Δ) curve of the corresponding material (Kinloch *et al.*, 1983 used with permission from ELSEVIER)

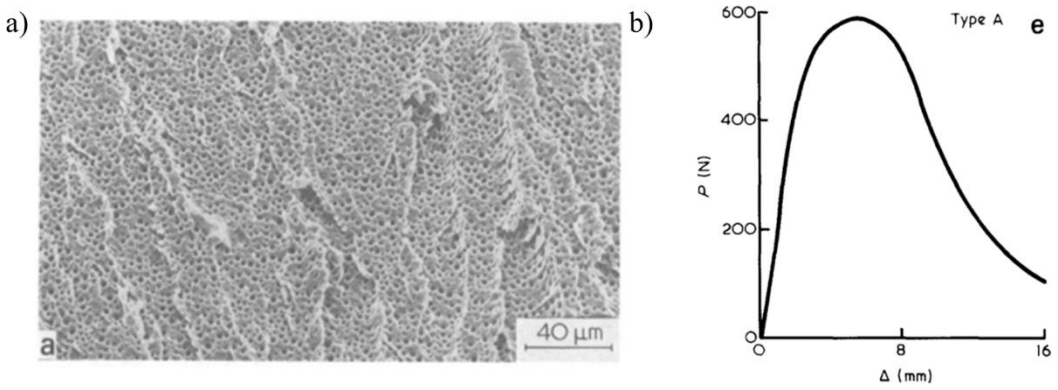

Figure 2.35: a) Ductile fracture of rubber-toughened epoxy with compact-tension (CT) specimen geometry that demonstrated stable crack propagation; small voids originated from the rubber particles, b) load-displacement (P-Δ) curve of the corresponding material (Kinloch *et al.*, 1983 used with permission from ELSEVIER)

In Mode I opening, such as DCB or RDCB tests, as the load increases, microcracks develop within the adhesive in front of the main crack that acts as a crack initiator in the adhesive bond. As the load increases, the local damage area (*i.e.* plastic yield zone) in front of the crack tip develops (Figure 2.16) and grows in size as the microcracks extend to meet with the main crack, which ultimately results in joint failure (Banea *et al.*, 2015). In the case of toughened adhesive, the added rubber particles become sites of cavitation, where voids grow and coalesce, which leads to shear band formation in the adhesive (Figure 2.36). The formation of shear bands improves the toughness of the adhesive (Pearson and Yee, 1986; Pardoen *et al.*, 2005). The dimple-like fracture is the result of the stretched and torn rubber particles (Figure 2.35a). Another Mode I fracture feature had ribbon formation and is observed when the growth of the microcrack is interrupted by the intersecting crack planes and unable to coalesce during a tensile load (Figure 2.37) (Greenhalgh, 2009).

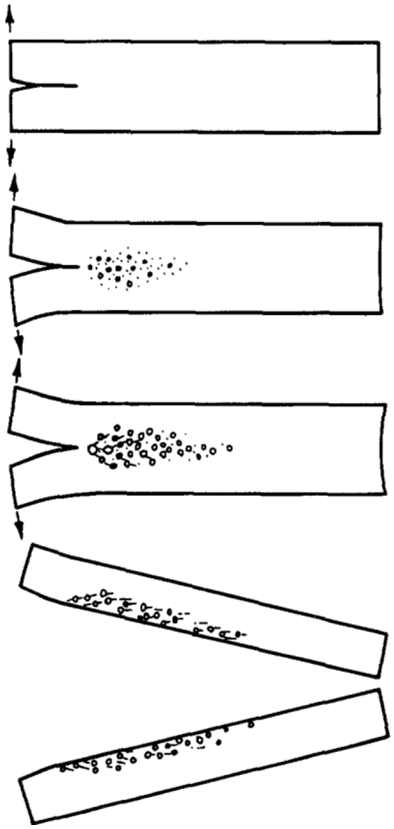

Figure 2.36: Mode I opening of rubber toughened epoxy illustrating local cavitation of rubber particles in front of the crack tip and as load increases, the cavities grow larger which leads to coalescence of voids and fracture occurs (crack progression begins from top to bottom) (Yee and Pearson, 1986 used with permission from SPRINGER NATURE)

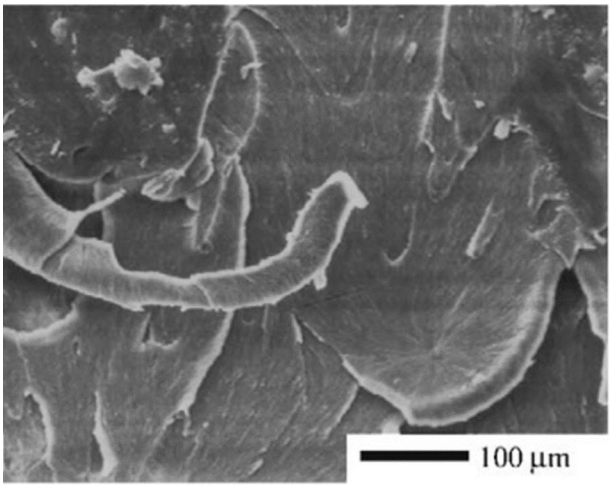

Figure 2.37: Mode I fracture feature-ribbon found on a ductile fracture of adhesive in tapered double cantilever beam (TDCB) test configuration (Pardoen *et al.*, 2005 used with permission from ELSEVIER)

During the fracture process under Mode II loading, shear hackles (also referred to as shear cusps) are observed on the adhesive fracture surface (Biel and Stigh, 2018) (Figure 2.38). The orientation of the shear hackles follows the maximum tensile stress within the bond. The microcracks develop in the adhesive and continue to propagate due to the tensile stress (σ_{max}). As load increases, the microcrack connects to neighbouring microcracks, eventually leading to a joint failure (Figure 2.40) (Chai, 1992). The fracture surfaces with shear hackles appear as a rough surface with pit-like holes (Figure 2.39).

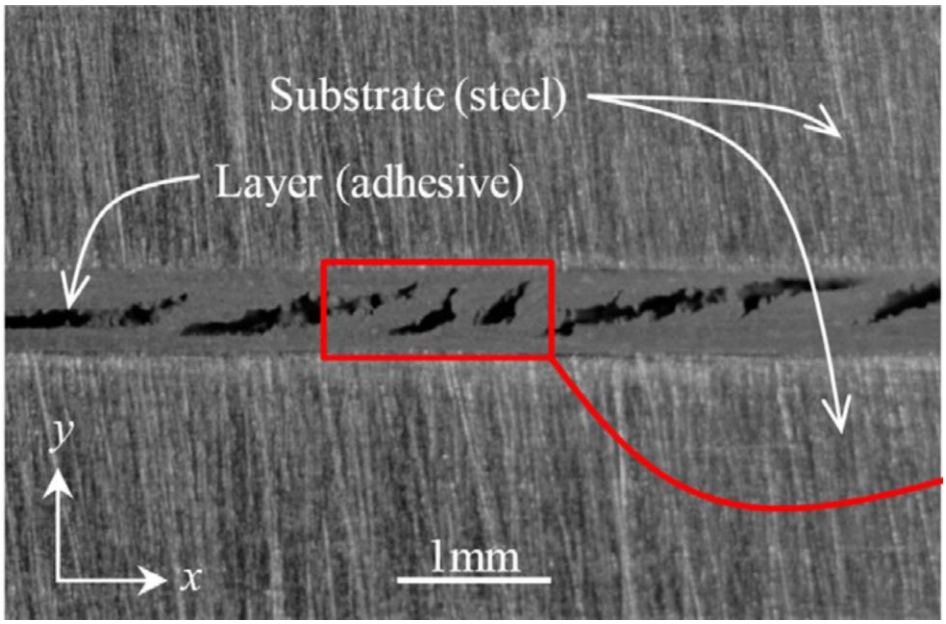

Figure 2.38: Mode II Shear deformation mechanism with shear hackle formation (Biel and Stigh, 2018 used with permission from ELSEVIER)

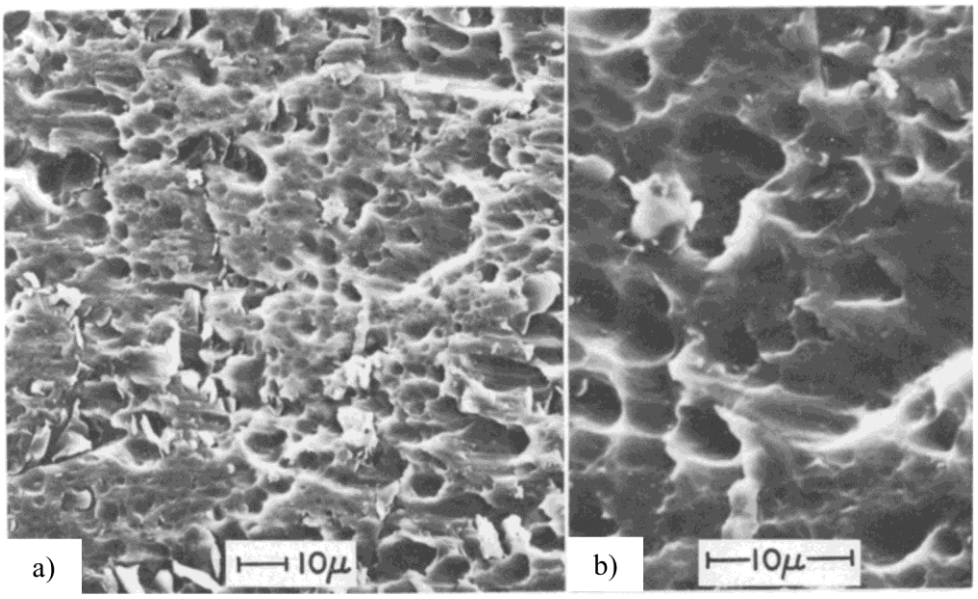

Figure 2.39: Fracture morphology of adhesive under Mode II with crack growth started from right to left (Chai, 1988 used with permission from SPRINGER NATURE)

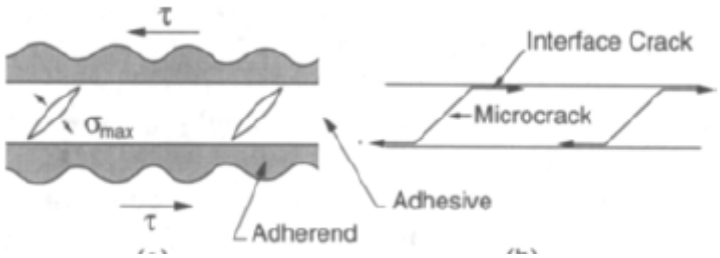

Figure 2.40: Mode II shear loading and the crack development in the adhesive (Chai, 1992 used with permission from SPRINGER NATURE)

2.4.2 Quantification of Fracture Surface

The fracture features of the adhesive described above have been used to qualitatively explain the adhesive fracture under a particular mode of loading. The following paragraph highlights notable works related to the quantification of adhesive fracture surfaces.

Arakawa and Takahashi (1991) attempted to establish a quantitative correlation between the surface roughness of a fractured bulk polymer to fracture parameters such as crack velocity and stress intensity

factor, but a relationship was not observed. However, a linear relationship between surface roughness and fracture toughness was established by Ameli *et al.* (2011) (Figure 2.41). Furthermore, Zhang *et al.* (2008) found distinct morphological differences in the fracture of unmodified resin and modified resin (Figure 2.42a) and demonstrated an increase in roughness with an increase in toughening agent content (Figure 2.42b). Unique modes of loading (I and II) and mixed-mode at different levels were characterized based on the cusp angle on the fracture surface, and a higher density of hackles was observed in Mode II dominant fractures (Gilchrist and Svensson, 1995). The fracture surfaces of adhesive can be quantified to better understand the failure mode of an adhesively bonded structure that has complex failure mode. Teixerira de Freitas and Sinke (2015) conducted a fractographic analysis of a component level adhesive joint that was loaded to failure under a pull-off test setup (Figure 2.43). The authors identified the change in fracture features that corresponded to distinct mode of loading; for example, pure Mode II shear loaded adhesive was found with steep shear cusps (*i.e.* shear hackles) and Mode I opening with shallow cusps. The fracture morphology of a specific mode of loading was distinctively identified and used to qualitatively describe the change in the mode of loading in a structural adhesive joint. Similar fracture analysis methods can be applied from a quantitative approach by using surface roughness parameters.

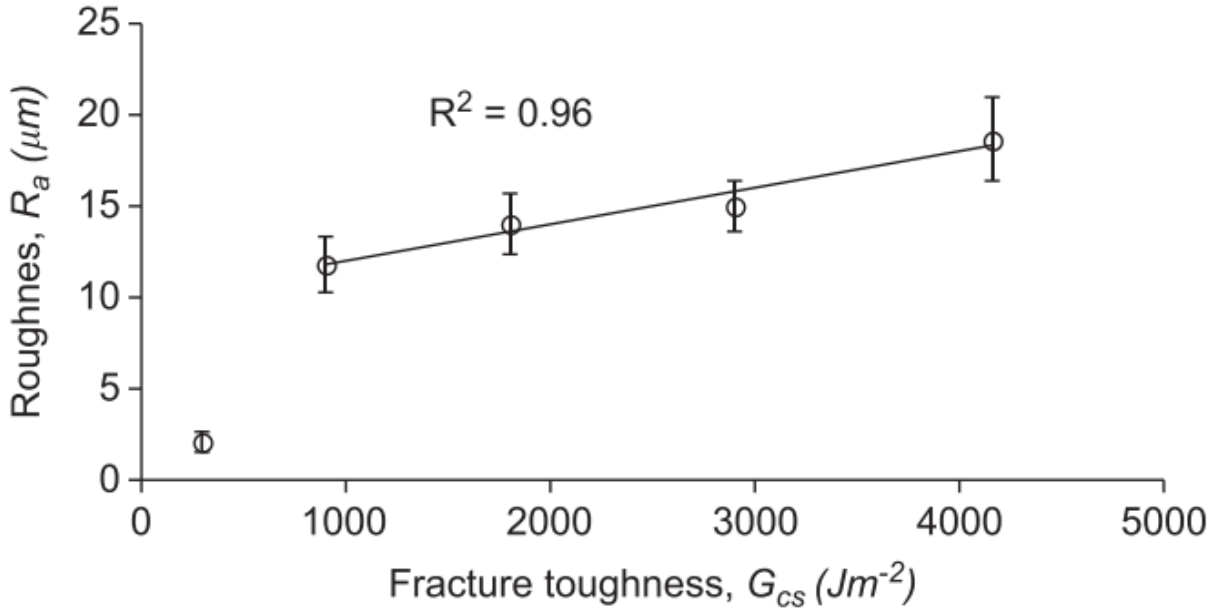

Figure 2.41: Relationship between surface roughness, Ra, of fracture surfaces and fracture toughness of epoxy from a mixed- fracture test (Ameli *et al.*, 2011 used with permission from ELSEVIER)

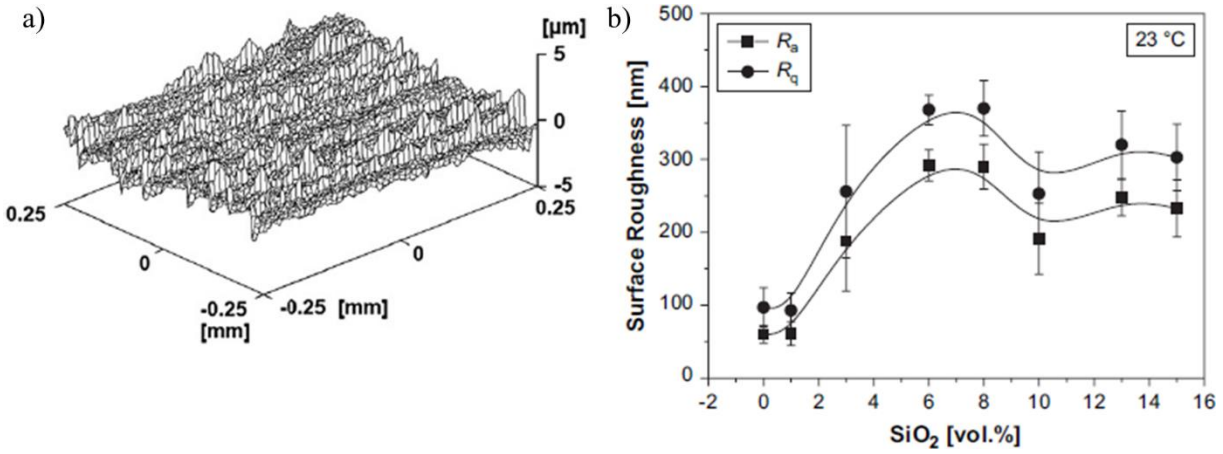

Figure 2.42: a) Fracture surface reproduced from the laser profilometer demonstrating fracture surface of a modified resin, b) surface roughness parameters as function of toughening agent volume content tested at 23 °C with a positive trend in the surface roughness with an increase of added toughening agent content (Zhang *et al.*, 2008 used with permission from ELSEVIER)

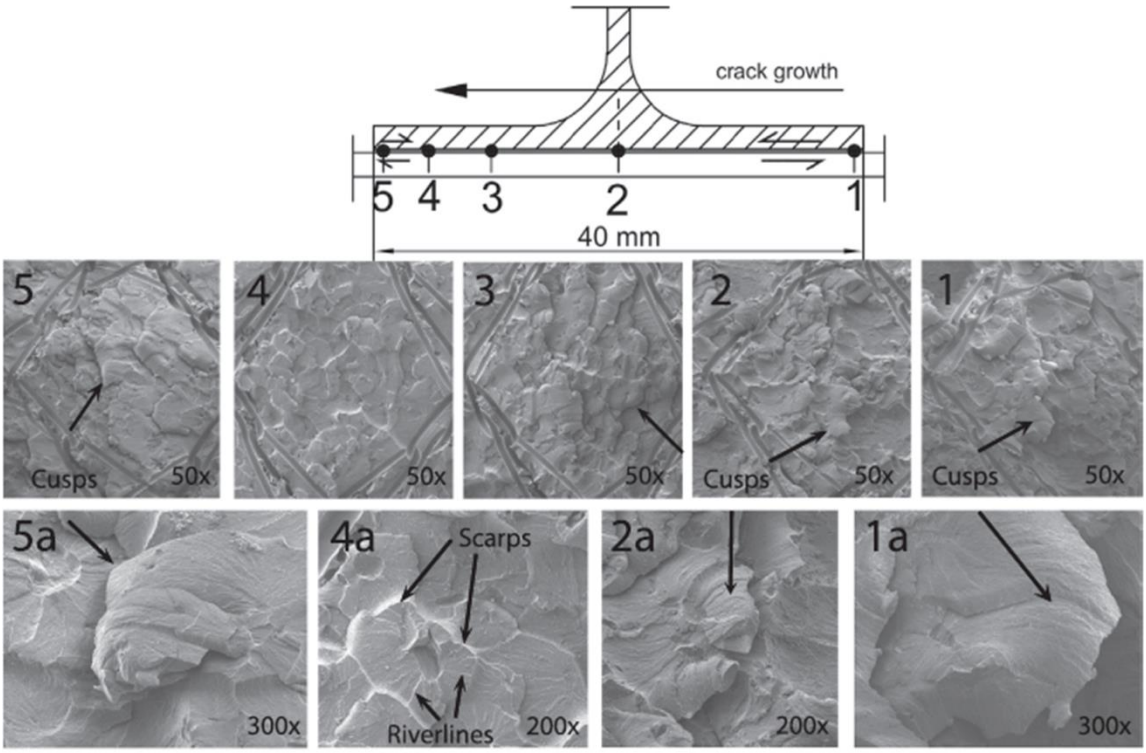

Figure 2.43: SEM fracture morphology evaluation according to the of loading; Point 1 to Point 3 had mixed of Mode I and Mode II with shallow cusps loading, Point 4 had a dominant Mode I component, and Point 5 showed increase in Mode II with taller cusps (Teiseira de Freitas and Sinke, 2015 used with permission from ELSEVIER)

2.5 Summary

The wide adoption of UHSS in vehicle BIW structures emphasizes the important role advanced materials can play in vehicle lightweighting while improving occupant safety. In parallel, adhesive joining solutions present new opportunities for advancing the next generation of multi-material lightweight vehicle structures. To date, there is limited work on adhesively bonded Al-Si coated boron steel compared to other structural steel, in part due to challenges presented by the intermetallic coating. Hence, the motivation for the present research comprises of assessing the surface and thermal treatments at a coupon level using the single-lap shear test. Furthermore, the material properties of Al-Fe-Si coating and formation of the coating during processing have been well documented in the literature, but there has been no detailed investigation of the failure mechanism of the coating delamination in an adhesive joint, despite this being reported as a failure mode in the literature with common coating systems (*e.g.* GI, GA coating). Finally, fractographic analysis is commonly conducted and reported qualitatively in the literature, but there is no quantitative fracture morphology analysis to assess different modes of loading and the corresponding fracture surfaces, which can inform on the efficacy of surface treatment and ultimately the joint strength.

Chapter 3. Methodology

This chapter presents the methodology adopted to investigate the adhesive joining of ultra-high strength hot formed steel with respect to surface treatment and steel intermetallic coating condition. As noted in the background, the Al-Fe-Si intermetallic coating created on the surface of the steel during hot forming may present challenges for adhesive bonding. Therefore, different surface preparations and adhesive joint configurations were investigated using the measured joint strength and fracture surface morphology to assess adhesive joining performance. The conditions investigated included: (i) three different surface preparation treatments; and (ii) a range of hot forming conditions and resulting intermetallic coating morphology. The joint performance was assessed using single-lap shear tests and butt joint tests and interpreted through analysis of the resulting fracture surface morphology.

3.1 Structural Adhesive

The structural adhesive used in this study was a two-part toughened epoxy, known as 3M™ Impact Resistant Structural Adhesive (IRSA) 7333, manufactured by 3M™ Canada Company (3M, 2016) (Table 3.1) that incorporates synthetic rubber particles for increased toughness and ductility. A preliminary study by the author compared IRSA to two other adhesives, 3M™ Panel Bonding Adhesive (08115) and 3M™ Developmental Acrylic Adhesive (B2020), and identified IRSA as the best candidate based on joint strength, ease of application in structures and material availability. Therefore, this adhesive was adopted for the current study.

The two-part IRSA adhesive was applied from a special two-chamber cartridge with separate chambers for the resin and hardener. A manual cartridge gun (MIXPAC™ DM 200-01, Sulzer Ltd.) was used to apply the adhesive, providing uniform pressure to the cartridge and combining the resin and hardener in the correct ratio via a mixing nozzle (3M™ Static Mixing Nozzle 08193/4, 3M™ Canada Company). The

uncured adhesive appears as a silver viscous fluid that turns purple to indicate the completion of the curing cycle (3M, 2016). The recommended curing cycle for the adhesive is 30 min at 80 °C; however, longer durations may be required for the adhesive to reach this temperature in the presence of large fixtures or structures, as was the case in this study.

Table 3.1: Two-part structural adhesive (IRSA) composition (3M, 2016)

Ingredient	Approx. % by Weight
Bis (3-Aminopropyl) Ether of Diethylene Glycol	15 to 40
Epoxy Copolymer (04499600-7155)	10 to 30
Aluminum	5 to 10
METHYLENEDI(CYCLOHEXYLAMINE)	5 to 10
Acrylic Copolymer	5 to 10
Synthetic Ruber (04499600-7150)	5 to 10
m-Xylene-.alpha.alpha' .Diamine	1 to 5
Tris(2,4,6-Dimethylaminomonomethyl)phenol	1 to 5
Inorganic Filler (04499600-7153)	1 to 5
Mineral Filler (04499600-7156)	1 to 5
Treated Filler (04499600-7152)	1 to 5
Formaldehyde, Polymer with Benzenamine, Hydrogenated	Less than 2

3.2 Al-Si Coated Boron Steel

Al-Si coated boron steel (boron steel), hot stamping steel grade 22MnB5, (Usibor® 1500-AS, ArcelorMittal Dofasco) was used as the adherend in order to assess three surface treatments: degreasing the surface using acetone (ACE), grit-blasting treatment (GB), and application of an adhesion promotor (AP). The acid-etch treatment, dry-ice blasting, and the laser treatment were not considered in this study due to the lack of infrastructure and necessary equipment to achieve the ideal experimental outcome. The study was carried out using three different levels of boron steel strength produced by three selected in-die quenching temperatures (room temperature, 400°C, and 700 °C) (Figure 3.1) to examine the adhesive joint response with respect to the strength of the adherend. The single-lap shear test was used to complete the surface treatment study. In this study, the terminology used to designate the test cases is *Surface Treatment_Thermal Treatment* (*e.g.* for a room temperature in-die quenched with grit-blasting treatment, it is GB_RT).

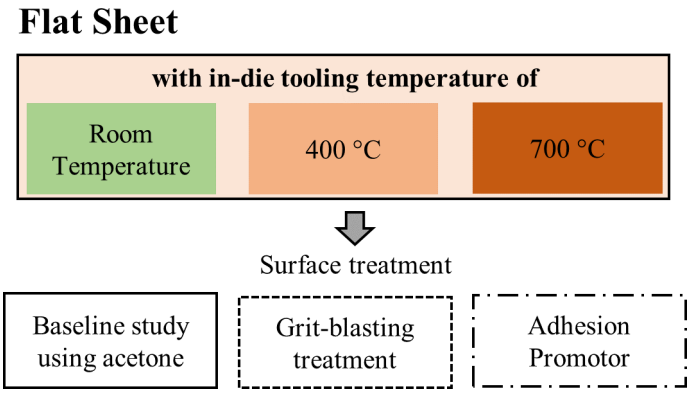

Figure 3.1: Single-lap shear test conditions for a surface treatment study

3.2.1 In-Die Quenching Procedure for Flat Sheet Boron Steel

The 1.2 mm thick boron steel was cut to a dimension of 304.8 mm by 304.8 mm (12" by 12") by a hydraulic shearing machining. The square blank was fed into an 18 kW furnace (Deltech Inc., USA) to begin the austenization process (Figure 3.2a). The boron steel was soaked in the furnace at 930°C for 6 min (Omer *et al.*, 2018) to 6 min 30 sec (ten Kortenaar, 2016) to heat the piece uniformly and provide sufficient time for the grain structure to transform into austenite throughout the sheet. The heated blank was then transferred to the flat die with a 4 second transfer time (Figure 3.2b). A 900-tonne hydraulic forming press (Macrodyne Technologies Inc., Ontario, Canada) applied 60 tonnes of compressive force (Omer *et al.*, 2018), translating to a contact pressure of roughly 6.4 MPa on the sheet. The duration of the in-die quenching process was subject to the desired thermal treatment: 10 seconds for the sheets cooled at room temperature (RT) producing fully martensitic boron steel, four seconds for the sheets to be in-die quenched at 400 and 700 °C (Table 3.2). All in-die quenched blanks were then taken out of the press and air-cooled to room temperature.

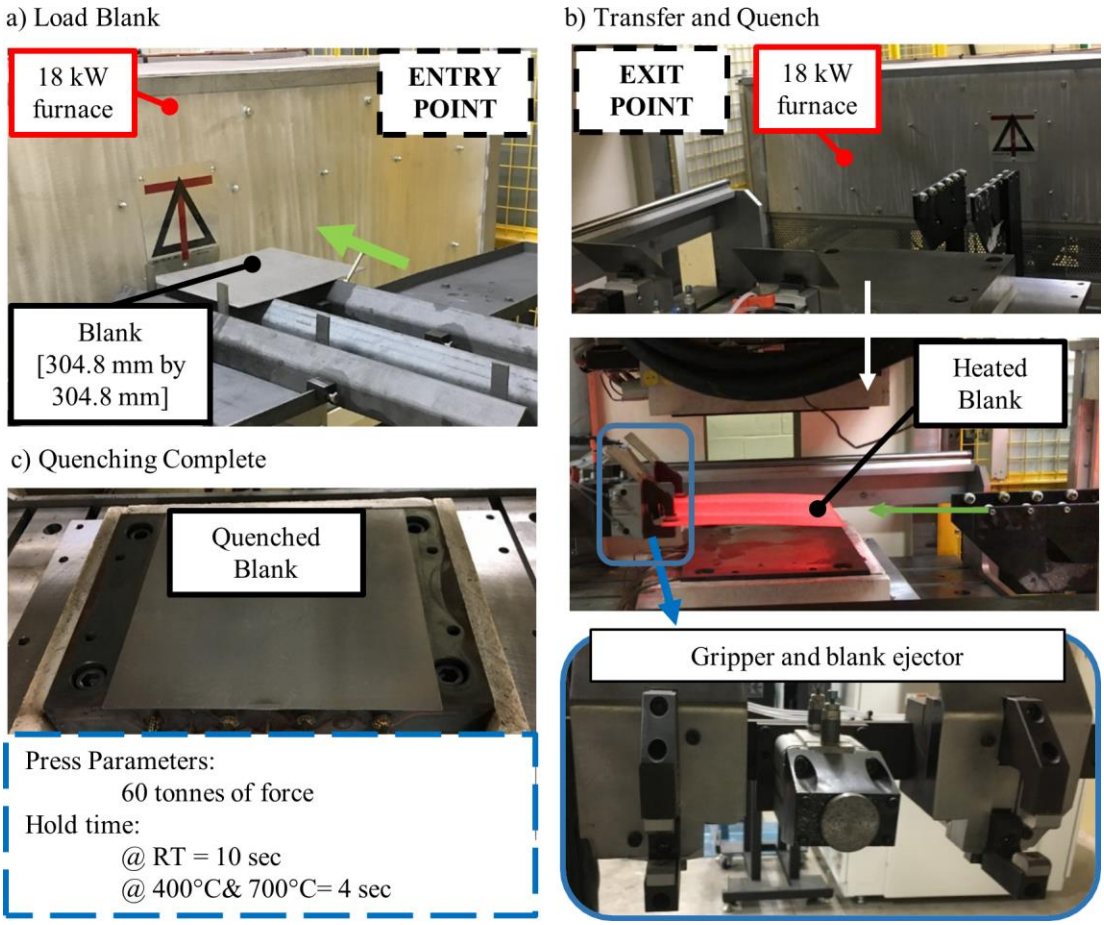

Figure 3.2: Step-by-step flat sheet quenching process; a) load the blank, b) heated blank transferred to the in-die heated flat die c) quenching complete

Table 3.2: Hot forming parameters for three different die temperatures (George *et al.*, 2012) (Omer, 2014) (O'Keeffe, 2018)

Usibor® 1500-AS (1.2 mm thick)			
In-Die Quenching Condition	**Room temperature**	**400°C**	**700°C**
Soak time - Furnace [sec]	390	360	
Press force [metric ton]	60		
Hold time - Press [sec]	10	4	

Four resistance heaters (1900 Watt and 600 Volt) (ASB Heating Elements Ltd., Canada) were uniformly spaced across the die-set; each with a length of 304.8 mm (12") and a diameter of 19 mm (0.75") (O'Keeffe, 2018) (Figure 3.3a). They provided the required in-die quenching temperature of 400 ºC (George, 2012) (Eller *et al.*, 2016) and 700 ºC (O'Keeffe, 2018). The die-sets were insulated using ZIRCAL-95 insulation

material with a thickness of 25.4 mm (1") (ZRCI, 2015) to minimize the heat loss from the die surfaces (Figure 3.3b), resulting in a small temperature gradient across the die surface. The use of flat sheets preserved the intermetallic coating and avoided macro-cracking that may result from forming processes.

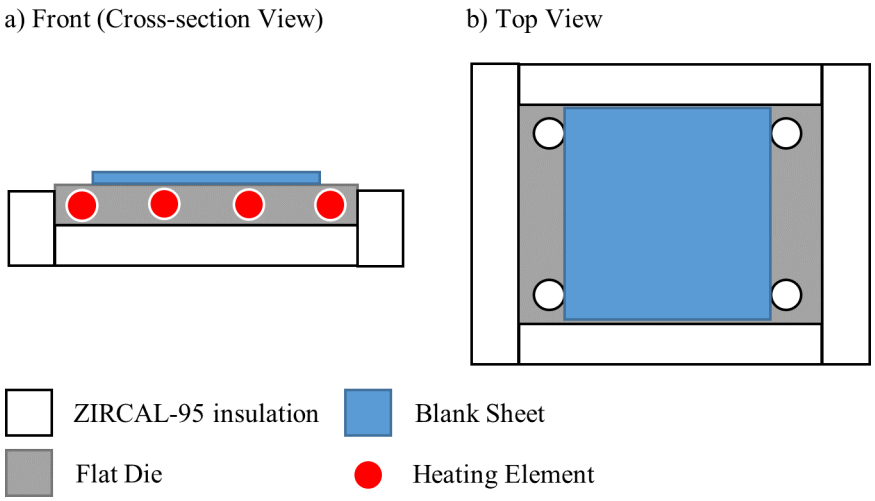

Figure 3.3: : Illustration of the bottom half of flat die set demonstrating the components that made up of the flat die-set; a) Front view, b) Top view

To consistently reproduce fully martensitic sheets, a water chilled plate made of aluminum was placed in between the flat die-sets to ensure the dies were cooled down to room temperature and removed when the heated blank was ready to be quenched (Figure 3.4). As for the two slower cooling rates (at 400 and 700°C), in order to maintain the intended die surface temperature generated by the heating elements, the top and bottom dies were closed, minimizing the heat exchange between the quenching surface and the air in the environment. Once the parts were austenized and about to exit the oven, the flat dies were opened for the heated flat sheets to be transferred and resume the slower rate in-die quenching operations.

a) Press position during sheet austenization for room temperature sheet quenching

b) Top view of flat die (bottom set)

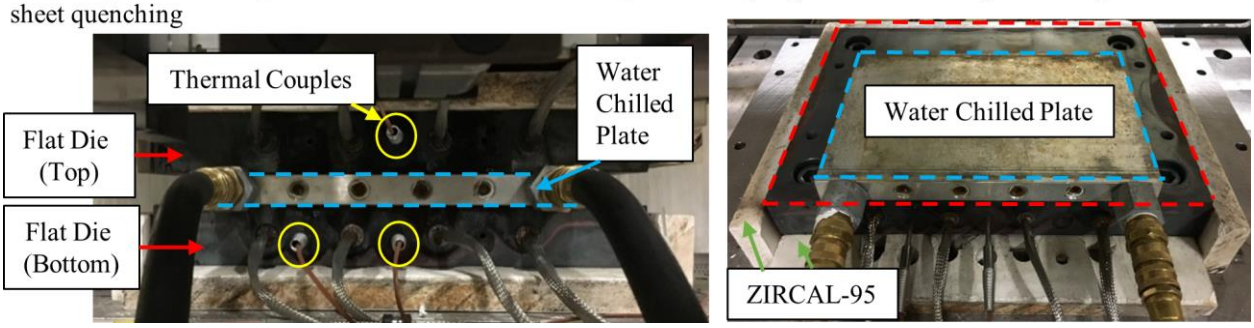

Figure 3.4: : a) Closed position with a water chilled plate in between flat die-set b) Area coverage of the water chilled plate resting on top of the flat die

Fully martensitic boron sheets were waterjet cut from the fully-quenched blanks in order to produce the adherends for the single-lap shear samples (Figure 3.5). The two softer thermal conditions were hand-sheared to size owing to the lower material strength.

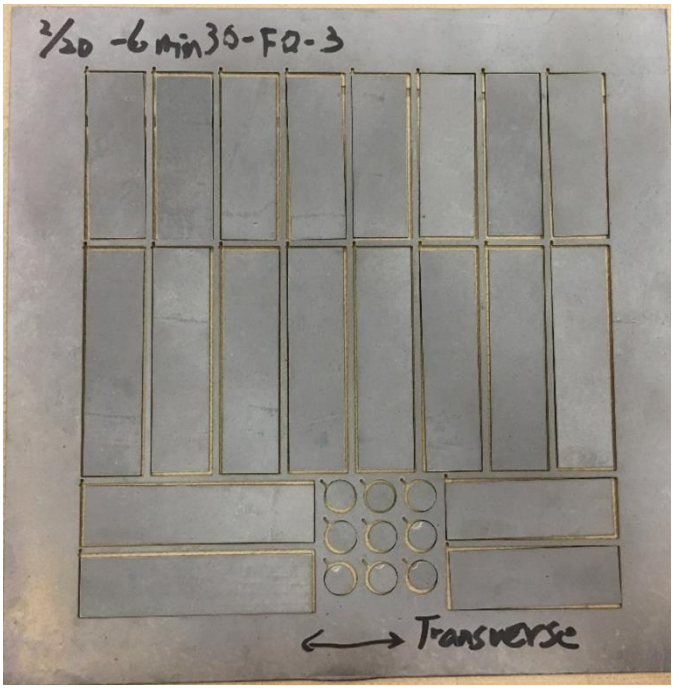

Figure 3.5: : Waterjet cut for single-lap shear adherends of 1” by 3” and 1” by 4” and the disc of ½” diameter

Microhardness

The measured microhardness value is used to verify the strength of the boron steel under different in-die quenching temperatures (Bardelcik *et al.*, 2010) (George *et al.*, 2012). Microhardness (with hardness scale HV1.0) measurements were used to determine material around the border of the sheets that did not meet the strength requirement due to the heat loss at the border region during the in-die quenching process. Coupons for hardness measurement were hot mounted in resin and polished with 4000 grit SiC sandpaper. A measurement load of 1000 g was used to determine the microhardness of the coupons using a commercial hardness tester (402 MVD, Wilson® Instruments). Hardness (HV1.0) was calculated using equation 3.1: $HV1.0 = \frac{F}{Area} = \frac{F}{\frac{d^2}{2\sin\left(\frac{136^\circ}{2}\right)}} \approx \frac{1.854F}{d^2}\ \left[\frac{kgf}{mm^2}\right]$ (Eq. 3.1), where F is the applied force (1.0 kgf) and d is the mean of the diagonal measurements ($d1$ and $d2$) of the indent.

The hardness distribution for the flat sheet identified that material located approximately 25.4 mm (1") from the edges of the sheet had higher hardness for 400°C (*i.e.* high strength material) and lower hardness for 700°C compared to the reported average microhardness by George *et al.*, 2012 and O'Keeffe, 2018 (Figure 3.6, Figure 3.7, and Figure 3.8). Thus, the border with 25.4 mm (1 inch) of material around the flat sheet was discarded when collecting adherends from the flat sheets (Figure 3.5).

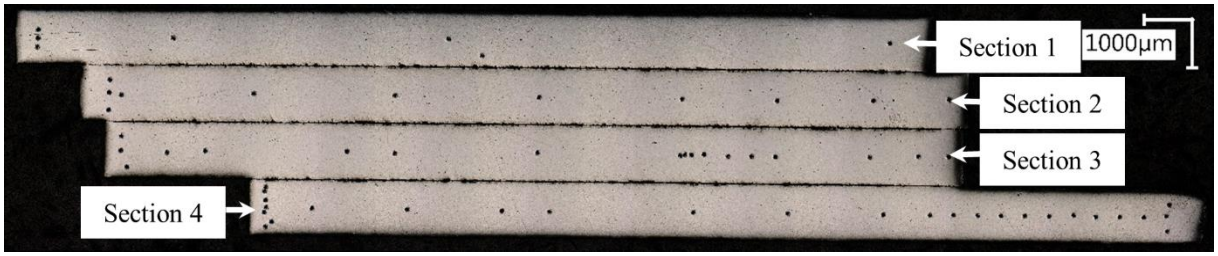

Figure 3.6: : Locations of the Vickers hardness measured (e.g. sample in-die quenched at 400 °C), sections identified in Figure 3.21

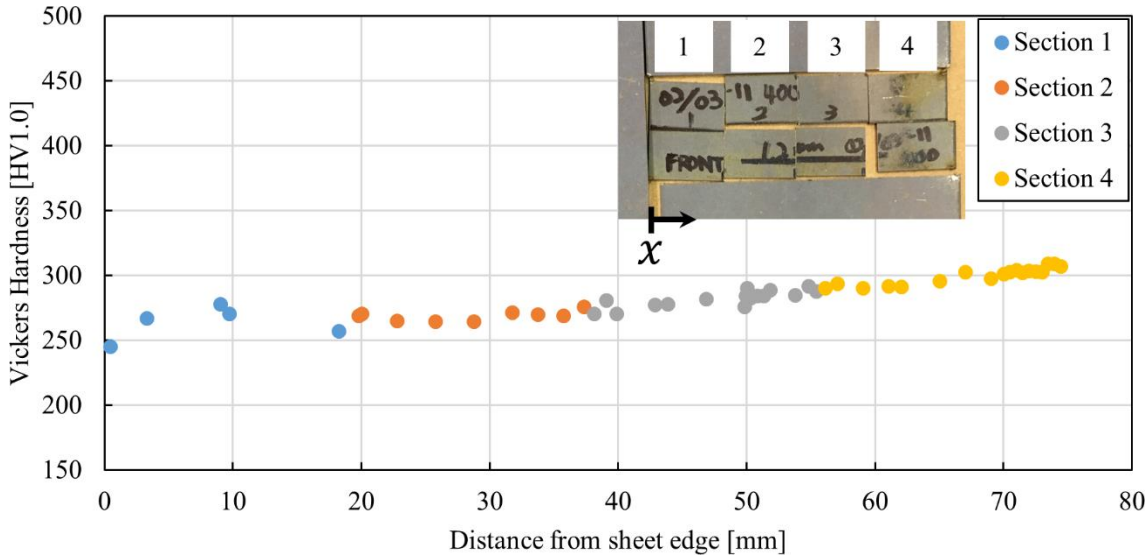

Figure 3.7: Hardness profile near the edge of the flat sheet quenched at 400℃

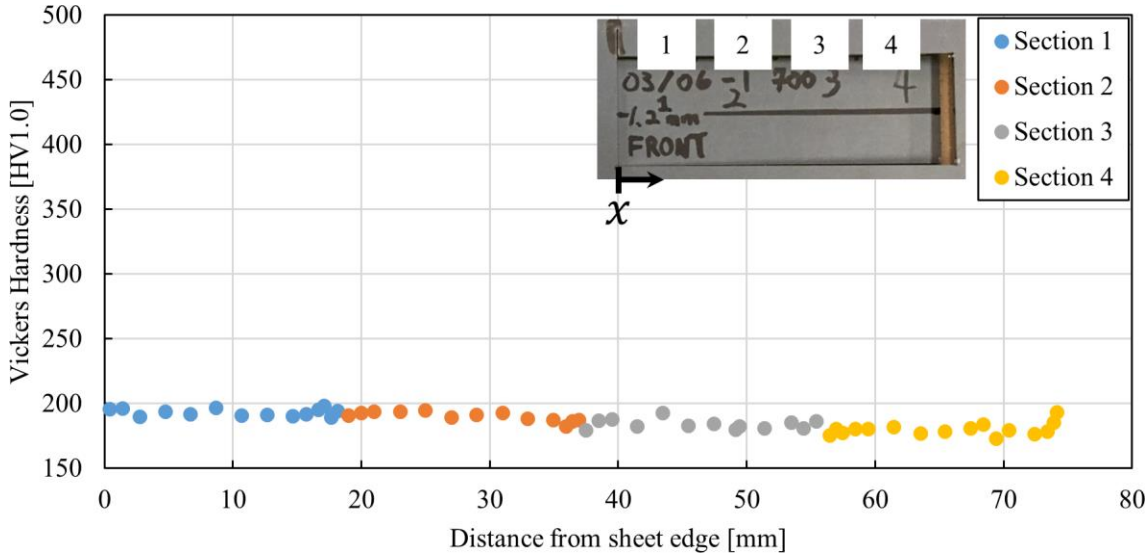

Figure 3.8: Hardness profile near the edge of the flat sheet quenched at 700℃

Fully quenched sheets had an average hardness value of 499 HV1.0 (Figure 3.3) demonstrating the dominant presence of martensite in the microstructure. At the intermediate cooling rate with an in-die heating temperature of 400 °C, the hardness level was 267 HV1.0, explained by the presence of bainite mixed with martensite (Bardelcik *et al.* 2012). Lastly, the lowest cooling rate, quenched at 700 °C, resulted in a measured microhardness of 192 HV1.0, suggesting the presence of softer phases of ferrite and bainite.

The reported values were in agreement with the work on the resistance spot welding of the in-die quenched boron steel by O'Keeffe (2018) and hat channel boron steel structures (Omer *et al.*, 2017).

Table 3.3: Vickers microhardness summary on three different quenching conditions

	Flat Die Temperature		
	Room Temperature (Fully Quenched)	**400°C**	**700°C**
Average [HV1.0]	499	267	192
Standard Deviation	9.2	7.8	3.5
Coeff. of Variance [%]	1.8	2.9	1.8

3.3 Specimen Manufacture and Experimental Testing

3.3.1 Single-Lap Shear Test

The single-lap shear (SLS) test is a widely used low-cost adhesive test comprising two adherends and a single bond line that can be loaded to failure in a standard tension testing machine. The adherends (test piece) in this study were 25.4 mm by 101.6 mm (1" by 4"), and were supported by backing plates (25.4 mm by 76.2 mm (1" by 3")) (Figure 3.9) to align the applied load with the bond line. The materials were cut to size using either a mechanical shear or a water jet cutter depending on the strength of the steel. The backing plates were 12.7 mm (0.5") shorter than ASTM standard D3165-07 while leaving the remaining dimensions identical to the standard (ASTM D3165-07, 2014). The shorter backing plate facilitated comparison with results from the surface treatment investigation by Nandwani (2015) who used these specimen dimensions. The sample had a nominal bond length of 12.7 mm (0.5") and a bond width of 25.4 mm (1.0").

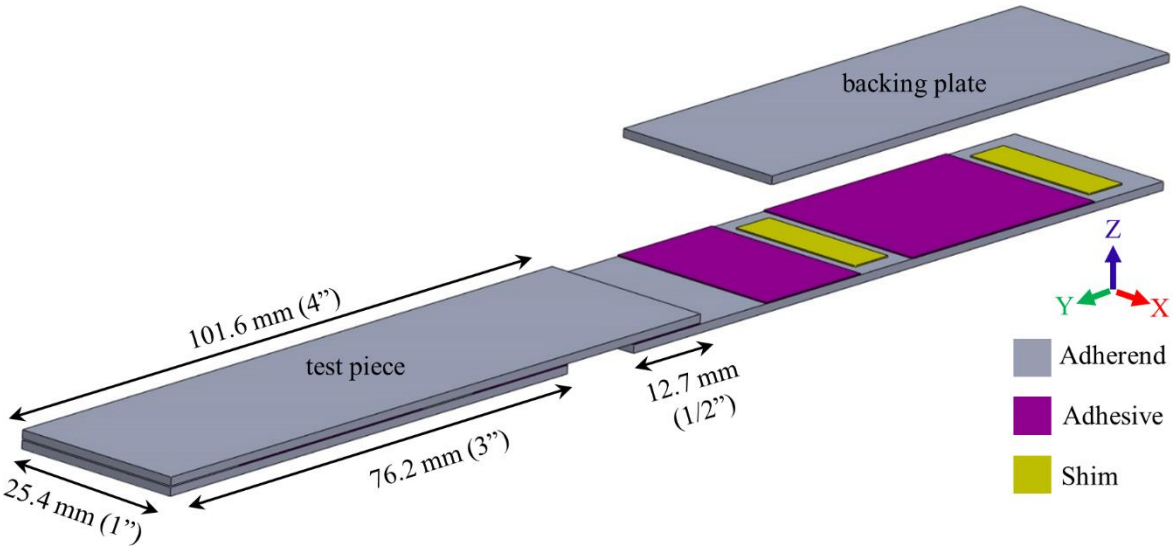

Figure 3.9: Single-lap shear test specimen, exploded view (modified ASTM standard D3165)

A surface treatment was applied to the adherends, as detailed in section 3.4. Following the surface treatment, brass shims with a thickness corresponding to the desired bond line thickness (0.1778 mm (0.007")) were placed near each end of the backing plate (Figure 3.10a). The two-part structural adhesive was applied in a

single continuous bead on the backing plates and spread using a putty knife to uniformly cover the bond area (Figure 3.10b and Figure 3.10c). The test piece was then placed on top of the backing plate forming the first sub-assembly of the sample. A small pressure was applied by hand on the test piece at the locations where the brass shims were placed, allowing the adhesive to flow and cover the bonding area (Figure 3.10d). These steps were repeated for the second sub-assembly. To join the two sub-assemblies, a continuous bead of adhesive was applied to form a nominal bond length of 12.7 mm (0.5") on each half of the test piece (Figure 3.10e) and spread using the putty knife. Each half of the sub-assembly was placed onto a sheet of tempered glass plate and with a nominal 12.7 mm (0.5") overlap. AA6061-T6 aluminum (1.6 mm thick) spacers were placed between each specimen to ensure the samples were aligned during the curing process (Figure 3.10f). Prior to assembly, the aluminum spacers and tempered glass were coated with a mold release solution (Frekote®, LOCTITE® 55-NC™ by Henkel Corp.) to enable removal of the samples following curing. The nominal bond area, A, was 12.7 mm (0.5") by 25.4 mm (1"). A second sheet of tempered glass was placed on top of the specimen assemblies, after which binder clips were used to clamp the glass plates and keep the samples in place during curing (Nandwani, 2015). The fixture was cured in a forced air convection oven (Binder FD-53, Binder Inc.) at a temperature of 80°C. In general, the curing time included a ramp up to 80°C that varied depending on the size of the samples and test fixture, and was followed by 30 minutes curing time at the specified temperature. A K-type thermal couple was attached to the single-lap shear jig and connected to a Data Acquisition System (OMB-DAQ-55^{TM}) to determine the time required to heat up the fixture to the curing temperature (Figure 3.11).

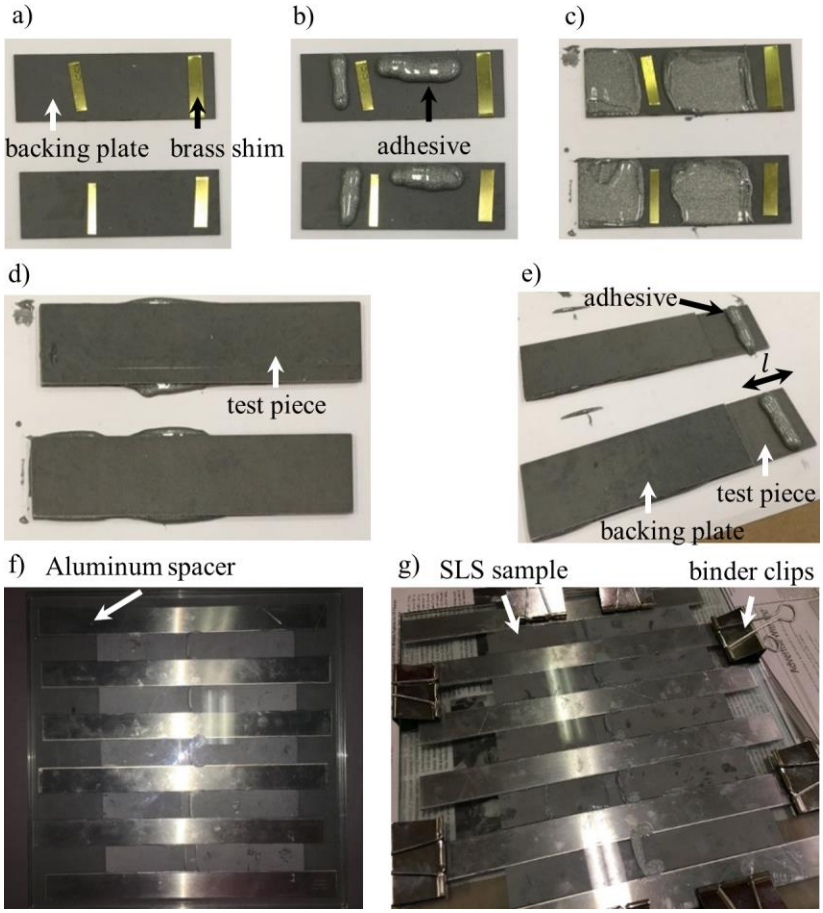

Figure 3.10: Single-lap shear sample assembly process; (a) Place brass shims on top of backing plates , (b) Apply adhesive in a single, continuous bead, (c) Spread the applied adhesive to cover the area, (d) Place the test piece on top of the backing plate, (e) Apply a single, continuous bead of adhesive to create a bond length of 12.7 mm (0.5"), (f) Place the samples on a tempered glass plate and separate each specimen by an aluminum spacer and (g) Place binder clips to bind the top and bottom tempered glass to keep the specimens in place

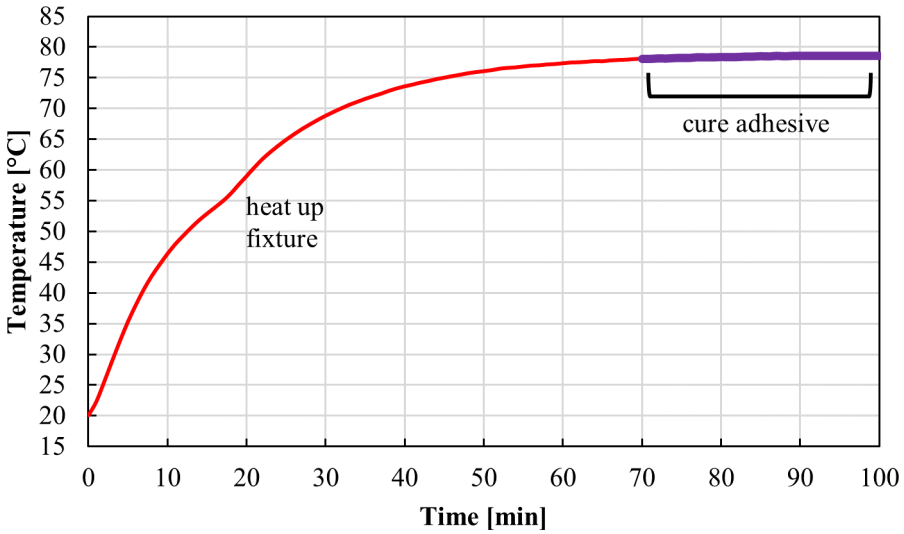

Figure 3.11: Heating temperature profile of the single-lap shear fixture

After the specimens were cured, spew fillets were present on the test specimens (Figure 3.12), corresponding to the excess adhesive that was squeezed out around the edge of the bond line. Since the spew fillets could influence the strength of the joint by reducing the stress concentration at the joint edges (Doru *et al.*, 2014), they were carefully removed using a vertical milling machine (Nunes *et al.*, 2016) to minimize the variability in the nominal joint strength that could originate from inconsistent spew fillet shape (Critchlow, 1997) (Figure 3.13). The bond line length and bond thickness of the specimens were measured using an opto-digital microscope (VHX-5000, KEYENCE Corporation) (Figure 3.14).

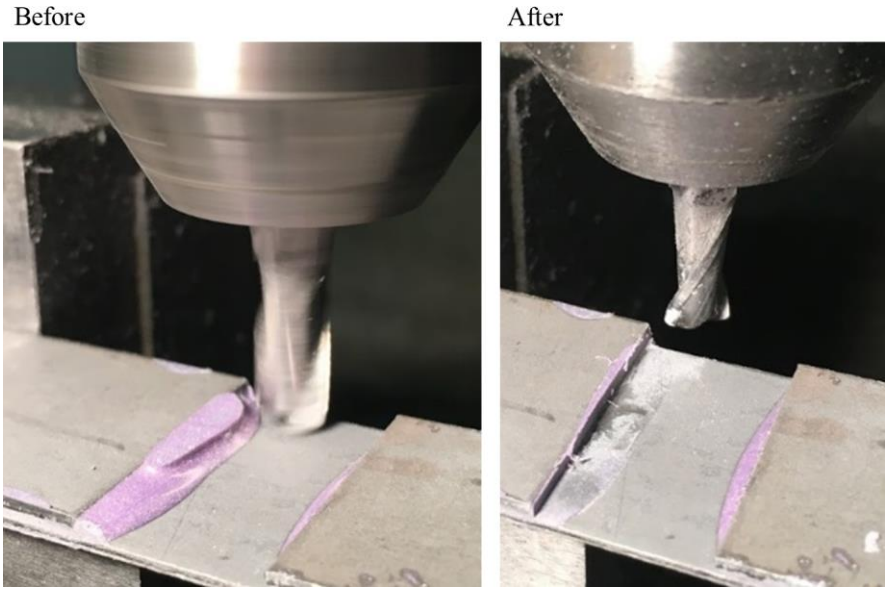

Figure 3.12: Structural adhesive spew fillet removed using a vertical milling machine

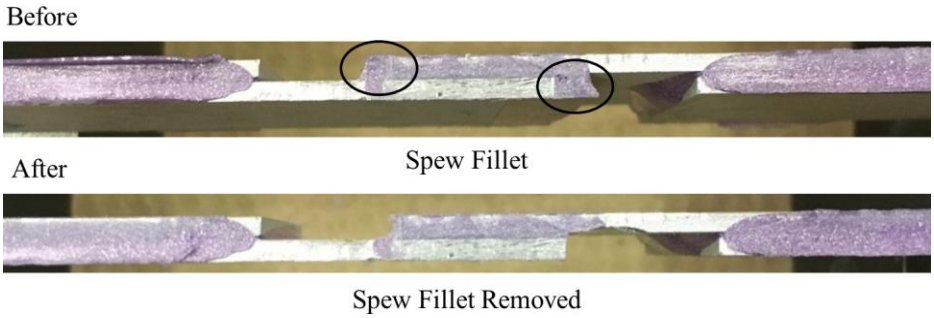

Figure 3.13: Single-lap shear specimen with spew fillet at the joint ends (top figure) and with spew fillet removed (bottom figure)

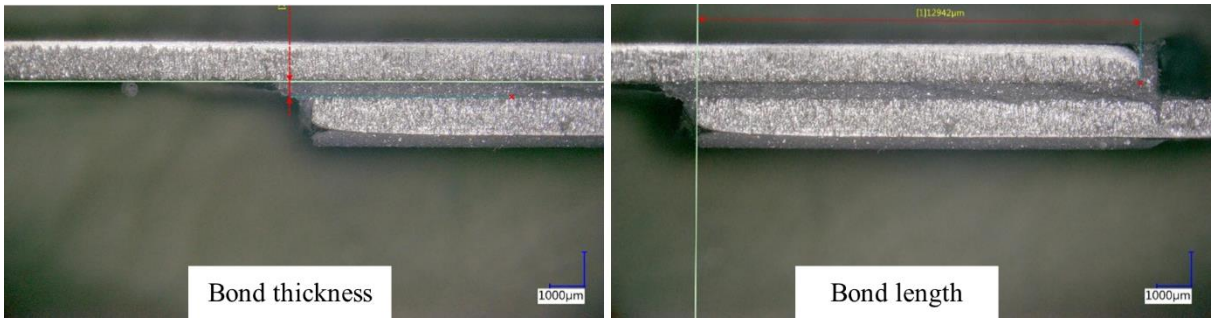

Figure 3.14: Single-lap shear bond thickness and length measurement using an optical digital microscope

The specimens were tested in a custom hydraulic frame at room temperature (Figure 3.15). The samples were clamped by a set of self-tightening wedge grips. The grip area was nominally 25.4 mm by 25.4 mm (1" by 1") on each side as specified in the ASTM D3165 standard. An MTS 407 controller applied a constant crosshead speed based on feedback from a linear variable differential transformer (LVDT). The specimens were tested at a constant engineering strain rate of 1.0 s^{-1}, corresponding to a crosshead speed of 0.178 mm/sec (0.007 inch/sec). An 89 kN (20,000 lb) load cell (SWP-20K, Transducer Techniques) measured the force applied on the adhesive joint. The force-crosshead displacement data was acquired at a frequency of 1000 Hz (USB-6210, National Instruments).

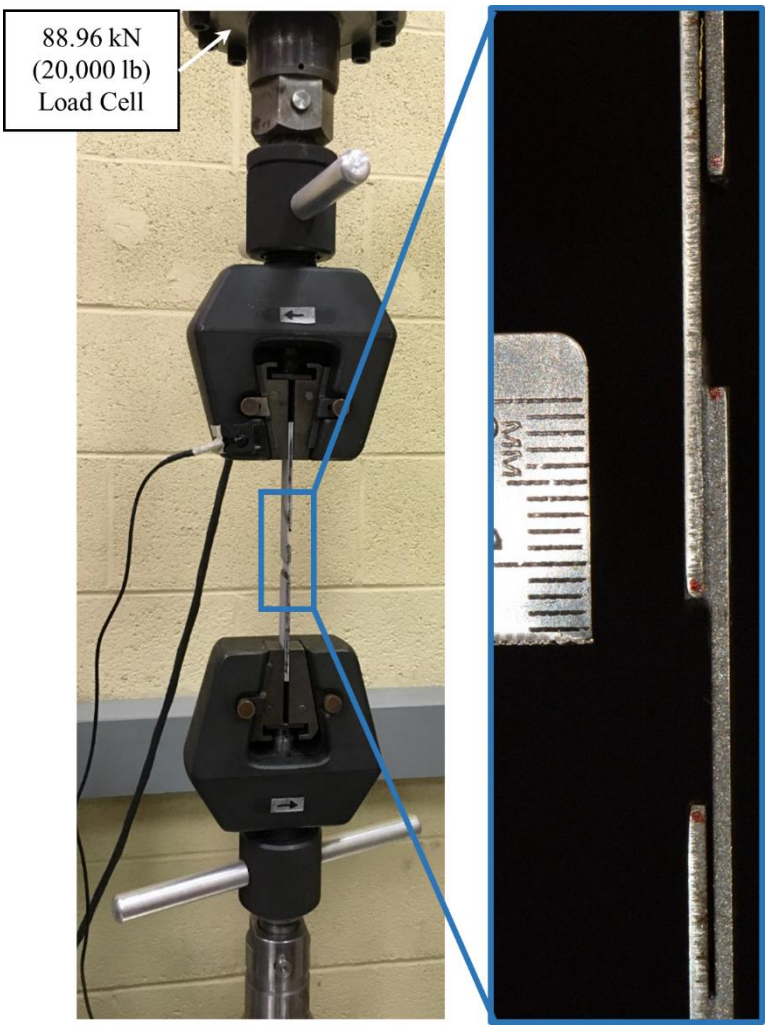

Figure 3.15: Custom hydraulic frame test setup for single-lap shear test

The local displacements in the vicinity of the joint were measured optically using a Nikon D3200 digital single-lens reflex (DSLR) camera. A macro lens (105 mm f/2.8) was connected to a two-times teleconverter lens to record the test at 1080p resolution resulting in an approximate resolution of 30 pixels/mm. Images were acquired at 30 frames per second. Markers were created on the specimens using a permanent marker (Figure 3.16) and were tracked using a video analysis tracking software (Tracker Video Analysis and Modeling Tool, Open Source Physics, USA) (Watson *et al.*, 2019). The software provided the data on the local displacement and the test piece joint rotation as the displacement was increased to failure of the sample.

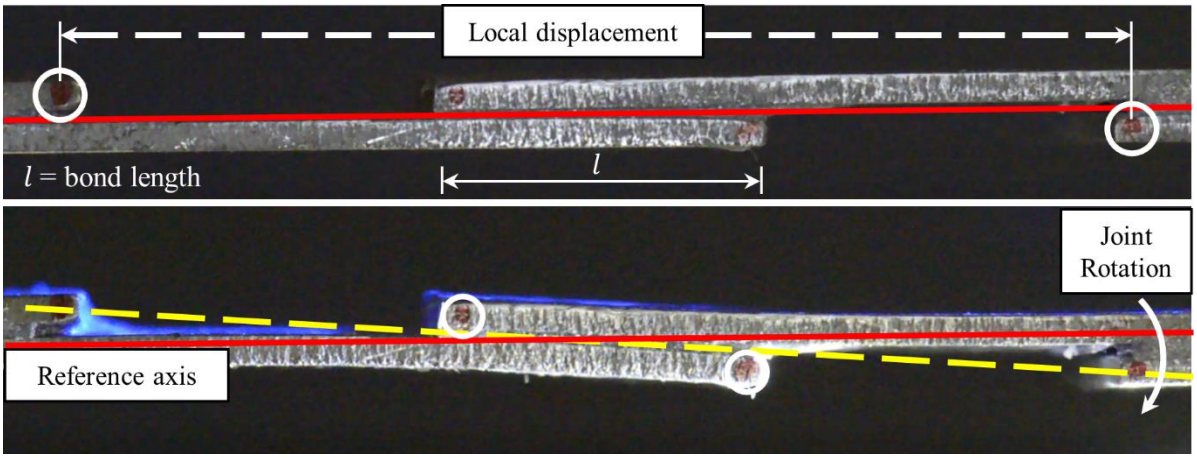

Figure 3.16: Single-lap shear test with the markers traced and the output (local displacement and progression of joint rotation) generated by Tracker

The shear strength, τ_{max}, was calculated using the maximum force measured during the test, F_{max}, and the initial bond area, A: $\tau_{max} = \frac{F_{max}}{A} = \frac{F_{max}}{wl}$ (Eq. 3.1), is where w is the width of the specimen and l is the adhesive bond length. The shear strength was used to compare the performance of the various surface treatments.

3.3.2 Butt Joint Test

The butt joint adherend geometry followed the dimensions outlined in ASTM-2094 (ASTM-2094, 2014) (Figure 3.17). The test configuration is generally used to measure adhesive tensile strength (Ikegami *et al.*, 1996) and, in some cases, the energy absorbed by the adhesive (Yokoyama, 2003). In this study, the ASTM standard test was modified by introducing an in-die quenched fully martensitic boron sheet sample between two rods (Figure 3.18), similar to the study conducted by Schiel *et al.*, (2015). The purpose of the modification was to induce a single mode tensile loading to the Al-Si intermetallic coating on the sheet sample and obtain the tensile adhesion strength of either the adhesive or the intermetallic coating. The butt joint sample is made of two 38.10 ± 0.25 mm (1.500 ± 0.010") long cold rolled steel rods with a 12.70 mm (0.5") diameter and a 12.70 mm (0.5") diameter Al-Si coated sheet sample. The sheet sample was waterjet cut from an ultra-high strength steel boron flat sheet coated with Al-Si with a diameter of 12.7 ± 0.127 mm

(0.5 ± 0.005”). A bonding jig was machined from cold rolled steel and was designed to enforce the required tolerance on two parameters controlling the sample alignment between the top and bottom rod (axial offset tolerance ± 0.076 mm (0.003”) and tilt angle ±0°10’) (ASTM-2094, 2014). The jig design was inspired by da Silva *et al.* (2012).

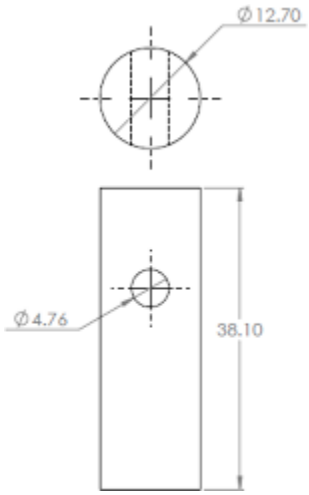

Figure 3.17: Top view and front view of the butt joint adherend (ASTM-2094) (dimension in mm)

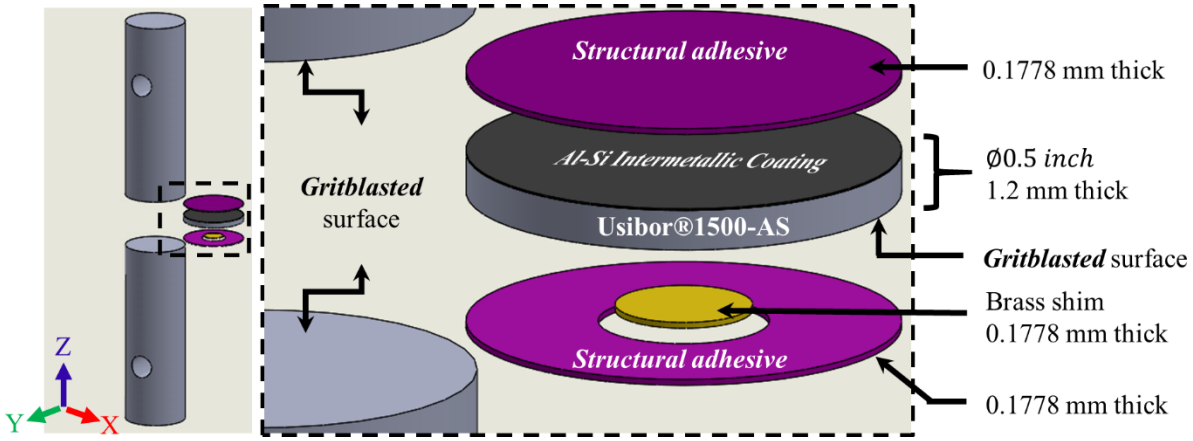

Figure 3.18: Butt joint sample with additional metal disc for measuring interface strength

The rigorous measurement of each component making up a butt joint sample (adherends, sheet sample, and brass shim) was necessary to take into account of the tolerance stack-up from the individual components, in order to consistently achieve the target adhesive bond line thickness (0.1778 mm (0.007”)). The initial thickness of the sheet sample, $t_{disc-initial}$, was measured using a micrometer. One side of the sheet sample

and the rods were grit-blasted at an air pressure of 483 kPa (70 psi) using 60 grit silicon carbide. The grit-blasted sheet sample surface established a strong bond between the sheet sample and the rod leaving the side with the coating to be tested. The final thickness of the sheet sample ($t_{disc-final}$) was measured to ensure the intermetallic coating was removed completely by the grit-blasting treatment. The rods and the discs were cleaned using acetone within one hour after the grit-blasting treatment.

A small brass shim (with a nominal thickness of 0.1778 mm and diameter of 4mm) was placed on top of the rod (Figure 3.19a) to produce a desired adhesive bond line thickness. The irregular shape of the flattened brass shim was from the burr when punched out from the brass sheet. The preliminary test demonstrated that the shim did not weaken the tensile strength and the failure occurred at the interface between the coating and the grit-blasted interface as intended. IRSA was applied around the shim and spread with a putty knife (Figure 3.19b). The sheet sample was placed on top of the brass shim spacer with the grit-blasted side facing the shim and adhesive. A gentle pressure was applied, holding the sheet sample at the edges to allow excess adhesive to flow out and ensured that the sheet sample was in direct contact with the shim (Figure 3.19c). A final layer of adhesive was applied on top of the disc and spread with a putty knife (Figure 3.19d). The sub-assembly was placed in the butt joint fixture and fastened using capscrews and a cold-rolled steel V-block (Figure 3.19e).

In order to repeatedly produce a nominal bond thickness of 0.1778 mm (0.007”) between the Al-Si coating surface and the grit-blasted steel rod surface, the length of the specific components for each sample were measured and documented. The distance required for the bond line thickness was determined by the total height of the jig subtracted from the sum of the length of the individual components (Figure 3.20). A digital caliper depth probe (with an accuracy of ±0.0254mm (±.001")) was used to set the calculated distance, and then the top adherend was locked in place by tightening the V-block (Figure 3.19f).

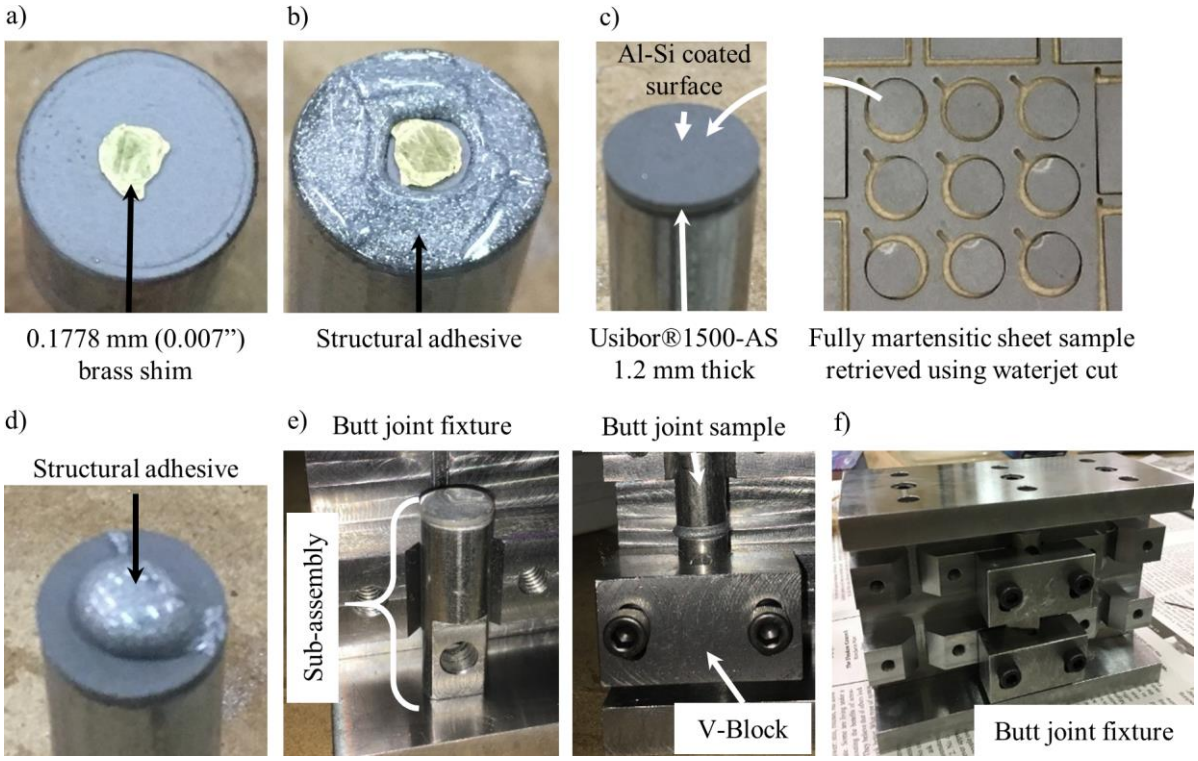

Figure 3.19: Butt joint sample assembly process a) Place a shim on top of the adherend, b) Apply structural adhesive around the brass shim, c) Place the sheet sample on top of the adherend, d) Apply structural adhesive on top of the Al-Si coated surface, e) Place the sub-assembly butt joint sample and secure in place by a V-block, and f) Secure the top adherend steel rod using the V-block

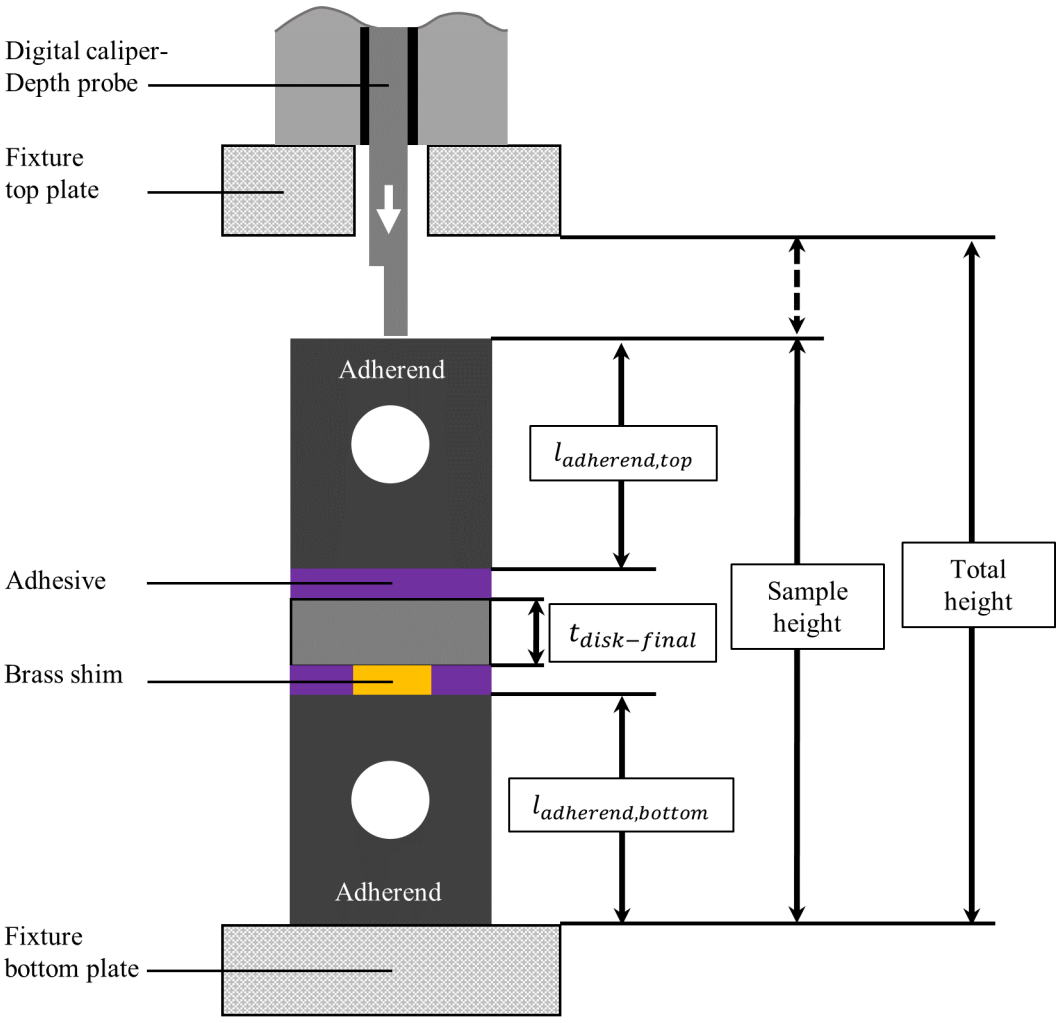

Figure 3.20: Butt joint fixture height diagram

The fixture was placed in a forced air convection oven for 130 min at 80 °C to ensure that the adhesive was fully cured. The jig was heated to 80 °C in 100 min, followed by 30 min to cure the adhesive in the samples. (Figure 3.21). A type-K thermal couple was attached to the jig and placed in the oven to record the thermal history of the assembly using the same data acquisition mentioned in Section 3.2.1. A total of six samples were made for the experiment.

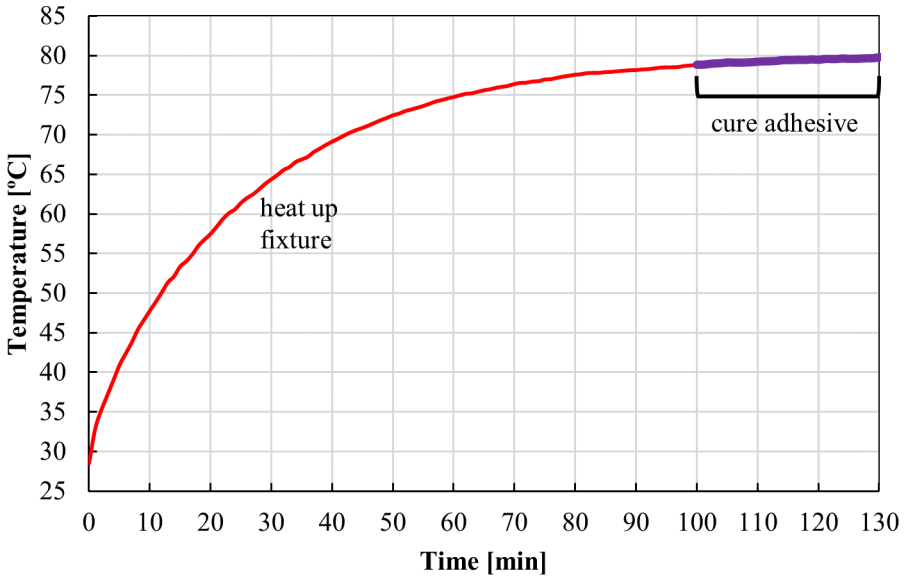

Figure 3.21: Heating temperature profile of butt joint jig

The excess structural adhesive was removed using 500 grit sandpaper and a razor blade. The spew was removed until the edges between the adherends and the disc became distinct. The alignment between the top and bottom adherends was then verified and the bond thickness was measured using an opto-digital microscope (Figure 3.22).

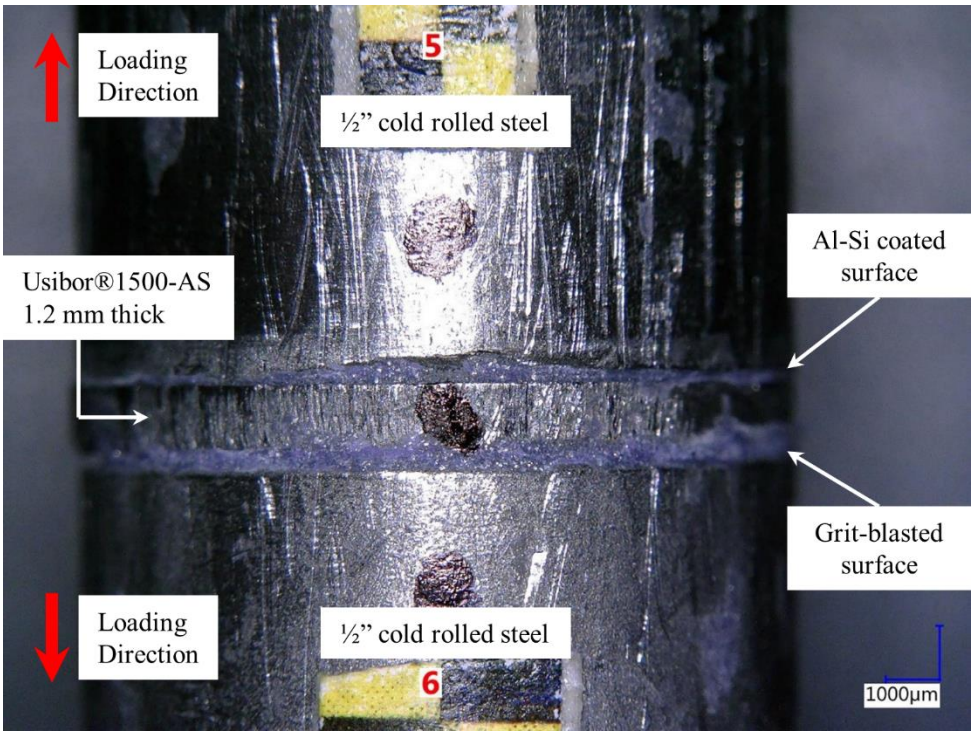

Figure 3.22: Adhesive thickness measurement of the butt joint sample

The butt-joint test used the same custom hydraulic frame as the single-lap shear test (Section 3.2.1). The samples were tested at 0.178mm/sec (0.007"/sec) and at room temperature. The interfacial strength (between the Al-Si coating and the adhesive surface) or the coating adhesion, $\sigma_t^{interface}$, was calculated using the maximum tensile load, $F_{t,max}$ and initial bond area, A_{disc}: $\sigma_t^{interface} = \frac{F_{t,max}}{A_{disc}} = \frac{F_{t,max}}{\pi r^2}$ (Eq. 3.2), where r is the radius of the sheet sample.

3.4 Surface Treatment Study

The following three surface treatments were investigated: degreased using acetone (ACE), grit-blasting (GB) surface treatment, and application of a silane-based adhesion promotor (AP).

Baseline study – Acetone (ACE)

The boron steel test pieces including the as-formed Al-Si intermetallic coating were swabbed using cotton pads soaked in acetone to remove contaminants (Figure 3.23a). A second rinse was then used to remove any lint or fabric that was left behind from the cotton pads (Figure 3.23b).

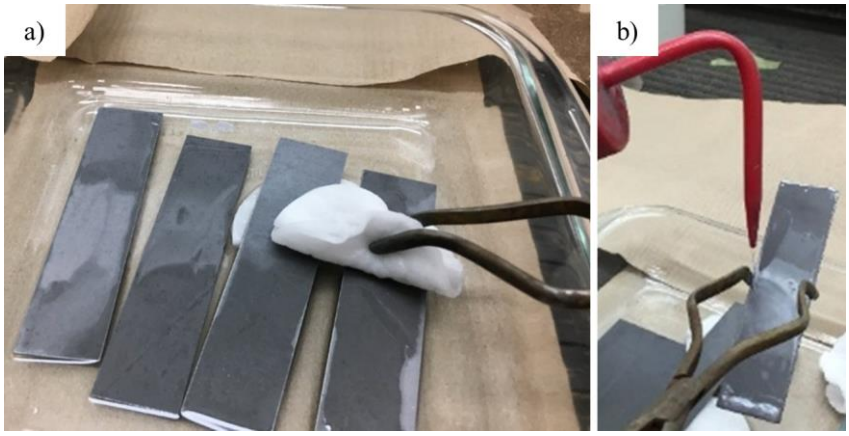

Figure 3.23: a) Swipe the adherend using a cotton pad to remove visible debris b) Wash off the remaining lint or fabric from the cotton pads

Grit-blasted (GB) + Acetone

The samples were grit-blasted using silicon carbide medium, with a 60 grit and an air pressure of 483 kPa (70 psi) (Nandwani, 2015). The treatment was intended to remove the Al-Si coating while roughening the surface of the underlying steel. The distance between the grit-blast gun and the target surface was between 63.5 mm to 152.4 mm (2.5” to 6”) (Figure 3.24). The duration of the mechanical surface roughening technique was 3 min per specimen (this included both sides of test pieces and of backing plates per specimen). The adherends were then placed in an acetone bath. After the surface was grit-blasted, the

degreasing procedure described in the baseline study was executed. The cotton pads were used to brush against the surface to remove possible grit media and grease.

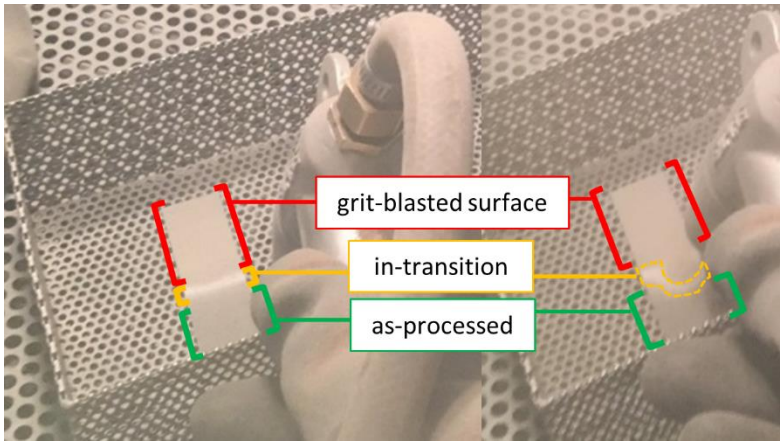

Figure 3.24: Grit-blasting process showing as-processed, in-transition, and grit-blasted surface

Effectiveness of grit-blasting on Al-Fe-Si coating removal

The Al-Fe-Si coating had different forms of defects such as microcracks, Kirkendall voids, and surface porosity which were formed during the austenization of the Al-Si coated boron steel (Figure 3.25) (Jenner *et al.*, 2010) (Fan *et al.*, 2012). In a preliminary investigation conducted by the author, the defects led to premature failure of an adhesive joint due to the coating delamination. A cross-section of the grit-blasted boron steel was observed under the opto-digital microscope to determine whether the grit-blasting treatment would remove the hard coating.

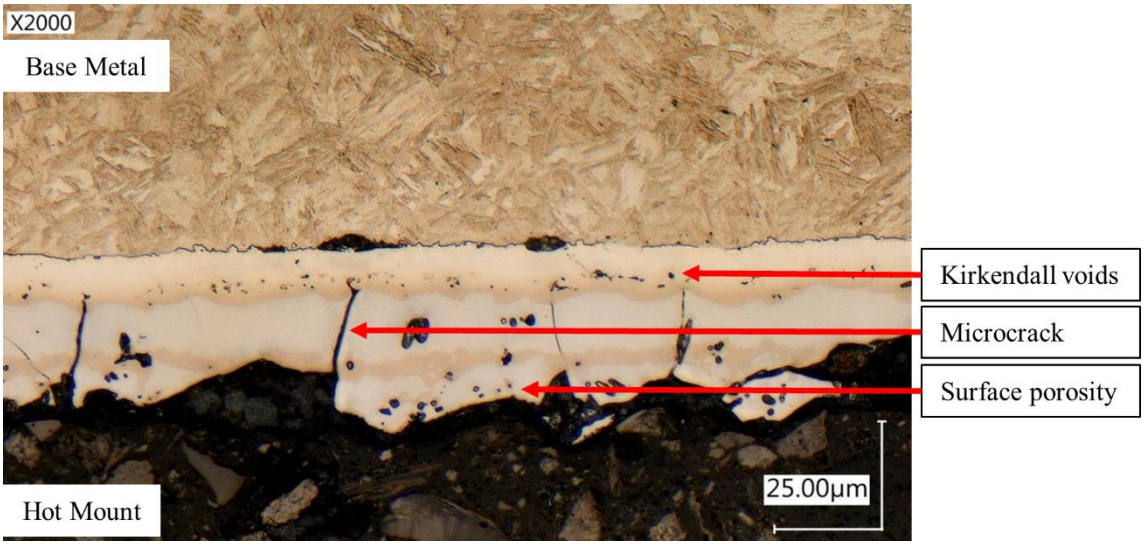

Figure 3.25: Al-Fe-Si intermetallic coating defects (cross-section view of fully martensitic boron steel)

Two control specimens were made: one with half of the surface grit-blasted (GB surface) and the other half remained intact (HT surface) and the other specimen completely grit-blasted (Figure 3.26). The samples were hot mounted, polished (started with 500 grit SiC sandpaper followed by progressively refined grinding media down to $1\mu m$ size diamond paste) and etched using 2% Nital solution (Bardelcik *et al.*, 2012) to verify whether the coating was removed.

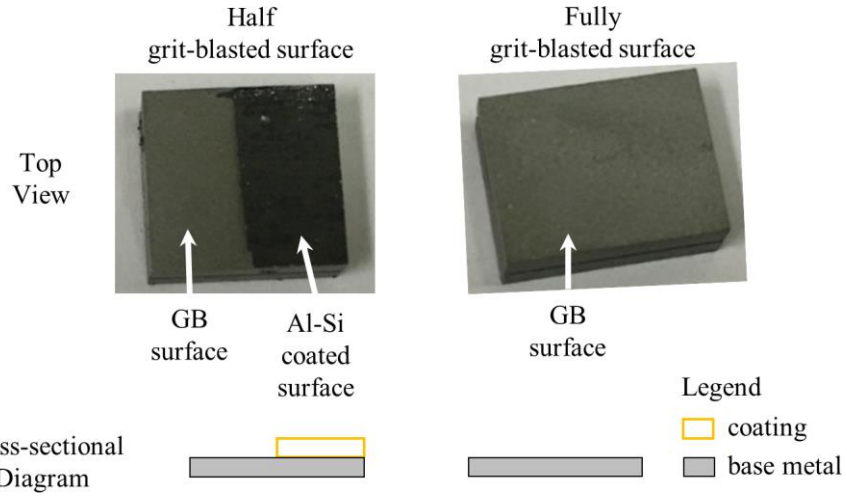

Figure 3.26: Non-grit blasted (intact Al-Si coating) and grit blasted cross-section surface observation

When observed under the opto-digital microscope, the grit-blasting approach removed the Al-Fe-Si intermetallic coating. A small trace of the coating (less than 5 µm thick of α-Fe phase) remained near the transition region (Figure 3.27a). To reaffirm the capability of the grit-blasting treatment to remove the coating, the cross-section of a fully grit-blasted surface demonstrated a coating-free surface (Figure 3.27b). Thus, the grit-blasting approach was selected as part of the surface treatment study for the coated boron steel.

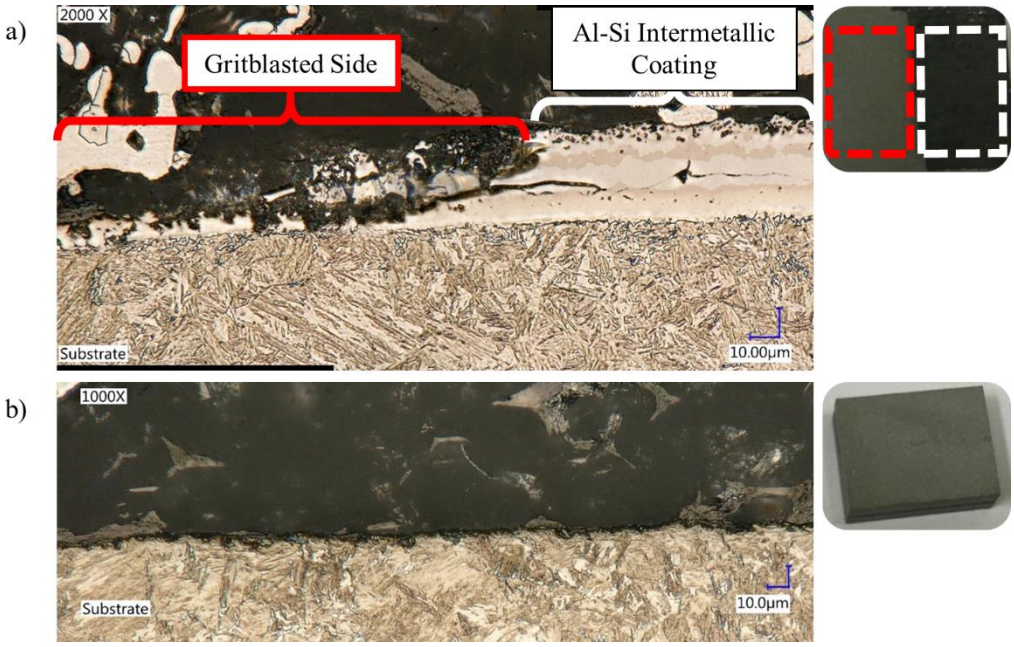

Figure 3.27: Effectiveness of grit-blasting onto the coated boron steel a) grit-blasted surface on Al-Fe-Si coated steel and the untreated surface and b) completely removed coating

GB + Acetone + Adhesion Promoter (GB-AP)

The third treatment introduced the step of applying the silane-based adhesion promotor (Scotch-Weld™ Metal Primer 3901, 3M™ Canada Company) after the grit-blasting treatment and degreasing treatment (3M, 2018). The amino silane enhanced the adhesion between the inorganic (metal substrate) and organic (epoxy) material and protected the adhesive joint against humidity, thereby, providing an improved interfacial strength (Ebnesajjad, 2014). The adhesion promotor was applied in a paint booth using a DeVilbiss JGA spray gun with a nominal line pressure of 414 kPA (60 psi) at a distance of 355.6 mm ± 25.4 mm (14”± 1”) away from the substrates, as recommended by the manufacturer. The primed surfaces were then put in the

forced air convection oven for 30 minutes at 88 °C (190 °F) (3M, 2011). The adherends were left to cool down for 15 min before the application of IRSA to avoid immediate adhesive curing.

3.4.1 Test Matrix for SLS Samples for Surface Treatment Study

A total of nine unique test cases were investigated in the surface treatment study for the coated boron steel, including three surface treatments for three different levels of strength and ductility of the boron steel (Table 3.4). Each test case had five repeats of the single-lap shear test.

Table 3.4: Single-lap shear test matrix showing the number of repeats for surface treatment study of coated boron steel

	Number of Samples		
Quenching Condition / **Surface Treatment**	**Room Temperature**	**400 °C**	**700 °C**
Baseline Study - acetone (ACE)	5	5	5
Grit-blasting treatment (GB)	5	5	5
Adhesive promotor (AP)	5	5	5

3.5 Adhesive Joining of Hot Stamped Structural Components

Hot forming of a metallic component into a specific shape (*e.g.* a hat channel) results in different surface finishes and coating morphologies, depending on the load applied to form the final shape of the hot stamped part, the nature of the contact with the tooling, and the extent of deformation of the material. In addition, the use of in-die heating during hot stamping will effect the adherend strength and possibly the corresponding joint performance. A study was undertaken considering three different locations (top section, side wall, and flange) of a hot formed hat channel to assess how forming an actual component may affect the surface coating, and how variations in the surface coating morphology may ultimately affect adhesive joint performance.

3.5.1 Hot Forming and Die Quenching Procedure for Hat Channels

Al-Si coated boron steel blanks with 1.8 mm nominal thickness were waterjet cut with a width of 220 mm and length of 590 mm, (not including the alignment tabs on each end of the blank (Figure 3.28a). The boron sheet was placed in a custom built furnace (Deltech Inc., USA) with a heating capacity of 18 kW with three heating elements on top and three heating elements at the bottom. The blank was in the furnace for 7 minutes at 930ºC to ensure that the blank was uniformly heated and that the austenite grain structure was formed throughout the sheet (Figure 3.28b). The heated blank was then transferred manually using a pair of extended pliers to a hydraulic forming press (Macrodyne Technologies Inc., Ontario, Canada) and hot formed into hat channels with in-die quenching at room temperature (Figure 3.28c). The manual transfer time was within five seconds to limit heat loss to the surrounding before the hot forming procedure. The hat channel forming cycle was 10 seconds, which included 4 seconds of hold time at 60 tons of force to obtain ultra-high strength in the hat sections (Figure 3.28d) (George, 2012) (Prajogo, 2015). The single-lap shear coupons were waterjet cut from the formed hat channels (Figure 3.29). The top section, side wall, and

flange sections were of interest to determine the influence of the adherend surface and forming to the resulting adhesive joint strength (Figure 3.30).

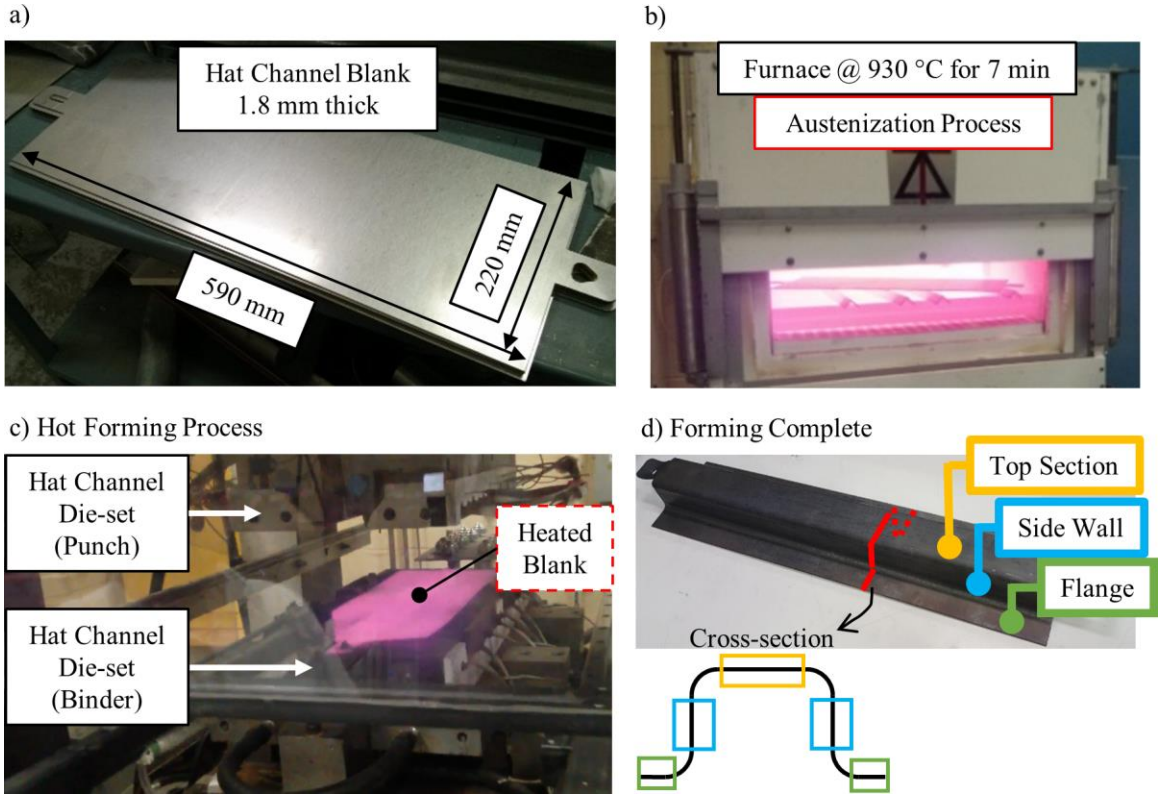

Figure 3.28: Hot forming in-die quenching of hat channel procedure; a) Usibor® 1500-AS hat channel blank, b) austenization process, c) hot forming of hat channel, e) hat channel highlighting each region

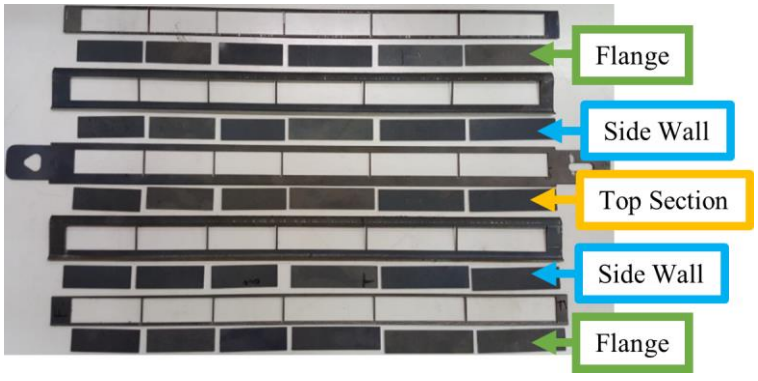

Figure 3.29: Single-lap shear adherends waterjet cut from three different sections of hat channel

Figure 3.30: Adherend surface finish from three sections of a hat channel

Microhardness Measurement of As-Formed Hat Channel

The microhardness of three areas (flange, side wall, and top) removed from the formed hat channels weas measured at the mid-thickness of the formed sheet (Figure 3.31). The flange section had a lower hardness (avg. 395 HV1.0, with a target hardness of 410 to 460 HV1.0 (Omer *et al.* 2017)) compared to the side wall and the top section due to the lower contact pressure between the sheet metal and the binder during the hot forming of the hat channel, which resulted in a slower cooling rate (Omer *et al.*, 2017) (Table 3.5).

Figure 3.31: Locations of the hardness measured (e.g. top section of a fully martensitic boron steel)

Table 3.5: Vickers microhardness summary of three different sections of a fully quenched hat channel

	Hat Channel Section		
	Flange	**Side Wall**	**Top**
Average [HV1.0]	395	455	496
Standard Deviation	15	7	8
Coeff. of Variance [%]	3.8	1.6	1.6

3.5.2 Test Matrix for SLS Samples Extracted from Hat Channel

The single-lap shear test was used to determine the influence of the surface finish of hot formed parts on the adhesive joint strength. The adherends were cleaned and degreased using methyl ethyl ketone (MEK) (Nandwani, 2015) prior to the sample preparation for the single-lap shear test. The test matrix is summarized

in Table 3.6. The measured maximum force was used to calculate the joint shear strength for comparison of the single lap shear samples created from the flange, side wall and top of the hat channel.

Table 3.6: Single-lap shear test matrix using adherends from 3 different sections of a hat channel

Section of the hat channel	Number of tests
Top	5
Side Wall	3
Flange	5

3.6 Intermetallic Coating Strength and Fracture Surface Study

The adhesive joining of Al-Si coated boron steel could lead to coating delamination in which the adhesive pulls off the coating from the steel substrate. The morphology of the Al-Si-Fe intermetallic coating was compared between the three thermal treatments to determine the effect of the thermal treatment on the coating and to establish a reference to examine the extent of the coating delamination. Butt joint tests and single-lap shear tests were conducted to determine the strength of the coated boron steel/adhesive interface under uniaxial tensile and mixed mode loading, respectively. Finally, the fracture surface of the test specimen was examined to investigate the underlying delamination mechanism of the intermetallic coating.

3.6.1 Intermetallic Coating Morphology Study

The Al-Fe-Si intermetallic coating formed during the in-die quenching of flat sheets (Section 3.3.1) and hat channels (Section 3.4.1) was imaged and measured using an opto-digital microscope, and the defects in the coating from the austenization process and hot forming were identified. Samples were cold mounted in resin and polished using silicon carbide (SiC) sandpaper in the following sequence: 500, 800, 1200, 2400, and 4000 grit and final polishing with diamond paste (3 μm and 1 μm). The final polished samples were etched using 2% Nital solution to provide clear boundaries between the developed coating and base metal.

3.6.2 Intermetallic Coating Strength Study

Butt joint tests were performed following the steps outlined in Section 3.2.2, which provided the tensile strength property (Eq. 3.2). Single-lap shear test results were from the surface treatment study (Section 3.3.2) with adherends in-die quenched at RT and treated by acetone (RT_ACE). The fracture surfaces of the specimens were examined to determine the extent of the coating delamination. The intermetallic coating failure sample was precision water-cut, mounted, and polished in the same manner outlined in Section 3.5.1 to provide a cross-sectional view of the failure.

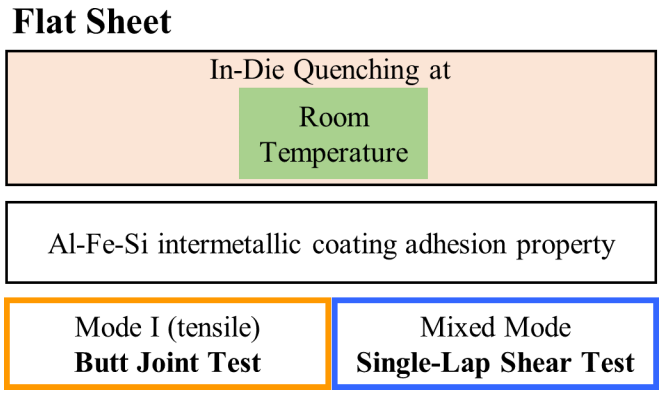

Figure 3.32: Butt joint test and single-lap shear test used to measure the intermetallic coating/steel interface strength

3.7 Adhesive Fracture Surface Morphology

Fracture surface analysis is introduced in this section with the objective of distinguishing the fracture morphology of adhesive joints under different modes of loading (such as tensile opening and shear) and capture the mixed mode failure in single-lap shear using the single-mode adhesive failure surfaces. Three single-mode adhesive joints (Mode I, II and Mixed Mode loaded at 45°) were prepared and mechanically tested by Watson (2019). The method intends to uncover the nature of the mixed mode failure in single-lap shear joint from the single mode of loading by comparing the fracture surfaces qualitatively and quantify the surface using the arithmetic mean surface roughness parameter, Ra.

The fracture surfaces of the test specimens were investigated using an opto-digital microscope to identify unique features of the adhesive joint under different modes of loading. Four types of adhesively bonded configuration were analyzed: (i) rigid double cantilever beam (RDCB) representing a Mode I tensile test; (ii) bonded shear sample (BDS) representing a Mode II shear test; (iii) a Mixed Mode sample configured at 45° orientation (MM45) with respect to the loading direction; and (iv) a single-lap shear sample with mixed-mode loading (Figure 3.33).

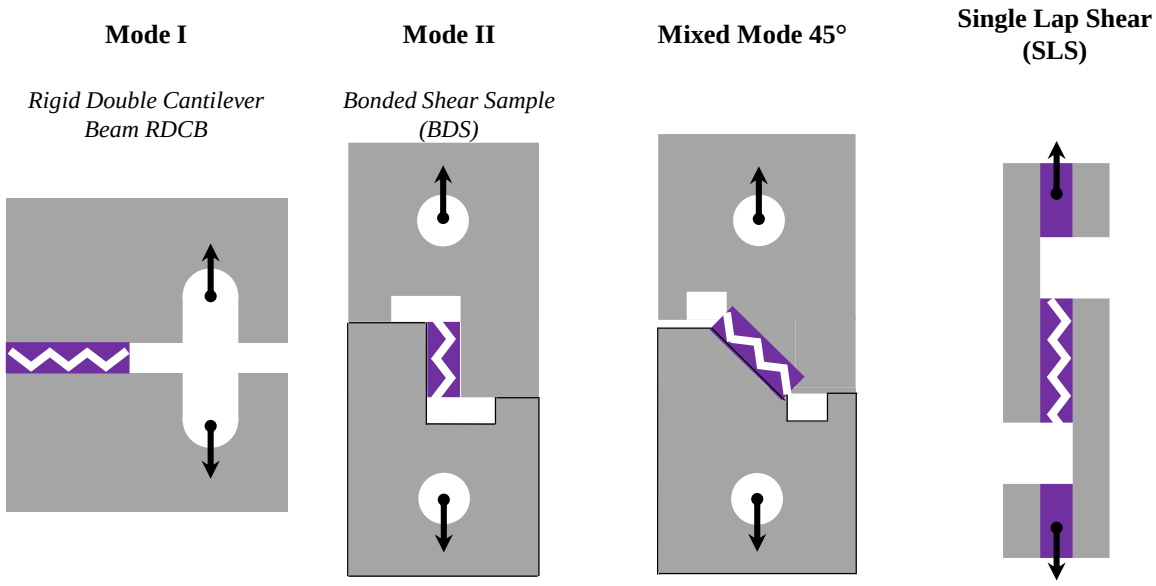

Figure 3.33: Four different adhesive joint failures from single mode loading to Mixed-Mode loading

Cold rolled steel adherends were used for Mode I, Mode II and mixed mode (MM45) specimens (Figure 3.34), except the single-lap shear sample which was made of ultra-high strength boron steel (from Section 3.4). The surfaces of the samples were first grit-blasted using 60 grit silicon carbide medium at an air pressure of 483 kPa and then cleaned using acetone before the application of IRSA (Watson, 2019). The surface preparation was necessary to ensure a good adhesion to promote failure at the adhesive layer (*i.e.* cohesive failure).

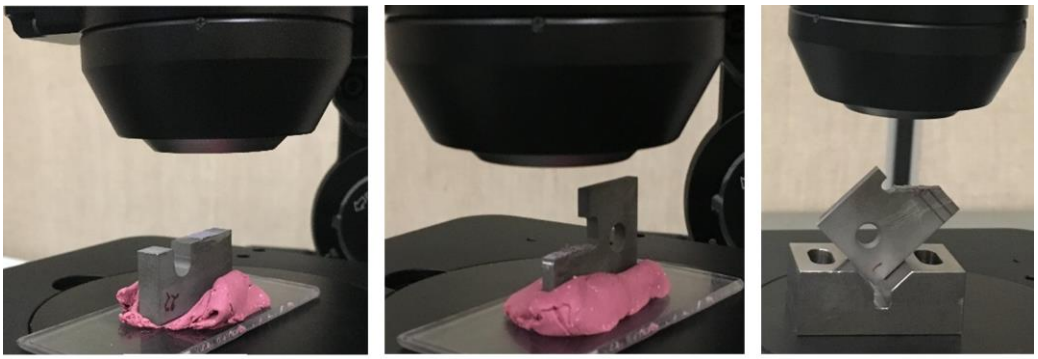

Figure 3.34: Fracture surface specimens observed under opto-digital microscope; Rigid Double Cantilever Beam (RDCB) specimen (L), Bonded Shear (BS) specimen (M), and Mixed Mode 45°specimen (R) (Pink putty ensures that the specimen is flat relative to the objective lens)

An opto-digital microscope coupled with a commercial depth composition software (VHX-5000 communication software, KEYENCE Corporation) was used to obtain high resolution images and topographic data of the fracture surfaces in this study. Samples were viewed at 200 x magnification. The topographic data was gathered by compiling focused images that were captured over the prescribed height by an increment of 10 µm. A single scanning area covered 1600 by 1200 pixels and adjacent images were stitched together digitally to provide a view of the entire fracture surface with a maximum area of 20000 by 20000 pixels. The result was a high resolution image of the fracture and the topographic data associated with each point across the surface.

The three-dimensional topographic data, containing the fracture profiles across the scanned surface, served as a quantitative tool to differentiate the four types of adhesive failure. The profiles were in the orientation of the crack propagation through the adhesive under Mode I and along the loading direction for Mode II, Mixed Mode at 45°, and single-lap shear specimens.

The arithmetic mean surface roughness, R_A, was measured to characterize each adhesive fracture surface (Eq. 3.3). R_A requires the height profile data, Z_i, provided by the digital microscope (with 1.092 μm per pixel) : $R_A = \frac{\sum_1^n(|Z_i|)}{n}$ (Eq. 3.3) where n is the total number of data points of the profile. A similar technique was applied to measure surface roughness by Demircioglu (2014).

Chapter 4. Results

4.1 Surface Treatment Study Using Single-Lap Shear Test

Single-lap shear (SLS) tests were conducted using adherends with three thermal treatments (RT, 400°C, and 700°C). Each thermal condition received one of three surface treatments (ACE, GB, and AP), creating a total of nine test cases (Table 3.4). Force-displacement response was measured during the test, and the maximum force was determined as a measure of the joint capacity. The shear strength (τ_{max}) was calculated from the measured maximum force and the initial bond area.

In a SLS test, followed by the initiation of loading, the test specimen joint began to rotate. A non-linear region followed a linear force-displacement region as the adhesive deformed plastically (i.e. permanent deformation), which was identified by a crack and joint detachment at the leading edges of the adhesive (Figure 4.1). After the peak force, the load gradually declined as the adhesive lost load-bearing capacity and the crack propagated within the joint resulting in an abrupt failure.

In this study, the shear strength and maximum joint rotation experimental data were each statistically processed using a two-way analysis of variance (ANOVA) with replication. Two-way ANOVA assesses the statistical significance of the individual effects from surface treatment and thermal treatment, and the interaction effect on shear strength and joint rotation. Next, if a statistical significance from the treatments or interaction of the two treatments was detected, one-way ANOVA is implemented to assess the statistical significance within the treatments. Finally, Tukey's honestly significant difference (HSD) post hoc ("after this") analysis compares among the treatments to assess if there was a statistically significant difference between the averages of the experimental data. The level of confidence (α) of the statistical analysis was selected as 0.05; that is, a 5 % probability that the null hypothesis (there was no significant difference between groups) is incorrectly rejected.

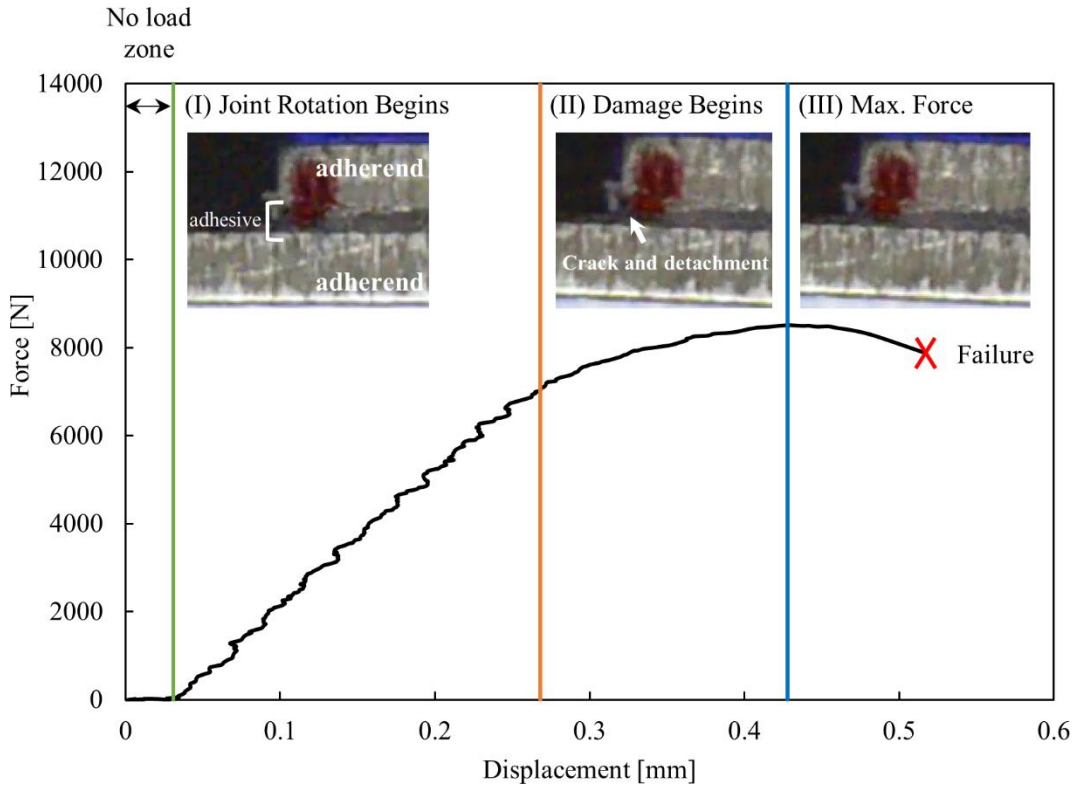

Figure 4.1: Typical force vs. local displacement response of a SLS test with corresponding images of the test specimen at important stages of the test (joint rotation, the start of damage and maximum force) (data from test specimen RT-AP-4)

4.1.1 Adhesive Joint Strength Measured Using SLS Tests

The ACE treatment produced the lowest average shear strength (13.9 MPa to 22.1 MPa) for the three thermal treatments (Table 4.1). The GB treatment produced test specimens with the highest shear strength (26.1 MPa to 27.8 MPa). The AP treatment provided a similar level of shear strength as the GB treatment (Figure 4.2). A high coefficient of variance (21.3% to 39.8%) reflected the high variability of shear strength in the ACE treatment. The variability in the results of GB treatment decreased, with the coefficient of variance ranging from 6.8% to 13.2%. The AP treatment had the lowest coefficient of variance (6.2% to 10.1%).

Table 4.1: Shear strength (τ_{max}) [MPa] with five repeats of single-lap shear configuration for combinations of three adherend thermal treatments (RT, 400°C or 700°C) and three surface treatments (degreased using acetone (baseline), grit-blast (GB), or adhesion promotor treatment (AP))

Surface Treatment	Baseline (ACE)			Grit-blast Treatment (GB)			Adhesion Promotor (AP)		
In-Die Quenching Temp.	RT	400°C	700°C	RT	400°C	700°C	RT	400°C	700°C
Test 1 [MPa]	27	16.4	11.2	21.1	25	25	28.9	23.5	25.4
Test 2 [MPa]	20.4	25.8	11	27.6	28.9	26	25.8	21.1	27.5
Test 3 [MPa]	27.1	7.8	18.3	29.4	26.6	24	24.9	26.2	24.8
Test 4 [MPa]	22.6	14.7	14.6	29.4	29.4	27	28.4	23.7	28
Test 5 [MPa]	13.3	16.1	14.2	25.2	29.1	28.5	27	27.4	28.9
Average [MPa]	22.1	16.2	13.9	26.6	27.8	26.1	27	24.4	26.9
Standard Deviation [MPa]	5.7	6.5	3.0	3.5	1.9	1.8	1.7	2.5	1.8
Coeff. Variance [%]	25.7	39.8	21.3	13.2	6.9	6.8	6.2	10.1	6.6

Table 4.2: Average shear strength improvement (in %) for SLS joint that received grit-blast (GB) treatment and adhesion promotor treatment (AP) over the degrease solution/baseline treatment (ACE) for three different thermal treatments of boron steel

	RT	400 °C	700 °C	
ACE [MPa]	***22.1***	***16.2***	***13.9***	**Average**
GB *vs.* ACE	+ 20 %	+ 72 %	+ 88 %	**+ 60 %** ↑
AP *vs.* ACE	+ 23 %	+ 50 %	+ 94 %	**+ 56 %** ↑

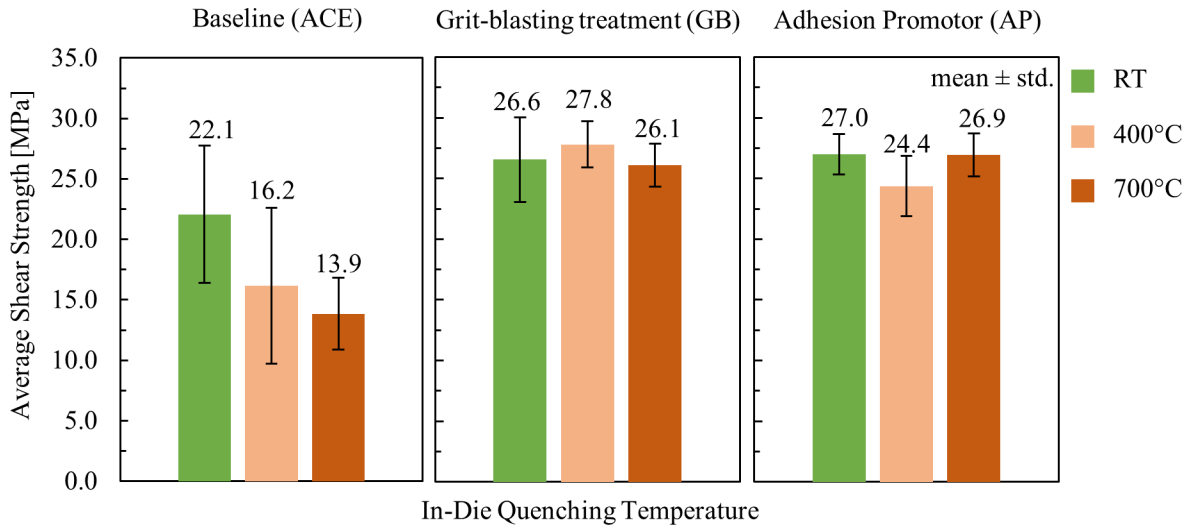

Figure 4.2: Graphical presentation of the shear strength (τ_{max}) result from the single-lap shear test for the surface treatment study on three different thermal treatments on the boron steel (RT, 400°C, and 700°C)

A two-way ANOVA was performed to determine the surface treatment and the thermal treatment effect on the shear strength of the adhesive. The main effect of the surface treatments was statistically significant ($p < .001$) (Table 4.3). The main effect of the thermal treatment was not statistically significant ($p = .069$). The interaction plot showed an increase in average shear strength from the ACE treatment to the AP treatment (Figure 4.3) with a 55.6% contribution from surface treatment and a 4.9% contribution from thermal treatment to shear strength. The interaction plot showed a negligible effect with minimal difference in shear strength among the three thermal treatments, especially among the GB and AP surface treatment. From the outcome of two-way ANOVA, the one-way ANOVA analysis focused on the surface treatment effect and determined that there is a statistical difference in shear strength detected between the three surface treatments ($p < .001$) (Table 4.4). Tukey's HSD post hoc test showed that test specimens that received GB and AP treatment had statistically higher shear strength than ACE treatment and there was no statistical difference in shear strength between GB and AP treatment (Table 4.5).

Table 4.3: Two-way analysis of variance (ANOVA) results, which identified the surface treatment with a statistical significant effect on the shear strength of single-lap shear test (*p*-value < .001; confidence level α=0.05) (bold and red font highlight a statistical significant difference)

Two-way analysis of variance (ANOVA) to Determine the Treatment Effects on Shear Strength

Source of Variation	*Sum of Squares (SS)*	*Degree of freedom (df)*	*Mean Square(MS)*	*F*-value	*P*-value	*F crit*	*% of Contribution*
Surface Treatment	831.3	2	415.7	32.91	**7.46E-09**	3.259	56%
Thermal Treatment	72.94	2	36.5	2.887	0.0687	3.259	5%
Interaction	136.5	4	34.1	2.703	0.0457	2.634	9%
Within	454.7	36	12.63				30%
Total	1495.6	44					100%

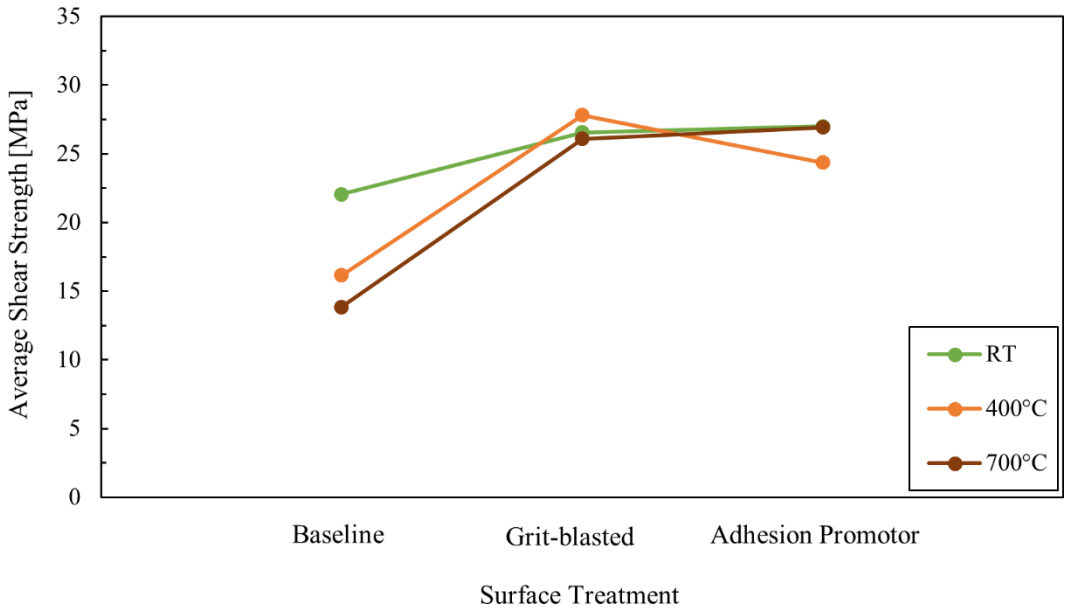

Figure 4.3: Interaction plot of surface treatment and thermal treatment effect on shear strength

Table 4.4: One-way ANOVA performed on three surface treatments (ACE, GB, and AP), which identified a statistical significant difference in shear strength among the three groups (*p*-value < 0.001; α=0.05) (bold and red font highlight a statistical significant difference)

One-way ANOVA to Determining Surface Treatment Effect on Shear Strength

Surface Treatments	*# of test samples in the group*	*Sum*	*Average Shear Strength* [MPa]	*Variance*
ACE	15	260.4	17.36	36.43
GB	15	402.3	26.82	5.99
AP	15	391.4	26.10	5.03

Source of Variation	*SS*	*df*	*MS*	*F*-value	*P*-value	*F crit*
Between Treatments	831.3	2	415.7	26.28	**3.96E-08**	3.22
Within Treatments	664.2	42	**15.8**			
Total	1495.6	44				

Table 4.5: Tukey's Honestly Significant Difference (HSD) Post Hoc Analysis which identifies group with the statistical significant average difference in shear strength

Tukey's Honestly Significant Difference (HSD) Post Hoc Analysis

# of groups	*# of comparison*	*df (within treatments)*	*level of confidence, α*	*q critical**	*# of test samples in a group, n*	*MS (Within Treatments)*	*HSD***
3	3	42	0.05	3.436	15	15.8	**3.528**

Comparison	*|Δ|*	*Statistically Significant Difference? (yes, if the difference is larger than HSD)*
ACE vs GB	***9.46***	**The average difference is statistically significant**
ACE vs AP	***8.74***	**The average difference is statistically significant**
GB vs AP	0.72	The average difference is not statistically significant

*q = critical value of Studentized range distribution (based on df = 42 and number of groups = 3)

**HSD = $q\sqrt{\frac{MS_{within}}{n}}$ =3.436$\sqrt{\frac{15.8}{15}}$=3.528;

The SLS test specimens made in this study had average bond line thicknesses ranging from 0.33 mm to 0.74 mm, which exceeds the intended bond line thickness of 0.178 mm (Table 4.6). The variability in bond line thickness highlighted the limitation in the current fixture and SLS assembly procedure. The clamps used to fix the test specimens were not providing adequate force to reach the target thickness determined by the 0.178 mm (0.007") thick brass shim within each test specimen.

Table 4.6: Single-lap shear sample bond length and bond line thickness measurement summary

Baseline (ACE)

Quenching Condition	RT		400 °C		700 °C	
Adhesive Parameter	Bond Length	Bond Thickness	Bond Length	Bond Thickness	Bond Length	Bond Thickness
Average [mm]	13.16	0.37	12.14	0.56	12.05	0.61
Standard Deviation [mm]	0.61	0.04	0.85	0.14	0.88	0.07
Coeff. Variance %	4.65	11.2	6.98	24.4	7.34	11.7

Grit-blasting treatment (GB)

Quenching Condition	RT		400 °C		700 °C	
Adhesive Parameter	Bond Length	Bond Thickness	Bond Length	Bond Thickness	Bond Length	Bond Thickness
Average [mm]	12.64	0.35	13.88	0.46	11.98	0.39
Standard Deviation [mm]	0.45	0.09	2.14	0.07	1.25	0.10
Coeff. Variance %	3.56	26.7	15.4	14.7	10.41	25.2

Adhesion Promotor (AP)

Quenching Condition	RT		400 °C		700 °C	
Adhesive Parameter	Bond Length	Bond Thickness	Bond Length	Bond Thickness	Bond Length	Bond Thickness
Average [mm]	12.83	0.33	12.32	0.50	11.65	0.49
Standard Deviation [mm]	1.38	0.05	0.79	0.10	1.91	0.09
Coeff. Variance %	10.7	14.7	6.40	19.5	16.4	18.1

In the ACE treatment, there was a trend of decreasing shear strength with increasing bond line thickness, particularly in the case of the RT and 700°C thermal treatment test specimens (Figure 4.4a), but this trend may be misleading since the intermetallic coating failure contributed to the high variability in joint strength. The bond line thickness effect was not present in the cases of GB treatment and AP treatment where shear strength obtained was more consistent for a large range of bond line thickness (Figure 4.4b and Figure 4.4c), suggesting an appropriate surface treatment may compensate for the variability in adhesive bond line thickness. However, a consistent bond line thickness study would be required to confirm the statement (*e.g.*, a test specimen with bond line thickness from 0.10 mm to 0.90 mm with a 0.20 mm increment with a tolerance of ± 0.02mm).

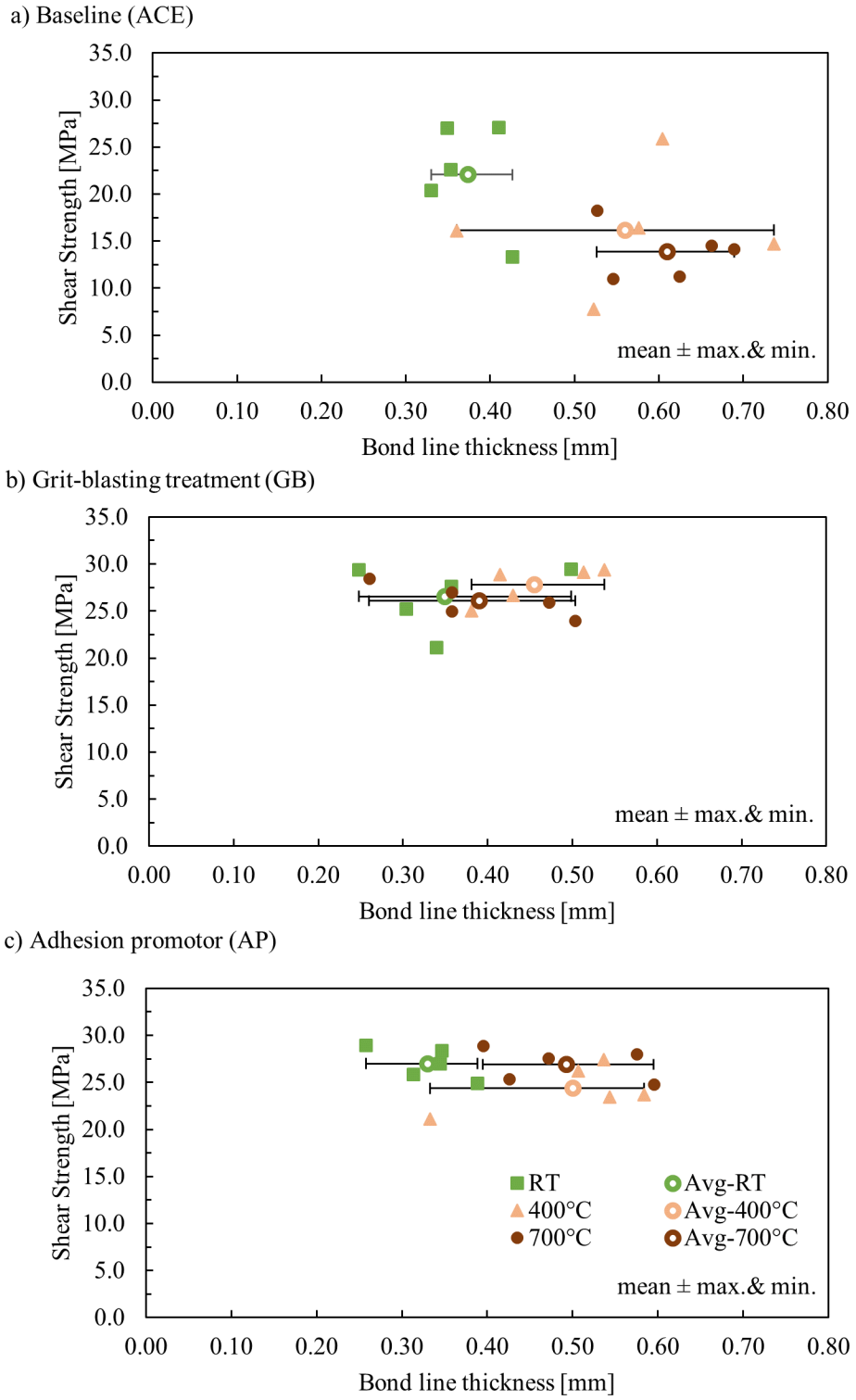

Figure 4.4: Shear strength from single-lap shear test vs. adhesive bond line thickness; a) baseline treatment, b) grit-blasting treatment, c) adhesion promotor treatment

4.1.2 Adhesive Joint Rotation Measured Using SLS Tests

The bond line of the SLS specimens rotated as the load increased during the test (Figure 4.5). The joint rotation parameter presents a more accurate single-lap shear kinematic response than the one-dimensional shear displacement, measured between the top half and bottom half of the specimen with a linear trend as the load increases. Therefore, the joint rotation relative to the loading direction was measured to complete the characterization of the kinematics of the SLS tests and the maximum joint rotation (i.e. angle at failure) was compared among the test cases in the surface treatment study. The objective is to identify possible effects of the surface and thermal treatments on the maximum joint rotation that may not have been detected based on the shear strength data.

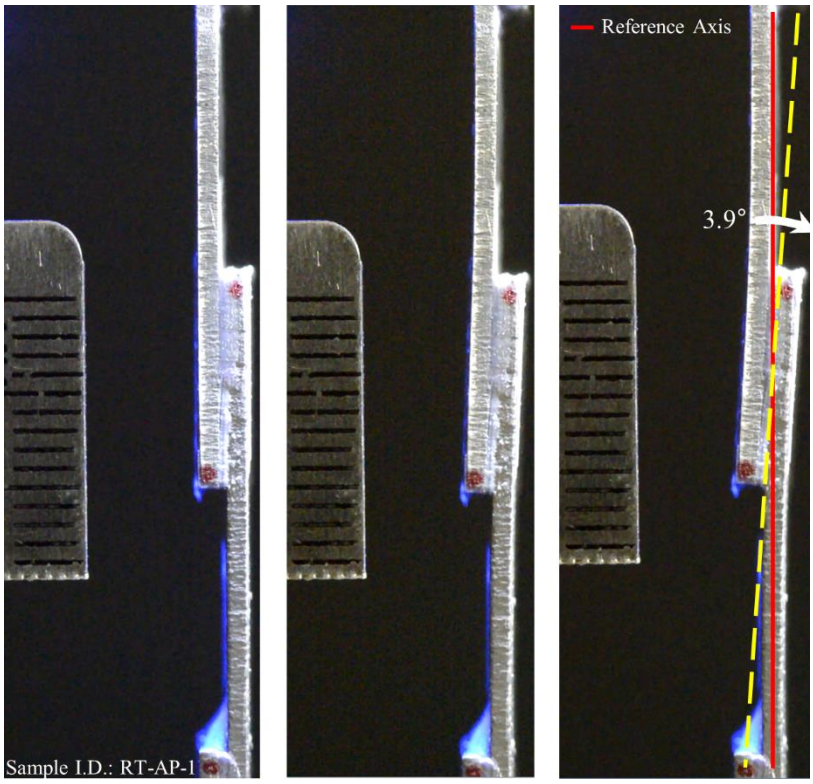

Figure 4.5: Single-lap shear test progression illustrating the adhesive joint rotation

The adhesive joint rotation increased in a non-linear manner (Figure 4.6b) compared to the force-displacement response (Figure 4.1). Therefore, the joint rotation was more sensitive to the load increase

compared to local shear displacement. During the test, the joint angle continued to increase beyond the peak force (Figure 4.6a). The adhesive progressively failed as the crack formed at the ends of the adhesive bond and the joint rotation increased until catastrophic joint failure.

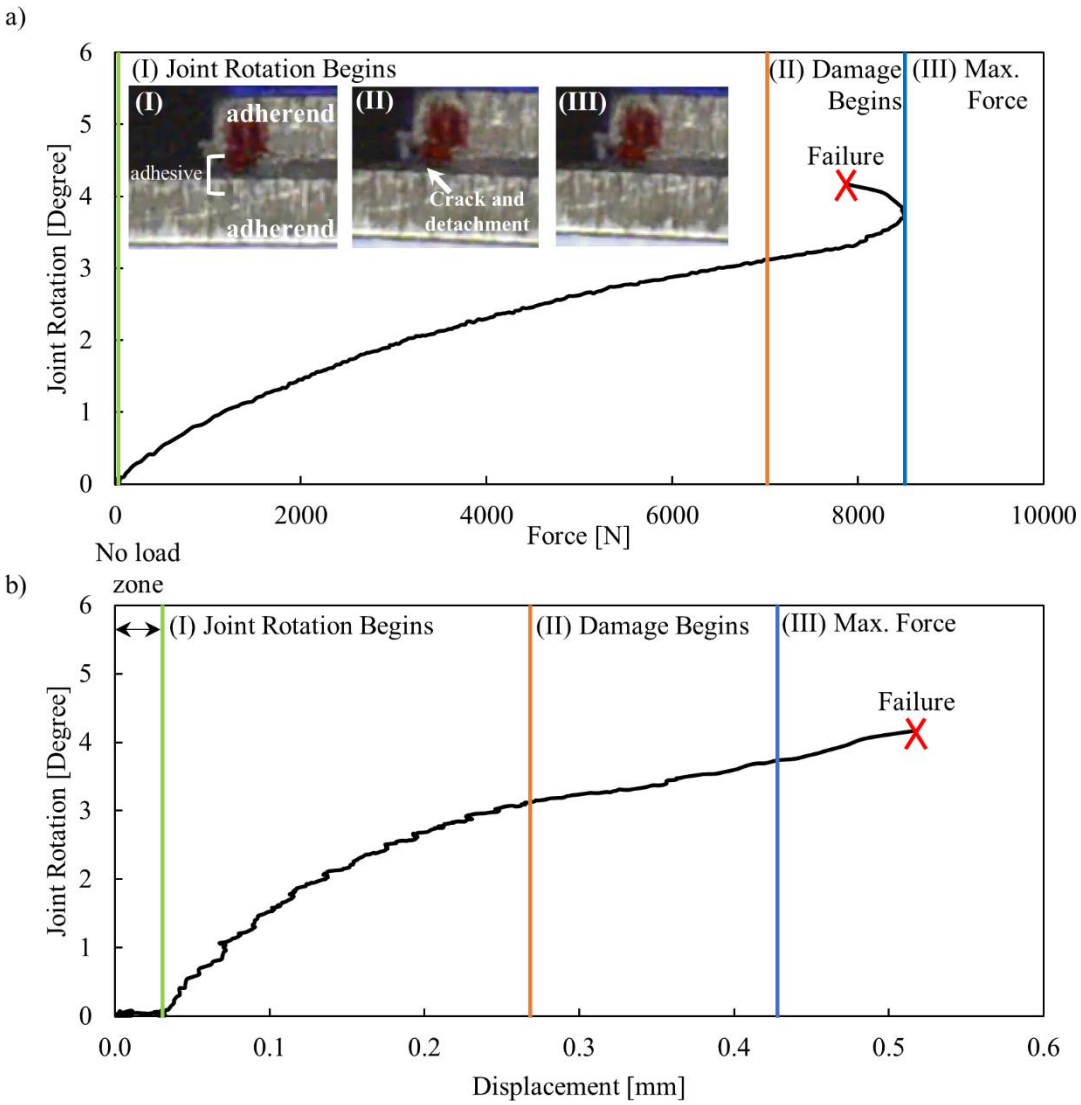

Figure 4.6: a) Typical adhesive joint rotation vs force response and b) joint rotation vs displacement of a SLS test with images of the test specimen at important stages of the test (response data and images are from test specimen: RT-AP-4)

In the ACE treatment, the average maximum joint rotation was between 2.5° to 2.8° (Table 4.7). The high level of variability observed in shear strength was reflected in the measured maximum joint rotation

(coefficient of variance between 21 to 25 %). The maximum joint rotation increased to approximately 4° to 5° in the cases of the GB and AP treatment and, in general, became more consistent (Table 4.7).

Table 4.7: Maximum joint rotation [in degrees] with five repeats of single-lap shear configuration for combinations of three adherend thermal treatments (RT, 400°C or 700°C) and three surface treatments (baseline, grit-blast, or adhesion promotor treatment)

Surface Treatment	Baseline (ACE)			Grit-blast Treatment (GB)			Adhesion Promotor (AP)		
In-Die Quenching Temp.	RT	400°C	700°C	RT	400°C	700°C	RT	400°C	700°C
Test 1 [Degree]	3.1	2.2	2.0	3.4	2.9	4.0	3.9	3.3	4.7
Test 2 [Degree]	2.9	3.5	2.8	3.3	5.0	4.9	3.6	2.8	5.1
Test 3 [Degree]	3.3	2.1	3.6	4.0	3.6	5.7	3.6	4.6	5.0
Test 4 [Degree]	3.0	2.2	2.9	4.0	4.0	5.2	4.2	2.8	4.3
Test 5 [Degree]	1.8	2.3	2.3	3.3	4.0	4.6	3.9	3.7	4.1
Average [Degree]	2.8	2.5	2.7	3.6	3.9	4.9	3.8	3.5	4.6
Standard Deviation [Degree]	0.6	0.6	0.6	0.4	0.7	0.6	0.2	0.7	0.4
Coeff. Variance [%]	20.8	25.1	23.1	10.6	19.2	13.3	6.3	21.5	8.8

Table 4.8: Average maximum joint rotation increase (in %) for SLS joint that received grit-blast (GB) treatment and adhesion promotor treatment(AP) over the degrease solution/baseline treatment (ACE) for three different thermal treatments of boron steel

	RT	400 °C	700 °C	
ACE [degree]	***2.8***	***2.5***	***2.7***	**Average**
GB *vs.* ACE	+ 29 %	+ 56 %	+ 81 %	**+ 55 %**
AP *vs.* ACE	+ 35 %	+ 40 %	+ 70 %	**+ 48 %**

The two-way analysis of variance (ANOVA) suggested the effects from the surface treatment and thermal treatment were statistically significant on the joint rotation ($p < .01$), and each contributed 48 % and 14 % to the maximum joint rotation, respectively (Table 4.9). The interaction effect between the surface treatment and thermal treatment on the maximum joint rotation was not statistically significant ($p = .087$). The interaction plot showed an increase in maximum joint rotation from the ACE treatment to AP treatment,

illustrating the dominant surface treatment effect (Figure 4.7). The thermal treatment effect on the maximum joint rotation was illustrated with an increase in maximum joint rotation from RT thermal treatment to 700°C thermal treatment in the interaction plot. The effect of the thermal treatment was more evident in the GB and AP treatment, where the adhesion was improved. The joint rotation parameter was more sensitive to the effect of the thermal treatment than the shear strength parameter. The maximum joint rotation parameter showed a dependency on the thermal treatment which was not reciprocated in the two-factor ANOVA on the shear strength parameter (p=.0687) (Table 4.3).

Table 4.9: Two-way analysis of variance (ANOVA) results, which identified the surface treatment and thermal treatment each having a statistical significant effect on maximum joint rotation of in single-lap shear test (p-value < 0.01; α=0.05) (bold and red font highlight a statistical significant difference)

Two-way analysis of variance (ANOVA) for Determining the Treatment Effects on Joint Rotation

Source of Variation	*Sum of Squares (SS)*	*Degree of freedom (df)*	*Mean Square(MS)*	*F*-value	*P*-value	*F crit*	*% of Contribution*
Surface Treatment	19.23	2	9.62	28.56	**3.71E-08**	3.26	48%
Thermal Treatment	5.52	2	2.76	8.19	**1.17E-03**	3.26	14%
Interaction	2.98	4	0.74	2.21	0.0874	2.63	7%
Within	12.12	36	0.34				30%
Total	39.84	44					100%

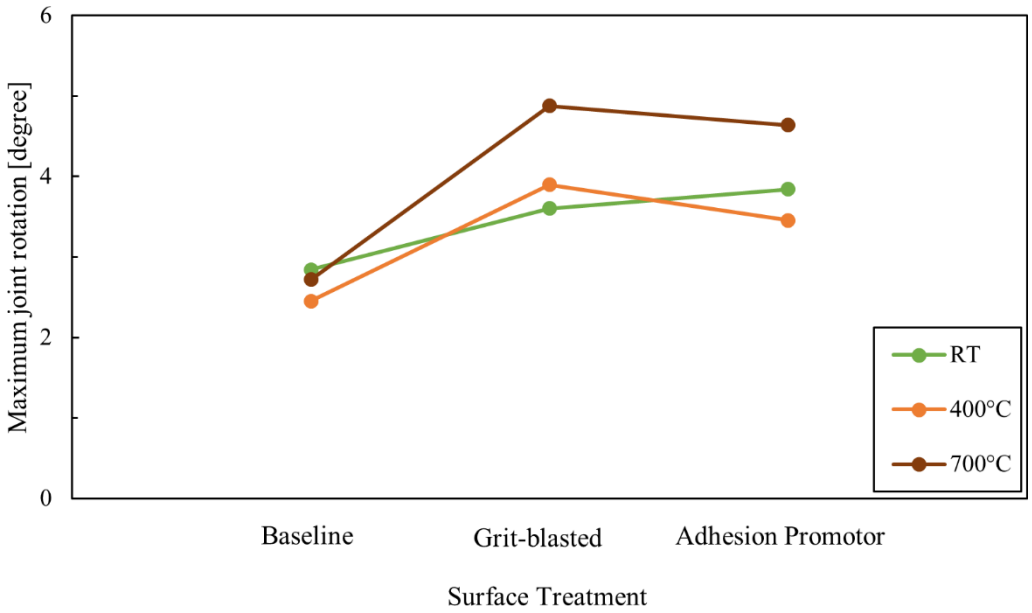

Figure 4.7: Interaction of surface treatment and thermal treatment with respect to maximum joint rotation

One-way ANOVA was conducted separately for each main effect (surface and thermal treatment) to determine if there was a statistical difference in maximum joint rotation among the treatments in respective surface and thermal treatments (Table 4.10). The results of one-way ANOVA confirmed statistical significant difference within the groups of surface treatments and the thermal treatments (p <.001 for surface treatment and p =.0437 for thermal treatment) (Table 4.10).

Table 4.10: One-way ANOVA performed on two main effects: surface treatments and thermal treatment, which identified a statistical significant difference in max. joint rotation among the groups (p-value < 0.01; α=0.05) (bold and red font highlight a statistical significant difference)

One-way ANOVA for Determining Surface Treatment Effect on Max. Joint Rotation

Surface Treatments	*# of test samples in the group*	*Sum*	*Average Max. Joint Rotation* [degree]	*Variance*
ACE	15	40.09	2.7	0.3504
GB	15	61.92	4.1	0.6400
AP	15	59.68	4.0	0.4818

Source of Variation	*SS*	*df*	*MS*	*F*-value	*P*-value	*F crit*
Between Treatments	19.23	2	9.616	19.59	**9.75E-07**	3.220
Within Treatments	20.61	42	**0.491**			
Total	39.84	44				

One-way ANOVA for Determining Thermal Treatment Effect on Max. Joint Rotation

Thermal Treatments	*# of test samples in the group*	*Sum*	*Average Max. Joint Rotation* [degree]	*Variance*
RT	15	51.46	3.4	0.353
400 °C	15	49.04	3.3	0.818
700 °C	15	61.19	4.1	1.281

Source of Variation	*SS*	*df*	*MS*	*F*-value	*P*-value	*F crit*
Between Treatments	5.517	2	2.758	3.375	**0.0437**	3.220
Within Treatments	34.32	42	**0.817**			
Total	39.84	44				

Finally, Tukey's HSD post hoc result showed the test specimens that received GB and AP treatment exhibited statistically higher maximum joint rotation than ACE treatment and no difference was detected

between GB and AP treatment (Table 4.11). As for the thermal treatments, post hoc comparisons using Tukey's HSD showed that the test specimens that received 700 °C thermal treatment had statistically higher maximum joint rotation than 400 °C thermal treatment and no statistical difference was detected between RT and 400 °C thermal treatment and RT and 700 °C thermal treatment (Table 4.11).

Table 4.11: Tukey's Honestly Significant Difference (HSD) Post Hoc Analysis which identifies group with the statistical significant average difference in maximum joint rotation

Tukey's Honestly Significant Difference (HSD) Post Hoc Analysis (Surface Treatment)

# of groups	*# of comparison*	*df (within treatments)*	*level of confidence, α*	*q critical**	*# of test samples in a group, n*	*MS (Within Treatments)*	*HSD***
3	3	42	0.05	3.436	15	0.491	**0.621**

Comparison	|Δ|	*Statistically Significant Difference? (yes, if the difference is larger than HSD)*
ACE vs GB	***1.5***	**The average difference is statistically significant**
ACE vs AP	***1.3***	**The average difference is statistically significant**
GB vs AP	0.1	The average difference is not statistically significant

*q = critical value of Studentized range distribution (based on df = 42 and number of groups = 3)

**HSD = $q\sqrt{\frac{MS_{within}}{n}}$ =3.436$\sqrt{\frac{0.491}{15}}$=0.621;

Tukey's Honestly Significant Difference (HSD) Post Hoc Analysis (Thermal Treatment)

# of groups	*# of comparison*	*df (within treatments)*	*level of confidence, α*	*q critical**	*# of test samples in a group, n*	*MS (Within Treatments)*	*HSD***
3	3	42	0.05	3.436	15	0.817	**0.802**

Comparison	|Δ|	*Statistically Significant Difference? (yes, if the difference is larger than HSD)*
RT vs 400 °C	*0.2*	The average difference is not statistically significant
RT vs 700 °C	*0.6*	The average difference is not statistically significant
400°C vs 700°C	**0.81**	**The average difference is statistically significant**

*q = critical value of Studentized range distribution (based on df = 42 and number of groups = 3)

**HSD = $q\sqrt{\frac{MS_{within}}{n}}$ =3.436$\sqrt{\frac{0.817}{15}}$=0.802;

In the post-test analysis, the test specimens did not exhibit plastic deformation for the RT thermal treatment in which there was essentially no plastic bending at the bond line with respect to the backing plate (Figure

4.8a). However, plastic deformation was observed at the leading edges of the adhesive joint in the softer adherends quenched with a die temperature of 400°C and 700°C that had GB or AP treatment. The plastic deformation was confirmed by the measured permanently bent adherends that were initially flat before the test and the side view of the specimens showed adherends with two to three degrees of bending at the bond line with respect to the backing plate (Figure 4.8b and Figure 4.8c).

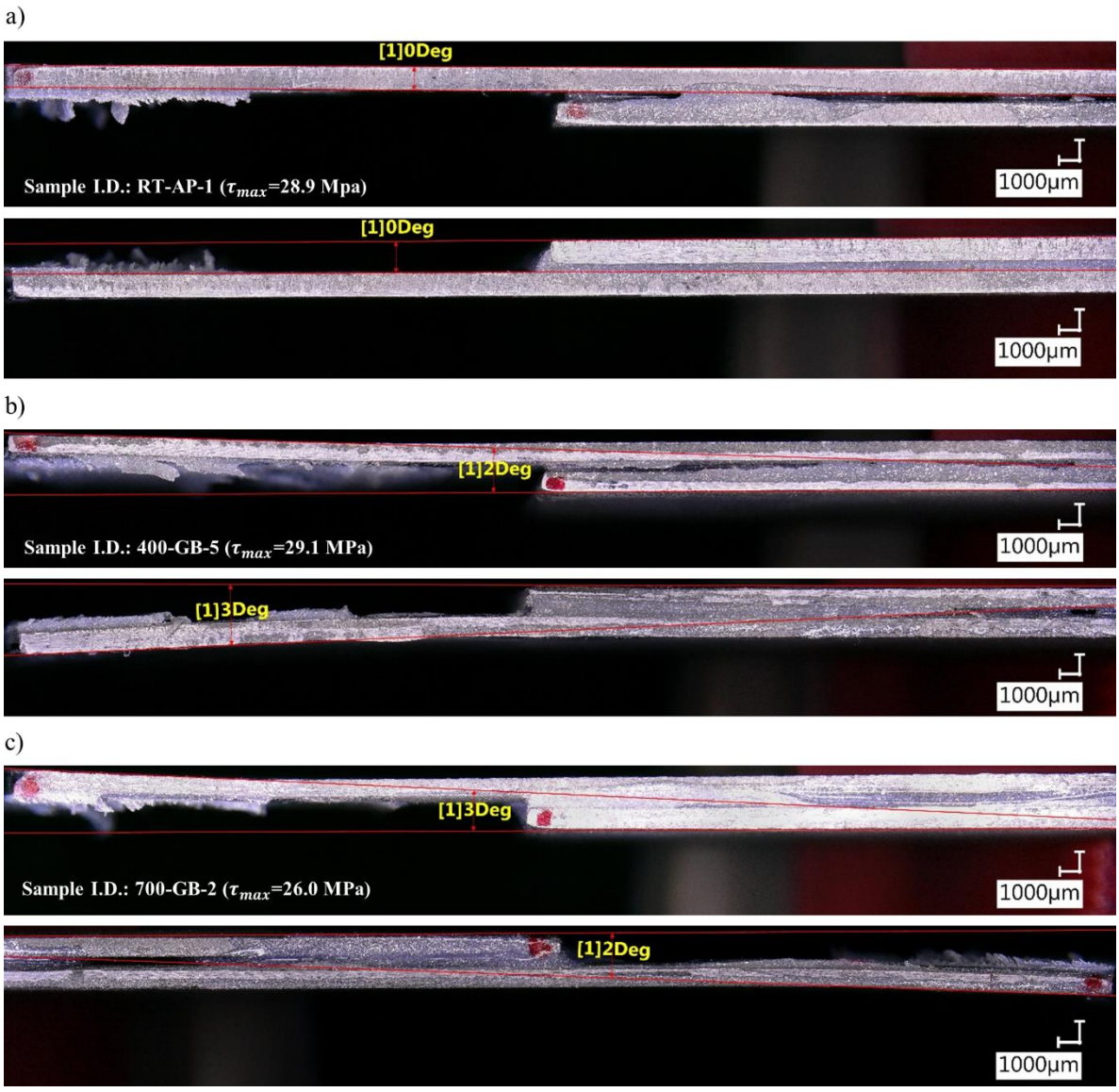

Figure 4.8: Side view of tested single-lap shear samples with corresponding shear strength: a) adherends with RT thermal treatment with no visible plastic deformation with 0° bending, b) adherends with 400°C thermal treatment with visible plastic deformation shown with 2° to 3° of adherend bending c) adherends with 700°C thermal treatment with visible plastic deformation shown with 2° to 3° of adherend bending

4.1.3 Visual Observations of SLS Joint Failure Mode

As part of the post-test analysis, high-resolution images of the failure surface showed the following fracture modes: intermetallic coating failure, interfacial failure (IF), cohesive failure (CF), and a mixture of IF and CF (Table 4.12) (Figure 4.9).

Table 4.12: Number of single-lap shear test specimen classified based on the types of adhesive failure (intermetallic coating failure, interfacial failure, cohesive failure, and mixed of cohesive and interfacial failure for the surface treatments tested(ACE, GB, and AP treatment)

	Number of Samples								
Surface Treatment	Baseline (ACE)			Grit-blast Treatment (GB)			Adhesion Promotor (AP)		
In-Die Quenching Temp.	RT	400°C	700°C	RT	400°C	700°C	RT	400°C	700°C
Mode of Failure									
Intermetallic Coating Failure	5	4	5	n.a.	n.a.	n.a.	n.a.	n.a.	n.a.
Interfacial Failure (IF)	-	1	-	-	2	-	-	-	-
Cohesive Failure (CF)	-	-	-	2	-	2	-	1	-
Mixed of IF and CF	-	-	-	3	3	3	5	4	5

In the ACE treatment, 14 out of 15 tests exhibited intermetallic coating failure, which was identified by the silver reflective surfaces, and one case demonstrated interfacial failure (Figure 4.9a). The delamination location and the amount of coating delaminated varied from specimen to specimen (Figure 4.10).

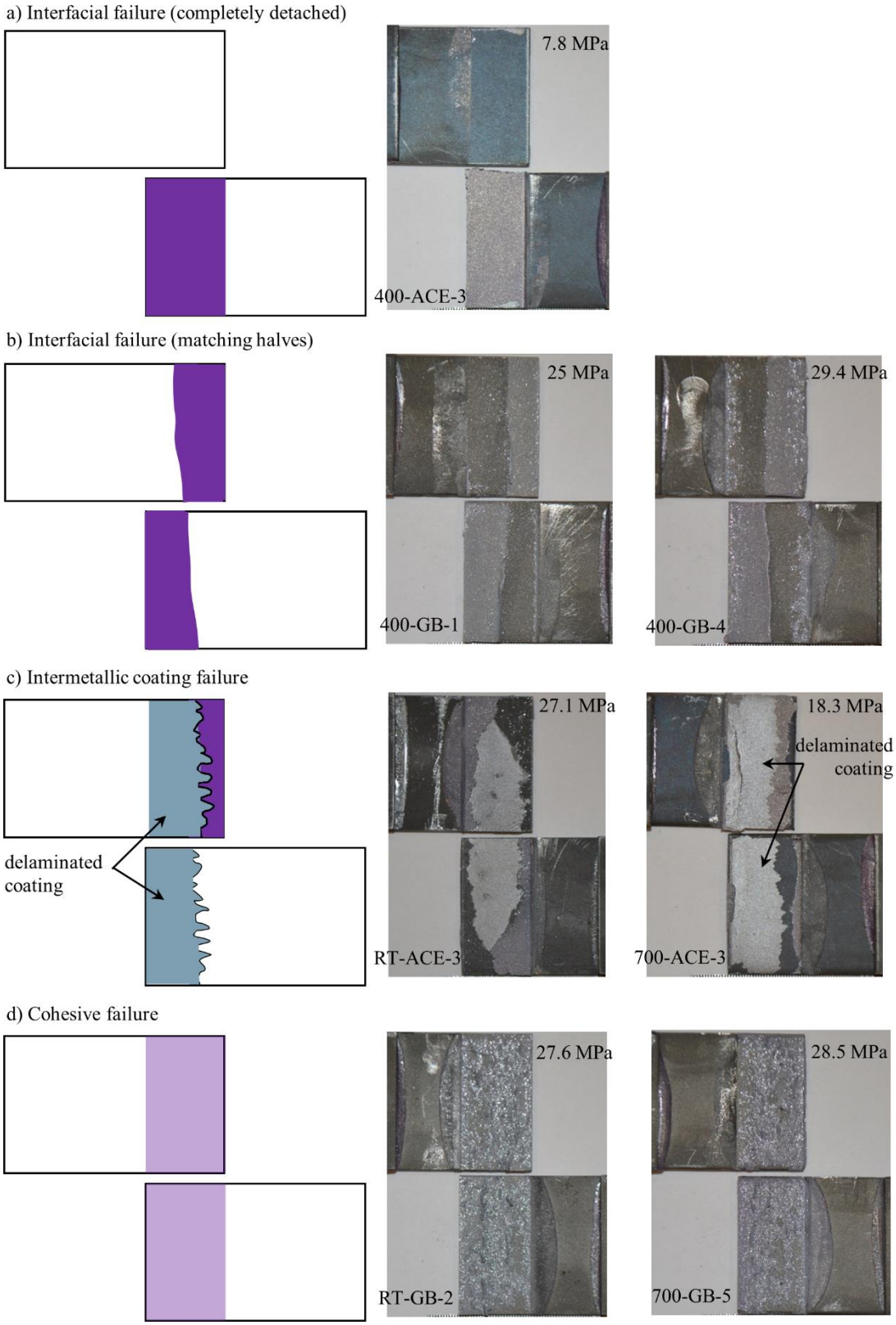

Figure 4.9: Typical fracture surfaces of IRSA in a single-lap shear test: a) interfacial failure, b) interfacial failure (matching halves), c) intermetallic coating failure, d) cohesive failure

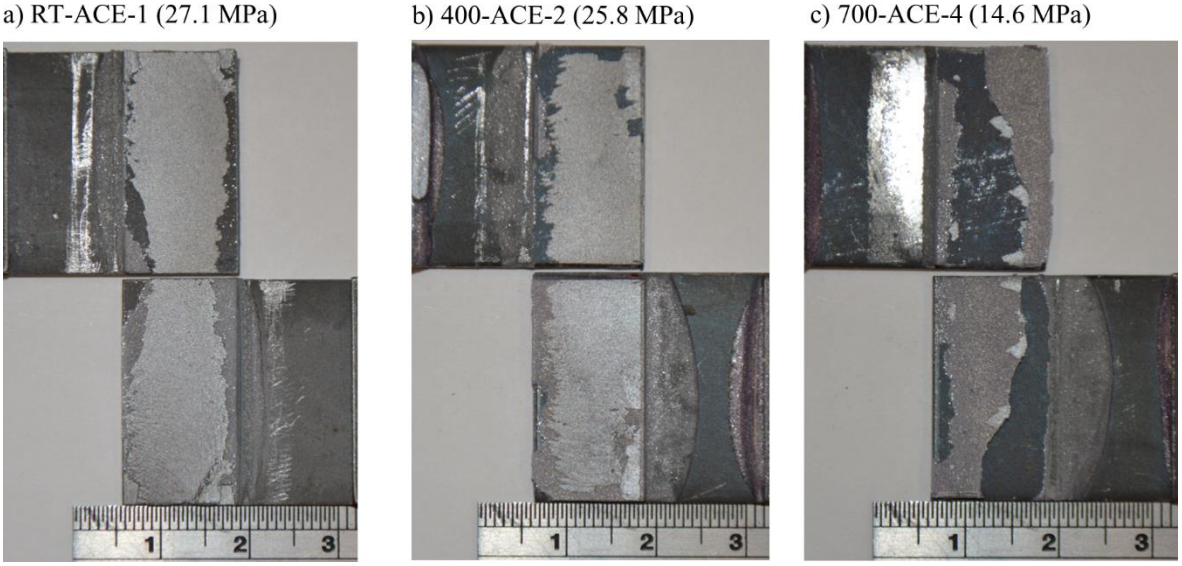

Figure 4.10: Baseline surface treatment demonstrating intermetallic coating failure for three thermal treatments: a) room temperature, b) 400°C, and c) 700°C

The fracture surfaces of the SLS test specimens that received the GB treatment (Figure 4.11) and AP treatment (Figure 4.12) showed a mixture of cohesive and interfacial failure. The shear strength obtained from the GB treatment and AP treatments were similar and higher compared to that of the ACE treatment despite presenting different extents of cohesive and interfacial failure. Test specimens were presenting interfacial failure with one-half of the fractured adhesive on one side of adherend and the remaining half on the opposite side of the adherend (Figure 4.9b). The cohesive failure presented various sizes of saw-tooth like fracture (also known as shear hackles) showing the shear loading at the adhesive from load up till failure (Figure 4.13) (Liu and Piggott, 1998). Similar shear hackles were noted in the single-lap shear test presented by Karachalios *et al.* (2013).

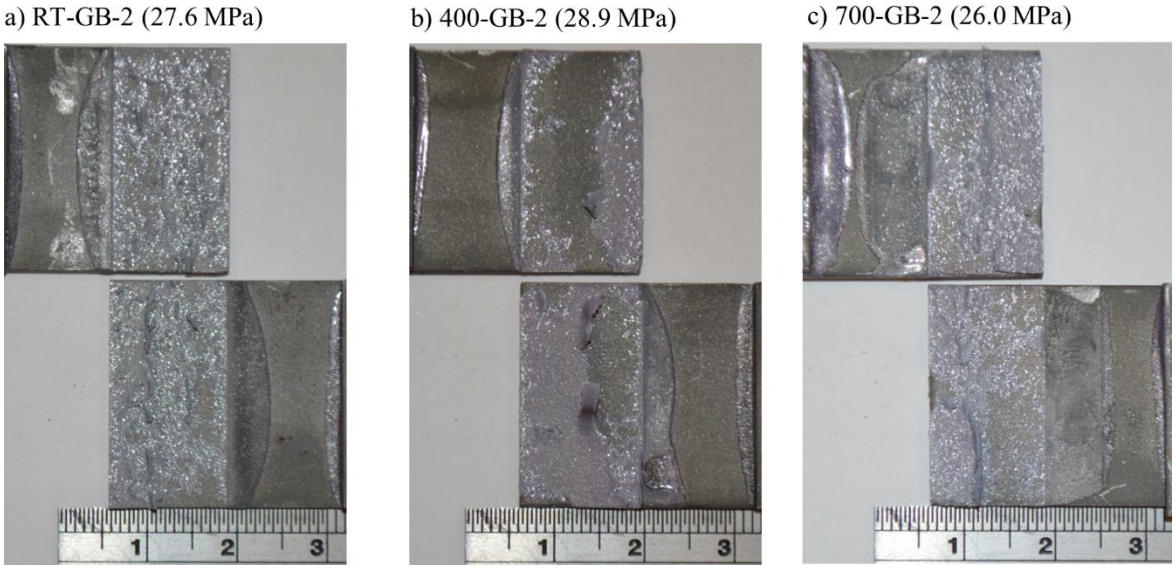

Figure 4.11: GB surface treatment demonstrating cohesive and mixed of interfacial and cohesive failure for three thermal treatments: a) room temperature, b) 400°C, and c) 700°C

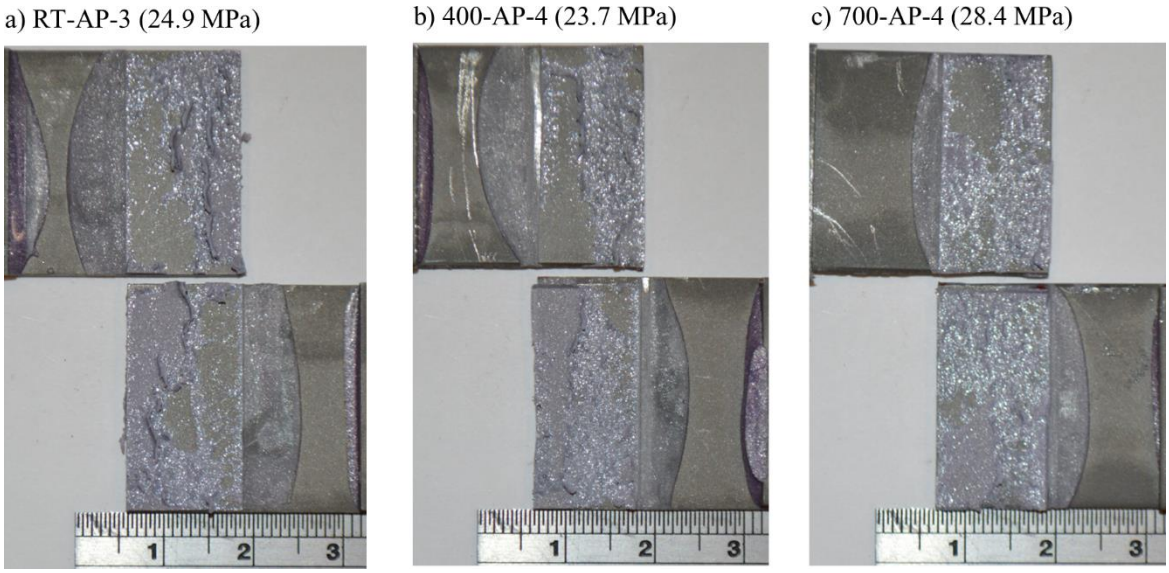

Figure 4.12: AP surface treatment demonstrating cohesive failure and mixed of interfacial and cohesive failure for three thermal treatments: a) room temperature, b) 400°C, and c) 700°C

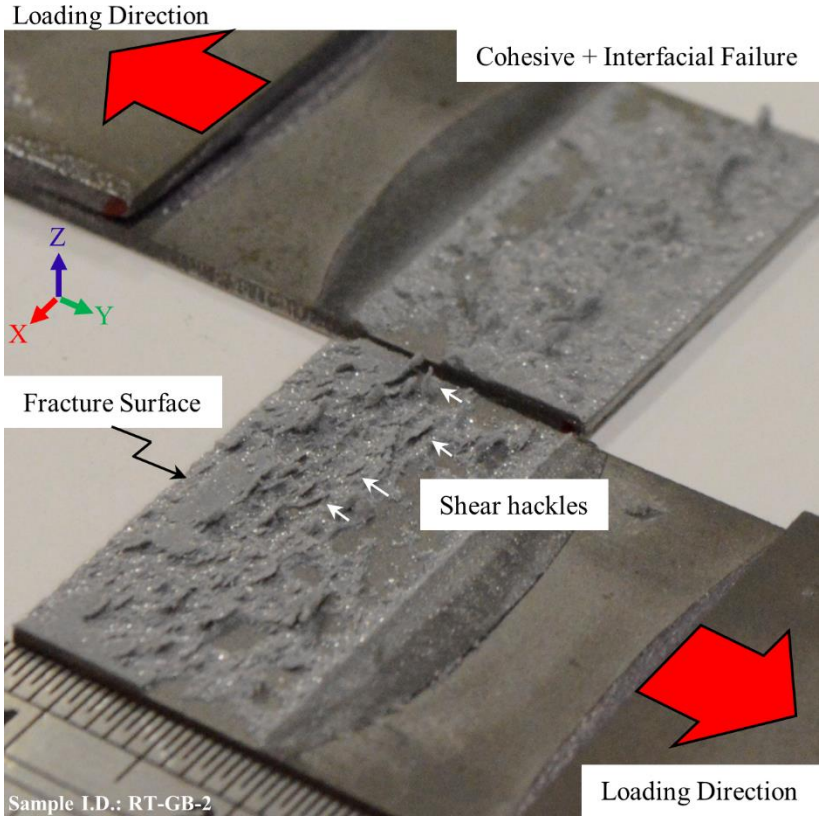

Figure 4.13: Isometric view of cohesive failure in a grit-blasted (GB) SLS configuration using adherends with RT thermal treatment demonstrating the "leaf-like" shape across the bond area known as shear hackles

4.2 Al-Fe-Si Intermetallic Coating Development, Defects, And Coating Strength

The Al-Fe-Si intermetallic coating was investigated using optical digital microscopy (ODM) to uncover the origin of intermetallic coating failure in the SLS joint. Modified butt joint and single-lap shear test specimens were tested to obtain the adhesion strength of the intermetallic coating under pure tension and Mixed-Mode loading, respectively.

Before the austenization process, the as-received Al-Si coating had a thickness ranging between 17 to 28 μm (Figure 4.14a). During the austenization process, the Al-Si coating was developed into a five-layered intermetallic coating with a total thickness ranging between 24 to 40 μm for all thermal treatments (Figure 4.14b to Figure 4.14c). The as-received Al-Si coating did not exhibit microcracks (Figure 4.14a). The intermetallic coating of all three thermal treatments showed microcracks, surface porosity, and Kirkendall voids.

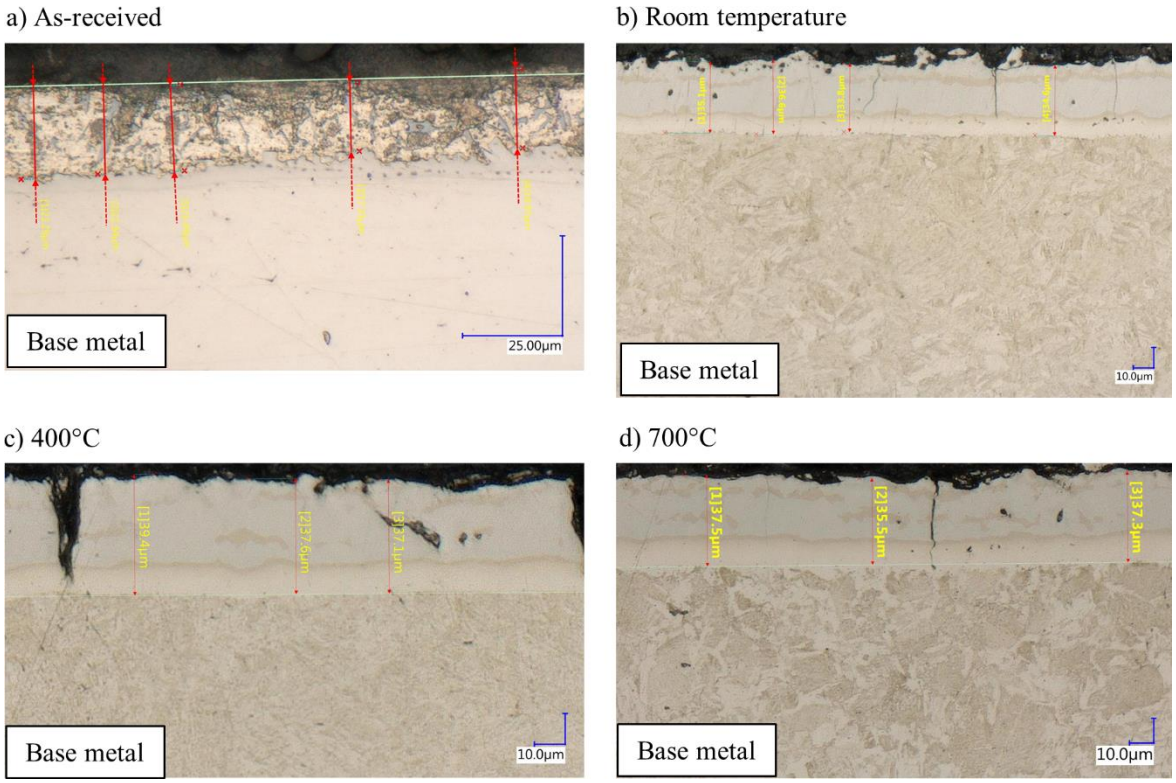

Figure 4.14: Al-Fe-Si intermetallic coating of a 1.2 mm thick boron steel a) as-received, b) in-die quenched at room temperature, c) in-die quenched at 400°C, and d) in-die quenched at 700°C

The microcrack density was calculated for each thermal treatment (Figure 4.15). The RT thermal treatment had an average of 16 ± 2 cracks per mm, the 400°C thermal treatment had an average of 14 ± 2 cracks per mm, and the 700°C thermal treatment had an average of 8 ±2 cracks per mm (Table 4.13). One-way ANOVA analysis confirmed that the thermal treatment has a statistically significant effect on the microcrack density ($p < .001$) (Table 4.14). The Tukey HSD test showed that the boron steel with RT thermal treatment (mean=15.7, SD=2.2) and 400°C thermal treatment (mean=14.5, SD=1.7) each had a statistically higher microcrack density than the ones with 700°C thermal treatment (mean=8.5, SD=1.9). There was no statistical difference in the microcrack density in the boron steel between RT thermal treatment and 400°C thermal treatment (Table 4.15).

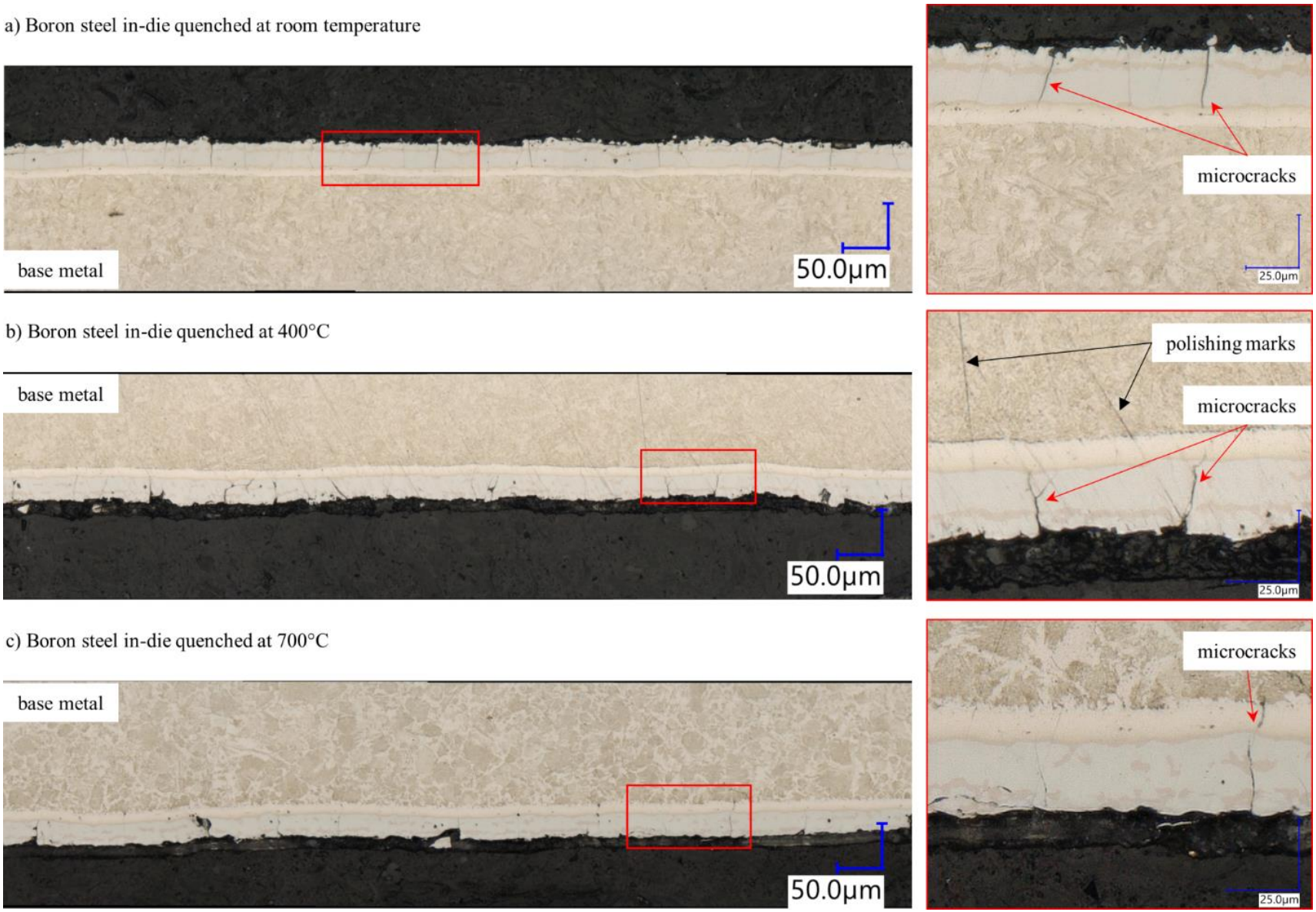

Figure 4.15: Microcracks in Al-Fe-Si coated boron steel in-die quenched at a) RT, b) 400°C, and c) 700°C

Table 4.13: Average microcrack density in the Al-Fe-Si intermetallic coating based on the thermal treatment

In-Die Quenching Temperature	Microcrack Density [/mm]			
	Average	Standard Deviation	Coeff. Variance	n
RT	15.7	2.2	14%	9
400 °C	14.5	1.7	12%	9
700 °C	8.5	1.9	22%	9

Table 4.14: One-way ANOVA performed on three thermal treatments (RT, 400°C, and 700°C), which identified a statistical significant difference in shear strength among the three groups (p-value < 0.001; α=0.05) (bold and red font highlights a statistical significant difference)

One-way ANOVA for Determining Thermal Effect on Crack Density in Al-Si-Fe Coating

Thermal Treatments	*# of test samples in the group*	*Sum*	*Average Crack Density* [/mm]	*Variance*
RT	9	140.9	15.7	5.0
400 °C	9	130.1	14.5	2.8
700 °C	9	76.2	8.5	3.6

Source of Variation	*SS*	*df*	*MS*	*F*-value	*P*-value	*F crit*
Between Treatments	267.1	2	133.5	35.09	**7.49E-08**	3.403
Within Treatments	91.32	24	**3.81**			
Total	358.4	26				

Table 4.15: Tukey's Honestly Significant Difference (HSD) Post Hoc Analysis which identifies group with the statistical significant average difference in microcrack density

Tukey's Honestly Significant Difference (HSD) Post Hoc Analysis

# of groups	*# of comparison*	*df (within treatments)*	*level of confidence, α*	*q critical**	*# of test samples in a group, n*	*MS (Within Treatments)*	*HSD***
3	3	24	0.05	3.532	9	3.81	**2.30**

Comparison	|Δ|	*Statistically Significant Difference? (yes, if the difference is larger than HSD)*
RT vs 400 °C	1.2	The average difference is not statistically significant
RT vs 700 °C	***7.2***	**The average difference is statistically significant**
400°C vs 700°C	***6.0***	**The average difference is statistically significant**

*q = critical value of Studentized range distribution (based on df = 24 and number of groups = 3)

**$HSD = q\sqrt{\frac{MS_{within}}{n}} = 3.532\sqrt{\frac{3.81}{9}} = 2.30$;

4.2.1 Interfacial Tensile Strength Characterization using the Butt Joint Test

The modified butt-joint test applied a tensile load onto a fully martensitic boron steel with a developed Al-Fe-Si intermetallic coating to induce the coating delamination under pure tension. All test specimens failed at the interface where the Al-Fe-Si intermetallic coating was situated rather than the interface between the two grit-blasted surfaces. Five out of six test specimens reported an interfacial failure with small fragments of delaminated intermetallic coating around the perimeter of the sheet sample (Figure 4.16 and Figure 4.17). Under pure tension, the coating did not delaminate, so the tensile strength presented in this study represented the interfacial tensile strength between the developed coating and the adhesive. The average tensile strength was 23.9 ± 3.6 MPa (Table 4.16). One test specimen (BJT05) had a mixture of cohesive and interfacial failure with a reported tensile strength of 29.1 MPa. With a cohesive fracture, the tensile strength represented the adhesive joint tensile strength rather than the strength of the interface, so the strength was not included in the calculation of the average interfacial tensile strength.

Table 4.16: Interfacial tensile strength and bond line thickness of butt joint samples (four thickness measurements taken per test specimen)

In-Die Quenching Condition	RT					
Sample ID	**BJT01**	**BJT02**	**BJT03**	**BJT04**	**BJT05**	**BJT06**
Interfacial Tensile Strength [MPa]	26.3	19.6	27.9	20.7	29.1	25.0
	Bond Line Thickness [mm]					
Average [mm]	0.31	0.29	0.33	0.30	0.30	0.29
Std. Deviation [mm]	0.02	0.04	0.05	0.02	0.05	0.03
Coeff. Variance %	5.6	12.7	14.2	5.5	15.6	9.9

The bond line thickness had an average of 0.30 ± 0.02 mm with a target thickness of 0.178 mm (Table 4.16). The reported bond line thickness was an average value measured at four quadrants of each test specimen. The relatively small coefficient of variance in thickness showed that the sheet sample was relatively flat with respect to the adherends and that the test specimen assembly methodology was repeatable.

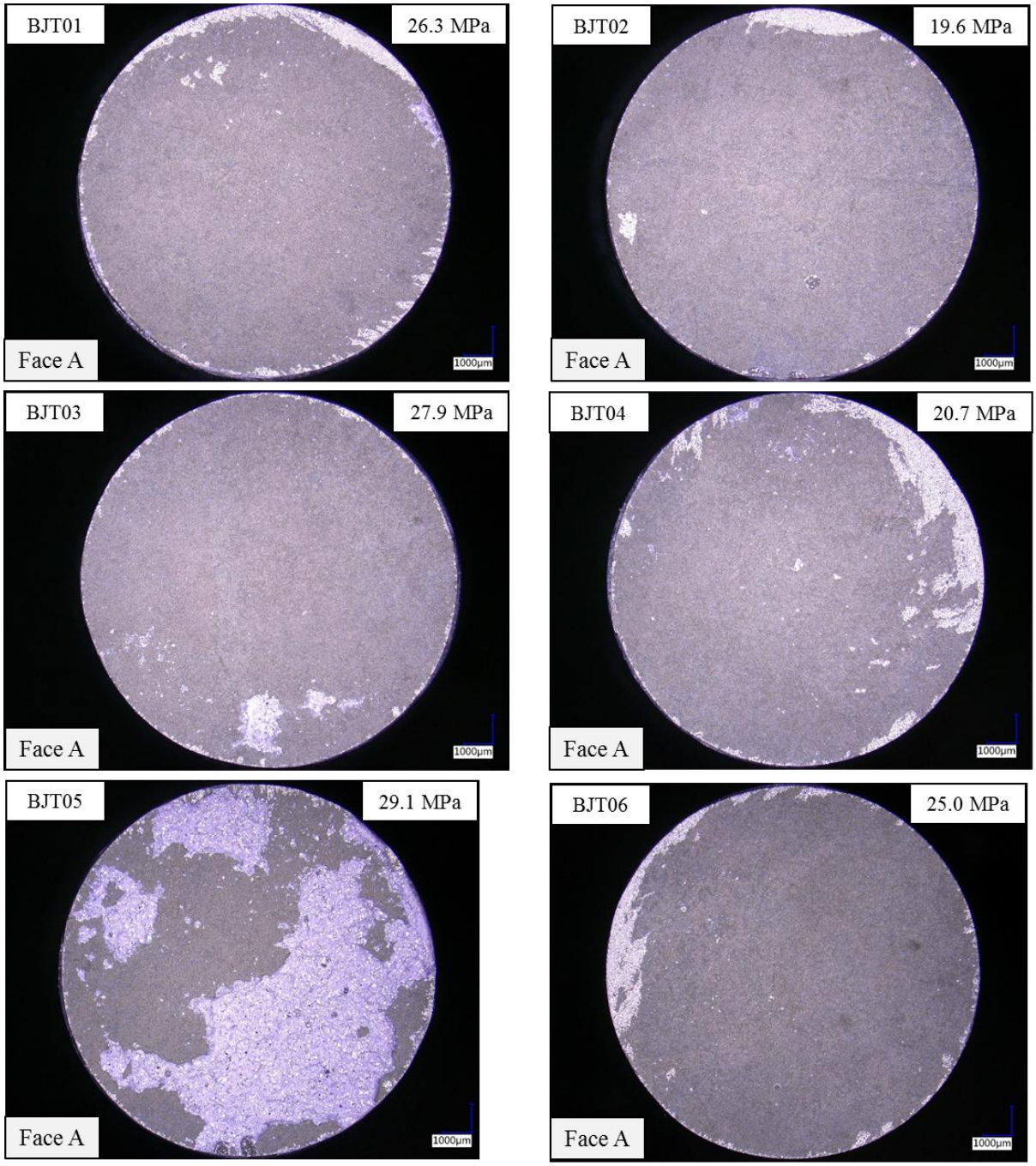

Figure 4.16: Top view of fracture surfaces of the butt joint test specimens with partial intermetallic coating failure (x 20 magnification)

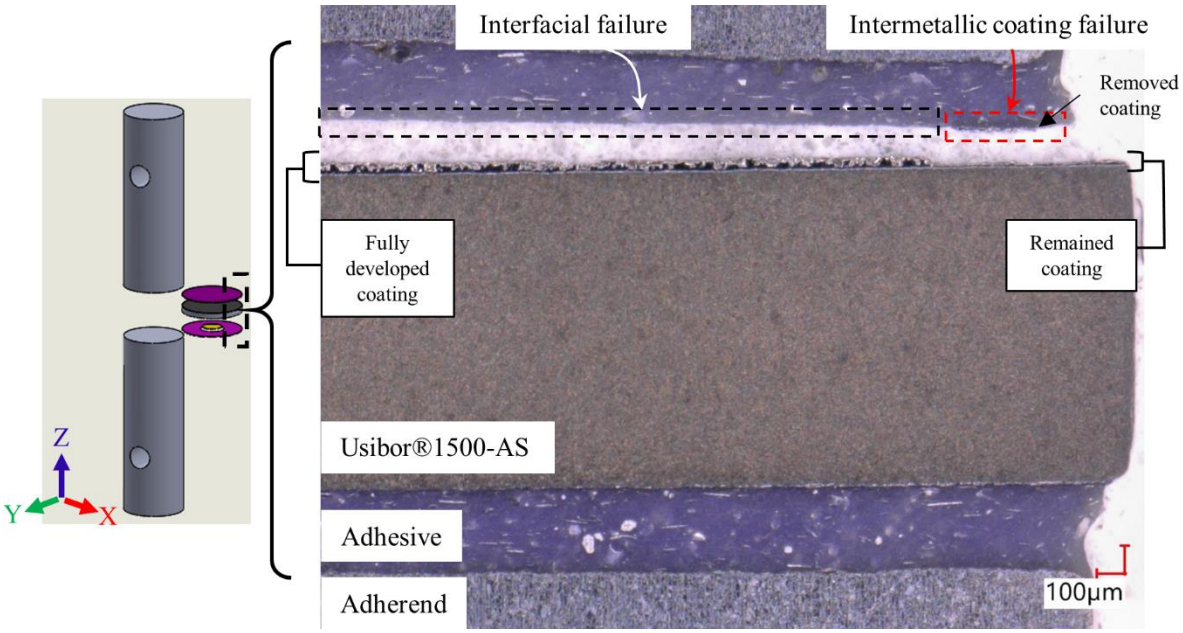

Figure 4.17: : Cross-section of the modified butt joint sample with predominant interfacial failure and small intermetallic coating failure observed only at the perimeter (at 140x magnification)

4.2.2 Investigating Coating Failure Mechanism in Single-Lap Shear Test

The single-lap shear test results reported in this section were from the surface treatment study (RT-ACE from Section 4.1.1). The intermetallic coating delamination occurred at a shear strength as low as 13 MPa, and as high as 27 MPa. The average shear strength was 22.1 ± 5.7 MPa. All five specimens presented intermetallic coating failure in various forms (Figure 4.18).

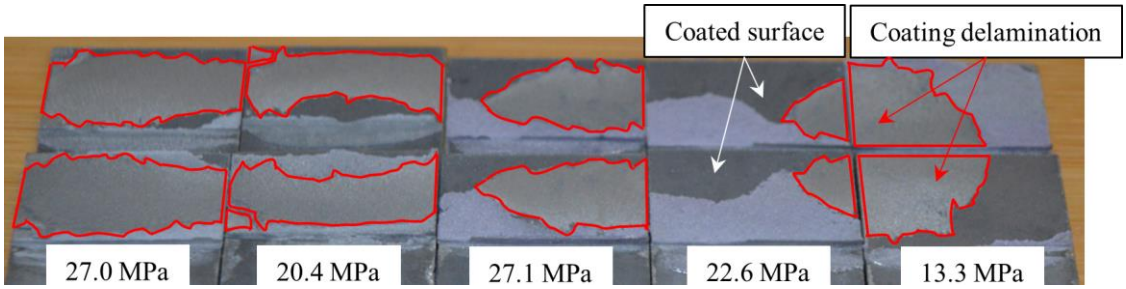

Figure 4.18: Fracture surfaces of single-lap shear samples with intermetallic coating delamination circled in red

Analysis of the fracture surface of a delaminated SLS, using an opto-digital microscope, illustrated the extent of the coating delamination within the intermetallic layer and was used to identify the origin of the coating delamination. Since the butt joint test specimens showed primarily interfacial failure, the single-lap

shear test was the focus of the investigation of the failure mechanism of the intermetallic coating. The optical digital microscopy (ODM) fractographs revealed one side of the test specimen with delaminated coating attached to the adhesive (Figure 4.19a) and the opposite side of the identical test specimen showing the adherend with the remaining intermetallic coating (Figure 4.19b). The Al-Si-Fe intermetallic coating did not delaminate completely from the base metal in the through-thickness direction. The structural adhesive removed part of the intermetallic coating. A thin layer of the coating remained above the base metal (Figure 4.19b).

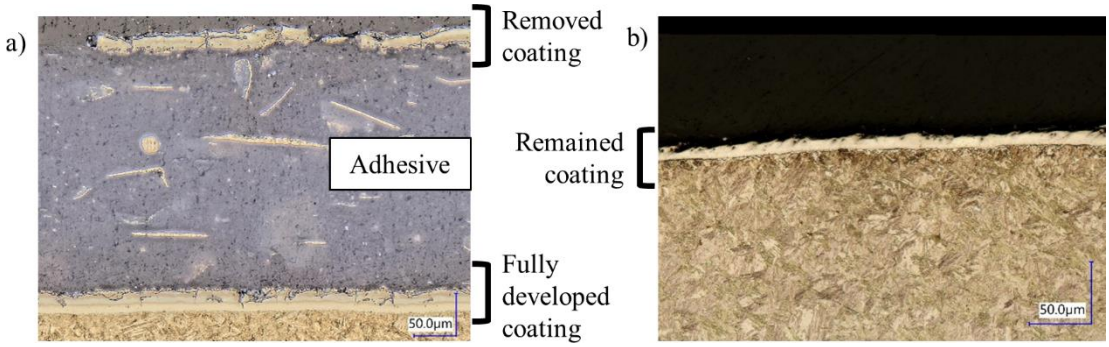

Figure 4.19: Cross-section of the single lap shear sample with intermetallic coating failure (at 500x magnification): a) the coating removed b) the coated boron steel with remained coating

The average thickness of the intermetallic coating removed was 17 µm, with a range of 13 µm to 20 µm (Figure 4.20b). The average thickness of the remaining coating was 10 µm, with a range of 8 µm to 12 µm (Figure 4.20c). By combining the average of the removed and the remaining coating thickness, the average thickness was 27 µm, which fell approximately in the range of the average intermetallic coating thickness of 24 µm (with a range of 21 and 28 µm) demonstrating that little, if any of the coating material was lost during the fracture event. This confirms that the polishing stage of sample preparation for the micrograph did not remove additional coating that would have affected the interpretation of the coating delamination mechanism. Upon inspecting the removed coating and the remaining coating, all microcracks were found in the removed coating, but none in the remaining coating. There were a few Kirkendall voids found near the top layer of the remaining coating.

a)

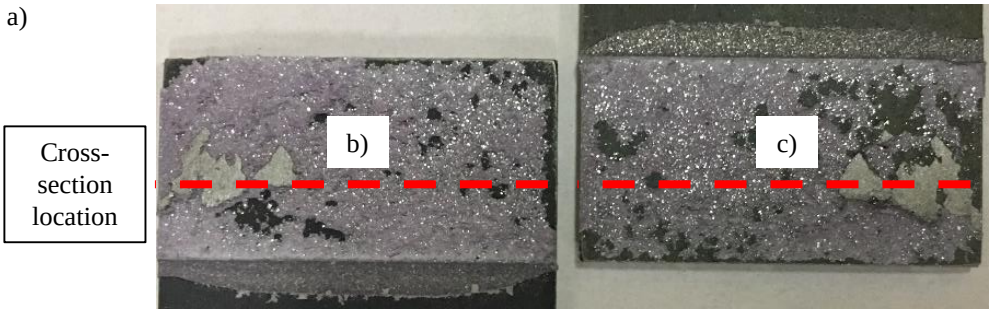

b)

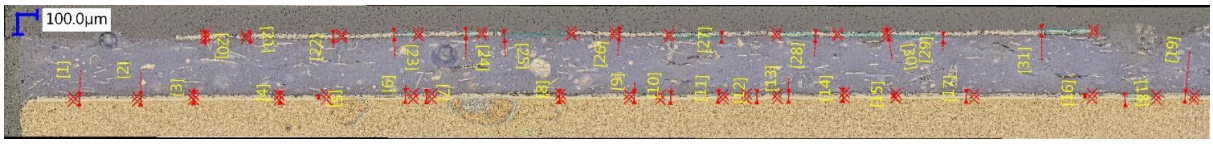

Layer	Total intermetallic coating thickness	Thickness of coating removed	Thickness of coating remained
Average Thickness [µm]	24	17	n.a.
Thickness Range [µm]	21 to 28	13 to 20	
n	19	12	

c)

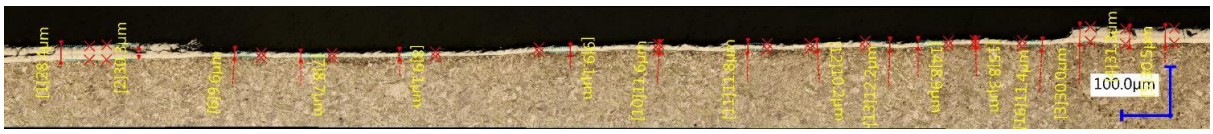

Layer	Total intermetallic coating thickness	Thickness of coating removed	Thickness of coating remained
Average Thickness [µm]	30	n.a.	10
Thickness Range [µm]	28 to 31		8 to 12
n	5		11

Figure 4.20: a) Macroscopic fractured surface of single-lap shear with coating failure b) cross-section of Al-Fe-Si coating removed thickness (500x) c) cross-section of remaining Al-Fe-Si coating thickness (500x)

4.3 Effect of Hot Stamped Deformation on Formed Surface and Effect of Formed Surface on Joint Strength

SLS test specimens were cut from the flanges, walls and top of hot formed hat channel sections to investigate the effect of forming and the resulting metal surface on adhesive joint strength. The adherends were degreased using methyl ethyl ketone (MEK) before the specimen preparation. Among the three sections of the hat channel, the side wall test specimens presented the lowest average shear strength of 21.7 ± 1.8 MPa and the top section test specimens had the highest average shear strength of 26.1 ± 2.1 MPa (Table 4.17) (Figure 4.21). However, a one-way ANOVA analysis concluded that there was no statistically significant difference in shear strength among the three sections of the hat channel (p= .061) (Table 4.18).

Table 4.17: Shear strength (τ_{max}) summary using the single-lap shear test

Hat Channel Section	Side Wall	Flange	Top
Test 1 [MPa]	23.0	23.6	28.7
Test 2 [MPa]	22.3	20.0	26.0
Test 3 [MPa]	19.7	26.2	27.3
Test 4 [MPa]	-	25.1	25.6
Test 5 [MPa]	-	26.3	23.1
Average [MPa]	21.7	24.2	26.1
Standard Deviation [MPa]	1.8	2.6	2.1
Coeff. Variance [%]	8.1	10.7	7.9

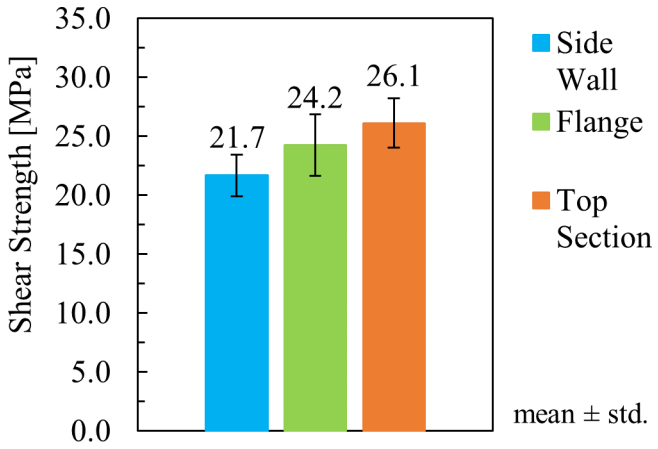

Figure 4.21: Average shear strength of single-lap shear test from three sections of the hat channel (side wall, flange, and top section)

Table 4.18:One-way ANOVA performed on shear strength obtained using three different sections of a hat channel (side wall, flange, and top section), which found no statistical significant difference in shear strength among the three groups (*p*-value = .061; α=0.05)

One-way ANOVA for Determining Hot Formed Surface Finish Effect on Shear Strength

Sections of Hat Channel	*# of test samples in the group*	*Sum*	*Average Shear Strength* [MPa]	*Variance*
Side Wall	3	65.01	21.7	3.07
Flange	5	121.1	24.2	6.77
Top Section	5	130.7	26.1	4.26

Source of Variation	*SS*	*df*	*MS*	*F*-value	*p*-value	*F crit*
Between Sections	37.69	2	18.85	3.748	**0.061**	4.103
Within Sections	50.28	10	5.028			
Total	87.98	12				

The fracture surfaces of the test specimens revealed interfacial failure for the side wall test specimens (Figure 4.22a), which reflected the lowest average shear strength out of the three sections. The flange and top sections test specimens had a mix of cohesive failure and intermetallic coating failure (Figure 4.22b and Figure 4.22c).

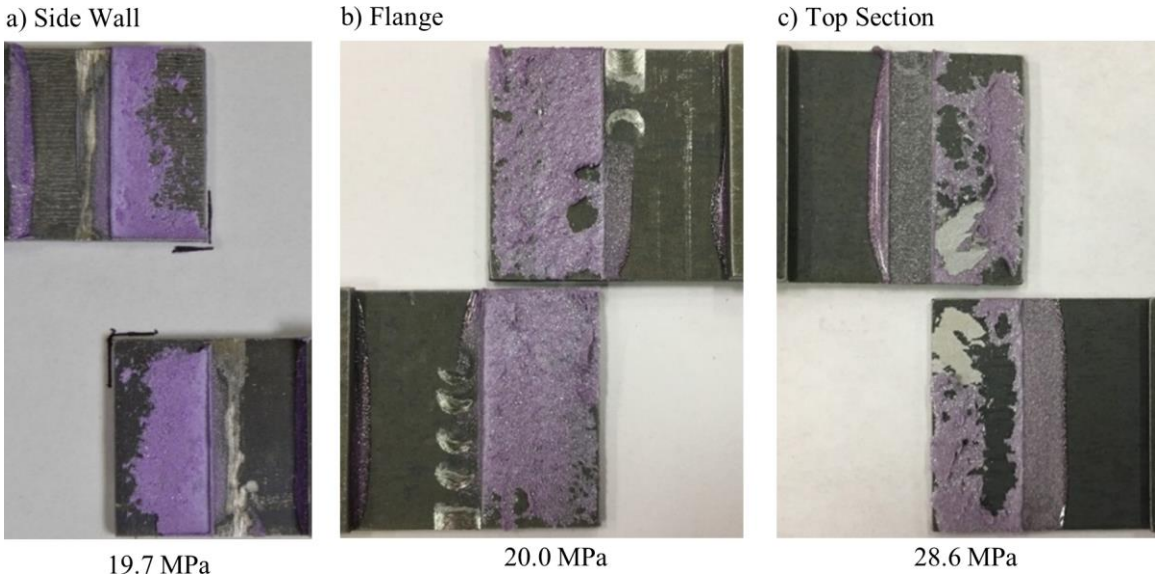

Figure 4.22: Representative adhesive fracture surfaces of single-lap shear tests from three locations on a hat channel, with corresponding shear strength

To better understand the effect of hot forming on the intermetallic coating, the three sections of a hat channel were cut and hot mounted in resin to observe the intermetallic coating morphology (Figure 4.23). Surface porosity and Kirkendall voids were present in all three sections. Microcracks were observed in the flange and top section, but for the side wall, the large microcracks were also observed within the intermetallic coating.

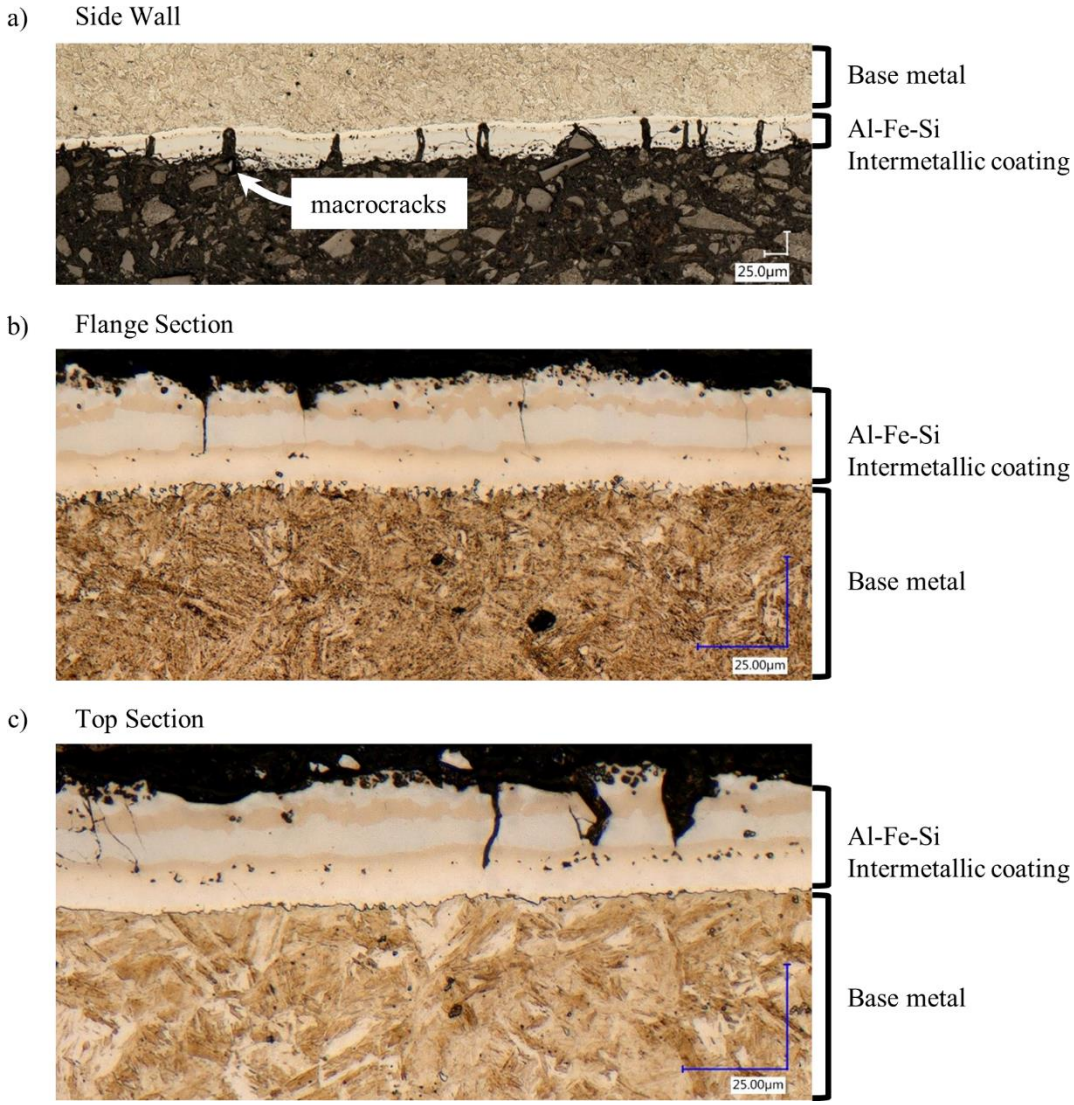

Figure 4.23: Al-Fe-Si coating developed in a 1.8 mm thick hat channel: a) side wall, b) flange, and c) top section

4.4 Adhesive Joint Fracture Morphology

This section explores the adhesive fracture morphology under four modes of fracture: Mode I (RDCB), Mode II (BDS), Mixed-Mode loaded at 45° (MM45), and Mixed-Mode using the single-lap shear test (SLS). The surface roughness from the three unique modes of loading (RDCB, BDS, and MM45) served to interpret the fracture surface of SLS. Fracture features, overall fracture morphology and specified surface roughness parameter, arithmetic mean roughness, Ra from unique mode of loading are analyzed to interpret a more complex loading in SLS specimen.

The RDCB, BDS, and MM45 were made from cold-rolled steel adherends and the single-lap shear specimen used fully martensitic boron steel as adherends. All specimens received grit-blast treatment and degreased using acetone before the adhesive application. The visual observations at 200 times magnification unveiled the unique fracture surface features of adhesives. The topographical data generated by an optical digital microscope (ODM) provided quantitative two-dimensional fracture profiles, which highlighted the unique features from each of the four modes of loading. The surface roughness parameter, arithmetic mean roughness (Ra), is calculated using the topographic data of the fracture surfaces to quantify the adhesive fracture under a particular mode of loading.

4.4.1 Fractographic Analysis

Top View of Fracture Surfaces

The fracture surfaces of RDCB test specimens (Mode I) demonstrated cohesive failure (Figure 4.24a), while BDS specimens (Mode II) resulted in a mix of cohesive and interfacial failure (Figure 4.24b). MM45 and SLS specimens had a predominantly cohesive failure with a small region of interfacial failure (Figure 4.24c and Figure 4.24d). Small pores were in all the bonded samples with a diameter of less than 0.25 mm, but in low quantity (Figure 4.25). The interfacial failure had an opaque and matt surface finish in which the aluminum particles were covered by a thin layer of purple resin (Figure 4.26). The aluminum particles are generally added as fillers in the adhesive formulation to dissipate heat and aid electrical conductivity in the adhesive (Kim *et al.*, 2011). Aluminum particles faces that lay flat relative to the incident source from the microscope appeared as a bright spot on the fracture surface and the oblique particles deflected the incident light and are perceived as the dark spots.

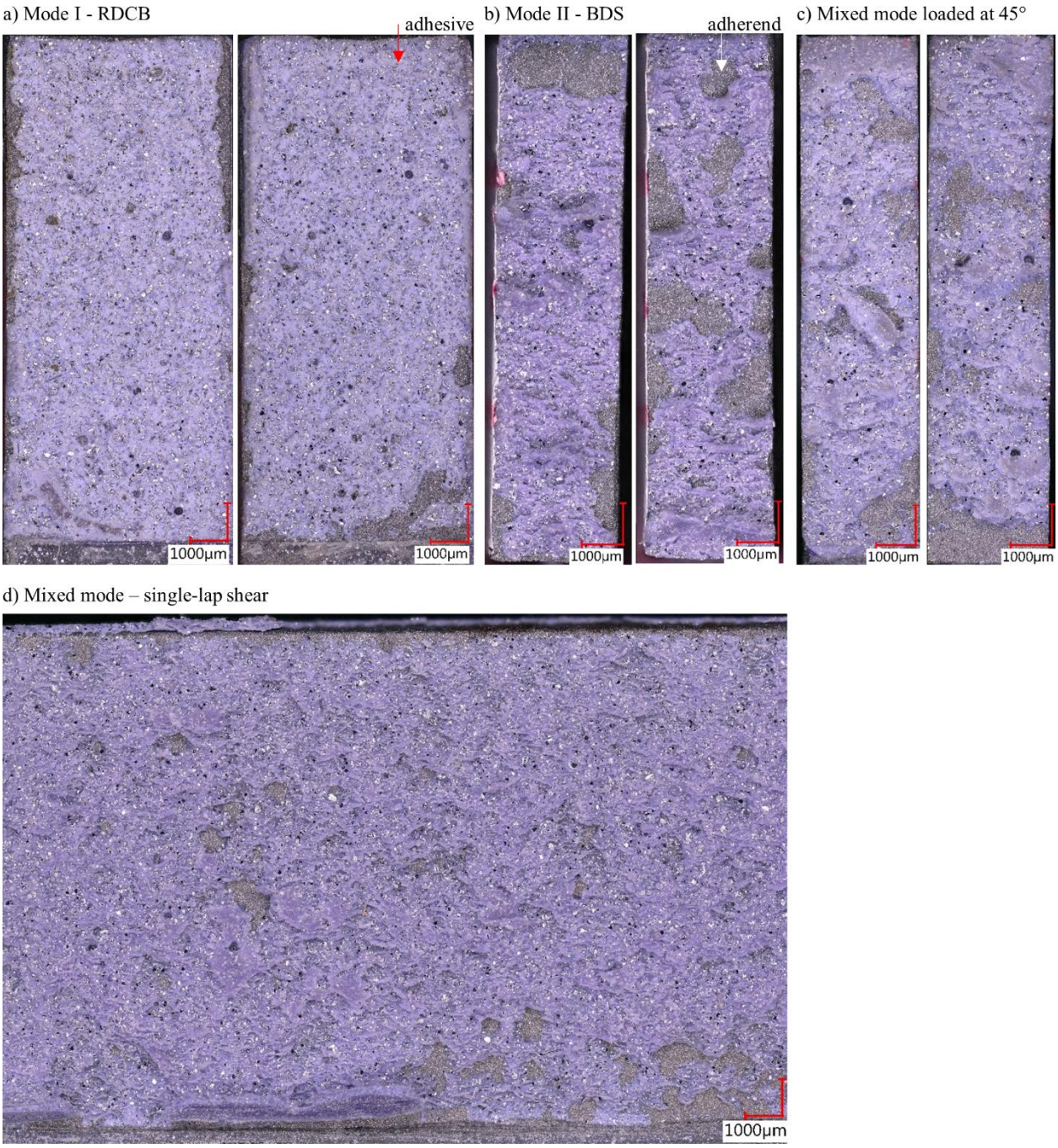

Figure 4.24: Adhesive joint fracture surfaces under four different loading conditions (at 200x magnification); a) cohesive failure under Mode I loading (crack propagated from the bottom to the top of the image), b) mix of cohesive failure and interfacial failure under Mode II loading (loading direction was from bottom to top of the image), c) predominantly cohesive failure with interfacial failure under mixed-mode loaded at 45° (loading direction was from top to bottom of the image), and d) cohesive failure under mixed-mode loading using single-lap shear (SLS) configuration (loading direction was from top to bottom of the image)

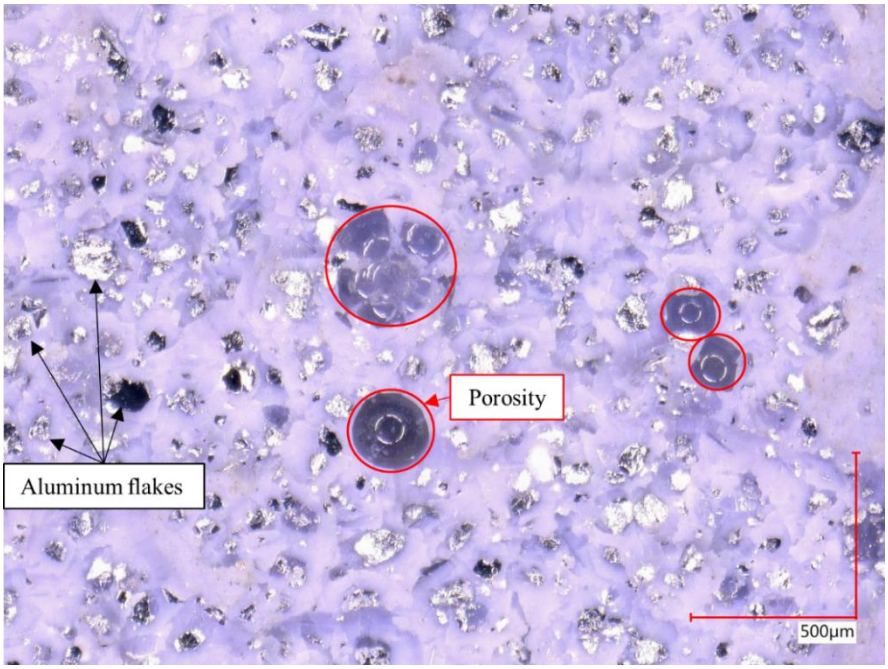

Figure 4.25: Top view of a fractured surface of adhesive under Mode I showing the aluminum particles as fillers in adhesive formulation and porosity

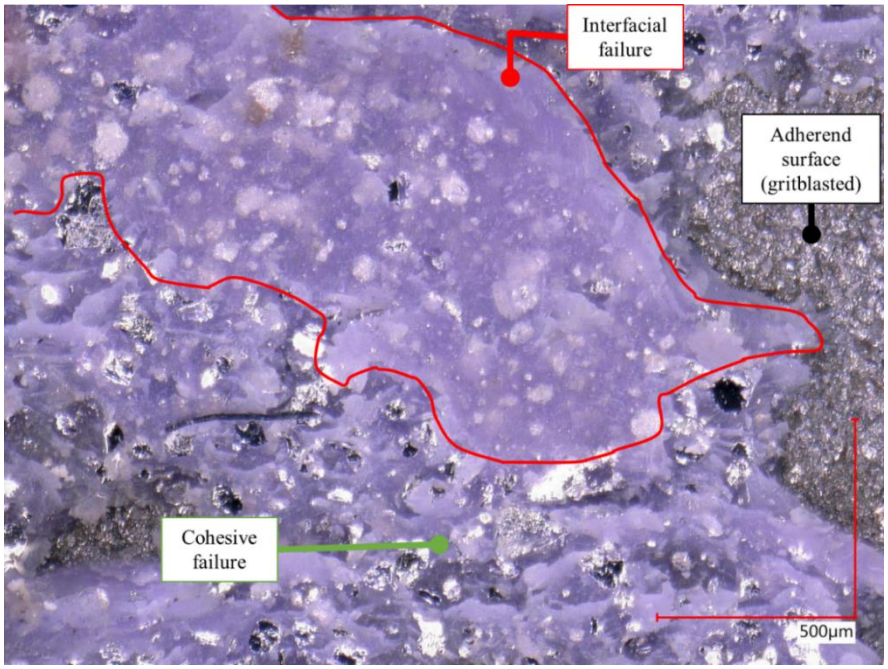

Figure 4.26: Top view of a fractured surface of adhesive under Mode II showing a mixed of cohesive and interfacial failure in a bonded structure

Cohesive failure of each mode of loading presented distinct morphological differences in the fracture. RDCB presented Mode I opening fracture in the form of short fracture edges oriented in all directions (Figure 4.27a). Mode I opening had a “smooth” fracture surface texture compared to shear loading (Mode II), Mixed-Mode loaded at 45°, and single-lap shear that all presented “rough” surface texture. The cohesive failure under Mode II showed crack edges developed across the width of the bond line, which were normal to the loading direction (Figure 4.27b). The length of the crack edges varied on the Mode II failure surface, and they are generally longer crack edges than RDB fracture surfaces. A cluster of the crack edges generated multiple crack fronts with the edges oriented toward the general loading direction of the mechanical test. The combination of the mentioned features resulted in the overall rough impression of the surface texture under shear loading. The crack edges formed under Mixed-Mode loaded at 45° (MM45) were developed in the normal direction to the loading direction, but the cracks have larger fracture facets, which reflected a smoother surface compared to Mode II fracture, but rougher than Mode I fracture (Figure 4.27c). Finally, single-lap shear fracture showed predominant Mode II fracture features of crack edges of all sizes formed in perpendicular to the loading directions (Figure 4.28). Finally, under Mode II, MM45 and the single-lap shear fracture surfaces all provided information related to the loading direction based on the edges of the cracks.

a) Mode I – Rigid Double Cantilever Beam (Sample I.D. R01)

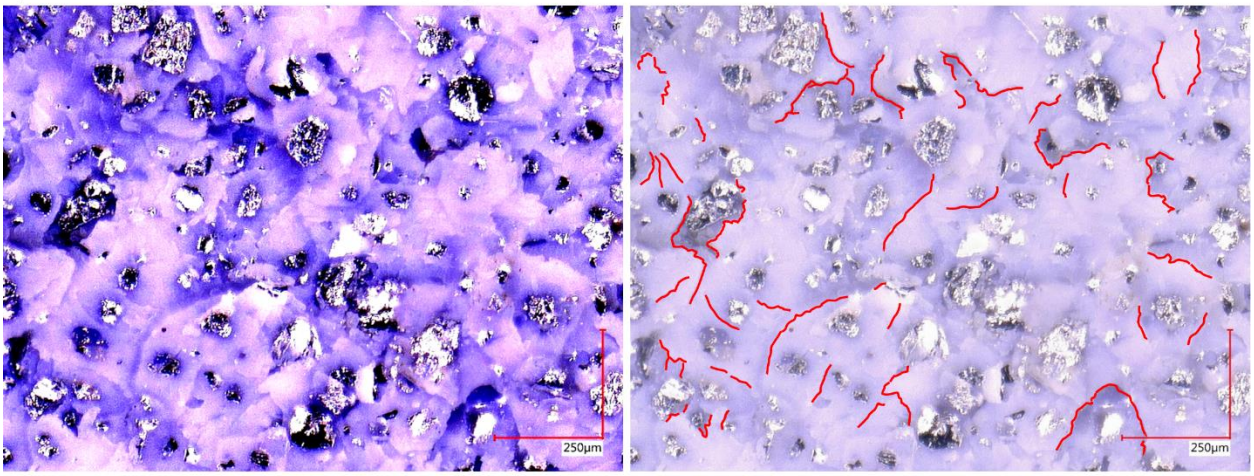

b) Mode II – Bonded Shear (Sample I.D. BDS-11 ; loading direction is bottom to top)

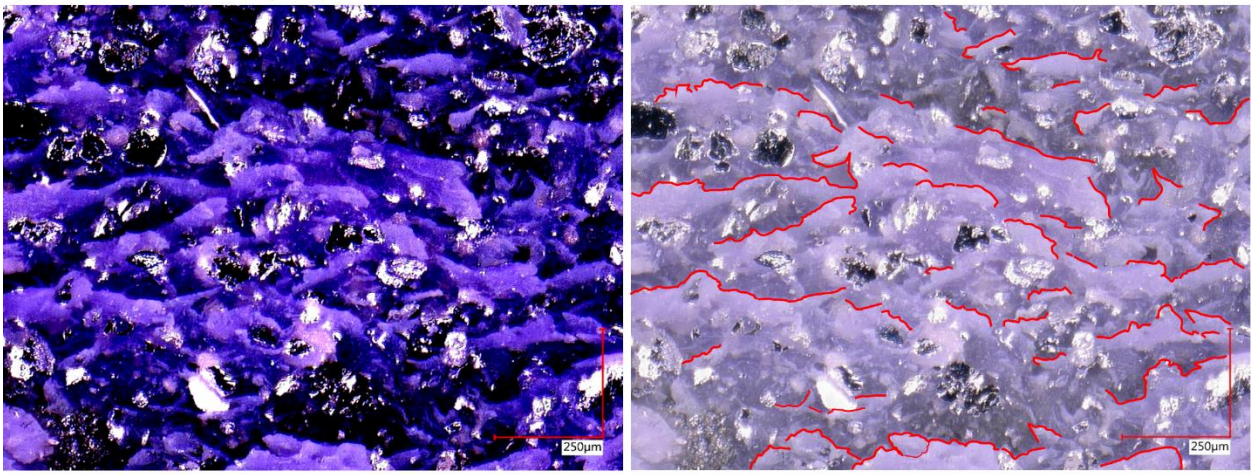

c) Mixed mode at 45° – MM45 (Sample I.D. MM45-01 ; loading direction is top to bottom)

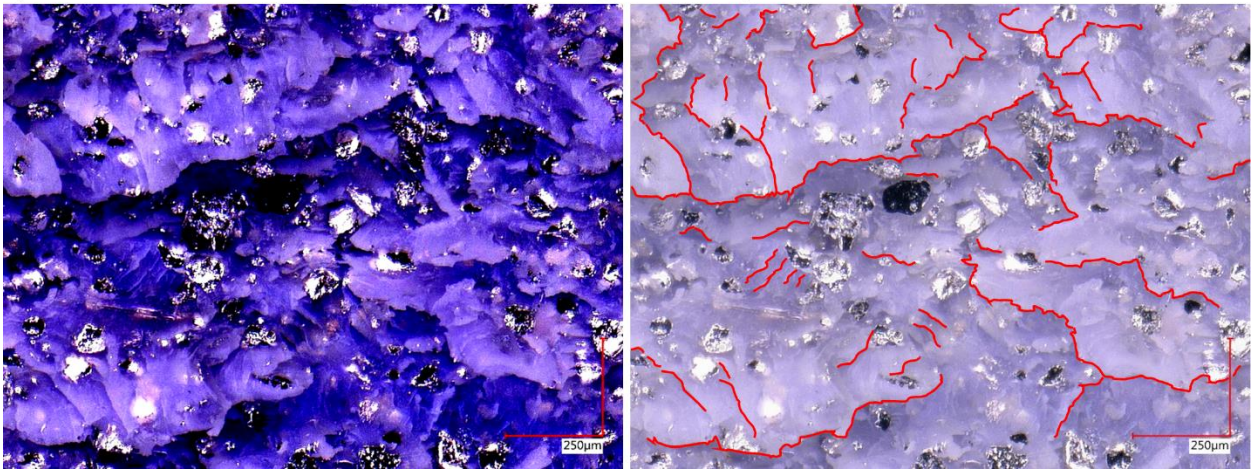

Figure 4.27: Magnified view of cohesive failure region under a) Mode I opening, b) Mode II shear, and c) Mixed mode loading at 45°; on the left are distinct crack edges of the peaks and depths of the valleys and on the right are the crack edges indicated by the red lines (figures on the left were post-processed with decreased brightness (-80) and increased contrast (+90); unprocessed images on the right)

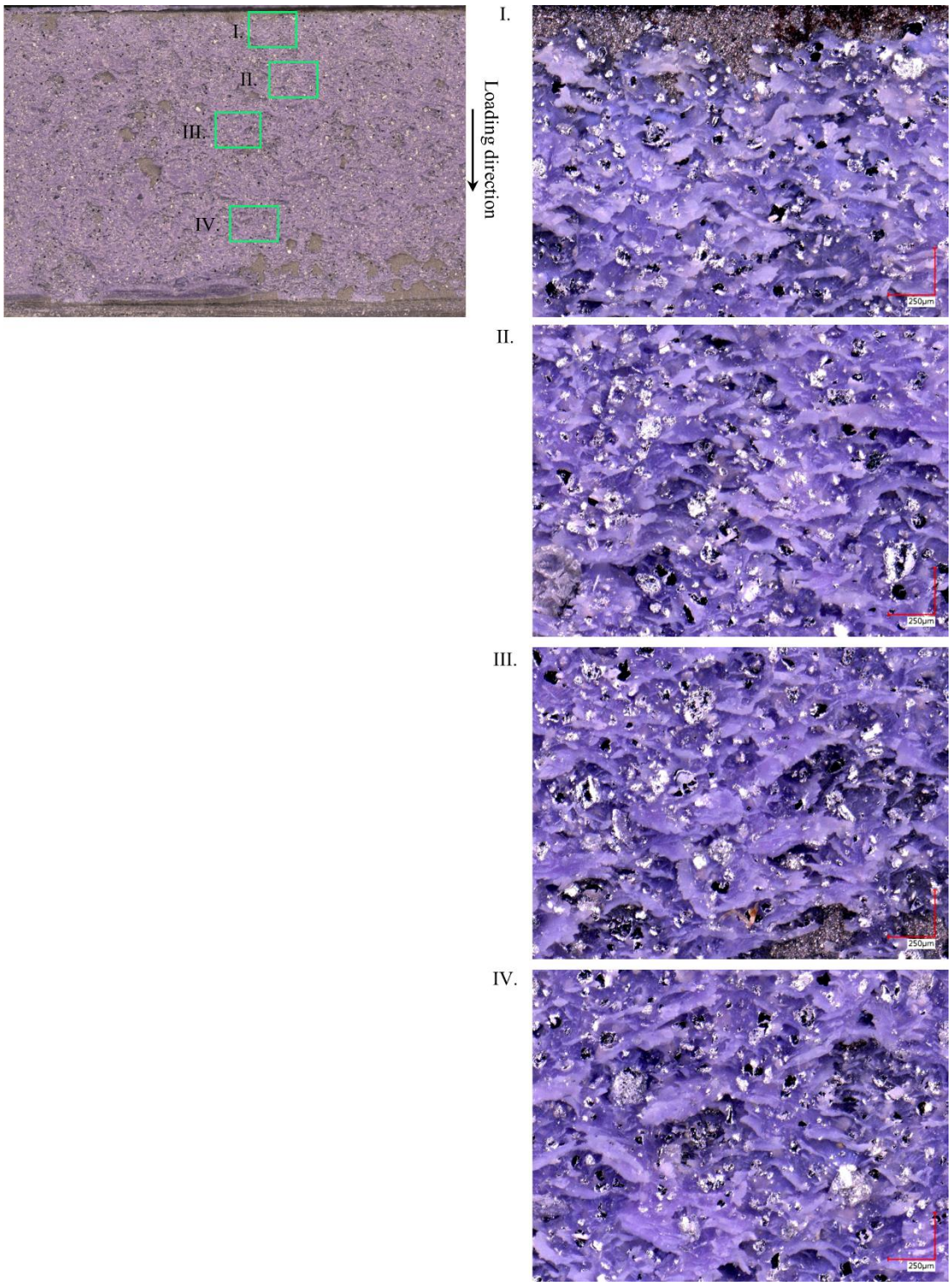

Figure 4.28: Magnified view of cohesive failure regions on single-lap shear specimen demonstrating Mode II shear fracture morphology similar to the features observed in BDS specimens throughout the SLS bond area

3D Fracture Surface Morphology

Three-dimensional (3D) contour plots were generated using the topographic data of the fracture surface measured using an optical digital microscope. Mode I opening fracture surfaces exhibited island-like features that were grouped closely with a more gradual transition of peaks and valleys across the bond area (Figure 4.29) compared to Mode II shear fracture surfaces (Figure 4.30). The fracture surfaces of BDS and MM45 test specimens exhibited sharp saw-tooth features of different heights formed across the bond area and oriented normal to the loading direction. The fracture of BDS sample showed stretched and wide fracture peaks along the width of the adherend and frequently appeared in the loading direction (Figure 4.30) and while MM45 samples had less pronounced (lower) peaks covering a larger area of the fracture surface (Figure 4.31). The fracture surface of all bonded samples presented irregularly developed peaks and valleys. The fracture surface of SLS showed asymmetric fracture surface in the width direction (left to right) (Figure 4.32). The asymmetric result could be due to microcracks formed and grew at one left side of the sample near the surface of the adherends and propagated toward the midplane of the adhesive (toward the right side of the fracture surface).

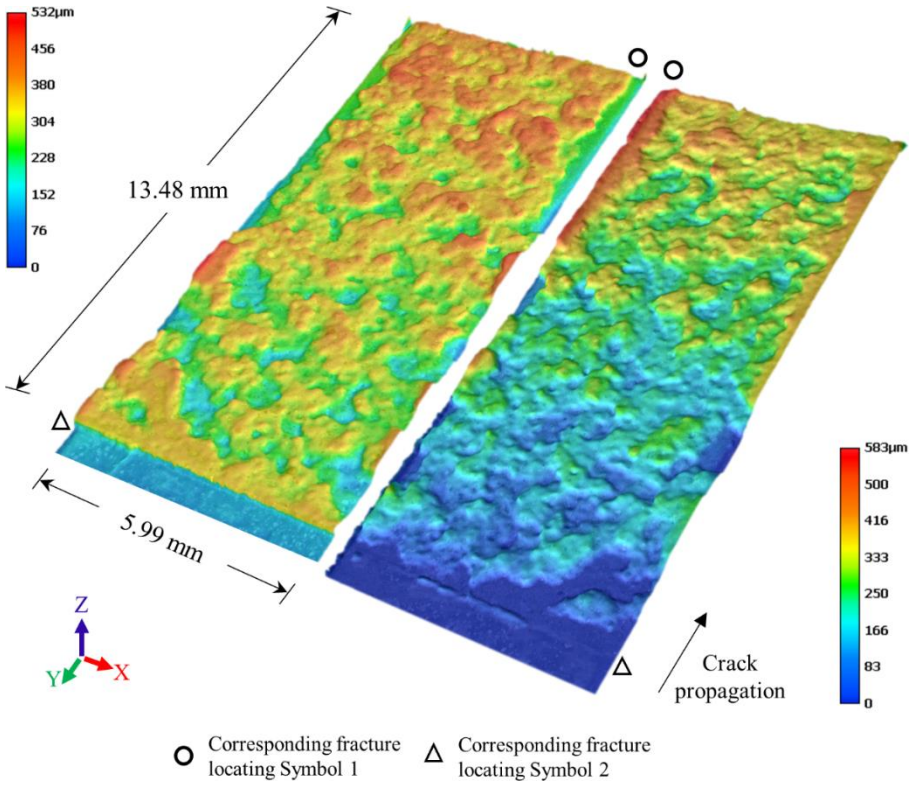

Figure 4.29: 3D fracture morphology of a rigid double cantilever beam test specimen (Mode I) (200x magnification)

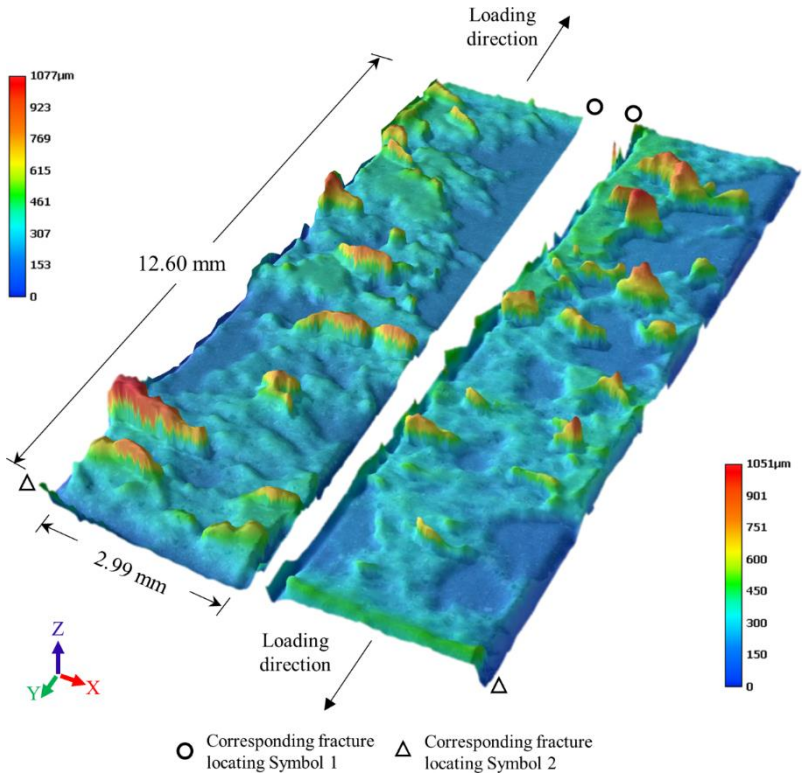

Figure 4.30: 3D fracture morphology of a bonded shear test specimen (Mode II) (200x magnification)

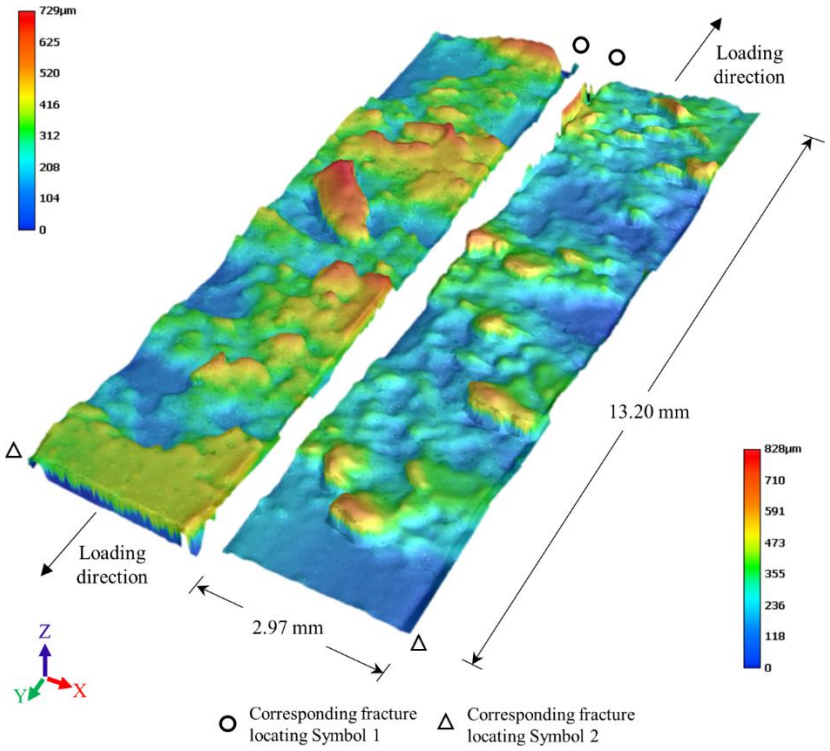

Figure 4.31: 3D fracture morphology of a mixed-mode test specimen loaded at 45° (200x magnification)

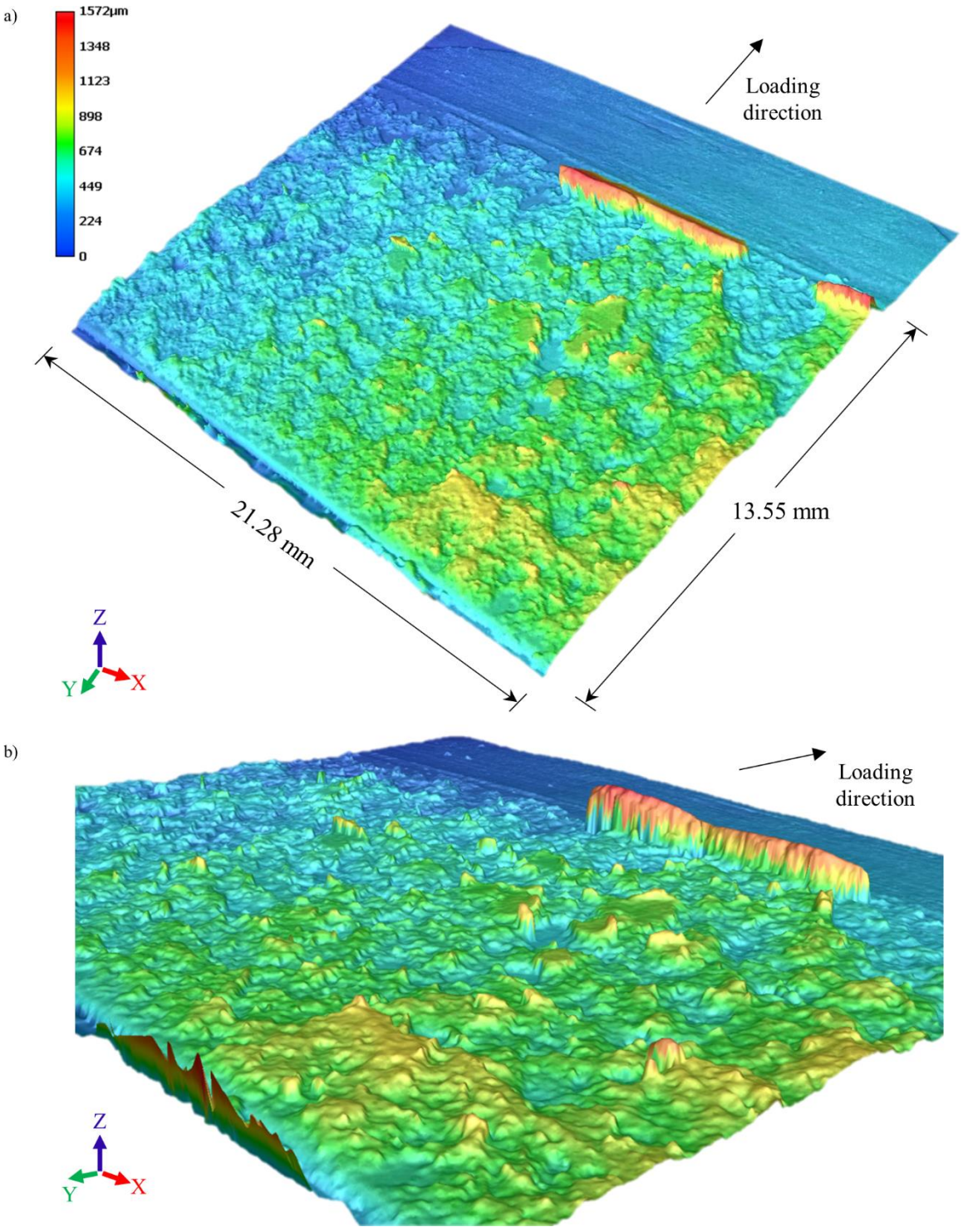

Figure 4.32: 3D fracture morphology of a single-lap shear test specimen: a) isometric view b) close up view of the identical fracture surface with peaks and valleys (200x magnification)

4.4.2 Fracture Profile and Arithmetic Mean Surface Roughness

Two-dimensional (2D) profiles of the adhesive joint fracture surfaces were collected from the topographic data to identify the distinct features of each mode of loading (Figure 4.33). The 2D fracture profiles highlighted the differences among the four distinct loading conditions and used to calculate the arithmetic mean roughness, Ra, to capture the fracture surface quantitatively.

The Mode I fracture surface from the RDCB test exhibited fracture profiles with smaller vertical distance between the local peaks and valleys compared to Mode II and mixed-mode fracture profiles. The Mode I fracture profiles presented a gradual transition of local peak-to-peak over the sampling length (Figure 4.33a). The Mode II shear fracture profiles differed from Mode I opening with a distinct sharp peak, as illustrated in the three-dimensional fracture surfaces in the previous section. The fracture profile had a sequence of the sharp peaks followed by shallow valleys and a gradual transition of shorter peaks over the sampling length. In general, the sharp peak spanned over a short sampling length, contrasting the fracture profile from Mode I (Figure 4.33b). The fracture surface profile of MM45 was a combination of fracture features from RDCB and BDS (Figure 4.33c). It had a more gradual transition of the peak to the valley over the entire sampling length, a feature shown in RDCB fracture profiles. MM45 fracture profiles also had the fracture profiles with high peaks followed by a gradual descent into the valley, which was a characteristic of BDS fracture. Finally, for the mixed-mode single-lap shear fracture surface (SLS), the fracture profile features showed features from RDCB and BDS as well. The high peaks and gradual valley features were similar to Mode II fracture and the profile continued with low peaks and valleys similar to the features of Mode I fracture (Figure 4.33d).

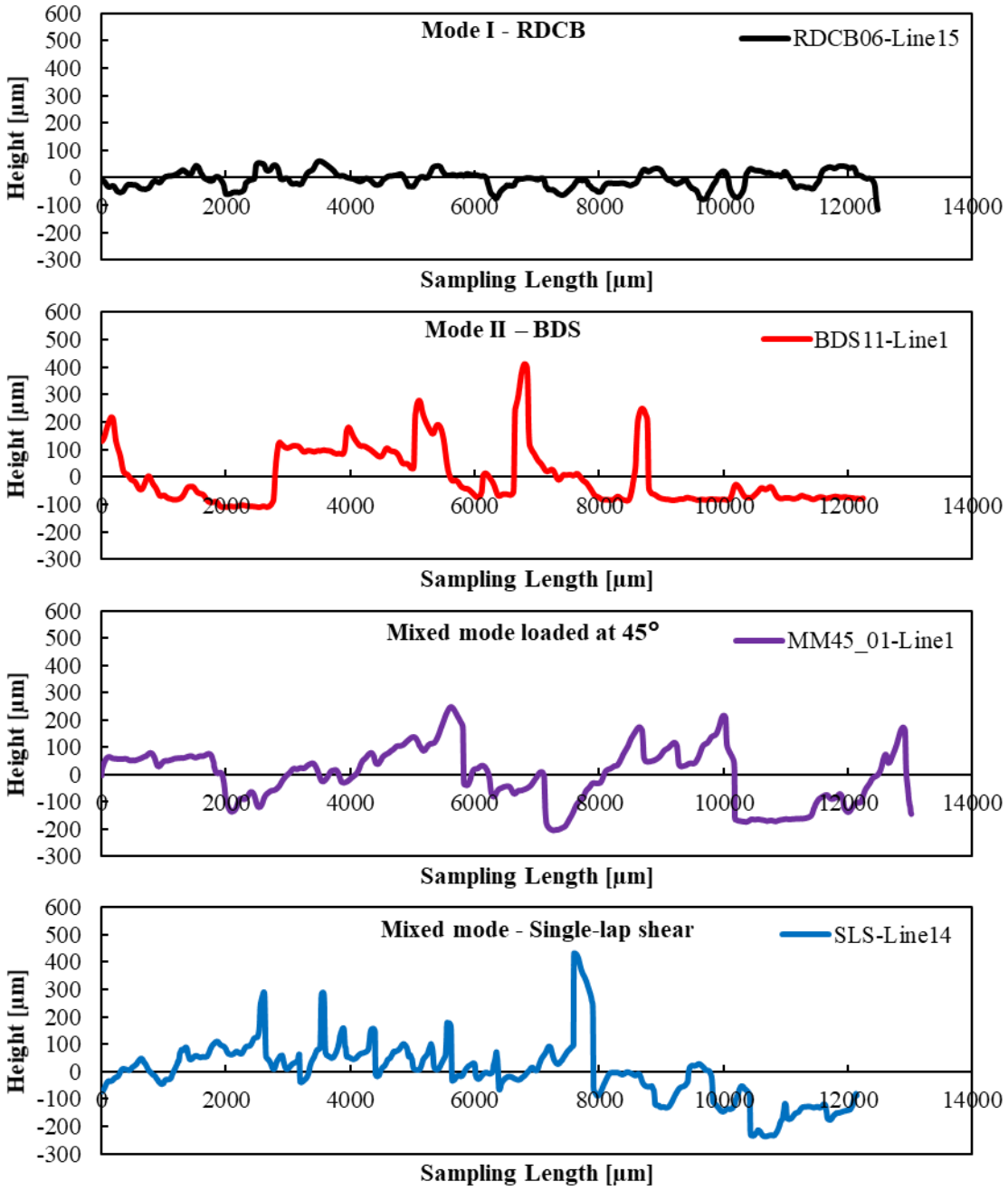

Figure 4.33: Representative fracture profiles of different bonded adhesive samples made of grit-blasted steel adherends with respective Ra roughness: a) RDCB (Mode I), b) BDS (Mode II), c) Mixed-mode at 45°, and d) single-lap shear (SLS)

Each of the four joint configurations listed above generated a minimum of nine fracture profiles to calculate the surface roughness. Fracture surfaces of RDCB were represented with an overall average Ra of 50 µm with a standard deviation (std.) that ranged from 3 µm to 11 µm. As for the Mode II shear fracture using

bonded shear (BDS), the overall average Ra increased to 103 µm with a higher standard deviation ranging between 11 µm and 29 µm compared to Mode I fracture result. The increase in roughness over Mode I fracture may be due to the tall shear hackles found on Mode II fracture surface. The shear hackles of different sizes in height found in the 3-dimensional fracture morphology may have contributed to the variability in roughness.

In the Mixed-Mode joint configurations, the test specimen loaded at 45° (MM45) fracture had a Ra roughness value classified between Mode I and Mode II fracture with an overall average of 80 µm and std. between 7 µm and 16 µm. Finally, the single-lap shear (SLS) that applied Mode I and Mode II to the adhesive presented an average surface roughness of 73 µm with a std. of 8 µm.

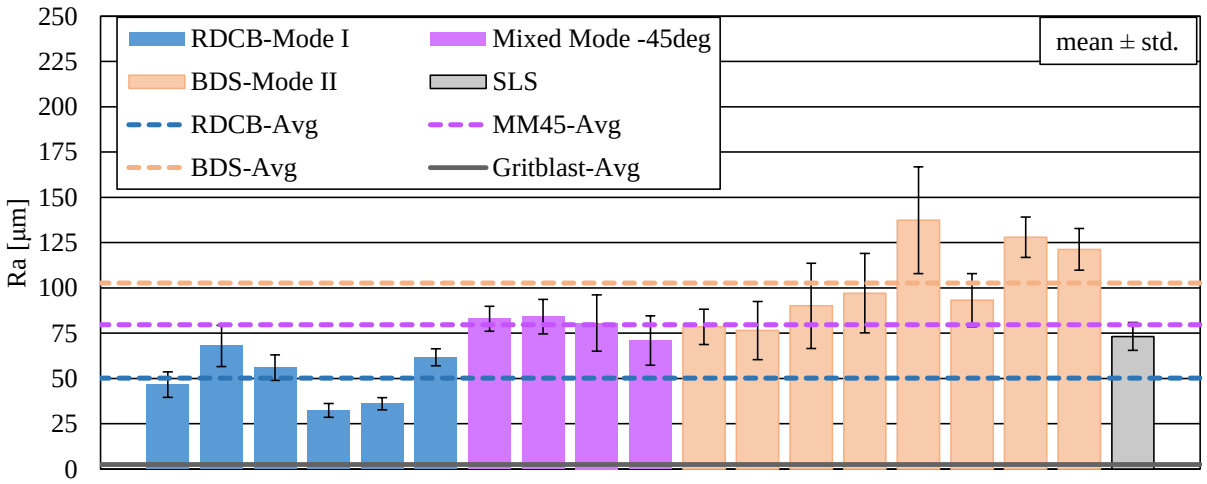

Figure 4.34: Average arithmetic mean roughness (Ra) of the adhesive joint failure surfaces under Mode I, II, Mixed-Mode at 45°, and single-lap shear (SLS)

In the bonded shear (BDS) test specimens, the fracture surfaces presented a mixture of interfacial and cohesive failure. The interfacial failure regions were noted in the fracture profiles and were used to calculate the Ra value that corresponded to the grit-blasted steel adherend surface (Figure 4.35). The interfacial failure surfaces had an average Ra value of 2.5 µm, which is greatly below the measured roughness of the fractured adhesive under different modes of loading (Mode I, II, Mixed Mode at 45° and SLS).

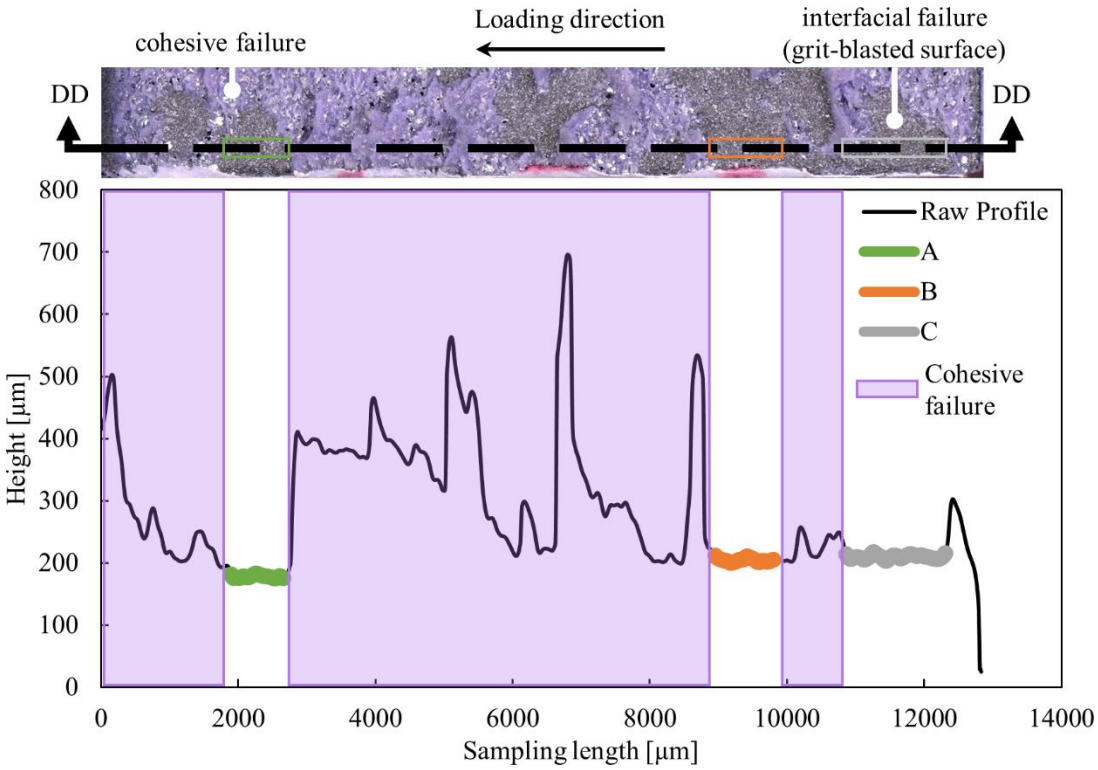

Figure 4.35: Fracture profile in bonded shear (BDS) sample at "DD" cross-section that discerned the regions of cohesive failure and interfacial failure segments with Region A, B, and C highlighted; the regions represent interfacial failure and the profile data were used to calculate arithmetic mean roughness value (Ra = 1.61 µm, 2.39 µm, and 2.44 µm, respectively) (profile presented is from test specimen BDS11-Line 1)

4.4.3 Cross-sectional view of the adhesive joint fracture

An optical digital microscope (ODM) generated the detailed 3-dimensional (3D) adhesive fracture morphology by digitally stitch all of the focused images in a vertical direction at a fine travel interval of 10 µm (Section 4.4.1). The fracture details from the side-view of the adhesive joint were bypassed by ODM as it collected the data from the top view approach. Therefore, the fracture surfaces of the as-tested specimens were sectioned to further examine the local topology of the adhesive fracture (Figure 4.36, Figure 4.37, and Figure 4.38). The opposite halves of the fracture surfaces were approximately repositioned to align the fracture surfaces to recreate the moment of failure of the adhesive material.

Under Mode I loading, the RDCB fracture was relatively shallow with gradual transition between peaks and valleys (Figure 4.36), which was consistent with the fracture profile in Figure 4.33. The cross-section

view of bonded shear test specimens (BDS) exhibited high peaks associated with the shear hackles observed in the representative fracture profiles (Figure 4.33). Similarly, the cross-sectional view of MM45 presented shear hackles, but with a less steep of a fractured adhesive (Figure 4.37). The cross-section of Mode I fracture did not exhibit such feature, but rather gradual peaks and valleys and can be reassembled back to initial adhesive bond without causing additional damage to the fractured adhesive. The tear of the shear hackles oriented toward the loading direction was facilitated by the tensile stress developed in the bond as the microcracks within the adhesive developed (Chai, 1992), which distinguished itself from the crack opening fracture of RDCB. Finally, the adhesive fracture of SLS test also presented shear hackle features that were oriented along the loading direction similar to BDS and also in the transverse direction (Figure 4.39).

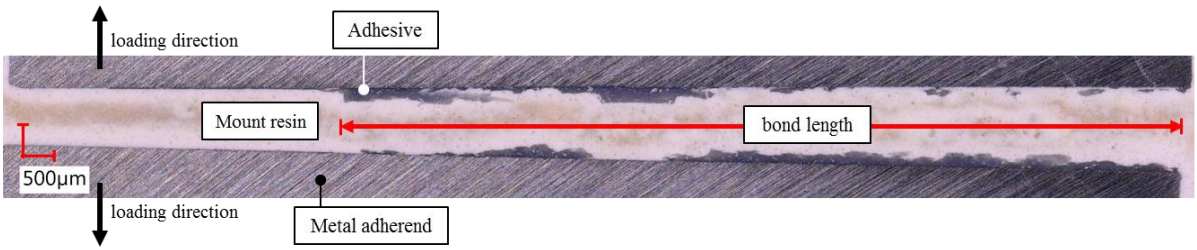

Figure 4.36: Cross-sectional view of a post-test rigid double cantilever beam (RDCB) specimen; the steel adherends repositioned to approximately match fracture patterns that illustrated the cohesive fracture with a gradual change in fracture height under Mode I loading

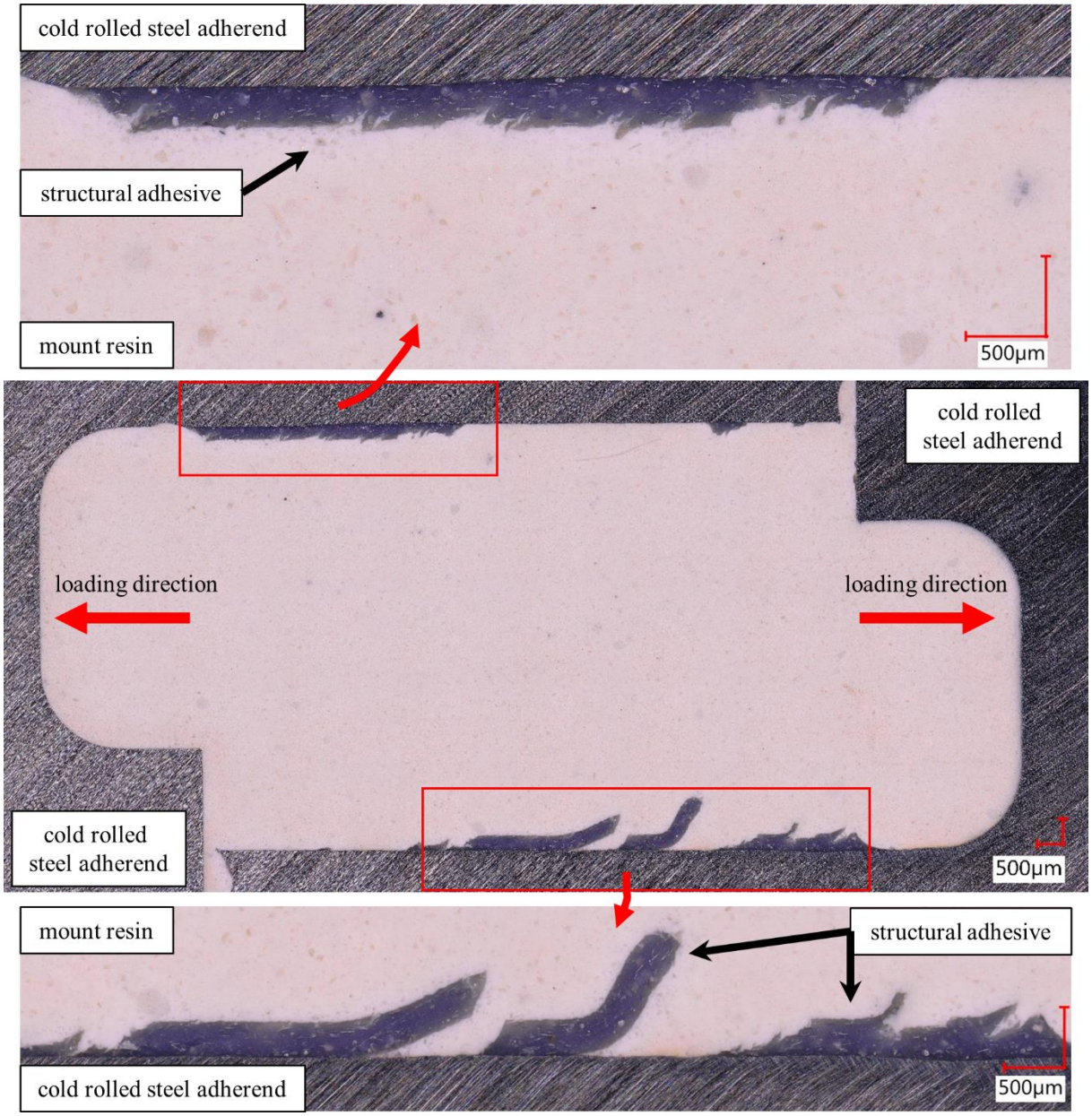

Figure 4.37: Cross-sectional view of a post-test bonded shear (BDS) specimen; adherends repositioned to align the adhesive fracture surfaces and illustrated the curvature of a failed structural adhesive with shear hackles

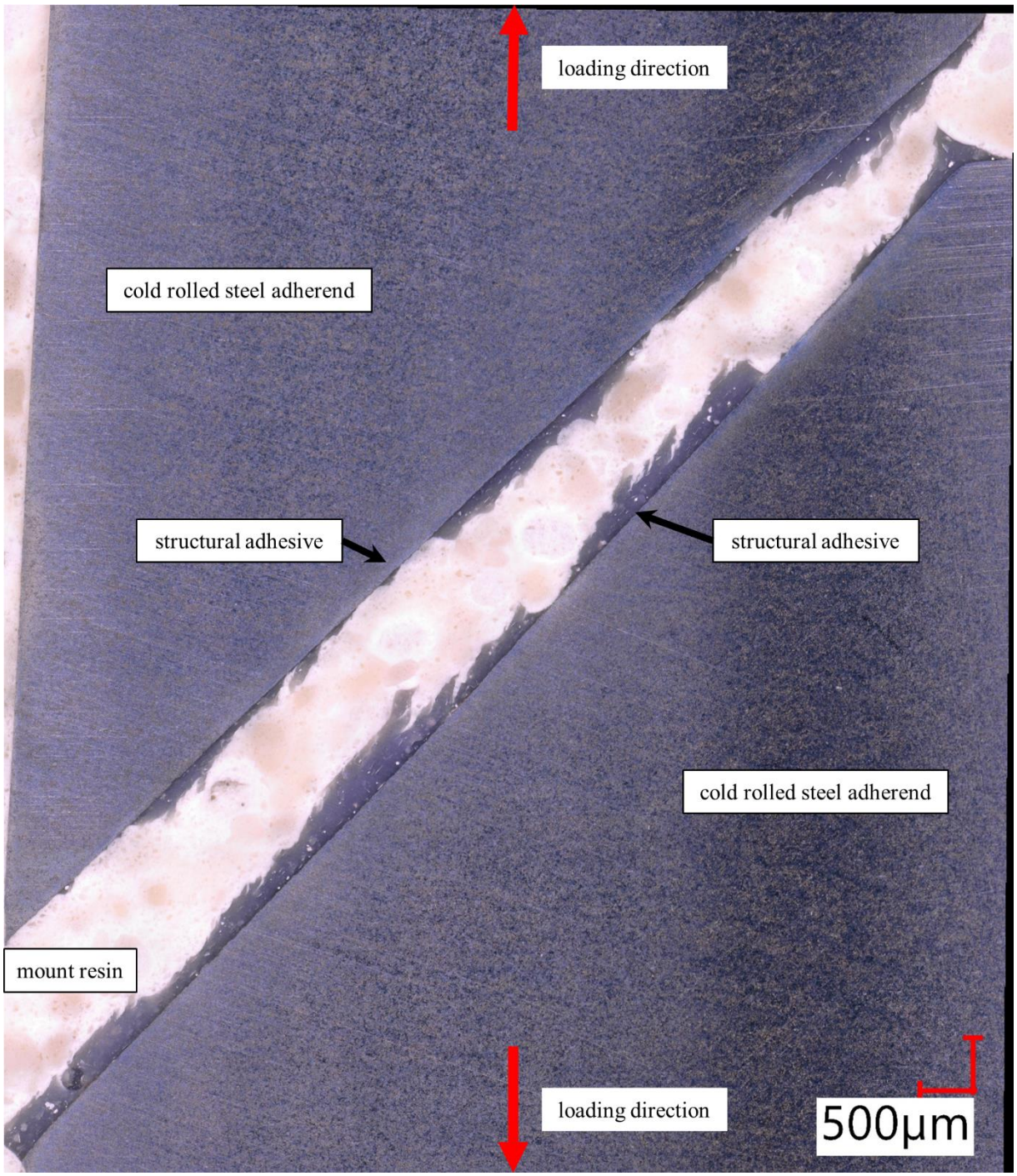

Figure 4.38: Cross-sectional view of a post-test mixed-mode specimen loaded at 45° (MM45); illustrating shear hackles, which are smaller than those observed in Mode II

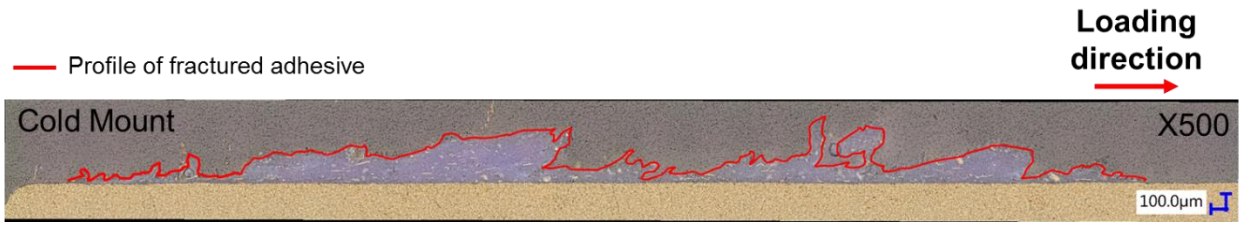

Figure 4.39: Cross-sectional view of a post-test single lap shear (SLS) specimen with cohesive failure surface illustrating the shear hackles oriented toward the loading direction and a fragment of the fracture oriented in the transverse direction that suggesting the influence of Mode I loading at the moment of fracture

Chapter 5. Discussion

The effect of surface treatment on joint performance was statistically significant for all three as-hot stamped material conditions (*e.g.* thermal treatments at RT, 400°C, and 700°C). On average, the grit-blasted (GB) and adhesion promotor (AP) treatments improved the shear strength by 60 % and 56 %, respectively, compared to the ACE treatment (Table 4.2). The ACE treatment used acetone to remove contaminants; however, the brittle intermetallic coating remained and induced a lower joint shear strength compared to the results obtained from GB and AP treatment. The reduced joint strength associated with the intermetallic coating failure in the Al-Si coated Usibor® 1500-AS was similar to that seen in zinc-based coatings, as reported by Lundgren (1989) and Bandekar *et al.* (2010).

As part of this research, the Al-Si-Fe intermetallic coating delamination mechanism in SLS was observed (Figure 5.1) and associated with the measured intermetallic coating thickness and the defects found in the coating (Figure 4.23). The microcracks and Kirkendall voids were the critical defects that facilitated coating delamination. As the SLS joint rotated during the loading, bending of the adherends may have widened the microcracks (Figure 5.1b). As the loading and joint rotation continued, the mode of loading shifted from shear to mixed Mode I and Mode II loading. The microcracks propagated perpendicular to the initial pre-existing microcrack through a mechanism of link-up of the neighbouring Kirkendall voids, ultimately leading to delamination of the coating. The remaining Al-Fe-Si intermetallic coating after delamination was found to be approximately 10 µm in thickness, and corresponded to the high iron content α-Fe phase layer in the coating (Wang *et al.*, 2017) (Figure 4.20c). This iron rich layer in the intermetallic coating corresponded to the diffusion layer and is reported to be more ductile compared to the remainder of the intermetallic coating, which is hard and brittle (Wang *et al.*, 2017; Kobayashi and Yakou, 2002).

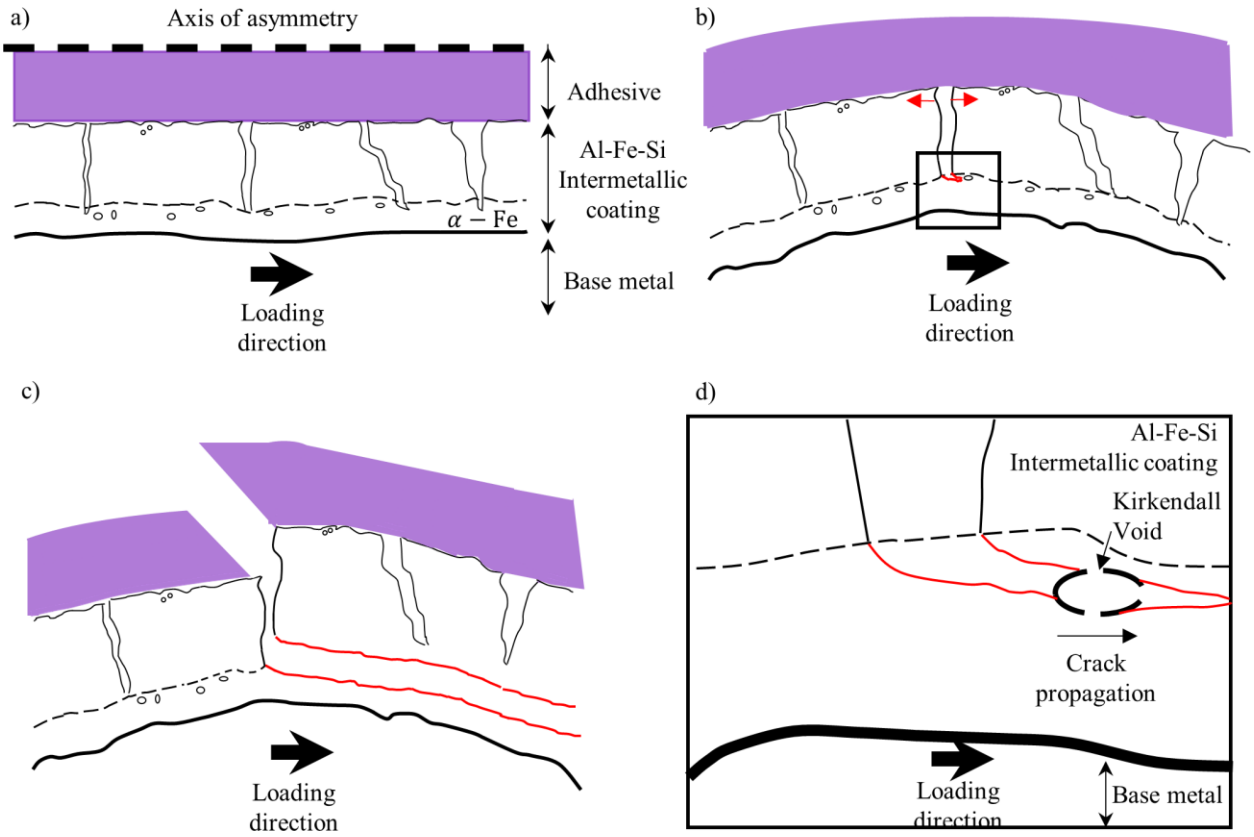

Figure 5.1: Cross-section diagrams illustrating the intermetallic coating failure in a single lap shear test; a) Al-Fe-Si intermetallic coating with defects, b) microcrack widened due to bending as the load increased and crack propagating to an adjacent void, c) intermetallic coating failure, and d) close-up view of the crack extension to the adjacent void

Removal of the intermetallic coating layer from the steel using the grit-blast process in the GB and AP treatments resulted in improved joint shear strength relative to the ACE treatment. The failure surfaces from the GB and AP treatments included partial and complete cohesive failure, which confirmed a strong interfacial adhesion between the grit-blasted surface and structural adhesive (Figure 4.11 and Figure 4.12). Similar performance improvements were reported by Critchlow *et al.* (2000) in adhesively bonded plain carbon steel joints who measured an increase in shear strength of 21% using a grit-blast treatment and 26 % using a silane-based treatment relative to a simple degreasing treatment. The improvement was attributed to the chemical bond created at the interface between the primed adherend surface and adhesive, at which

the silane solution on the adherend surface acted as a link between the inorganic (boron steel) and organic (structural adhesive) materials (Ebnesajjad, 2014).

The relative performance of the SLS joints tested in the current work (Figure 5.2) demonstrates that there was no statistically significant difference in measured joint strength between the GB and AP treated test specimens. This result suggests that the grit-blast treatment alone was sufficient to provide a roughened surface to which the adhesive could adhere and that the additional silane treatment was unnecessary for the grit-blasted adherend. The cohesive failure (*i.e.* failure within the adhesive) found on test specimens with the GB and AP treatment confirmed that the measured joint strength was derived from the structural adhesive material strength.

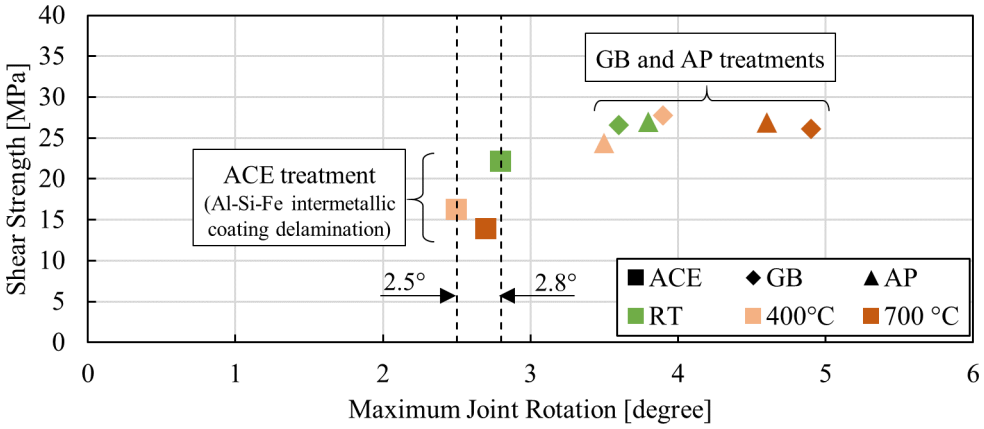

Figure 5.2: Shear strength vs. maximum joint rotation of SLS tests with different combinations of surface and thermal treatments

The effect of the hot stamping condition on adhesive joint performance varied and depended strongly on the surface preparation. In the case of the ACE surface treatment, where the adhesive was bonded to the brittle intermetallic coating, it was found that the average shear strength decreased as the thermal treatment temperature (*i.e.* quenching die surface temperature) increased. This result was somewhat surprising since the microcrack density after the hot stamping thermal treatment tended to decrease as the die temperature was increased (Table 4.13), and an adhesive joint of a higher microcrack density surface might be expected to lead to a lower joint strength. Interestingly, the opposite trend was observed and this may be attributed

to the reduction in adherend yield strength as die temperature increased. Work by Reis *et al.*, 2011 and Watson *et al.*, 2019 have shown that joint shear strength can be a function of adherend stiffness. In the test cases with ACE surface treatment, the lower adherend strength achieved from a higher quenching die temperature (*e.g.* at 700 °C) may explain the corresponding drop in measured joint shear strength. The ACE test specimens all failed at a joint rotation in the range of 2.5° to 2.8° (Figure 5.2), which suggested that the onset of Al-Si-Fe intermetallic coating delamination was correlated with joint rotation and that the critical level of joint rotation was reached earlier, with lower force for the SLS test specimens made of lower yield strength adherends.

In the surface treatment study, the spew fillets were removed by machining to create consistent test specimens (Figure 3.12). However, in practical applications, the spew fillet may not always be accessible and therefore would likely remain on the joint. The presence of the spew fillet has been shown to increase joint strength by reducing the local stress concentration in the adhesive joint (Lang and Mallick, 1998), and therefore the method used in this study provides conservative estimates of joint strength.

The effect of deformation during hot stamping was studied using formed hat channel sections. The side wall section of the as-hot stamped hat channel exhibited large microcracks resulting from the large plastic strain (>0.3) during forming (Omer *et al.*, 2018). SLS specimens made from side wall sections all presented interfacial failure of the adhesive joint, as opposed to delamination failure within the coating itself. The large microcracks occurring in the side wall may result in incomplete wetting of the bond surface, as seen in Figure 5.3. The incomplete wetting may lead to fewer anchoring sites for adhesive to bond, causing the change in failure mode and a reduction in joint strength (21.7 MPa) compared to SLS specimens made from flange or top sections of the hat channels (24.2 MPa and 26.1 MPa, respectively) (Table 4.15).

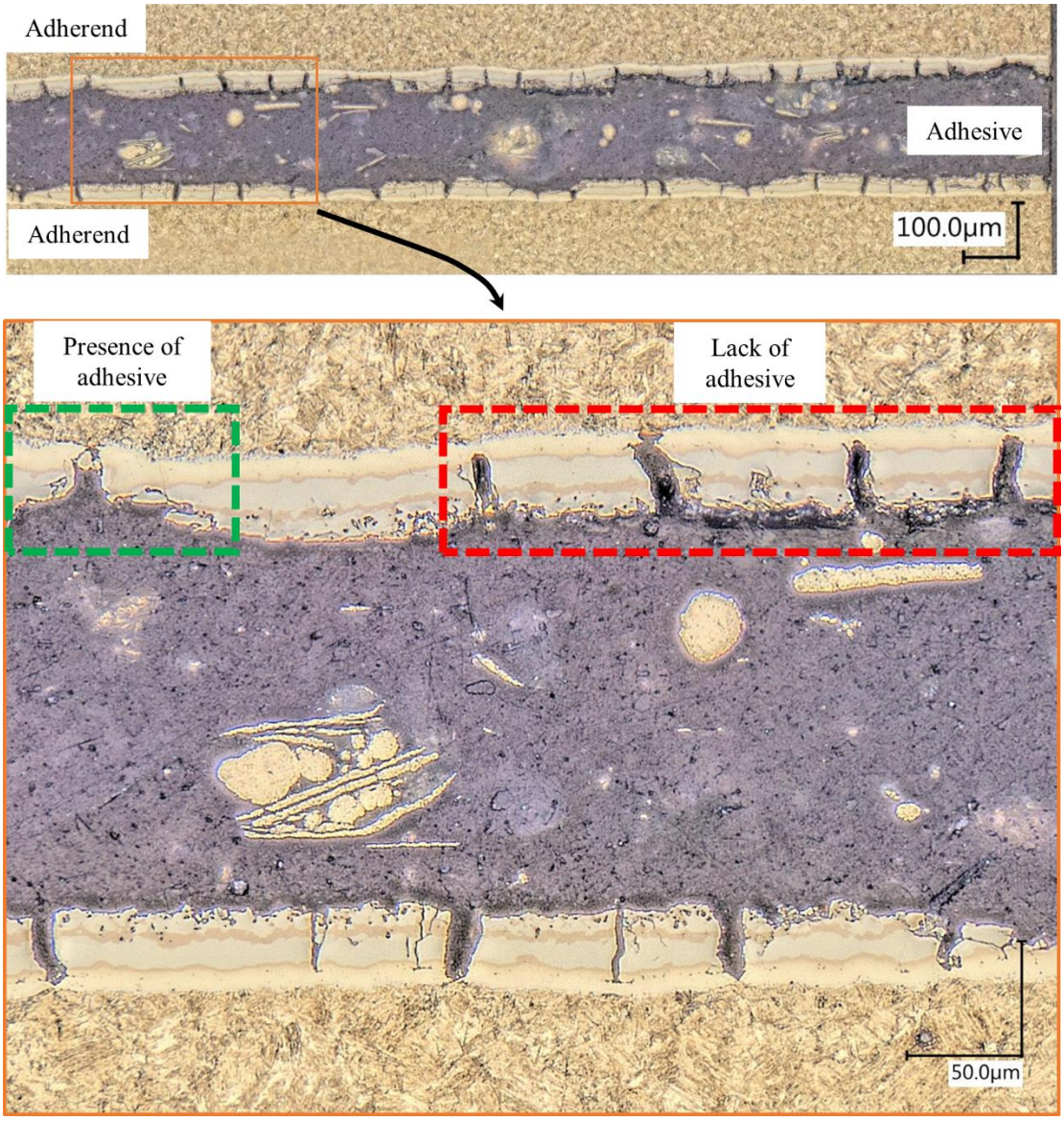

Figure 5.3: Cross-section of adhesively bonded SLS from the side wall of a hat section demonstrating the lack of adhesive near the large microcracks

Finally, the quantification of adhesive fracture surface morphology identified surface features corresponding to each of the distinct modes of loading. The surface roughness between different modes of loading was calculated based on fracture profiles from cohesive failures (*i.e.* fracture of the adhesive). It was assumed that the fracture surface roughness resulting from cohesive failure would be independent of the adherend material. In the experimental tests, the SLS adherends were UHSS while the remaining test

specimens used cold rolled steel adherends with larger dimensions that increased the bending stiffness of the adherends. The Mode I opening corresponded to a low surface roughness of 50 μm. The Mode II shear loading resulted in a high surface roughness of 103 μm, reflecting the existence of tall shear hackles. The Mixed-Mode (45° loading orientation, MM45) and the single-lap shear specimens had fracture surface roughness values of 80 μm and 73 μm, respectively. Despite the similar averages in R_a value between the MM45 and SLS fracture surfaces, the qualitative assessment indicated that the SLS was a shear dominated failure, whereas and the MM45 sample exhibited a mixture of Mode I and Mode II loading. The quantification of fracture surfaces using R_a provided additional information enabling identification of the mode of loading based on fracture surface morphology, and avoids misinterpretation of the fracture surfaces that could incorrectly categorize a fracture feature associated to a particular type of loading condition. However, it was noted that quantitative assessment using arithmetic mean roughness (R_a) cannot be the sole diagnostic tool to differentiate the adhesive failure surfaces between specific modes of loading, and required qualitative fracture surface assessment to uniquely identify the mode of loading.

Chapter 6. Conclusions and Recommendations

6.1 Conclusions

Ultra-high strength boron steel provides an important design option for vehicle structural engineers. The high strength is achieved through thermal processing during hot stamping, which leads to the generation of an Al-Fe-Si intermetallic coating to mitigate decarburization of the steel material, but presents challenges for adhesive joining.

The joint strength for adhesively bonded boron steel, measured using a traditional single-lap shear testing, was highly dependant on the presence and condition of the intermetallic coating. The baseline surface treatment (ACE) in which the intermetallic coating remained intact, demonstrated the lowest joint strength, on the order of 14 MPa, and highest variability (±6.5 MPa) among the three surface treatments tested. The low joint strength was attributed to failure or delamination of the brittle intermetallic coating. Removing the intermetallic coating by grit-blasting (GB) improved the joint strength (on average by 60%) and resulted in cohesive failure of the adhesive. Including an adhesion promoter (AP) to the grit-blast treatment did not further improve the joint strength, since the joint was already exhibiting a cohesive failure mode with grit-blasting treatment alone. However, one potential benefit of the surface coatings such as the AP treatment could be to mitigate surface corrosion of the UHSS following removal of the intermetallic coating by grit blasting. Coatings that may prevent surface corrosion and are amenable to adhesive joining should be investigated further.

The SLS test specimens that received ACE treatment showed a decrease in joint shear strength as thermal treatment temperature increased (*i.e.* decrease in adherend strength). The Al-Si-Fe intermetallic coating included defects such as microcracks, Kirkendall voids, and surface porosity. The density of microcracks was lower for the 700 °C thermal treatment compared to the 400°C and RT thermal treatments. The decrease

in shear strength measured for the ACE treatment and higher thermal treatment was attributed to the lower force required to bend the adherends owing to the lower yield strength. The increased adherened bending caused the SLS to reach the critical level of joint rotation, between 2.5° and 2.8°, leading to coating delamination. The coating delamination was associated with bending of the adherend, leading to coating fracture at the locations of the microcracks and Kirkendall voids. This hypothesis was supported by microscope observations of metallurgical cross-section that showed the removal of intermetallic coating and the lack of coating failure under pure tensile loading in the modified butt joint test. This trend was not observed in GB and AP test specimens, where the intermetallic coating was removed prior to adhesive application and failure occurred within the adhesive (cohesive failure).

The adherend thermal treatment resulted in a secondary effect on the joint strength of the GB and AP test specimens. In these cases, for which the coating was removed, there was no statistically significant difference between measured joint strengths; however, a significant increase in the measured joint rotation at failure was detected for the higher quenching die temperature (700 °C). This increased rotation was attributed to the lower yield strength of the adherend material, which enabled a higher amount of plastic deformation.

The effect of forming and large-scale deformation during the hot stamping process was investigated for the intermetallic coating using formed hat channel sections. Large microcracks were observed at the side wall of the hat channel, attributed to the large tensile strains occurring during the hot forming process. The resulting large microcracks led to poor wetting of the adhesive on the metal surface and lower average joint shear strength (21.7 MPa) compared to specimens extracted from the flange and top sections of the hat channel (24.2 MPa and 26.1 MPa, respectively). However, while the top and flange sections did not exhibit large microcracks and their measured average shear strengths were higher than side wall section, a statistically significant difference in joint strength was not detected in SLS test specimens made from the three sections of the hat channels.

Finally, specific adhesive fracture surface morphologies were associated with different modes of loading: Mode I presented a faceted surface, Mode II demonstrated shear hackles, and Mixed-Mode (45°) loading (MM45) lead to a mixture of the two morphologies, with R_a roughness values of 50 µm, 103 µm and 80 µm, respectively. The SLS fracture surface exhibited a shear-dominated fracture mode due to the stiff UHSS adherends, although the surface roughness was 73 µm. Even though the overall roughness of the SLS approximately matched that of MM45 (73 µm vs 80 µm), the differences in fracture features between the two loading conditions showed that the current quantitative technique works best alongside the qualitative descriptions to have the most accurate representation of the adhesive fracture surfaces.

6.2 Recommendations

The present study answered important questions regarding adhesive joint strength of boron steel for different surface and thermal treatments, and the corresponding intermetallic coating failure pathways and their effect on joint strength measured using a single-lap shear test. However, given the complex nature of adhesive joining for a coated material, some future studies are recommended.

To reduce the bond thickness variability found in single-lap shear test specimens, a clamping mechanism can be implemented to the assembly fixture that would apply sufficient pressure on each test specimen against the shim, which would dictate the final bond line thickness. The idea is a similar to a fixture design presented by Broughton and Gower (2001).

Furthermore, the surface treatment study on boron steel should be expanded to include alternative techniques such as dry-ice blasting (cryoblast) (Uhlmann and Mernissi, 2008) and laser-based ablation treatment, which may provide an effective means to partially or fully remove the intermetallic coating.

The joint durability (*i.e.* fatigue loading) should be investigated in the future to determine the strength retention at the interface between the adhesive/adherend for each surface treatment. Studies have shown

that initial joint strength (or static strength) is not necessarily reflected in joint durability test results (Davis and Fay, 1993; Critchlow *et al.*, 2000).

Adhesives are polymeric materials that exhibit strain rate sensitivity. The present study focused on quasi-static test methods and it is recommended that future testing consider elevated strain rates, which are relevant to automotive structures in crash scenarios.

References

3M. 2018. “3M™ Metal Primer 3901 Technical Data Sheet.”

3M. 2016. “3M™ Impact Resistant Structural Adhesive 07333/57333 Safety Data Sheet.”

3M. 2016. “3M™ Impact Resistant Structural Adhesive 07333 / 57333 Technical Data Sheet.” (January).

Aakkula, Jarkko, and Olli Saarela. 2014. “Silane Based Field Level Surface Treatment Methods for Aluminium, Titanium and Steel Bonding.” *International Journal of Adhesion and Adhesives* 48: 268–79. http://dx.doi.org/10.1016/j.ijadhadh.2013.09.039.

Allen, K. W., and H. S. Alsalim. 1976. “Surface Preparation of a Stainless Steel for Adhesive Bonding.” *The Journal of Adhesion* 8(3): 183–94.

Ameli, A., M. Papini, and J. K. Spelt. 2011. “Evolution of Crack Path and Fracture Surface with Degradation in Rubber-Toughened Epoxy Adhesive Joints: Application to Open-Faced Specimens.” *International Journal of Adhesion and Adhesives* 31(6): 530–40. http://dx.doi.org/10.1016/j.ijadhadh.2011.04.007.

Arakawa, K., and K. Takahashi. 1991. “Relationships between Fracture Parameters and Fracture Surface Roughness of Brittle Polymers.” *International Journal of Fracture* 48: 103–14.

ArcelorMittal. 2010. “Personal Communication with ArcelorMittal Who Kindly Shared the Analytical Process to Obtain Coating Weight and Composition of Aluminized Steel.”

Arenas, José M., Julián J. Narbón, and Cristina Alía. 2010. “Optimum Adhesive Thickness in Structural Adhesives Joints Using Statistical Techniques Based on Weibull Distribution.” *International Journal of Adhesion and Adhesives* 30(3): 160–65.

Arnott, D R et al. 1993. “Studies of the Degradation Analysis Techniques.” *Applied Surface Science* 71: 109–13.

Askeland, Donald R., Fulay, Pradeep P., Wright, Wendelin J. 2011. “The Science and Engineering of Materials.” *Textbook* 6th Edition: 944.

ASTM D1002-10. 2019. “Standard Test Method for Apparent Shear Strength of Single-Lap-Joint Adhesively Bonded Metal Specimens by Tension Loading (Metal-to- Metal).” *Annual Book of ASTM Standards*.

ASTM D1876-08. 2015. “Standard Test Method for Peel Resistance of Adhesives (T-Peel Test).” *Annual Book of ASTM Standards*.

ASTM D2094-00. 2014. “Standard Practice for Preparation of Bar and Rod Specimens for Adhesion Tests.” *Annual Book of ASTM Standards*.

ASTM D2651-01. 2016. “Standard Guide for Preparation of Metal Surfaces for Adhesive Bonding.” *Annual Book of ASTM Standards*.

ASTM D3165-07. 2014. “Strength Properties of Adhesives in Shear by Tension Loading of Single-Lap-Joint Laminated Assemblies.” *Annual Book of ASTM Standards*.

ASTM D3433-99. 2012. “Standard Test Method for Fracture Strength in Cleavage of Adhesives in Bonded Metal Joints.” *Annual Book of ASTM Standards*.

ASTM D5656-10. 2017. “Standard Test Method for Thick-Adherend Metal Lap-Shear Joints for Determination of the Stress-Strain Behavior of Adhesives in Shear by Tension Loading.” *Annual Book of ASTM Standards*.

Baldan, A. 2012. “Adhesion Phenomena in Bonded Joints.” *International Journal of Adhesion and Adhesives* 38: 95–116. http://dx.doi.org/10.1016/j.ijadhadh.2012.04.007.

Baldan, A. 2004. “Adhesively-Bonded Joints and Repairs in Metallic Alloys, Polymers and Composite Materials: Adhesives, Adhesion Theories and Surface Pretreatment.” *Journal of Materials Science* 39(1): 1–49.

Bamberg, P. A.M.G.P. et al. 2018. “Digital Image Correlation Analysis Of The Effects Of The Overlap Length, Adhesive Thickness And Adherends Yield Strength Over Similar And Dissimilar Joints Of High Strength Steel And Aluminum Alloys.” *International Journal of Adhesion and Adhesives* 83: 69–75. https://doi.org/10.1016/j.ijadhadh.2018.02.010.

Bandekar, Jagdeesh et al. 2010. “Bonding Studies between Fracture Toughened Adhesives and Galvannealed Steels with Zinc Coating.” *SAE Technical Papers*.

Banea, M. D., and L. F.M. Da Silva. 2009. “Adhesively Bonded Joints in Composite Materials: An Overview.” *Proceedings of the Institution of Mechanical Engineers, Part L: Journal of Materials: Design and Applications* 223(1): 1–18.

Banea, M. D., L.F.M. Da Silva, and R.D.S.G. Campilho. 2015. “The Effect of Adhesive Thickness on the Mechanical Behavior of a Structural Polyurethane Adhesive.” *Journal of Adhesion* 91(5): 331–46.

Banea, M.D., M Rosioara, R J C Carbas, and L F M da Silva. 2018. “Multi-Material Adhesive Joints for Automotive Industry.” *Composites Part B: Engineering Engineering* 151: 71–77. https://doi.org/10.1016/j.compositesb.2018.06.009.

Bardelcik, A., M. J. Worswick, S. Winkler, and M. A. Wells. 2012. “A Strain Rate Sensitive Constitutive Model for Quenched Boron Steel with Tailored Properties.” *International Journal of Impact Engineering* 50: 49–62. http://dx.doi.org/10.1016/j.ijimpeng.2012.06.007.

Bardelcik, Alexander et al. 2010. “Effect of Cooling Rate on the High Strain Rate Properties of Boron Steel.” *International Journal of Impact Engineering* 37(6): 694–702. http://dx.doi.org/10.1016/j.ijimpeng.2009.05.009.

Beaulieu, A. J. 1970. “Transversely Excited Atmospheric Pressure CO2 Lasers.” *Applied Physics Letters* 16(12): 504–5.

Biel, Anders, and Stigh, Ulf. 2018. “Strength and Toughness in Shear of Constrained Layers.” *International Journal of Solids and Structures* 138: 50–63. https://doi.org/10.1016/j.ijsolstr.2017.12.028.

Billur, Eren. 2019. Springer Nature Switzerland AG *Introduction. In: Billur E. (Eds) Hot Stamping of Ultra High-Strength Steels*. ed. Eren Billur. Springer.

Birky, Alicia K, and Zhenhong Laughlin, Michael, Tartaglia, Katie, Price, Rebecca, Lin. 2017. *Transportation Electrification beyond Light Duty: Technology and Market Assessment*. https://info.ornl.gov/sites/publications/Files/Pub72938.pdf

Boutar, Yasmina et al. 2016. “Effect of Adhesive Thickness and Surface Roughness on the Shear Strength of Aluminium One-Component Polyurethane Adhesive Single-Lap Joints for Automotive Applications.” *Journal of Adhesion Science and Technology* 30(17): 1913–29. http://dx.doi.org/10.1080/01694243.2016.1170588.

Brewis, D. M., G. W. Critchlow, and C. A. Curtis. 1999. “Cryoblasting as a Pretreatment to Enhance Adhesion to Aluminum Alloys: An Initial Study.” *International Journal of Adhesion and Adhesives* 19(4): 253–56.

Broughton, Bill, and Mike Gower. 2001. “Measurement Good Practice Guide No. 47; Preparation and Testing of Adhesive Joints.” (47): 84.

Campilho, R.D.S.G., A.M.G. Pinto, M.D. Banea, and L.F.M. Da Silva. 2012. “Optimization Study of Hybrid Spot-Welded/Bonded Single-Lap Joints.” *International Journal of Adhesion and Adhesives* 37: 86–95. http://dx.doi.org/10.1016/j.ijadhadh.2012.01.018.

Carbas, R. J.C., E. A.S. Marques, L. F.M. Da Silva, and A. M. Lopes. 2014. “Effect of Cure Temperature on the Glass Transition Temperature and Mechanical Properties of Epoxy Adhesives.” *Journal of Adhesion* 90(1): 104–19.

Carley, Sanya et al. 2019. “The Macroeconomic Effects of 2017 Through 2025 Federal Fuel Economy and Greenhouse Gas Emissions Standards.” *Journal of Policy Analysis and Management* 38(3): 732–63.

Chai, Herzl. 1992. “Experimental Evaluation of Mixed-Mode Fracture in Adhesive Bonds.” *Experimental Mechanics* 32(4): 296–303.

Chai, Herzl. 1988. “Shear Fracture.” *International Journal of Fracture* 37(2): 137–59.

Cheah, Lynette W. 2010. Engineering “Cars on a Diet : The Material and Energy Impacts of Passenger Vehicle Weight Reduction in the U . S . - Doctoral Thesis.” MASSACHUSETTS INSTITUTE OF TECHNOLOGY.

Chiang, Martin, McKenna, Gregory B. 1995. “Hygrothermal Effects on the Performance of Polymers and Polymeric Composites.” *ElectroComponent Science and Technology* 9(2): 165–66. http://www.hindawi.com/journals/apec/1981/601467/abs/.

Cho, Tae Min et al. 2009. “Effect of Surface Roughness on the Adhesive Strength of the Heat-Resistant Adhesive RTV88.” *Journal of Adhesion Science and Technology* 23(15): 1875–82.

Critchlow, G W, K H Bedwell, and M E Chamberlain. 1998. “Pretreatments to Improve the Bondability of Hot Dipped Galvanised Mild Steel.” *Transactions of the IMF* 76(6): 209–12.

Critchlow, G W, C A Cottam, D M Brewis, and D C Emmony. 1997. “Further Studies into the Effectiveness of C02-1aser Treatment of Metals for Adhesive Bonding.” *International Journal of Adhesion and Adhesives* 17: 143–50.

Critchlow, G. W., K. H. Bedwell, and C. A. Cottam. 1998. “The Effectiveness of TEA CO2-Laser Ablation for the Treatment of Hot Dipped Galvanized Mild Steel Prior to Adhesive Bonding.” *Transactions of the Institute of Metal Finishing* 76(5): 203–6.

Critchlow, G. W., P. W. Webb, C. J. Tremlett, and K. Brown. 2000. “Chemical Conversion Coatings for Structural Adhesive Bonding of Plain Carbon Steels.” *International Journal of Adhesion and Adhesives* 20(2): 113–22.

Critchlow, G.W. 1997. “Pretreatments for Metal-to-Metal Bonding - Doctoral Thesis.” Loughborough University. https://dspace.lboro.ac.uk/2134/7525.

Crocombe, A. D., and R. D. Adams. 1981. “Influence of the Spew Fillet and Other Parameters on the Stress Distribution in the Single Lap Joint.” *The Journal of Adhesion* 13(2): 141–55.

da Silva, Lucas F M, G.W. Critchlow, and M.A.V. Figueiredo. 2008. “Parametric Study of Adhesively Bonded Single Lap Joints by the Taguchi Method.” *Journal of Adhesion Science and Technology* 22(13): 1477–94.

da Silva, Lucas F M et al. 2012. “Manufacture of Quality Specimens.” *Testing Adhesive Joints, Best Practices*: 1–77.

da Silva, Lucas F M et al. 2006. “Effect of Adhesive Type and Thickness on the Lap Shear Strength.” *Journal of Adhesion* 82(11): 1091–1115.

da Silva, Lucas F.M. et al. 2009a. “Effect of Material, Geometry, Surface Treatment and Environment on the Shear Strength of Single Lap Joints.” *International Journal of Adhesion and Adhesives* 29(6): 621–32.

da Silva, Lucas F.M., Paulo J.C. das Neves, R. D. Adams, and J. K. Spelt. 2009b. "Analytical Models of Adhesively Bonded Joints-Part I: Literature Survey." *International Journal of Adhesion and Adhesives* 29(3): 319–30.

da Silva, Lucas F.M., F. A.C.R.G. De Magalhães, F. J.P. Chaves, and M. F.S.F. De Moura. 2010. "Mode II Fracture Toughness of a Brittle and a Ductile Adhesive as a Function of the Adhesive Thickness." *Journal of Adhesion* 86(9): 891–905.

Darwish, S. M., A. Niazi, A. Ghania, and M. E. Kassem. 1991. "Improving the Electrical Properties of Structural Epoxy Resin Adhesives." *International Journal of Adhesion and Adhesives* 11(1): 37–42.

Darwish, S. M.H., and A. Ghanya. 2000. "Critical Assessment of Weld-Bonded Technologies." *Journal of Materials Processing Technology* 105(3): 221–29.

Dastjerdi, A. Khayer, E. Tan, and F. Barthelat. 2013. "Direct Measurement of the Cohesive Law of Adhesives Using a Rigid Double Cantilever Beam Technique." *Proceedings of the Society for Experimental Mechanics, Inc.* 53(6): 1763–72.

Davis, R. E., and P. A. Fay. 1993. "The Durability of Bonded Coated Steel Joints." *International Journal of Adhesion and Adhesives* 13(2): 97–104.

Debski, M., M. E.R. Shanahan, and J. Schultz. 1986. "Mechanisms of Contaminant Elimination by Oil-Accommodating Adhesives Part 2: A Model of the Processes Involved." *International Journal of Adhesion and Adhesives* 6(3): 150–52.

Demircioglu, Pinar. 2014. "Estimation of Surface Topography for Dental Implants Using Advanced Metrological Technology and Digital Image Processing Techniques." *Measurement: Journal of the International Measurement Confederation* 48(1): 43–53. http://dx.doi.org/10.1016/j.measurement.2013.10.036.

Doru, Muhammet Onur, Adnan Özel, Salih Akpinar, and Murat Demir Aydin. 2014. "Effect of the Spew Fillet on Adhesively Bonded Single-Lap Joint Subjected to Tensile Loading: Experimental and 3-D Non-Linear Stress Analysis." *Journal of Adhesion* 90(3): 195–209.

Du Bois, Paul. et al. 2004. "Vehicle Crashworthiness and Occupant Protection." *American Iron and Steel Institute*: 372.

Ebnesajjad, Sina. 2014. *Surface Treatment of Materials for Adhesive Bonding*. 2nd ed.

Elbing, F., N. Anagreh, L. Dorn, and E. Uhlmann. 2003. "Dry Ice Blasting as Pretreatment of Aluminum Surfaces to Improve the Adhesive Strength of Aluminum Bonding Joints." *International Journal of Adhesion and Adhesives* 23(1): 69–79.

Eller, T. K. et al. 2016. "Determination of Strain Hardening Parameters of Tailor Hardened Boron Steel up to High Strains Using Inverse FEM Optimization and Strain Field Matching."

Journal of Materials Processing Technology 228: 43–58. http://dx.doi.org/10.1016/j.jmatprotec.2015.09.036.

Fan, Dong W., Han S. Kim, and Bruno C. De Cooman. 2009. "Review of the Physical Metallurgy Related to the Hot Press Forming of Advanced High Strength Steel." *Steel Research International* 80(3): 241–48. http://onlinelibrary.wiley.com/doi/10.1002/srin.201090074/abstract.

Fan, Dong Wei, and Bruno C. De Cooman. 2012. "State-of-the-Knowledge on Coating Systems for Hot Stamped Parts." *Steel Research International* 83(5): 412–33.

Fan, Dong Wei et al. 2010. "Coating Degradation in Hot Press Forming." *ISIJ International* 50(4): 561–68. http://joi.jlc.jst.go.jp/JST.JSTAGE/isijinternational/50.561?from=CrossRef.

Fernando, D., J. G. Teng, T. Yu, and X. L. Zhao. 2013. "Preparation and Characterization of Steel Surfaces for Adhesive Bonding." *Journal of Composites for Construction* 17(6): 1–10.

Fujimoto, Hiroki et al. 2018. "Study on Static and Fatigue Strength of Structural Adhesive-Bonded Joints of Steel Sheets for Automotive Application." *Welding International* 32(5): 353–62. https://doi.org/10.1080/09507116.2017.1346853.

George, R, A Bardelcik, and M J Worswick. 2012. "Hot Forming of Boron Steels Using Heated and Cooled Tooling for Tailored Properties." *Journal of Materials Processing Tech.* 212(11): 2386–99. http://dx.doi.org/10.1016/j.jmatprotec.2012.06.028.

George, Ryan. 2011. "Hot Forming of Boron Steels with Tailored Mechanical Properties - Experiments and Numerical Simulations - MASc Thesis." University of Waterloo. http://hdl.handle.net/10012/5927.

Ghaffari, B. et al. 2012. "A Matrix Array Technique for Evaluation of Adhesively Bonded Joints." *SAE Technical Papers*.

Ghiotti, A, S Bruschi, and F Borsetto. 2011. "Tribological Characteristics of High Strength Steel Sheets under Hot Stamping Conditions." *Journal of Materials Processing Tech.* 211(11): 1694–1700. http://dx.doi.org/10.1016/j.jmatprotec.2011.05.009.

Ghosh, Amit Kumar et al. 2015. "Optimisation of Wet Chemical Silane Deposition to Improve the Interfacial Strength of Stainless Steel / Epoxy." *Applied Surface Science* 324: 134–42. http://dx.doi.org/10.1016/j.apsusc.2014.10.075.

Gilat, Amos, Robert K. Goldberg, and Gary D. Roberts. 2005. "Strain Rate Sensitivity of Epoxy Resin in Tensile and Shear Loading." *Journal of Aerospace Engineering* 20(2): 75–89.

Gilchrist, M. D., Svensson, N. 1995. "A Fractographic Analysis of Delamination within Multidirectional Carbon/Epoxy Laminates." *Composites Science and Technology* 55(2): 195–207.

Gledhill, R. A., S. J. Shaw, and D. A. Tod. 1990. “Durability of Adhesive-Bonded Joints Employing Organosilane Coupling Agents.” *International Journal of Adhesion and Adhesives* 10(3): 192–98.

Goland, M, and Reissner, E. 1944. “The Stresses in Cemented Joints.” *Appl. Mech., Trans. ASME*. (66): A17–27.

Grant, L. D.R., R. D. Adams, and Lucas F.M. da Silva. 2009. “Experimental and Numerical Analysis of Single-Lap Joints for the Automotive Industry.” *International Journal of Adhesion and Adhesives* 29(4): 405–13.

Greenhalgh, E. S. 2009. “Failure Analysis and Fractography of Polymer Composites.”

Gui, Zhong xiang, Wei kang Liang, Yong Liu, and Yi sheng Zhang. 2014. “Thermo-Mechanical Behavior of the Al-Si Alloy Coated Hot Stamping Boron Steel.” *Materials and Design* 60: 26–33. http://dx.doi.org/10.1016/j.matdes.2014.03.011.

Harris, A F, and A Beevers. 1999. “The Effects of Grit-Blasting on Surface Properties for Adhesion.” *Journal Of Adhesion* 19(November 1998).

Hein, Philipp, and Joël Wilsius. 2008. “Status and Innovation Trends in Hot Stamping of USIBOR 1500 P.” *Steel Research International* 79(2): 85–91.

Hertveldt, I., B. C. De Cooman, K. Meseure, and C. Xhoffer. 1999. “The Shear Strength of Galvannealed Coatings on If Steels.” *ISIJ International* 39(12): 1280–88.

Honda Motor Co. 2019. “2019 RDX Model Series : New Body Repair Information (Version 2).” *Acura RDX- Body Repair News* (June). techinfo.honda.com.

Ighodaro, O L, E Biro, and Y N Zhou. 2016. “Comparative Effects of Al-Si and Galvannealed Coatings on the Properties of Resistance Spot Welded Hot Stamping Steel Joints.” *Journal of Materials Processing Technology* 236: 64–72.

Ikegami, K. et al. 1996. “Benchmark Tests on Adhesive Strengths in Butt, Single and Double Lap Joints and Double-Cantilever Beams.” *International Journal of Adhesion and Adhesives* 16(4): 219–26.

Imanaka, Makoto, Xinwei Liu, and Masaki Kimoto. 2017. “Comparison of Fracture Behavior between Acrylic and Epoxy Adhesives.” *International Journal of Adhesion and Adhesives* 75(January): 31–39. http://dx.doi.org/10.1016/j.ijadhadh.2017.02.011.

Jenner, Frank, Mark E. Walter, Raj Mohan Iyengar, and Ron Hughes. 2010. “Evolution of Phases, Microstructure, and Surface Roughness during Heat Treatment of Aluminized Low Carbon Steel.” *Metallurgical and Materials Transactions A: Physical Metallurgy and Materials Science* 41A(6): 1554–63.

Kahraman, Ramazan, and Mamdouh Al-Harthi. 2005. “Moisture Diffusion into Aluminum Powder-Filled Epoxy Adhesive in Sodium Chloride Solutions.” *International Journal of Adhesion and Adhesives* 25(4): 337–41.

Kanninen, Melvin F., and Carl H. Popelar. 1986. Journal of Engineering Materials and Technology *Advanced Fracture Mechanics*. Oxford University Press.

Karachalios, E. F., R. D. Adams, and Lucas F.M. da Silva. 2013. “Single Lap Joints Loaded in Tension with High Strength Steel Adherends.” *International Journal of Adhesion and Adhesives* 43: 81–95. http://dx.doi.org/10.1016/j.ijadhadh.2013.01.016.

Karbasian, H, and A E Tekkaya. 2010. “A Review on Hot Stamping.” *Journal of Materials Processing Technology* 210(15): 2103–18. http://dx.doi.org/10.1016/j.jmatprotec.2010.07.019.

Kilik, R., and R. Davies. 1989. “Mechanical Properties of Adhesive Filled with Metal Powders.” *International Journal of Adhesion and Adhesives* 9(4): 224–28.

Kim, Hyung Ju, Gregory A. Keoleian, and Steven J. Skerlos. 2010. “Economic Assessment of Greenhouse Gas Emissions Reduction by Vehicle Lightweighting Using Aluminum and High-Strength Steel.” *Journal of Industrial Ecology* 15(1): 64–80.

Kim, Hyun-Joong; Lim, Dong-Hyuk; Hwang, Hyeon-Deuk; Lee, Byoung-Ho. 2011. “Composition of Adhesives. In: Da Silva L.F.M., Öchsner A., Adams R.D. (Eds).” In *Handbook of Adhesion Technology*, ed. Robert D. da Silva, Lucas F.M., Ochsner, Andreas , Adams.

Kinloch, A. J., and S. J. Shaw. 1981. “The Fracture Resistance of a Toughened Epoxy Adhesive.” *The Journal of Adhesion* 12(1): 59–77.

Kinloch, A. J., S. J. Shaw, D. A. Tod, and D. L. Hunston. 1983. “Deformation and Fracture Behaviour of a Rubber-Toughened Epoxy: 1. Microstructure and Fracture Studies.” *Polymer* 24(10): 1341–54.

Knox, E. M., and M. J. Cowling. 2000. “Rapid Durability Test Method for Adhesives.” *International Journal of Adhesion and Adhesives* 20(3): 201–8.

Kobayashi, Shigeaki, and Takao Yakou. 2002. “Control of Intermetallic Compound Layers at Interface between Steel and Aluminum by Diffusion-Treatment.” *Materials Science and Engineering A* 338(1–2): 44–53.

Kolnerova, Michaela, Sobotka, Jiri, Korecek, David, Solfronk, Pavel, Schiffmann, Tomas. 2017. “STRENGTH OF THE ADHESIVE JOINTS AT THE CAR-BODY PARTS FROM THE AHSS WITH AL-SI COATING.” *MM Science Journal*: 1901–4.

Köster, U. Liu, W. Liebertz, H. Michel, M. 1993. “Mechanical Properties of Quasicrystalline and Crystalline Phases in Al-Cu-Fe Alloys.” *Journal of Non-Crystalline Solids* 153–154: 446–52.

Lang, T. P., and P. K. Mallick. 1998. “Effect of Spew Geometry on Stresses in Single Lap Adhesive Joints.” *International Journal of Adhesion and Adhesives* 18(3): 167–77.

Liu, K, and M R Piggott. 1998. “Fracture Failure Processes in Polymers. II. Fractographic Evidence.” *Polymer Engineering and Science* 38(1): 69–78. http://dx.doi.org/10.1002/pen.10166.

Liu, Yi Hung, Hiroyuki Maruyama, and Shuji Matsusaka. 2011. “Effect of Particle Impact on Surface Cleaning Using Dry Ice Jet.” *Aerosol Science and Technology* 45(12): 1519–27.

Lopes, R M, R D S G Campilho, F J G Silva, and T M S Faneco. 2016. “Comparative Evaluation of the Double-Cantilever Beam and Tapered Double-Cantilever Beam Tests for Estimation of the Tensile Fracture Toughness of Adhesive Joints.” *International Journal of Adhesion and Adhesives* 67: 103–11. http://dx.doi.org/10.1016/j.ijadhadh.2015.12.032.

Lundgren, Anders H. 1989. “Volvo Laboratory Study of Zinc-Coated Steel Sheet-Adhesive Bonding Properties.” *SAE Technical Papers*.

Mallick, P. K. 2010. “Joining for Lightweight Vehicles.” In *Materials, Design and Manufacturing for Lightweight Vehicles*, ed. P.K. Mallick. Woodhead Publishing, 275–308.

Mandolfino, C. et al. 2015. “Effect of Laser and Plasma Surface Cleaning on Mechanical Properties of Adhesive Bonded Joints.” *Procedia CIRP* 33: 458–63. http://dx.doi.org/10.1016/j.procir.2015.06.054.

Martinsen, K, S.J. Hu, and B.E. Carlson. 2015. “Joining of Dissimilar Materials.” *CIRP Annals - Manufacturing Technology* 64: 679–99.

Marzi, S., O. Hesebeck, M. Brede, and F. Kleiner. 2009. “A Rate-Dependent Cohesive Zone Model for Adhesively Bonded Joints Loaded in Mode I.” *Journal of Adhesion Science and Technology* 23(6): 881–98.

Mega, Tetsuya, Kohei Hasegawa, and Hidetaka Kawabe. 2004. “Ultra High-Strength Steel Sheets for Bodies, Reinforcement Parts, and Seat Frame Parts of Automobile—Ultra High-Strength Steel Sheets Leading to Great Improvement in Crashworthiness—.” *JFE technical report* 4(11): 38–43.

Merklein, M., and J. Lechler. 2006. “Investigation of the Thermo-Mechanical Properties of Hot Stamping Steels.” *Journal of Materials Processing Technology* 177(1–3): 452–55.

Naderi, Malek. 2007. “Hot Stamping of Ultra High Strength Steels - Doctoral Thesis.”.

Nandwani, Yogesh. 2015. “Characterization of Structural Adhesives Using Lap Shear and Pin and Collar Tests - MASc Thesis.” University of Waterloo. http://hdl.handle.net/10012/9799.

Nguyen, Tien Cuong, Yu Bai, Xiao Ling Zhao, and Riadh Al-Mahaidi. 2012. “Durability of Steel/CFRP Double Strap Joints Exposed to Sea Water, Cyclic Temperature and Humidity.” *Composite Structures* 94(5): 1834–45. http://dx.doi.org/10.1016/j.compstruct.2012.01.004.

Nunes, S. L.S. et al. 2016. “Comparative Failure Assessment of Single and Double Lap Joints with Varying Adhesive Systems.” *Journal of Adhesion* 92(7–9): 610–34. http://dx.doi.org/10.1080/00218464.2015.1103227.

OKeeffe, Cameron. 2018. “Investigation of Resistance Spot Weld Failure in Tailored Hot Stamped Assemblies - MASc Thesis.” University of Waterloo. http://hdl.handle.net/10012/12938.

Omer, Kaab. 2014. “Development and Testing of a Hot Stamped Axial Crush Member with Tailored Properties - MASc Thesis.” University of Waterloo. http://hdl.handle.net/10012/9024.

Omer, Kaab et al. 2018. “Development of a Hot Stamped Channel Section with Axially Tailored Properties – Experiments and Models.” *International Journal of Material Forming*: 149–64.

Omer, Kaab et al. 2017. “Testing of a Hot Stamped Axial Crush Member with Tailored Properties – Experiments and Models.” *International Journal of Impact Engineering* 103: 12–28. http://dx.doi.org/10.1016/j.ijimpeng.2017.01.003.

Omer, Kaab et al. 2017. “Testing of a Hot Stamped Axial Crush Member with Tailored Properties – Experiments and Models.” *International Journal of Impact Engineering* 103: 12–28. http://dx.doi.org/10.1016/j.ijimpeng.2017.01.003.

Özdemir, Alp, İbrahim Kocabaş, and Pavel Svanda. 2016. “Improving the Strength of Adhesively Bonded Joints through the Introduction of Various Surface Treatments.” *Journal of Adhesion Science and Technology* 30(23): 2573–95.

Packham, David E. 2017. “Theories of Fundamental Adhesion. In: Da Silva L., Öchsner A., Adams R. (Eds).” In *Handbook of Adhesion Technology*, ed. Adams R. da Silva L., Öchsner A. Springer, Cham.

Pardoen, T., T. Ferracin, C. M. Landis, and F. Delannay. 2005. “Constraint Effects in Adhesive Joint Fracture.” *Journal of the Mechanics and Physics of Solids* 53(9): 1951–83.

Park, Sang Yoon et al. 2010. “Recent Trends in Surface Treatment Technologies for Airframe Adhesive Bonding Processing: A Review (1995-2008).” *Journal of Adhesion* 86(2): 192–221.

Pearson, R. A., and A. F. Yee. 1986. “Toughening Mechanisms in Elastomer-Modified Epoxies - Part 2 Microscopy Studies.” *Journal of Materials Science* 21(7): 2475–88.

Petrie, E M. 2006. “Epoxy Adhesive Formulations.” http://books.google.fr/books?id=738MPfO5FEkC.

Plueddemann, Edwin P. 1988. “Silane Primers for Epoxy Adhesives.” *Journal of Adhesion Science and Technology* 2(1): 179–88.

Prajogo, Yonathan. 2015. “Hot Stamping of a Boron Steel Side Impact Beam - MASc Thesis.” University of Waterloo. http://hdl.handle.net/10012/9784.

Purslow, D. 1981. “Some Fundamental Aspects of Composites Fractography.” *Composites* 12(4): 241–47.

Reis, P. N.B., J. A.M. Ferreira, and F. Antunes. 2011. “Effect of Adherends Rigidity on the Shear Strength of Single Lap Adhesive Joints.” *International Journal of Adhesion and Adhesives* 31(4): 193–201. http://dx.doi.org/10.1016/j.ijadhadh.2010.12.003.

Schiel, M et al. 2015. “Behavior of Adhesively Bonded Coated Steel for Automotive Applications under Impact Loads.” *International Journal of Adhesion and Adhesives* 56: 32–40. http://dx.doi.org/10.1016/j.ijadhadh.2014.07.009.

Şekercíoğlu, Tezcan, Hikmet Rende, Alper Gülsöz, and Cemal Meran. 2003. “The Effects of Surface Roughness on the Strength of Adhesively Bonded Cylindrical Components.” *Journal of Materials Processing Technology* 142(1): 82–86.

Siviour, Clive R., and Jennifer L. Jordan. 2016. “High Strain Rate Mechanics of Polymers: A Review.” *Journal of Dynamic Behavior of Materials* 2(1): 15–32.

Spaggiari, A., and E. Dragoni. 2013. “Effect of Mechanical Surface Treatment on the Static Strength of Adhesive Lap Joints.” *Journal of Adhesion* 89(9): 677–96.

Sterrett, T. L. 1981. “The Prebond Surface Preparation of 301 Stainless Steel Alloy.” *International Journal of Adhesion and Adhesives* 1(4): 208–12.

Suehiro, Masayoshi, and Masahiro Ohgami. 2003. “Properties of Aluminum-Coated Steels for Hot-Forming.” 2003(88): 16–21.

Tan, Man-Shin; Sharifian, Nozhan. 2011. “Adhesively Bonded Steel Structures - Master Thesis.” Chalmers University of Technology. https://hdl.handle.net/20.500.12380/152928.

Tavakkolizadeh, M., and H. Saadatmanesh. 2001. “G Alvanic C Orrosion of C Arbon and S Teel.” *Journal of Composites for Construction* 5(August): 200–210.

Taylor, T., and A. Clough. 2018. “Critical Review of Automotive Hot-Stamped Sheet Steel from an Industrial Perspective.” *Materials Science and Technology (United Kingdom)* 34(7): 809–61. https://doi.org/10.1080/02670836.2018.1425239.

Teixeira de Freitas, Sofia, and Jos Sinke. 2015. “Failure Analysis of Adhesively-Bonded Skin-to-Stiffener Joints: Metal-Metal vs. Composite-Metal.” *Engineering Failure Analysis* 56: 2–13. http://dx.doi.org/10.1016/j.engfailanal.2015.05.023.

ten Kortenaar, Lukas. 2016. “Failure Characterization of Hot Formed Boron Steels with Tailored Mechanical Properties - MASc Thesis.” https://uwspace.uwaterloo.ca/handle/10012/10351.

Trimiño, Luis F., and Duane S. Cronin. 2016. “Evaluation of Numerical Methods to Model Structural Adhesive Response and Failure in Tension and Shear Loading.” *Journal of Dynamic Behavior of Materials* 2(1): 122–37.

Tsai, M. Y., and J. Morton. 1995. “The Effect of a Spew Fillet on Adhesive Stress Distributions in Laminated Composite Single-Lap Joints.” *Composite Structures* 32(1–4): 123–31.

U.S. Dep of Energy. 2013. *Workshop Report: Light-Duty Vehicles Technical Requirements and Gaps for Lightweight and Propulsion Materials (Final Report).* https://www1.eere.energy.gov/vehiclesandfuels/pdfs/wr_ldvehicles.pdf.

Uhlmann, E. Mernissi, A. El. 2008. “Pre-Treatment by Dry Ice Blasting for Adhesive Bonding.” *Prod. Eng. Res. Devel.*: 133–38.

Vaissiere, L., J. P. Laurent, and A. Reinhardt. 2002. “Development of Pre-Coated Boron Steel for Applications on PSA Peugeot Citroën and RENAULT Bodies in White.” *SAE TECHNICAL PAPER SERIES*.

Varacalle, Dominic J. et al. 2006. “Effect of Grit-Blasting on Substrate Roughness and Coating Adhesion.” *Journal of Thermal Spray Technology* 15(3): 348–55.

Vazirani, H.N. 1969. “Surface Preparation of Steel for Adhesive Bonding and Organic Coatings.” *The Journal of Adhesion* 1(3): 222–32.

Walker, P. 1991. “Organosilanes As Adhesion Promoters.” *Journal of Adhesion Science and Technology* 5(4): 279–305.

Wan, Hailang, Jianping Lin, and Junying Min. 2018. “Effect of Laser Ablation Treatment on Corrosion Resistance of Adhesive-Bonded Al Alloy Joints.” *Surface and Coatings Technology* 345(January): 13–21. https://doi.org/10.1016/j.surfcoat.2018.03.087.

Wang, Binhua, Xiaozhi Hu, and Pengmin Lu. 2017. “Improvement of Adhesive Bonding of Grit-Blasted Steel Substrates by Using Diluted Resin as a Primer.” *International Journal of Adhesion and Adhesives* 73: 92–99. http://dx.doi.org/10.1016/j.ijadhadh.2016.11.012.

Wang, Kai, Yongming Jin, Bin Zhu, and Yisheng Zhang. 2017. “Investigation on Cracking Characteristics of Al–Si Coating on Hot Stamping Boron Steel Parts Based on Surface Strain Analysis.” *Surface and Coatings Technology* 309: 282–94. http://dx.doi.org/10.1016/j.surfcoat.2016.11.046.

Watson, Brock. 2019. “Personal Communication with Brock Watson Who Kindly Provided the Tested Specimens of Mode I (RDCB), Mode II (BDS), and Mixed-Mode (MM45) Tested Specimens.”

Watson, Brock, Chi Hsiang Liao, Michael J. Worswick, and Duane Steven Cronin. 2018. “Mode I Traction-Separation Measured Using Rigid Double Cantilever Beam Applied to Structural Adhesive.” *Journal of Adhesion*: 1–21. 10.1080/00218464.2018.1502666.

Watson, Brock, Yogesh Nandwani, Michael J. Worswick, and Duane S. Cronin. 2019. “Metallic Multi-Material Adhesive Joint Testing and Modeling for Vehicle Lightweighting.” *International Journal of Adhesion and Adhesives* 95. https://doi.org/10.1016/j.ijadhadh.2019.102421.

Watson, Brock, Michael J. Worswick, and Duane S. Cronin. 2019. “Identification of Shear Sample Test Geometry for Bulk Adhesive Characterization.” *Conference Proceedings of the Society for Experimental Mechanics Series* 4: 47–50.

Windmann, M, A Röttger, and W Theisen. 2013. “Phase Formation at the Interface between a Boron Alloyed Steel Substrate and an Al-Rich Coating.” *Surface & Coatings Technology* 226: 130–39. http://dx.doi.org/10.1016/j.surfcoat.2013.03.045.

Windmann, M, A Röttger, and W Theisen. 2014. “Formation of Intermetallic Phases in Al-Coated Hot-Stamped 22MnB5 Sheets in Terms of Coating Thickness and Si Content.” *Surface and Coatings Technology* 246: 17–25.

Wolf, Susan J et al. 2011. “Adhesive Bonding Performance of GA Coated 590 MPa Tensile Strength Steels.” *SAE International*.

Yee, A. F., and R. A. Pearson. 1986. “Toughening Mechanisms in Elastomer-Modified Epoxies - Part 1 Mechanical Studies.” *Journal of Materials Science* 21(7): 2462–74.

Yokoyama, T. 2003. “Experimental Determination of Impact Tensile Properties of Adhesive Butt Joints with the Split Hopkinson Bar.” *Journal of Strain Analysis for Engineering Design* 38(3): 233–45.

Zhang, Hui et al. 2008. “Fracture Behaviours of in Situ Silica Nanoparticle-Filled Epoxy at Different Temperatures.” *Polymer* 49(17): 3816–25.

Appendix A: Copyright Permissions

ELSEVIER LICENSE
TERMS AND CONDITIONS

May 06, 2020

This Agreement between Chi-Hsiang ("You") and Elsevier ("Elsevier") consists of your license details and the terms and conditions provided by Elsevier and Copyright Clearance Center.

License Number	4823220684722
License date	May 06, 2020
Licensed Content Publisher	Elsevier
Licensed Content Publication	Journal of Materials Processing Technology
Licensed Content Title	A review on hot stamping
Licensed Content Author	H. Karbasian,A.E. Tekkaya
Licensed Content Date	Nov 19, 2010
Licensed Content Volume	210
Licensed Content Issue	15
Licensed Content Pages	16
Start Page	2103
End Page	2118
Type of Use	reuse in a thesis/dissertation
Portion	figures/tables/illustrations
Number of figures/tables/illustrations	1
Format	both print and electronic
Are you the author of this Elsevier article?	No
Will you be translating?	No
Title	Effect of Surface Treatment on Joint Performance and Fracture Morphology in Adhesively Bonded Al-Si Coated Ultra-High Strength Steel
Institution name	University of Waterloo
Expected presentation date	May 2020
Portions	Figure 2.1
Requestor Location	Chi-Hsiang 200 University Avenue Waterloo, ON N2L 3E9 Canada Attn: Chi-Hsiang
Publisher Tax ID	GB 494 6272 12
Total	0.00 CAD

SPRINGER NATURE LICENSE
TERMS AND CONDITIONS

May 06, 2020

This Agreement between Chi-Hsiang ("You") and Springer Nature ("Springer Nature") consists of your license details and the terms and conditions provided by Springer Nature and Copyright Clearance Center.

License Number	4823221026903
License date	May 06, 2020
Licensed Content Publisher	Springer Nature
Licensed Content Publication	International Journal of Material Forming
Licensed Content Title	Development of a hot stamped channel section with axially tailored properties – experiments and models
Licensed Content Author	Kaab Omer et al
Licensed Content Date	Feb 24, 2017
Type of Use	Thesis/Dissertation
Requestor type	academic/university or research institute
Format	print and electronic
Portion	figures/tables/illustrations
Number of figures/tables/illustrations	2
Will you be translating?	no
Circulation/distribution	30 - 99
Author of this Springer Nature content	no
Title	Effect of Surface Treatment on Joint Performance and Fracture Morphology in Adhesively Bonded Al-Si Coated Ultra-High Strength Steel
Institution name	University of Waterloo
Expected presentation date	May 2020
Portions	Figure 2.5 and Figure 2.6
Requestor Location	Chi-Hsiang 200 University Avenue Waterloo, ON N2L 3E9 Canada Attn: Chi-Hsiang
Total	0.00 CAD

ELSEVIER LICENSE
TERMS AND CONDITIONS
May 06, 2020

This Agreement between Chi-Hsiang ("You") and Elsevier ("Elsevier") consists of your license details and the terms and conditions provided by Elsevier and Copyright Clearance Center.

License Number	4823221134506
License date	May 06, 2020
Licensed Content Publisher	Elsevier
Licensed Content Publication	Journal of Materials Processing Technology
Licensed Content Title	Tribological characteristics of high strength steel sheets under hot stamping conditions
Licensed Content Author	A. Ghiotti,S. Bruschi,F. Borsetto
Licensed Content Date	Nov 1, 2011
Licensed Content Volume	211
Licensed Content Issue	11
Licensed Content Pages	7
Start Page	1694
End Page	1700
Type of Use	reuse in a thesis/dissertation
Portion	figures/tables/illustrations
Number of figures/tables/illustrations	2
Format	both print and electronic
Are you the author of this Elsevier article?	No
Will you be translating?	No
Title	Effect of Surface Treatment on Joint Performance and Fracture Morphology in Adhesively Bonded Al-Si Coated Ultra-High Strength Steel
Institution name	University of Waterloo
Expected presentation date	May 2020
Portions	Figure 2.7a and Figure 2.9
Requestor Location	Chi-Hsiang 200 University Avenue Waterloo, ON N2L 3E9 Canada Attn: Chi-Hsiang
Publisher Tax ID	GB 494 6272 12
Total	0.00 CAD

ELSEVIER LICENSE
TERMS AND CONDITIONS
May 06, 2020

This Agreement between Chi-Hsiang ("You") and Elsevier ("Elsevier") consists of your license details and the terms and conditions provided by Elsevier and Copyright Clearance Center.

License Number	4823221221507
License date	May 06, 2020
Licensed Content Publisher	Elsevier
Licensed Content Publication	Surface and Coatings Technology
Licensed Content Title	Formation of intermetallic phases in Al-coated hot-stamped 22MnB5 sheets in terms of coating thickness and Si content
Licensed Content Author	M. Windmann,A. Röttger,W. Theisen
Licensed Content Date	May 15, 2014
Licensed Content Volume	246
Licensed Content Issue	n/a
Licensed Content Pages	9
Start Page	17
End Page	25
Type of Use	reuse in a thesis/dissertation
Portion	figures/tables/illustrations
Number of figures/tables/illustrations	1
Format	both print and electronic
Are you the author of this Elsevier article?	No
Will you be translating?	No
Title	Effect of Surface Treatment on Joint Performance and Fracture Morphology in Adhesively Bonded Al-Si Coated Ultra-High Strength Steel
Institution name	University of Waterloo
Expected presentation date	May 2020
Portions	Figure 2.7b
Requestor Location	Chi-Hsiang 200 University Avenue Waterloo, ON N2L 3E9 Canada Attn: Chi-Hsiang
Publisher Tax ID	GB 494 6272 12
Total	0.00 CAD

ELSEVIER LICENSE
TERMS AND CONDITIONS
May 06, 2020

This Agreement between Chi-Hsiang ("You") and Elsevier ("Elsevier") consists of your license details and the terms and conditions provided by Elsevier and Copyright Clearance Center.

License Number	4823230179134
License date	May 06, 2020
Licensed Content Publisher	Elsevier
Licensed Content Publication	Surface and Coatings Technology
Licensed Content Title	Investigation on cracking characteristics of Al–Si coating on hot stamping boron steel parts based on surface strain analysis
Licensed Content Author	Kai Wang,Yongming Jin,Bin Zhu,Yisheng Zhang
Licensed Content Date	Jan 15, 2017
Licensed Content Volume	309
Licensed Content Issue	n/a
Licensed Content Pages	13
Start Page	282
End Page	294
Type of Use	reuse in a thesis/dissertation
Portion	figures/tables/illustrations
Number of figures/tables/illustrations	2
Format	both print and electronic
Are you the author of this Elsevier article?	No
Will you be translating?	No
Title	Effect of Surface Treatment on Joint Performance and Fracture Morphology in Adhesively Bonded Al-Si Coated Ultra-High Strength Steel
Institution name	University of Waterloo
Expected presentation date	May 2020
Portions	Figure 2.10 and Figure 2.12
Requestor Location	Chi-Hsiang 200 University Avenue Waterloo, ON N2L 3E9 Canada Attn: Chi-Hsiang
Publisher Tax ID	GB 494 6272 12
Total	0.00 CAD

SPRINGER NATURE LICENSE
TERMS AND CONDITIONS

May 06, 2020

This Agreement between Chi-Hsiang ("You") and Springer Nature ("Springer Nature") consists of your license details and the terms and conditions provided by Springer Nature and Copyright Clearance Center.

License Number	4823230274479
License date	May 06, 2020
Licensed Content Publisher	Springer Nature
Licensed Content Publication	Metallurgical and Materials Transactions A
Licensed Content Title	Evolution of Phases, Microstructure, and Surface Roughness during Heat Treatment of Aluminized Low Carbon Steel
Licensed Content Author	Frank Jenner et al
Licensed Content Date	Apr 1, 2010
Type of Use	Thesis/Dissertation
Requestor type	academic/university or research institute
Format	print and electronic
Portion	figures/tables/illustrations
Number of figures/tables/illustrations	1
Will you be translating?	no
Circulation/distribution	50000 or greater
Author of this Springer Nature content	no
Title	Effect of Surface Treatment on Joint Performance and Fracture Morphology in Adhesively Bonded Al-Si Coated Ultra-High Strength Steel
Institution name	University of Waterloo
Expected presentation date	May 2020
Portions	Figure 2.11
Requestor Location	Chi-Hsiang 200 University Avenue Waterloo, ON N2L 3E9 Canada Attn: Chi-Hsiang
Total	0.00 CAD

ELSEVIER LICENSE
TERMS AND CONDITIONS
May 06, 2020

This Agreement between Chi-Hsiang ("You") and Elsevier ("Elsevier") consists of your license details and the terms and conditions provided by Elsevier and Copyright Clearance Center.

License Number	4823251380071
License date	May 06, 2020
Licensed Content Publisher	Elsevier
Licensed Content Publication	International Journal of Adhesion and Adhesives
Licensed Content Title	Behavior of adhesively bonded coated steel for automotive applications under impact loads
Licensed Content Author	M. Schiel,S. Kreling,C. Unger,F. Fischer,K. Dilger
Licensed Content Date	Jan 1, 2015
Licensed Content Volume	56
Licensed Content Issue	n/a
Licensed Content Pages	9
Start Page	32
End Page	40
Type of Use	reuse in a thesis/dissertation
Portion	figures/tables/illustrations
Number of figures/tables/illustrations	1
Format	both print and electronic
Are you the author of this Elsevier article?	No
Will you be translating?	No
Title	Effect of Surface Treatment on Joint Performance and Fracture Morphology in Adhesively Bonded Al-Si Coated Ultra-High Strength Steel
Institution name	University of Waterloo
Expected presentation date	May 2020
Portions	Figure 2.14
Requestor Location	Chi-Hsiang 200 University Avenue Waterloo, ON N2L 3E9 Canada Attn: Chi-Hsiang
Publisher Tax ID	GB 494 6272 12
Total	0.00 CAD

ELSEVIER LICENSE
TERMS AND CONDITIONS
May 06, 2020

This Agreement between Chi-Hsiang ("You") and Elsevier ("Elsevier") consists of your license details and the terms and conditions provided by Elsevier and Copyright Clearance Center.

License Number	4823260019979
License date	May 06, 2020
Licensed Content Publisher	Elsevier
Licensed Content Publication	International Journal of Adhesion and Adhesives
Licensed Content Title	Chemical conversion coatings for structural adhesive bonding of plain carbon steels
Licensed Content Author	G.W Critchlow,P.W Webb,C.J Tremlett,K Brown
Licensed Content Date	Apr 1, 2000
Licensed Content Volume	20
Licensed Content Issue	2
Licensed Content Pages	10
Start Page	113
End Page	122
Type of Use	reuse in a thesis/dissertation
Portion	figures/tables/illustrations
Number of figures/tables/illustrations	2
Format	both print and electronic
Are you the author of this Elsevier article?	No
Will you be translating?	No
Title	Effect of Surface Treatment on Joint Performance and Fracture Morphology in Adhesively Bonded Al-Si Coated Ultra-High Strength Steel
Institution name	University of Waterloo
Expected presentation date	May 2020
Portions	Figure 2.25
Requestor Location	Chi-Hsiang 200 University Avenue Waterloo, ON N2L 3E9 Canada Attn: Chi-Hsiang
Publisher Tax ID	GB 494 6272 12
Total	0.00 CAD

ELSEVIER LICENSE
TERMS AND CONDITIONS
May 06, 2020

This Agreement between Chi-Hsiang ("You") and Elsevier ("Elsevier") consists of your license details and the terms and conditions provided by Elsevier and Copyright Clearance Center.

License Number	4823260080115
License date	May 06, 2020
Licensed Content Publisher	Elsevier
Licensed Content Publication	Journal of Materials Processing Technology
Licensed Content Title	The effects of surface roughness on the strength of adhesively bonded cylindrical components
Licensed Content Author	Tezcan Şekercíoğlu,Hikmet Rende,Alper Gülsöz,Cemal Meran
Licensed Content Date	Nov 10, 2003
Licensed Content Volume	142
Licensed Content Issue	1
Licensed Content Pages	5
Start Page	82
End Page	86
Type of Use	reuse in a thesis/dissertation
Portion	figures/tables/illustrations
Number of figures/tables/illustrations	1
Format	both print and electronic
Are you the author of this Elsevier article?	No
Will you be translating?	No
Title	Effect of Surface Treatment on Joint Performance and Fracture Morphology in Adhesively Bonded Al-Si Coated Ultra-High Strength Steel
Institution name	University of Waterloo
Expected presentation date	May 2020
Portions	Figure 2.27
Requestor Location	Chi-Hsiang 200 University Avenue Waterloo, ON N2L 3E9 Canada Attn: Chi-Hsiang
Publisher Tax ID	GB 494 6272 12
Total	0.00 CAD

SPRINGER NATURE LICENSE
TERMS AND CONDITIONS

May 06, 2020

This Agreement between Chi-Hsiang ("You") and Springer Nature ("Springer Nature") consists of your license details and the terms and conditions provided by Springer Nature and Copyright Clearance Center.

License Number	4823260200220
License date	May 06, 2020
Licensed Content Publisher	Springer Nature
Licensed Content Publication	Production Engineering
Licensed Content Title	Pre-treatment by dry ice blasting for adhesive bonding
Licensed Content Author	E. Uhlmann et al
Licensed Content Date	Apr 22, 2008
Type of Use	Thesis/Dissertation
Requestor type	academic/university or research institute
Format	print and electronic
Portion	figures/tables/illustrations
Number of figures/tables/illustrations	1
Will you be translating?	no
Circulation/distribution	50000 or greater
Author of this Springer Nature content	no
Title	Effect of Surface Treatment on Joint Performance and Fracture Morphology in Adhesively Bonded Al-Si Coated Ultra-High Strength Steel
Institution name	University of Waterloo
Expected presentation date	May 2020
Portions	Figure 2.30
Requestor Location	Chi-Hsiang 200 University Avenue Waterloo, ON N2L 3E9 Canada Attn: Chi-Hsiang
Total	0.00 CAD

ELSEVIER LICENSE
TERMS AND CONDITIONS
May 06, 2020

This Agreement between Chi-Hsiang ("You") and Elsevier ("Elsevier") consists of your license details and the terms and conditions provided by Elsevier and Copyright Clearance Center.

License Number	4823260454592
License date	May 06, 2020
Licensed Content Publisher	Elsevier
Licensed Content Publication	International Journal of Adhesion and Adhesives
Licensed Content Title	Cryoblasting as a pretreatment to enhance adhesion to aluminium alloys: an initial study
Licensed Content Author	D.M. Brewis,G.W. Critchlow,C.A. Curtis
Licensed Content Date	Aug 1, 1999
Licensed Content Volume	19
Licensed Content Issue	4
Licensed Content Pages	4
Start Page	253
End Page	256
Type of Use	reuse in a thesis/dissertation
Portion	figures/tables/illustrations
Number of figures/tables/illustrations	2
Format	both print and electronic
Are you the author of this Elsevier article?	No
Will you be translating?	No
Title	Effect of Surface Treatment on Joint Performance and Fracture Morphology in Adhesively Bonded Al-Si Coated Ultra-High Strength Steel
Institution name	University of Waterloo
Expected presentation date	May 2020
Portions	Figure 2.31
Requestor Location	Chi-Hsiang 200 University Avenue Waterloo, ON N2L 3E9 Canada Attn: Chi-Hsiang
Publisher Tax ID	GB 494 6272 12
Total	0.00 CAD

ELSEVIER LICENSE
TERMS AND CONDITIONS
May 06, 2020

This Agreement between Chi-Hsiang ("You") and Elsevier ("Elsevier") consists of your license details and the terms and conditions provided by Elsevier and Copyright Clearance Center.

License Number	4823260540742
License date	May 06, 2020
Licensed Content Publisher	Elsevier
Licensed Content Publication	Surface and Coatings Technology
Licensed Content Title	Effect of laser ablation treatment on corrosion resistance of adhesive-bonded Al alloy joints
Licensed Content Author	Hailang Wan,Jianping Lin,Junying Min
Licensed Content Date	Jul 15, 2018
Licensed Content Volume	345
Licensed Content Issue	n/a
Licensed Content Pages	9
Start Page	13
End Page	21
Type of Use	reuse in a thesis/dissertation
Portion	figures/tables/illustrations
Number of figures/tables/illustrations	3
Format	both print and electronic
Are you the author of this Elsevier article?	No
Will you be translating?	No
Title	Effect of Surface Treatment on Joint Performance and Fracture Morphology in Adhesively Bonded Al-Si Coated Ultra-High Strength Steel
Institution name	University of Waterloo
Expected presentation date	May 2020
Portions	Figure 2.33
Requestor Location	Chi-Hsiang 200 University Avenue Waterloo, ON N2L 3E9 Canada Attn: Chi-Hsiang
Publisher Tax ID	GB 494 6272 12
Total	0.00 CAD

ELSEVIER LICENSE
TERMS AND CONDITIONS
May 06, 2020

This Agreement between Chi-Hsiang ("You") and Elsevier ("Elsevier") consists of your license details and the terms and conditions provided by Elsevier and Copyright Clearance Center.

License Number	4823260614352
License date	May 06, 2020
Licensed Content Publisher	Elsevier
Licensed Content Publication	Polymer
Licensed Content Title	Deformation and fracture behaviour of a rubber-toughened epoxy: 1. Microstructure and fracture studies
Licensed Content Author	A.J. Kinloch,S.J. Shaw,D.A. Tod,D.L. Hunston
Licensed Content Date	Oct 1, 1983
Licensed Content Volume	24
Licensed Content Issue	10
Licensed Content Pages	14
Start Page	1341
End Page	1354
Type of Use	reuse in a thesis/dissertation
Portion	figures/tables/illustrations
Number of figures/tables/illustrations	4
Format	both print and electronic
Are you the author of this Elsevier article?	No
Will you be translating?	No
Title	Effect of Surface Treatment on Joint Performance and Fracture Morphology in Adhesively Bonded Al-Si Coated Ultra-High Strength Steel
Institution name	University of Waterloo
Expected presentation date	May 2020
Portions	Figure 2.34 and Figure 2.35
Requestor Location	Chi-Hsiang 200 University Avenue Waterloo, ON N2L 3E9 Canada Attn: Chi-Hsiang
Publisher Tax ID	GB 494 6272 12
Total	0.00 CAD

SPRINGER NATURE LICENSE
TERMS AND CONDITIONS

May 06, 2020

This Agreement between Chi-Hsiang ("You") and Springer Nature ("Springer Nature") consists of your license details and the terms and conditions provided by Springer Nature and Copyright Clearance Center.

License Number	4823260689571
License date	May 06, 2020
Licensed Content Publisher	Springer Nature
Licensed Content Publication	Journal of Materials Science (full set)
Licensed Content Title	Toughening mechanisms in elastomer-modified epoxies
Licensed Content Author	A. F. Yee et al
Licensed Content Date	Jan 1, 1986
Type of Use	Thesis/Dissertation
Requestor type	academic/university or research institute
Format	print and electronic
Portion	figures/tables/illustrations
Number of figures/tables/illustrations	1
Will you be translating?	no
Circulation/distribution	50000 or greater
Author of this Springer Nature content	no
Title	Effect of Surface Treatment on Joint Performance and Fracture Morphology in Adhesively Bonded Al-Si Coated Ultra-High Strength Steel
Institution name	University of Waterloo
Expected presentation date	May 2020
Portions	Figure 2.36
Requestor Location	Chi-Hsiang 200 University Avenue Waterloo, ON N2L 3E9 Canada Attn: Chi-Hsiang
Total	0.00 CAD

ELSEVIER LICENSE
TERMS AND CONDITIONS
May 06, 2020

This Agreement between Chi-Hsiang ("You") and Elsevier ("Elsevier") consists of your license details and the terms and conditions provided by Elsevier and Copyright Clearance Center.

License Number	4823260774850
License date	May 06, 2020
Licensed Content Publisher	Elsevier
Licensed Content Publication	Journal of the Mechanics and Physics of Solids
Licensed Content Title	Constraint effects in adhesive joint fracture
Licensed Content Author	T. Pardoen,T. Ferracin,C.M. Landis,F. Delannay
Licensed Content Date	Sep 1, 2005
Licensed Content Volume	53
Licensed Content Issue	9
Licensed Content Pages	33
Start Page	1951
End Page	1983
Type of Use	reuse in a thesis/dissertation
Portion	figures/tables/illustrations
Number of figures/tables/illustrations	1
Format	both print and electronic
Are you the author of this Elsevier article?	No
Will you be translating?	No
Title	Effect of Surface Treatment on Joint Performance and Fracture Morphology in Adhesively Bonded Al-Si Coated Ultra-High Strength Steel
Institution name	University of Waterloo
Expected presentation date	May 2020
Portions	Figure 2.37
Requestor Location	Chi-Hsiang 200 University Avenue Waterloo, ON N2L 3E9 Canada Attn: Chi-Hsiang
Publisher Tax ID	GB 494 6272 12
Total	0.00 CAD

ELSEVIER LICENSE
TERMS AND CONDITIONS
May 06, 2020

This Agreement between Chi-Hsiang ("You") and Elsevier ("Elsevier") consists of your license details and the terms and conditions provided by Elsevier and Copyright Clearance Center.

License Number	4823260832820
License date	May 06, 2020
Licensed Content Publisher	Elsevier
Licensed Content Publication	International Journal of Solids and Structures
Licensed Content Title	Strength and toughness in shear of constrained layers
Licensed Content Author	Anders Biel,Ulf Stigh
Licensed Content Date	1 May 2018
Licensed Content Volume	138
Licensed Content Issue	n/a
Licensed Content Pages	14
Start Page	50
End Page	63
Type of Use	reuse in a thesis/dissertation
Portion	figures/tables/illustrations
Number of figures/tables/illustrations	1
Format	both print and electronic
Are you the author of this Elsevier article?	No
Will you be translating?	No
Title	Effect of Surface Treatment on Joint Performance and Fracture Morphology in Adhesively Bonded Al-Si Coated Ultra-High Strength Steel
Institution name	University of Waterloo
Expected presentation date	May 2020
Portions	Figure 2.38
Requestor Location	Chi-Hsiang 200 University Avenue Waterloo, ON N2L 3E9 Canada Attn: Chi-Hsiang
Publisher Tax ID	GB 494 6272 12
Total	0.00 CAD

SPRINGER NATURE LICENSE
TERMS AND CONDITIONS

May 06, 2020

This Agreement between Chi-Hsiang ("You") and Springer Nature ("Springer Nature") consists of your license details and the terms and conditions provided by Springer Nature and Copyright Clearance Center.

License Number	4823270954139
License date	May 06, 2020
Licensed Content Publisher	Springer Nature
Licensed Content Publication	International Journal of Fracture
Licensed Content Title	Shear fracture
Licensed Content Author	Herzl Chai
Licensed Content Date	Dec 31, 1969
Type of Use	Thesis/Dissertation
Requestor type	academic/university or research institute
Format	print and electronic
Portion	figures/tables/illustrations
Number of figures/tables/illustrations	2
Will you be translating?	no
Circulation/distribution	50000 or greater
Author of this Springer Nature content	no
Title	Effect of Surface Treatment on Joint Performance and Fracture Morphology in Adhesively Bonded Al-Si Coated Ultra-High Strength Steel
Institution name	University of Waterloo
Expected presentation date	May 2020
Portions	Figure 2.39
Requestor Location	Chi-Hsiang 200 University Avenue Waterloo, ON N2L 3E9 Canada Attn: Chi-Hsiang
Total	0.00 CAD

SPRINGER NATURE LICENSE
TERMS AND CONDITIONS

May 06, 2020

This Agreement between Chi-Hsiang ("You") and Springer Nature ("Springer Nature") consists of your license details and the terms and conditions provided by Springer Nature and Copyright Clearance Center.

License Number	4823260977189
License date	May 06, 2020
Licensed Content Publisher	Springer Nature
Licensed Content Publication	Experimental Mechanics
Licensed Content Title	Experimental evaluation of mixed-mode fracture in adhesive bonds
Licensed Content Author	Herzl Chai
Licensed Content Date	Dec 31, 1969
Type of Use	Thesis/Dissertation
Requestor type	academic/university or research institute
Format	print and electronic
Portion	figures/tables/illustrations
Number of figures/tables/illustrations	1
Will you be translating?	no
Circulation/distribution	50000 or greater
Author of this Springer Nature content	no
Title	Effect of Surface Treatment on Joint Performance and Fracture Morphology in Adhesively Bonded Al-Si Coated Ultra-High Strength Steel
Institution name	University of Waterloo
Expected presentation date	May 2020
Portions	Figure 2.40
Requestor Location	Chi-Hsiang 200 University Avenue Waterloo, ON N2L 3E9 Canada Attn: Chi-Hsiang
Total	0.00 CAD

ELSEVIER LICENSE
TERMS AND CONDITIONS
May 06, 2020

This Agreement between Chi-Hsiang ("You") and Elsevier ("Elsevier") consists of your license details and the terms and conditions provided by Elsevier and Copyright Clearance Center.

License Number	4823261060517
License date	May 06, 2020
Licensed Content Publisher	Elsevier
Licensed Content Publication	International Journal of Adhesion and Adhesives
Licensed Content Title	Evolution of crack path and fracture surface with degradation in rubber-toughened epoxy adhesive joints: Application to open-faced specimens
Licensed Content Author	A. Ameli,M. Papini,J.K. Spelt
Licensed Content Date	Sep 1, 2011
Licensed Content Volume	31
Licensed Content Issue	6
Licensed Content Pages	11
Start Page	530
End Page	540
Type of Use	reuse in a thesis/dissertation
Portion	figures/tables/illustrations
Number of figures/tables/illustrations	1
Format	both print and electronic
Are you the author of this Elsevier article?	No
Will you be translating?	No
Title	Effect of Surface Treatment on Joint Performance and Fracture Morphology in Adhesively Bonded Al-Si Coated Ultra-High Strength Steel
Institution name	University of Waterloo
Expected presentation date	May 2020
Portions	Figure 2.41
Requestor Location	Chi-Hsiang 200 University Avenue Waterloo, ON N2L 3E9 Canada Attn: Chi-Hsiang
Publisher Tax ID	GB 494 6272 12
Total	0.00 CAD

ELSEVIER LICENSE
TERMS AND CONDITIONS
May 06, 2020

This Agreement between Chi-Hsiang ("You") and Elsevier ("Elsevier") consists of your license details and the terms and conditions provided by Elsevier and Copyright Clearance Center.

License Number	4823261115694
License date	May 06, 2020
Licensed Content Publisher	Elsevier
Licensed Content Publication	Polymer
Licensed Content Title	Fracture behaviours of in situ silica nanoparticle-filled epoxy at different temperatures
Licensed Content Author	Hui Zhang,Long-Cheng Tang,Zhong Zhang,Klaus Friedrich,Stephan Sprenger
Licensed Content Date	Aug 11, 2008
Licensed Content Volume	49
Licensed Content Issue	17
Licensed Content Pages	10
Start Page	3816
End Page	3825
Type of Use	reuse in a thesis/dissertation
Portion	figures/tables/illustrations
Number of figures/tables/illustrations	2
Format	both print and electronic
Are you the author of this Elsevier article?	No
Will you be translating?	No
Title	Effect of Surface Treatment on Joint Performance and Fracture Morphology in Adhesively Bonded Al-Si Coated Ultra-High Strength Steel
Institution name	University of Waterloo
Expected presentation date	May 2020
Portions	Figure 2.42
Requestor Location	Chi-Hsiang 200 University Avenue Waterloo, ON N2L 3E9 Canada Attn: Chi-Hsiang
Publisher Tax ID	GB 494 6272 12
Total	0.00 CAD

ELSEVIER LICENSE
TERMS AND CONDITIONS
May 06, 2020

This Agreement between Chi-Hsiang ("You") and Elsevier ("Elsevier") consists of your license details and the terms and conditions provided by Elsevier and Copyright Clearance Center.

License Number	4823261156971
License date	May 06, 2020
Licensed Content Publisher	Elsevier
Licensed Content Publication	Engineering Failure Analysis
Licensed Content Title	Failure analysis of adhesively-bonded skin-to-stiffener joints: Metal–metal vs. composite–metal
Licensed Content Author	Sofia Teixeira de Freitas,Jos Sinke
Licensed Content Date	Oct 1, 2015
Licensed Content Volume	56
Licensed Content Issue	n/a
Licensed Content Pages	12
Start Page	2
End Page	13
Type of Use	reuse in a thesis/dissertation
Portion	figures/tables/illustrations
Number of figures/tables/illustrations	2
Format	both print and electronic
Are you the author of this Elsevier article?	No
Will you be translating?	No
Title	Effect of Surface Treatment on Joint Performance and Fracture Morphology in Adhesively Bonded Al-Si Coated Ultra-High Strength Steel
Institution name	University of Waterloo
Expected presentation date	May 2020
Portions	Figure 2.43
Requestor Location	Chi-Hsiang 200 University Avenue Waterloo, ON N2L 3E9 Canada Attn: Chi-Hsiang
Publisher Tax ID	GB 494 6272 12
Total	0.00 CAD